# HIGHER-ORDER EFFECTS IN CONDENSED PHASE SPECTROSCOPY AND DYNAMICS

Thomas Paul Cheshire

A dissertation submitted to the faculty at the University of North Carolina at Chapel Hill in partial fulfillment of the requirements for the degree of Doctor of Philosophy in the Department of Chemistry.

Chapel Hill
2018

Approved by:

Andrew Moran

Yosuke Kanai

Max Berkowitz

Jim Cahoon

Joanna Atkin

© 2018
Thomas Paul Cheshire
ALL RIGHTS RESERVED

## ABSTRACT

Thomas Paul Cheshire: Higher-Order Effects in Condensed Phase Spectroscopy and Dynamics
(Under the direction of Andrew M. Moran)

Researchers in the 1970s wondered whether traditional Raman experiments could distinguish homogeneous and inhomogeneous line broadening mechanisms. Since then, a feedback between experiment and theory has spawned and matured the field of multidimensional Raman spectroscopy and laid the groundwork for modeling nonlinear photoinduced reaction pathways. Here two-dimensional resonance Raman (2DRR) spectroscopy is developed to investigate photochemical reaction mechanisms and structural heterogeneity in condensed phase systems. Models are developed to understand 2DRR spectra and extended to incorporate non-radiative transitions.

The photodissociation reaction of triiodide serves to uncover the capabilities of 2DRR. A unique pattern of 2DRR resonances is associated with the transition of a nuclear wavepacket from reactant to product. The pattern of resonances is reproduced by modeling the photodissociation as a vibronic coherence transfer. Transient absorption experiments performed on a transition metal complex composed of titanium and catechol, $[Ti(cat)_3]^{2-}$, exhibit signatures of coherent wavepacket motion initiated by back-electron transfer. The model used for triiodide photodissociation applies to this system, and calculations predict that vibrational coherences in the product are independent of whether the reactant undergoes coherent nuclear motion. Vibrational population-to-coherence transitions could accelerate the electron transfer (ET) process, regardless if vibrational dephasing is faster than the reaction rate--a prediction not captured by traditional ET models.

2DRR spectroscopy is further used to investigate oxygen- and water-ligated myoglobin line broadening mechanisms. Vibrational modes proximal to propionic acid side chains of the heme exhibit significant heterogeneity in the 2DRR spectra. A hydrophobic pocket encompasses the heme, but the side chains are exposed to solvent. Molecular dynamics (MD) simulations suggest that fluctuations in the side chain geometries are correlated with the heterogeneity. 2DRR spectra and MD simulations reveal that the side chains function as effective pathways for thermal relaxation.

Despite progress, a major challenge still plagues multidimensional Raman spectroscopy. Cascading signals radiated in the same direction as the desired signal can render a signal impossible to analyze. Simulations of 2DRR, femtosecond stimulated Raman spectroscopy, and the accompanying artifacts suggest solute-solute and solute-solvent interactions can significantly affect measured signals if experimental parameters are not carefully selected.

*To Aleksandra and Theia, without your love and support I would be lost.*

## ACKNOWLEDGEMENTS

I would like to express my sincerest gratitude for my research advisor, Dr. Andrew Moran. His resolute guidance has steered me true during my graduate studies. This spirit of mentorship has been passed along to former and present members of his research team, of which I am truly thankful. Dr. Paul Giokas and Dr. Brian Molesky were instrumental to my initiation and maturation in the field of nonlinear spectroscopy. And finally, the work in this dissertation was done in parallel with that of Dr. Zhenkun Guo, to whom I would like to extend my appreciation. Our research has been complementary over the last several years, and he has been patient, kind, and helpful every step along our path. For these reasons, these individuals, and so much more, I am deeply grateful.

## TABLE OF CONTENTS

## LIST OF TABLES

## LIST OF FIGURES

## LIST OF ABBREVIATIONS

| | |
|---|---|
| 2DRR | Two-dimensional resonance Raman |
| AP | Actinic pump |
| BBO | Beta barium borate |
| BET | Back electron transfer |
| CCD | Charge-coupled device |
| CMOS | Complementary metal oxide semiconductor |
| CSRS | Coherent stimulated Raman spectroscopy |
| CT | Charge transfer |
| DOS | Density of States |
| EFRC | Energy Frontier Research Center |
| ESA | Excited state absorption |
| ESE | Excited state emission |
| ET | Electron transfer |
| FSRS | Femtosecond stimulated Raman spectroscopy |
| FWHM | Full width half maximum |
| GSB | Ground state bleach |
| HGS | Hot ground state |
| HWHM | Half width half maximum |
| LEPS | London-Eyring-Polanyi-Sato |
| LMCT | Ligand to metal charge transfer |
| MD | Molecular dynamics |
| MEM | Maximum entropy method |
| PP | Pump-probe spectroscopy |
| RP | Raman pump |

| | |
|---|---|
| RP-D4WM | Resonant pump degenerate four wave mixing |
| St | Stokes pulse |
| TR-ISRS | Time resolved impulsive stimulated Raman spectroscopy |
| TRSRS | Time resolve spontaneous Raman spectroscopy |
| UV | Ultraviolet |
| VIS | Visible |

## LIST OF SYMBOLS

| | |
|---|---|
| $1D$ | One dimensional |
| $2D$ | Two dimensional |
| $A(\omega)$ | Molecular absorption spectrum |
| $a$ | Annihilation operator |
| $a^{\dagger}$ | Creation operator |
| $\alpha^2$ | Polarizability magnitude squared |
| $\alpha(\omega)$ | Frequency dependent polarizability |
| $\alpha(t)$ | Time dependent polarizability |
| $\mathring{A}$ | Angstrom |
| $atm$ | Atmosphere |
| $B_m$ | Boltzmann population of a vibrational state, such that $m$ is an integer representing the vibrational state |
| $C$ | Concentration |
| $c$ | Speed of light |
| $CaF_2$ | Calcium fluoride |
| $cm$ | Centimeter |
| $cm^{-1}$ | Wavenumber |
| $CS_2$ | Carbon disulfide |
| $\chi^{(n)}$ | Susceptibility of nth order |
| $D$ | Debye |
| $D(\tau)$ | Time dependent vibrational wavepacket |
| $\Delta(t)$ | Full width at half maximum |

| | |
|---|---|
| $\Delta^2$ | Variance in electronic energy gap |
| $d$ | Dimensionless displacement |
| $E(t)$ | Electric Field |
| $E^{(n)}$ | Signal field of nth order |
| $E_i$ | Energy level of state $i$, where $i$ can be an electronic or vibrational energy |
| $e$ | Electronic excited state index |
| $eV$ | Electron volt |
| $\varepsilon_0$ | Vacuum permittivity |
| $fs$ | Femtosecond |
| $\Phi_{L(R)}$ | Dihedral angle |
| $G(\eta_a, \eta_b)$ | Two dimensional Gaussian distribution |
| $\Delta G^0_{eg}$ | Free energy gap |
| $g$ | Electronic ground state index |
| $g/mm$ | Grooves per millimeter |
| $g/mol$ | Molar mass |
| $\Gamma_{eg}$ | Electronic dephasing |
| $\Gamma_{ij}$ | Dephasing of states $i$ and $j$, where $i$ and $j$ are vibrational states |
| $\Gamma_{rp}$ | Reactant-product dephasing |
| $\Gamma_{vib}$ | Vibrational dephasing |
| $\gamma(t)$ | Line broadening function |
| $H$ | Hamiltonian operator |
| h | Reduced Planck's constant |

| | |
|---|---|
| $\eta_a$ | Deviation of harmonic mode frequency, $a$. |
| $I_2^-$ | Diiodide |
| $I_3^-$ | Triiodide |
| $J(\omega)$ | Vibrational wavepacket |
| $K^{(n)}$ | Rate function of nth order |
| $k$ | Rate constant |
| $\boldsymbol{k_i}$ | Wavevector $i$, where $i$ represents field-matter interaction |
| $k_B$ | Boltzmann constant |
| $kHz$ | Kilohertz |
| $KI$ | Potassium iodide |
| $l$ | Path length |
| $\Lambda_{AP}$ | Actinic pump pulse width |
| $\Lambda_{RP}$ | Raman pump pulse width |
| $\Lambda_{UV}$ | UV pump pulse width |
| $\Lambda_{VIS}$ | VIS pump pulse width |
| $\Lambda^{-1}$ | Time scale of nuclear relaxation |
| $\lambda$ | Reorganization energy |
| $\lambda(t)$ | Absorption peak wavelength |
| $L(\omega)$ | Line shape function |
| $m$ | mass |
| $MbO_2$ | Oxymyoglobin |
| metMb | Metmyoglobin |

| | |
|---|---|
| $\mu J$ | Microjoule |
| $\mu m$ | Micrometer |
| $mL$ | Milliliter |
| $mm$ | Millimeter |
| $mM$ | Milli molar |
| $mmol$ | Milli mole |
| $mOD$ | Milli optical density |
| $\hat{\mu}$ | Dipole operator |
| $\mu_{ij}$ | Transition dipole magnitude between states $i$ and $j$, where $i$ and $j$ are electronic states |
| $N$ | Number of 'particles' |
| $N_A$ | Avogadro's number |
| $N_{\alpha m}$ | Number of vibrational quanta of normal mode $\alpha$ in basis $m$ |
| $nJ$ | Nanojoule |
| $nm$ | Nanometer |
| $ns$ | Nanosecond |
| $n(\omega)$ | Frequency dependent refractive index |
| $\omega$ | Angular frequency |
| $\mathrm{h}\omega_{eg}$ | Electronic energy gap |
| $\mathrm{h}\omega_{ij}$ | Energy difference between states $i$ and $j$, where $i$ and $j$ can be electronic, vibrational, or vibronic states |
| $\mathrm{h}\omega_{vib}$ | Vibrational energy difference |
| $\bar{\omega}_a$ | Average harmonic mode frequency, a |
| $\omega_{AP}$ | Actinic pump frequency |

| | |
|---|---|
| $\omega_L$ | Carrier frequency of incident light |
| $\omega_{RP}$ | Raman pump frequency |
| $\omega_{UV}$ | UV pump frequency |
| $\omega_{VIS}$ | VIS pump frequency |
| $\langle \omega_{vib}(\tau) \rangle$ | Average vibrational frequency |
| $P^{(n)}$ | Nth order polarization |
| $p(p*)$ | Ground (excite) state index of product |
| $ps$ | Picosecond |
| $Q$ | Primary oscillator coordinate |
| q | Generalized coordinate |
| $R^{(n)}$ | Nth order response function |
| $r(r*)$ | Ground (excite) state index of reactant |
| $\rho$ | Inter-mode correlation parameter |
| $\rho_{i,j}$ | Density matrix element for states $i$ and $j$, where $i$ and $j$ are vibronic states |
| $S^{(n)}(\tau,\omega)$ | Signal of $n$ field-matter interactions |
| $S_{\mathrm{P}}$ | Signal of parallel pump and probe |
| $S_{\perp}$ | Signal of perpendicular pump and probe |
| $\sigma_A$ | Absorption cross-section |
| $\sigma_a$ | Width of inhomogeneous distribution in mode, a |
| $\frac{\partial \sigma_R}{\partial \Omega}$ | Raman differential cross-section |
| $T$ | Temperature |

| | |
|---|---|
| $t$ | Time variable |
| $\tau$ | Time delay/interval |
| $Ti$ | Titanium |
| $\left[Ti\left(cat\right)_3\right]^{2-}$ | Titanium catechol anion |
| $TiO_2$ | Titanium dioxide |
| $U_{ijk}$ | Cubic expansion coefficient |
| $V_{eg}$ | Donor-acceptor coupling |
| $\xi_{AP}$ | Actinic pump electric field amplitude |
| $\xi_L$ | Carrier pulse electric field amplitude |
| $\xi_{RP}$ | Raman pump electric field amplitude |
| $\xi_{St}$ | Stokes pulse electric field amplitude |
| $\xi_{UV}$ | UV pump electric field amplitude |
| $\xi_{VIS}$ | VIS pump electric field amplitude |

# CHAPTER I: INTRODUCTION

## I. Overview

The central theme of this dissertation is the evolution of ideas from the feedback between experiment and theory. In this chapter, the history of multidimensional Raman spectroscopy and its challenges are explored as a foundation to the research in later chapters. The progress made in the field of multidimensional Raman spectroscopy would not have been possible without the parallel development in the theory of nonlinear optical spectroscopy. Chapters 2 and 3 will discuss the development of two-dimensional resonant Raman (2DRR) spectroscopy in the context of coherence transfer during the photodissociation reaction of triiodide. Coherence transfer is further discussed in chapter 6, as it relates to back-electron transfer in a transition metal complex. Chapter 4 investigates heterogeneity in the spectra of oxygen- and water-ligated myoglobin. And in chapter 7, the persistent challenge of cascading signals is explored in detail. Through these topics, this dissertation aims to accomplish the following:

- Development of six-wave mixing response functions for higher-order Raman spectroscopies
- Development of a model that yields transient absorption signatures of vibronic coherence transfer processes coupled to a chemical reaction
- Use simulations of 2DRR line shapes of myoglobin with molecular dynamics simulations and an *ab initio* map to analyze line broadening mechanisms
- First theoretical analysis of third-order cascades involving solute and solvent molecules

## II. Promises and Pitfalls of Multidimensional Raman Spectroscopies

### IIA. History of Higher-Order Raman Spectroscopies

Once the specialty of a handful of experimental groups, multidimensional laser spectroscopies have become fairly widespread in the past 20 years with applications spanning the traditional disciplines of chemistry, biology, and physics. A technique commonly referred to as two-dimensional spectroscopy, which adds a "pump" dimension to traditional pump-probe spectroscopy, is the most commonly employed multidimensional technique, but this was not always the case.[1-10] The development of modern multidimensional laser spectroscopies is rooted in the coherent Raman spectroscopies of the late 1970's and early 1980's.[11-14] It was unclear at the time whether or not traditional one-dimensional coherent Raman measurements could distinguish homogeneous and inhomogeneous line broadening mechanisms. Landmark theoretical papers by Mukamel and co-workers showed that higher-order (i.e. multidimensional) methods were indeed required,[15-16] and early success was achieved in Raman echo experiments (i.e., eight-wave mixing).[17] Several experimental groups took up the challenge of six-wave mixing experiments in the mid-1990's but met substantial technical challenges.[18-22] Success in these six-wave mixing measurements was achieved after nearly a decade of exhaustive efforts.[22-23] Problems encountered in these pioneering works significantly slowed the development of multidimensional Raman techniques. However, interest in this class of experiments has been reinitiated by related methods used to study molecular photochemistries.[24-28] The techniques developed in this dissertation involve aspects of both the old and new versions of multidimensional Raman spectroscopies.

Time-resolved spontaneous resonance Raman spectroscopy (TRSRRS) is technically a higher-order (three-photon) nonlinear spectroscopy, although it is typically not considered a multidimensional technique because of its incoherent nature (i.e., the probe step involves a

spontaneous Raman transition). Nonetheless, TRSRRS are among the most indispensible tools used to investigate photochemistries because resonance enhancement enables studies of dilute solutions and active sites in complex systems.[29-33] In TRSRRS, the process of interest is initiated with a laser pulse before interrogation with a time-delayed resonance Raman probe. Structural changes that accompany a wide variety of chemical reactions can be elucidated in this way (e.g., photochemical ring opening, proton transfer, and isomerization).[34-36] Despite strong selling points for studies of slower processes, TRSRRS experiments are inherently insensitive to dynamics on the 100-fs time-scale because of the tradeoff between time and frequency resolution made in the probing step. In essence, the spontaneous nature of the probe translates into uncertainty in the delay between the excitation and detection processes.

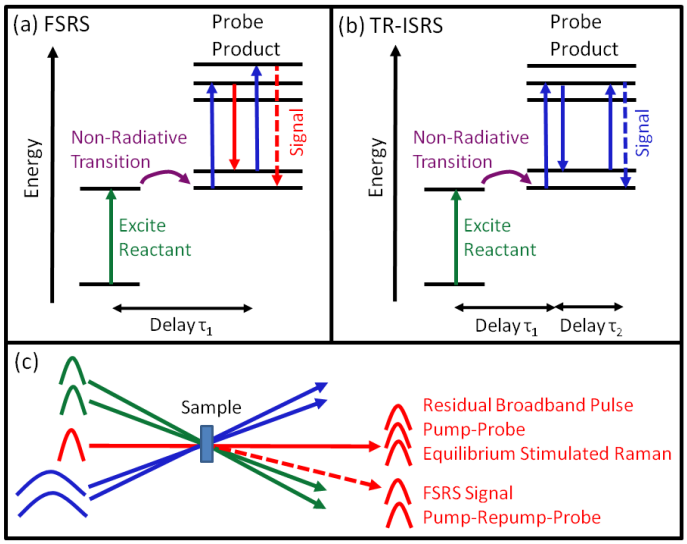


***Figure 1.1.*** *Key ideas associated with FSRS and TR-ISRS are illustrated with energy level diagrams. In both methods, a non-radiative transition is induced (e.g., electron transfer) by photoexciting a reactant. Vibrational resonances of the product are probed with either (a) a mixture of narrowband and broadband pulses in FSRS or (b) a sequence of femtosecond laser pulses in TR-ISRS. (c) The proposed experiments will be conducted with four or five incident laser beams to eliminate much of the undesired background present in conventional approaches. Sources of background are listed for FSRS; however, TR-ISRS is subject to analogous sources of background.*

Access to 100-fs time-scales requires use of a stimulated (rather than spontaneous) Raman probe. One popular approach of this type is known as Femtosecond Stimulated Raman Spectroscopy (FSRS).[25-26] In FSRS, the delay between the excitation and probe steps is known with high precision because vibrational motion is stimulated with a short laser pulse rather than "waiting" for a spontaneous fluctuation of the radiation field.[37-38] The time delay may be known with 100-fs precision; however, the frequency of the vibration can notably evolve while the vibration dephases (e.g., an effect that has been observed in rhodopsin).[38-39] Time-Resolved Impulsive Stimulated Raman Spectroscopies (TR-ISRS) is a closely related approach that employs only femtosecond laser pulses.[24] TR-ISRS is particularly useful for detecting low-frequency modes that are inaccessible to FSRS.[27-28] Key ideas associated with these two techniques are summarized in Figure 1.1.

### IIB. Susceptibility of Higher-Order Raman Spectroscopies to Insidious Artifacts: Third-Order Cascades

Cascading signals have been recognized as a serious experimental complication in off-resonant fifth-order (i.e. 2D) Raman experiments conducted on pure liquids.[18, 21-22, 40-42] As indicated in Figure 1.2, this artifact represents a process in which the four-wave mixing response from one molecule radiates a signal field that drives a four-wave mixing process on a second molecule. The second four-wave mixing signal (i.e., the cascaded signal) is radiated in the same direction as the desired response and carries many of the same spectroscopic signatures. In contrast, all five field-matter interactions take place with an individual molecule in a genuine six-wave mixing process, thereby yielding a direct fifth-order signal field. Under off-resonant conditions, the cascaded response can be many orders of magnitude larger than the 2D Raman signal. Success in measuring the off-resonant 2D Raman spectrum of $CS_2$ was finally achieved in 2002 when clever experimental geometries and detection schemes were developed to suppress

the cascaded signal intensity.[22-23] The possibility of conducting 2DRR spectroscopy without contributions from cascaded artifacts was first studied by our group in 2014.[43] Cascades were more recently shown to be negligible in a related fifth-order method.[44] These investigations suggest potential for even higher-order nonlinear spectroscopies such as the Raman echo.[15, 17]

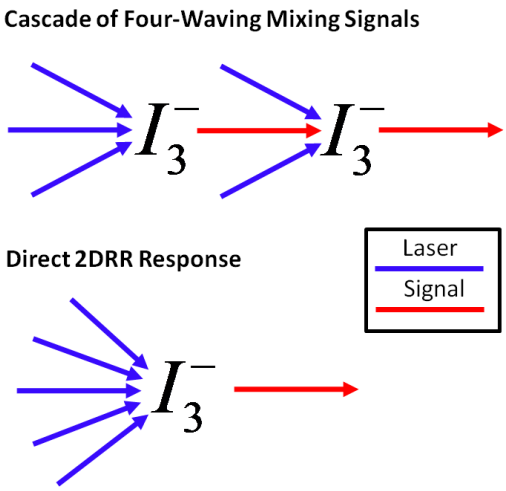


***Figure 1.2.*** *Cascades of four-wave mixing signals generally dominate in off-resonant 2D Raman experiments. In the desired 'direct' process, all six field-matter interactions take place with an individual molecule. The cascaded response is generally negligible in 2DRR spectroscopy because it involves eight field-matter interactions, whereas the direct process only requires six. Both types of nonlinearities are subject to the same selection rules under electronically resonant conditions. Reproduced from Z. Guo, B. P. Molesky, T. P. Cheshire, and A. M. Moran Top Curr Chem (Z) (2017) 375:87, with the permission of Springer Publishing.*

In our initial efforts, we ruled out cascaded signals with control experiments based on the signal phases, concentration dependence, and variation of the beam geometry.[43, 45] Our model calculations suggest that cascades dominate off-resonant experiments because the 2D Raman and cascaded responses are respectively forbidden and allowed for harmonic systems (i.e., they are subject to different selection rules). Of course, this is also why off-resonant 2D Raman experiments are useful for investigating anharmonicities in pure liquids.[16] The problem is that the cascaded signal is more intense because it relies on lower-order terms in the expansion of the potential energy and/or polarizability. Tuning laser pulses into electronic resonance obviates

such selection rules. Vibrational modes contribute to the 2DRR signals if they are Franck-Condon active (i.e., whether they are harmonic or not). Moreover, the 2DRR signal intensity is larger than that associated with cascades because cascades involve two more field-matter interactions (i.e., the cascade is higher-order in this sense). This can be proven by summing the interactions in Figure 1.2.

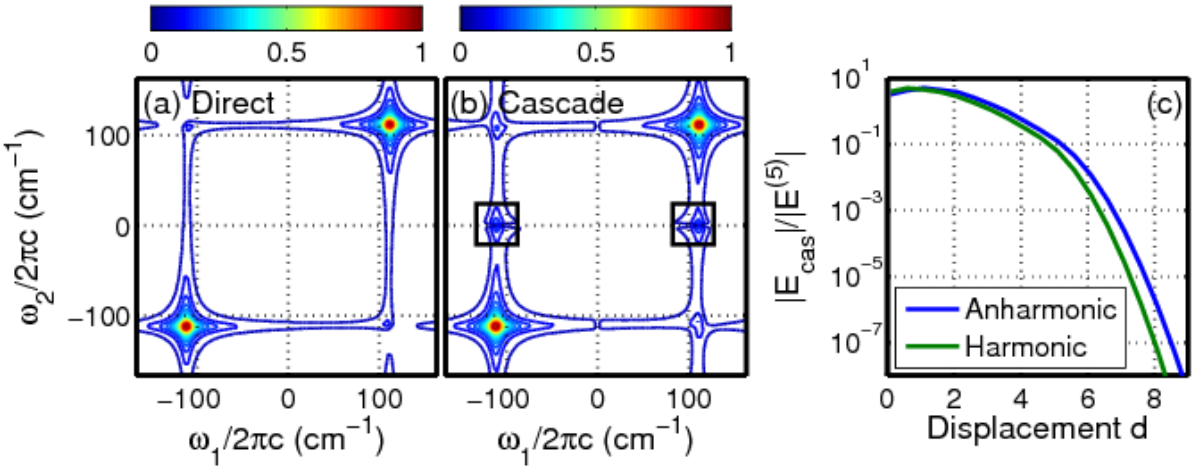


***Figure 1.3.*** *Absolute values of the (a) direct fifth-order and (b) cascaded third-order signals of triiodide at* $\omega_1 = \omega_2 = \pm 112$ *cm*$^{-1}$ *are computed with an empirical anharmonic excited state potential energy surface. The ratio,* $\left|E_{cas}(\omega_1,\omega_2)\right| / \left|E^{(5)}(\omega_1,\omega_2)\right|$*, is computed using (blue) an empirical anharmonic model and (green) a harmonic model with equal ground and excited state frequencies (112 cm*$^{-1}$*.* [46] *The features at* $\omega_2 = 0$ *cm*$^{-1}$ *(enclosed in boxes) in the cascaded signal spectrum represent imperfect subtraction of the non-oscillatory component of the signal, not vibrational resonances. Reproduced from B. M. Molesky, P. G. Giokas, Z. Guo, and A. M. Moran J. Chem. Phys. 141, 114202 (2014), with the permission of AIP Publishing.*

While electronically resonant 2D Raman spectroscopy is less susceptible to cascades than off-resonant 2D Raman spectroscopy, the calculations presented in Figure 1.3 demonstrate that it is still important to keep the optical density low, but not so low that the solvent response becomes comparable to that of the solute. The model predicts that the 2DRR response will generally dominate in transmissive beam geometries; however, optically dense systems like molecular crystals, where a reflective geometry is required, will certainly be problematic. In

Figure 1.3, we present the ratio between the cascaded and 2DRR signal field magnitudes, $\left|E_{cas}\left(\omega_1,\omega_2\right)\right|/\left|E^{(5)}\left(\omega_1,\omega_2\right)\right|$, versus the dimensionless mode displacement, $d$, between ground and excited state potential energy surfaces of the vibration. Importantly, the ratio is close to unity at values of the displacement commonly found for Franck-Condon active modes in many larger molecules ($d < 2$).

**IIC. Modern Assumptions about Third-Order Cascades**

It has been understood for more than 20 years that Fourier transform 2D Raman spectroscopies can be contaminated with cascading signals. It has been shown for a small number of systems that the situation is much improved under electronically resonant conditions. However, cascades can easily exceed 20% of the total signal on resonance if care is not taken to minimize the concentration and/or choose an appropriate beam geometry. A more general analysis of the susceptibility of such experiments to cascades has not yet been undertaken. Moreover, the potential for solvent and solute to combine in a third-order cascade has not been analyzed in any previous work of which we are aware. This will be one of the primary contributions of this thesis. In addition, we address the conventional wisdom that the vibrationally coherent part of a FSRS and/or TR-ISRS signal is more susceptible to cascades than is the vibrational population response.

In our previous work on FSRS, we calculated the ratio of the desired signal to the cascaded response under the assumption that two solute molecules were involved in the cascade. This analysis was motivated by the electronically resonant response of the solute and weak Raman response of the solvent (ethanol). The additional variable that must be considered is the concentration of a particular species. While the Raman cross-section for a solute on resonance is typically a factor of $10^5$ larger than that of a solvent, the solvent can still achieve the same signal

intensity because its concentration is often $10^5$ times that of the solute. This fortuitous offset in variables is exploited in resonance Raman intensity analyses where solvent resonances are used as an internal standard to parameterize Raman cross-sections for solute molecules.

The technique is typically used to monitor the vibrational spectrum of a system that is undergoing an ultrafast chemical reaction. Thus, the response in the experimentally controlled delay time is often "incoherent" in that it does not exhibit oscillations. For this reason (and perhaps others), it has been assumed that FSRS is immune to cascaded nonlinearities. Numerous applications of FSRS have been reported since the late 1990's and not a single study has presented a control experiment that rules out the possibility of cascades. We showed in our own work that the magnitude of the cascaded nonlinearity can exceed 10% if the experimental conditions, such as sample concentration and/or beam geometry, are not carefully tuned.

## III. Multidimensional Treatment of Non-Equilibrium Effects on Electron Transfer Reactions

### IIIA. Non-Equilibrium Effects on Electron Transfer Processes

Biological materials (e.g. DNA and complex proteins), push-pull chromophores, and organometallics are among an extensive list of systems through which electron transfer has been studied. The development of photochemical cells has been a principal motivation for investigations into ultrafast electron transfer mechanisms at molecule-semiconductor interfaces.[53-70] Early spectroscopic studies on dye-sensitized $TiO_2$ nanoparticle systems established 100-fs photoinduced electron injection time-scales.[58, 71] Evidence suggests a picture of sequential processes in which an electron is injected into the $TiO_2$ conduction band following light absorption by the molecular chromophore.[72-73] Models of non-radiative relaxation dynamics starting from a Fermi's Golden Rule description[74-76] produce rates predominantly governed by the magnitude of the donor-acceptor coupling and the density of states (DOS) of the

semiconductor at the energy of the excited molecular donor. Such models are relevant when electron transfer is on the same time-scale of nuclear motion, but approximating the rate as a linear response breaks down with sub-picosecond injection times. Photoinduced nonequilibrium nuclear relaxation has been considered in several elegant theories,[77-86] though they lack clear connection to experiments. A model transparent to researchers spanning a vast array of interdisciplinary fields with physically defined parameters obtainable from spectroscopic measurements and first principles calculations would be a considerable bolster for scientific inquiries.

The three-level system in Figure 1.4 reveals the short-comings of using linear response to approximate ultrafast electron transfer dynamics. Level $a$ represents the electronic ground state, with the electron donor and acceptor states respectively indicated by $b$ and $c$ . The collective bath coordinate, defined by solvent degrees of freedom and low frequency intramolecular modes, induce energy level fluctuations in states $a$ , $b$ , and $c$ , necessitating the description of the electronic energies as surfaces rather than discrete levels.[87-88] In the process of interest, photoexcitation from equilibrium conditions on the ground state to the electron donor state precede electron transfer to the acceptor. When kinetics are largely determined by the equilibrium distribution of state $b$ , it is justifiable to discuss electron transfer in terms of activation energy barriers.[89] However, in the regime where the time-scale of electron transfer is much shorter than that of nuclear relaxation, non-equilibrium wavepacket motions must be considered. Displacement of the wavepacket from the intersection of diabatic surfaces $b$ and $c$ determines the dynamic transition probability; the likelihood of a transition improves as the wavepacket crosses the intersection. The objective is to formulate a quantitative model with well-defined approximations from this simple idea.

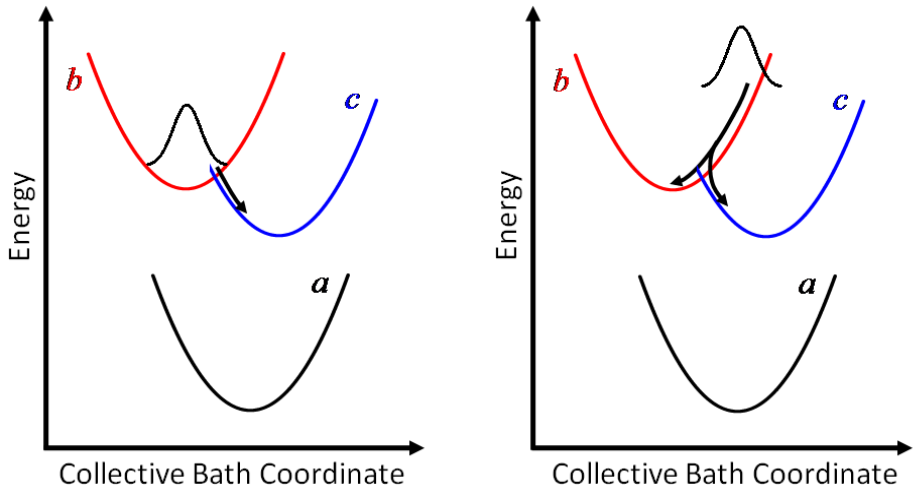


***Figure 1.4.*** *State $b$ is first photoexcited then transfers population to state $c$ by way of an electron transfer transition in the process of interest. Linear reponse rate theories describe the scenario on the left, where thermalization of the wavepacket occurs before electron transfer to state $c$. The understanding of ultrafast electron transfer processes is complicated by the time-coincident electron transfer and nuclear relaxation dynamics, which are indicated on the right.*

**IIIB. Incorporating Intramolecular Vibrational Modes: System versus Bath**

Being able to reproduce kinetic trends observed in experiment is vital in developing robust insights into fundamental processes. While being able to capture excited state nuclear relaxation dynamics during ultrafast electron transfer is a momentous step forward, there remain regimes that are inadequately addressed. Traditional equilibrium models are well-suited to describe electron transfer on time-scales that are slow compared to nuclear motion; the direct effect of bath degrees of freedom, such as solvent and low frequency intramolecular modes, is negligible upon the rate of electron transfer. Following photoexcitation, relaxation in the excited state is instantaneous to a good approximation, and barrier crossing is governed by thermal fluctuations for many systems. Non-radiative relaxation to the acceptor state would be an increasingly rare event with increasingly larger barriers. The picture begins to break down when electron transfer is on the femtosecond time-scale, in which case nuclear effects become directly relevant. In the non-equilibrium model proposed previously, 1) light absorption precedes

electron transfer, 2) electron transfer is on a time-scale comparable to nuclear relaxation, and 3) bath coordinates impose friction much larger than the frequencies of the primary oscillators (i.e. the overdamped limit). These conditions account for the effect of proximity to the donor-acceptor intersection on the acceleration of population transfer. For systems in which vibronic structure is not observed in the absorption line shape, this model for ultrafast electron transfer is broadly applicable. However, in cases with relaxation rate (friction) negligible to high frequency modes strongly coupled to electronic transitions, our original model is inappropriate.[90]

High frequency modes included either explicitly or stochastically in the description of the system indicate the focus of the physical picture we wish to represent, but formally these depictions are identical.[87] By relegating these modes to the bath coordinates, we are defining a set of Brownian oscillators with weak non-negligible damping. Inclusion of underdamped and overdamped oscillators in the bath allow us to capture the effects of coherent reaction dynamics, periodic bursts of population transfer, with particular attention given to the change of rate between the general electronic donor and acceptor states.

### IIIC. Spectroscopic Signatures of Vibronic Coherence Transfer in Electron Transfer Reactions

For more than a quarter-century, a great body of work has been driven by the aspiration to understand coherent reaction mechanisms.[91-98] In the early 90s, initial experimental studies of femtosecond dynamics in the bacterial photosynthetic reaction center probed the role that vibronic coherence poses in electron transfer processes.[91-92] Similar behavior was recognized in subsequent investigations of various biological systems including photo-induced isomerization of bacteriorhodopsin[93] and photo-dissociation in myoglobin.[95] Comprehensive studies of coherent electron transfer mechanisms in mixed valence systems,[99] photosynthetic proteins,[100] polymer-fullerene blends,[101] and molecule-semiconductor interfaces[102-103] have been facilitated

by recent advances in femtosecond laser spectroscopies. Electron transfer time-scales shorter than vibrational dephasing and/or solvation dynamics were exhibited in each system, which suggests a non-equilibrium regime that should not be modeled by linear response.[87-89, 104] Recurrences of the donor at the transition state could induce intermittent bursts in acceptor population.[91-92, 96, 100-101, 105] Coherent reaction dynamics in hot electron transfer processes potentially could be leveraged to bolster the efficiency of solar energy conversion.[106-109]

We presented an electron transfer rate formula in earlier work, accounting for non-equilibrium dynamics induced by photoexcitation. Reaction rate profiles associated with photoexcitation at any wavelength can be predicted at this level of theory; however, the model did not yield transient absorption signal spectra, which would be useful for experimentalists who conduct such measurements. In chapter X of this thesis, this model is extended to incorporate two field-matter interactions with a probe pulse, thereby yielding transient absorption signal spectra. In addition, the vibronic coordinates of the solute are partitioned into the system Hamiltonian in order to capture vibronic coherence transfer processes.

The system under investigation is a transition metal complex in which a titanium atom is bonded to three catechol ligands, $[Ti(cat)_3]^{2-}$. A charge transfer state near 400 nm indicates strong coupling between the catechol and $TiO_2$ moieties.[110] While absorption of incident light initiates electron transfer from catechol to titanium, robust titanium-catechol interactions buoy the successive fast back electron transfer (BET).[111] We exploit the well-defined nature of $[Ti(cat)_3]^{2-}$ to gain insights into how BET initiates coherent nuclear motion in the product state. The charge transfer nature of the electronic resonance of $[Ti(cat)_3]^{2-}$ is essential for this investigation because it guarantees significant projections of Franck-Condon active modes onto the reaction coordinate. [96, 112-116] Coherent BET mechanisms are integrated into a non-

equilibrium model parameterized with inspiration from earlier work[96, 114-116] to determine normal mode displacements from resonance Raman spectroscopy.

Photoexcitation and BET are decomposed into four "pathways" in Figure 1.5. Traditional (equilibrium) linear kinetic models describe the pathway connected by red arrows for thermalized excited states. The other three possibilities involve coherent nuclear motion before and/or after the BET process. Coherent nuclear motion is directly initiated by light absorption in most of the previous experimental studies discussed above (i.e., a stimulated Raman process). Bursts of population into the product state may be observed in such cases, and coherence can be retained in the product state (i.e., a vibronic coherence transfer transition).[91-92, 96, 100-101, 105] Using a density matrix approach in an earlier theoretical study, Fleming and Jean asserted that it is still possible for vibrational coherence to be initiated in the product state in systems that do not undergo coherent nuclear motion in the reactant.[117] The two pathways in which BET initiates vibrational coherence in the product are of primary interest in this work (i.e., paths ending on top in Figure 1.5).

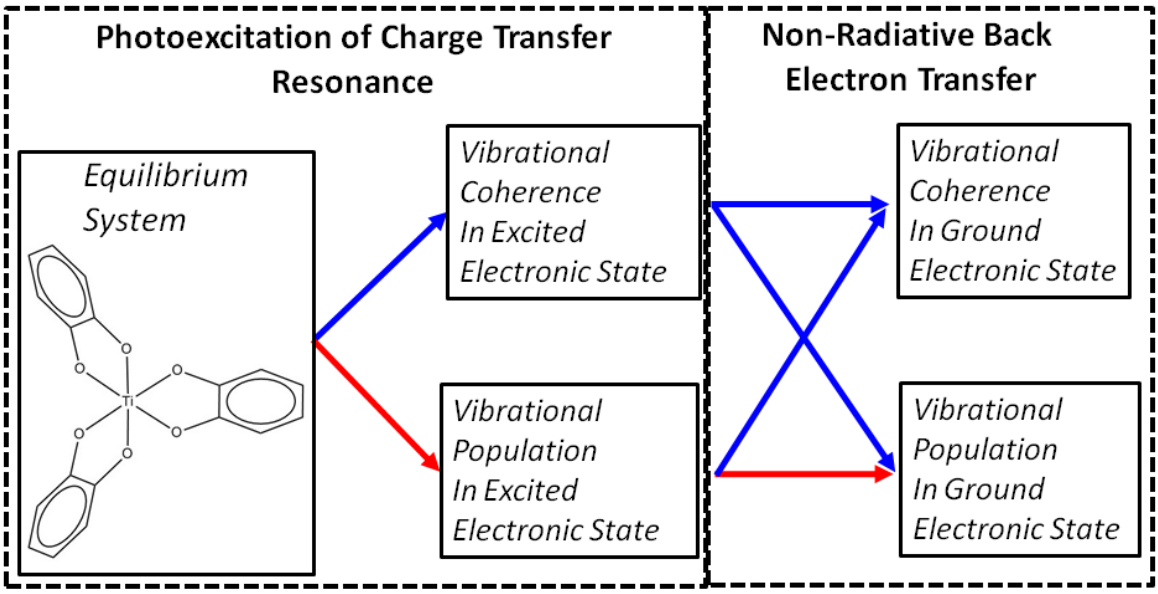


***Figure 1.5.*** *The photoinduced back-electron transfer dynamics of* $[Ti(cat)_3]^{2-}$ *can be described with four potential pathways. The pathway connected by red arrows can be described with traditional models if a Boltzmann distribution of vibrational quanta is established before back-electron transfer; however, a non-equilibrium electron transfer model is required if this condition is not satisfied. The pathways involving vibrational coherences contribute if back-electron transfer is faster than vibrational dephasing.*

## REFERENCES


1. Asplund, M. C.; Zanni, M. T.; Hochstrasser, R. M., Two-Dimensional Infrared Spectroscopy of Peptides by Phase-Controlled Femtosecond Vibrational Photon Echoes *Proc. Natl. Acad. Sci.* **2000,** *97*, 8219-8224.

2. Golonzka, O.; Khalil, M.; Demirdöven, N.; Tokmakoff, A., Vibrational Anharmonicities Revealed by Coherent Two-Dimensional Infrared Spectroscopy. *Phys. Rev. Lett.* **2000,** *86*, 2154-2157.

3. Jonas, D. M., Two-Dimensional Femtosecond Spectroscopy. *Annu. Rev. Phys. Chem.* **2003,** *54*, 425-463.

4. Brixner, T.; Mancal, T.; Stiopkin, I. V.; Fleming, G. R., Phase-Stabilized Two-Dimensional Electronic Spectroscopy. *J. Chem. Phys.* **2004,** *121*, 4221-4236.

5. Cowan, M. L.; Ogilvie, J. P.; Miller, R. J. D., Two-Dimensional Spectroscopy Using Diffractive Optics Based Phase-Locked Photon Echoes. *Chem. Phys. Lett.* **2004,** *386*, 184-189.

6. Ogilvie, J. P.; Kubarych, K. J., Multidimensional Electronic and Vibrational Spectroscopy: An Ultrafast Probe of Molecular Relaxation and Reaction Dynamics *Adv. At. Mol. Opt. Phys.* **2009,** *57*, 249-321.

7. Pakoulev, A. V.; Block, S. B.; Yurs, L. A.; Mathew, N. A.; Kornau, K. M.; Wright, J. C., Multiply Resonant Coherent Multidimensional Spectroscopy: Implications for Materials Science. *J. Phys. Chem. Lett.* **2010,** *1*, 822-828.

8. Hamm, P.; Zanni, M. T., *Concepts and Methods of 2D Infrared Spectroscopy*. Cambridge University Press: Cambridge, 2011.

9. Wright, J. C., Multiresonant Coherent Multidimensional Spectroscopy. *Annu. Rev. Phys. Chem.* **2011,** *62*, 209-230.

10. Slenkamp, K. M.; Lynch, M. S.; Van Kuiken, B. E.; Brookes, J. F.; Bannan, C. C.; Daifuku, S. L.; Khalil, M., Investigating Vibrational Anharmonic Couplings in Cyanide-Bridged Transition Metal Mixed Valence Complexes Using Two-Dimensional Infrared Spectroscopy. *J. Chem. Phys.* **2014,** *140*, 084505.

11. Laubereau, A.; Kaiser, W., Vibrational Dynamics of Liquids and Solids Investigated by Picosecond Light Pulses. *Rev. Mod. Phys.* **1978,** *50*, 607-665.

12. Hesp, B. H.; Wiersma, D. A., Vibrational Relaxation in Neat Crystals of Naphthalene by Picosecond CARS. *Chem. Phys. Lett.* **1980,** *75*, 423-426.

13. Velsko, S.; Trout, J.; Hochstrasser, R. M., Quantum Beating of Vibrational Factor Group Components in Molecular Solids *J. Chem. Phys.* **1983,** *79*, 2114-2120.

14. Schosser, C. L.; Dlott, D. D., A Picosecond CARS Study of Vibron Dynamics in Molecular Crystals: Temperature Dependence of Homogeneous and Inhomogeneous Linewidths *J. Chem. Phys.* **1984,** *80*, 1394-1406.

15. Loring, R. F.; Mukamel, S., Selectivity in Coherent Transient Raman Measurements of Vibrational Dephasing in Liquids. *J. Chem. Phys.* **1985,** *83*, 2116-2126.

16. Tanimura, Y.; Mukamel, S., Two-Dimensional Femtosecond Vibrational Spectroscopy of Liquids. *J. Chem. Phys.* **1993,** *99*, 9496-9511.

17. Berg, M.; Vanden Bout, D. A., Ultrafast Raman Echo Measurements of Vibrational Dephasing and the Nature of Solvent−Solute Interactions. *Acc. Chem. Res.* **1997,** *30*, 65-71.

18. Ivanecky III, J. E.; Wright, J. C., An investigation of the origins and efficiencies of higher-order nonlinear spectroscopic processes *Chem. Phys. Lett.* **1993,** *206*, 437-444.

19. Tominaga, K.; Yoshihara, K., Fifth-Order Nonlinear Spectroscopy on the Low-Frequency Modes of Liquid $CS_2$ *J. Chem. Phys.* **1996,** *104*, 4419-4426.

20. Steffen, T.; Duppen, K., Time Resolved Four- and Six-wave Mixing in Liquids. II. Experiments *J. Chem. Phys.* **1997,** *106*, 3854-3864.

21. Blank, D. A.; Kaufman, L. J.; Fleming, G. R., Fifth-order two-dimensional Raman spectra ofCS 2 are dominated by third-order cascades *J. Chem. Phys.* **1999,** *111*, 3105-3114.

22. Kubarych, K. J.; Milne, C. J.; Lin, S.; Astinov, V.; Miller, R. J. D., Diffractive optics-based six-wave mixing:Heterodyne detection of the full $c^{(5)}$ tensor of liquid $CS_2$. *J. Chem. Phys.* **2002,** *116*, 2016-2042.

23. Kaufman, L. J.; Heo, J.; Ziegler, L. D.; Fleming, G. R., Heterodyne-Detected Fifth-Order Nonresonant Raman Scattering from Room Temperature CS2. *Phys. Rev. Lett.* **2002,** *88*, 207402:1-4.

24. Fujiyoshi, S.; Takeuchi, S.; Tahara, T., Time-Resolved Impulsive Raman Scattering from Excited-State Polyatomic Molecules in Solution. *J. Phys. Chem. A* **2003,** *107*, 494-500.

25. McCamant, D. W.; Kukura, P.; Yoon, S.; Mathies, R. A., Femtosecond Broadband Stimulated Raman Spectroscopy: Apparatus and Methods *Rev. Sci. Instrum.* **2004,** *75*, 4971-4980.

26. Kukura, P.; McCamant, D. W.; Mathies, R. A., Femtosecond stimulated Raman spectroscopy. *Annu. Rev. Phys. Chem.* **2007,** *58*, 461-488.

27. Marek, M. S.; Buckup, T.; Motzkus, M., Direct Observation of a Dark State in Lycopene Using Pump-DFWM. *J. Phys. Chem. B* **2011,** *115*, 8328-8337.

28. Kraack, J. P.; Wand, A.; Buckup, T.; Motzkus, M.; Ruhman, S., Mapping Multidimensional Excited State Dynamics Using Pump-Impulsive-Vibrational-Spectroscopy and Pump-Degenerate-Four-Wave-Mixing. *Phys. Chem. Chem. Phys.* **2013,** *15*, 14487-14501.

29. Petrich, J. W.; Martin, J. L.; Houde, D.; Poyart, C.; Orszag, A., Time-Resolved Raman Spectroscopy with Subpicosecond Resolution: Vibrational Cooling and Delocalization of Strain Energy in Photodissociated (Carbonmonoxy)hemoglobin. *Biochemistry* **1987,** *26*, 7914-7923.

30. Butler, R. M.; Lynn, M. A.; Gustafson, T. L., Solvent-Solute Interactions Probed by Picosecond Transient Raman Spectroscopy: Band Assignments and Vibrational Dynamics of S1 trans-4,4'-diphenylstilbene. *J. Phys. Chem.* **1993,** *97*, 2609-2617.

31. Iwata, K.; Yamaguchi, S.; Hamaguchi, H.-O., Construction of a Transform-Limited Picosecond Time-Resolved Raman Spectrometer. *Rev. Sci. Instrum.* **1993,** *64*, 2140-2146.

32. Zhu, L.; Kim, J.; Mathies, R. A., Picosecond Time-Resolved Raman System for Studying Photochemical Reaction Dynamics: Application to the Primary Events in Vision. *J. Raman. Spectrosc.* **1999,** *30*, 777-783.

33. Kruglik, S. G.; Lambry, J.-C.; Martin, J.-L.; Vos, M. H.; Negrerie, M., Sub-Picosecond Raman Spectrometer for Time-Resolved Studies of Structural Dynamics in Heme Proteins. *J. Raman. Spectrosc.* **2010,** *265-275*.

34. Reid, P. J.; Lawless, M. K.; Wickham, S. D.; Mathies, R. A., Determination of Pericyclic Photochemical Reaction Dynamics with Resonance Raman Spectroscopy. *J. Phys. Chem.* **1994,** *98*, 5597-5606.

35. Reid, P. J.; Doig, S. J.; Mathies, R. A., Picosecond time-resolved UV resonance Raman spectroscopy of the photochemical ring opening of 1,3,5-cyclooctatriene and α-phellandrene. *J. Phys. Chem.* **1990,** *94*, 8396-8399.

36. Kim, J. E.; McCamant, D. W.; Zhu, L.; Mathies, R. A., Resonance Raman Structural Evidence that the Cis-to-Trans Isomerization in Rhodopsin Occurs in Femtoseconds. *J. Phys. Chem. B* **2001,** *105*, 1240-1249.

37. Dorfman, K. E.; Fingerhut, B. P.; Mukamel, S., Time-Resolved Broadband Raman Spectroscopies; A Unified Six-wave mixing Representation". *J. Chem. Phys.* **2013,** *139*, 124113.

38. McCamant, D. W., A Re-Evaluation of Rhodopsin's Relaxation Kinetics Determined from Femtosecond Stimulated Raman Lineshapes. *J. Phys. Chem. B* **2012,** *115*, 9299-9305.

39. Kukura, P.; McCamant, D. W.; Yoon, S.; Wandschneider, D. B.; Mathies, R. A., Structural Observation of the Primary Isomerization in Vision with Femtosecond-Stimulated Raman. *Science* **2005,** *310*, 1006-1009.

40. Ulness, D. J.; Kirkwood, J. C.; Albrecht, A. C., Competitive Events in Fifth Order Time Resolved Coherent Raman Scattering: Direct Versus Sequential Processes. *J. Chem. Phys.* **1998,** *108*, 3897-3902.

41. Jansen, T. I. C.; Snijders, J. G.; Duppen, K., Interaction induced effects in the nonlinear Raman response of liquidCS 2 : A finite field nonequilibrium molecular dynamics approach *J. Chem. Phys.* **2001,** *114*, 109210-10921.

42. Mehlenbacher, R.; Lyons, B.; Wilson, K. C.; Du, Y.; McCamant, D. W., Theoretical analysis of anharmonic coupling and cascading Raman signals observed with femtosecond stimulated Raman spectroscopy *J. Chem. Phys.* **2009,** *131*, 244512.

43. Molesky, B. P.; Giokas, P. G.; Guo, Z.; Moran, A. M., Multidimensional Resonance Raman Spectroscopy by Six-Wave Mixing in the Deep UV. *J. Chem. Phys.* **2014,** *114*, 114202.

44. Hutson, W. O.; Spencer, A. P.; Harel, E., Isolated Ground-State Coherence Measured by Fifth-Order Single-Shot Two-Dimensional Electronic Spectroscopy. *J. Phys. Chem. Lett.* **2016,** *7*, 3636-3640.

45. Molesky, B. P.; Guo, Z.; Moran, A. M., Femtosecond Stimulated Raman Spectroscopy by Six-Wave Mixing. *J. Chem. Phys.* **2015,** *142*, 212405.

46. Johnson, A. E.; Myers, A. B., Emission cross-sections and line shapes for photodissociating triiodide in ethanol: Experimental and computational studies. *J. Chem. Phys.* **1995,** *104*, 3519-3533.

47. Broo, A.; Larsson, S., Electron transfer in azurin and the role of aromatic side groups of the protein. *The Journal of Physical Chemistry* **1991,** *95* (13), 4925-4928.

48. Everest, A. M.; Wallin, S. A.; Stemp, E. D. A.; Nocek, J. M.; Mauk, A. G.; Hoffman, B. M., Aromatic hole superexchange through position 82 of cytochrome c is not required for intracomplex electron transfer to zinc cytochrome c peroxidase. *Journal of the American Chemical Society* **1991,** *113* (11), 4337-4338.

49. Farver, O.; Pecht, I., Long range intramolecular electron transfer in azurins. *Journal of the American Chemical Society* **1992,** *114* (14), 5764-5767.

50. J N Onuchic; D N Beratan; J R Winkler, a.; Gray, H. B., Pathway Analysis of Protein Electron-Transfer Reactions. *Annual Review of Biophysics and Biomolecular Structure* **1992,** *21* (1), 349-377.

51. Casimiro, D. R.; Richards, J. H.; Winkler, J. R.; Gray, H. B., Electron transfer in ruthenium-modified cytochromes c. .sigma.-tunneling pathways through aromatic residues. *The Journal of Physical Chemistry* **1993,** *97* (50), 13073-13077.

52. Gray, H. B.; Winkler, J. R., Electron Transfer in Proteins. *Annual Review of Biochemistry* **1996,** *65* (1), 537-561.

53. O'Regan, B.; Grätzel, M., A low-cost, high-efficiency solar cell based on dye-senstized colloidal $TiO_2$ films. *Nature* **1991,** *353*, 737-740.

54. Grätzel, M., Photoelectrochemical cells. *Nature* **2001,** *414*, 338-344.

55. Hagfeldt, A.; Boschloo, G.; Sun, L.; Kloo, L.; Pettersson, H., Dye-Sensitized Solar Cells. *Chem. Rev.* **2010,** *110*, 6595-6663.

56. Gregg, B. A., Excitonic Solar Cells. *J. Phys. Chem. B* **2003,** *107*, 4688-4698.

57. Zou, Z.; Ye, J.; Sayama, K.; Arakawa, H., Direct splitting of water under visible light irradiation with an oxide semiconductor photocatalyst. *Nature* **2001,** *414*, 625-627.

58. Asbury, J. B.; Hao, E.; Wang, Y.; Ghosh, H. N.; Lian, T., Ultrafast Electron Transfer Dynamics from Molecular Adsorbates to Semiconductor Nanocrystalline Thin Films. *J. Phys. Chem. B* **2001,** *105*, 4545-4557.

59. Concepcion, J. J.; Jurss, J.; Brennaman, M. K.; Hoertz, P. G.; Patrocinio, A. O. T.; Iha, N. Y. M.; Templeton, J. L.; Meyer, T. J., Making Oxygen with Ruthenium Complexes. *Acc. Chem. Res.* **2009,** *42*, 1954-1965.

60. Kamat, P. V., Meeting the Clean Energy Demand: Nanostructure Architectures for Solar Energy Conversion. *J. Phys. Chem. C* **2007,** *111*, 2834-2860.

61. Mallouk, T. E., The emerging technology of solar fuels. *J. Phys. Chem. Lett.* **2010,** *1*, 2738-2739.

62. Shoute, L. C. T.; Loppnow, G. R., Excited-State Metal-to-Ligand Charge Transfer Dynamics of a Ruthenium(II) Dye in Solution and Adsorbed on TiO2 Nanoparticles from Resonance Raman Spectroscopy. *J. Amer. Chem. Soc.* **2003,** *125*, 15636-15646.

63. Smeigh, A. L.; Katz, J. E.; Brunschwig, B. S.; Lewis, N. S.; McCusker, J. K., Effect of the Presence of Iodide on the Electron Injection Dynamics of Dye-Sensitized TiO2-Based Solar Cells. *J. Phys. Chem. C* **2008,** *112*, 12065-12068.

64. Morandeira, A.; Boschloo, G.; Hagfeldt, A.; Hammarström, L., Coumarin 343−NiO Films as Nanostructured Photocathodes in Dye-Sensitized Solar Cells: Ultrafast Electron Transfer, Effect of the I3−/I− Redox Couple and Mechanism of Photocurrent Generation. *J. Phys. Chem. C* **2008,** *112*, 9530-9537.

65. Xiong, W.; Laaser, J. E.; Paoprasert, P.; Franking, R. A.; Hamers, R. J.; Gopalan, P.; Zanni, M. T., Transient 2D IR Spectroscopy of Charge Injection in Dye-Sensitized Nanocrystalline Thin Films. *J. Am. Chem. Soc.* **2009,** *131*, 18040-18041.

66. Ardo, S.; Meyer, G. J., Photodriven heterogeneous charge transfer with transition-metal compounds anchored to TiO2 semiconductor surfaces. *Chem. Soc. Rev.* **2009,** *38*, 115-164.

67. Morris-Cohen, A. J.; Frederick, M. T.; Cass, L. C.; Weiss, E. A., Simultaneous Determination of the Adsorption Constant and the Photoinduced Electron Transfer Rate for a Cds Quantum Dot–Viologen Complex. *J. Am. Chem. Soc.* **2011,** *133*, 10146-10154.

68. Huss, A. S.; Rossini, J. E.; Ceckanowicz, D. J.; Bohnsack, J. N.; Mann, K. R.; Gladfelter, W. L.; Blank, D. A., Photoinitiated Electron Transfer Dynamics of a Terthiophene Carboxylate on Monodispersed Zinc Oxide Nanocrystals. *J. Phys. Chem. C* **2011,** *115*, 2-10.

69. Tseng, H.-W.; Wilker, M. B.; Damraurer, N. H.; Dukovic, G., Charge Transfer Dynamics between Photoexcited CdS Nanorods and Mononuclear Ru Water-Oxidation Catalysts. *J. Am. Chem. Soc.* **2013,** *135*, 3383-3386.

70. Sarkany, L.; Wasylenko, J. M.; Roy, S.; Higgins, D. A.; Elles, C. G.; Chikan, V., Investigation of Fluorescence Emission from CdSe Nanorods in PMMA and P3HT/PMMA Films. *J. Phys. Chem. C* **2013,** *117*, 18818-18828.

71. Anderson, N. A.; Lian, T., Ultrafast Electron Transfer at the Molecule-Semiconductor Nanoparticle Interface. *Annu. Rev. Phys. Chem.* **2005,** *56*, 491-519.

72. Duncan, W. R.; Prezhdo, O. V., Theoretical Studies of Photoinduced Electron Transfer in Dye-Sensitized $TiO_2$. *Annu. Rev. Phys. Chem.* **2007,** *58*, 143-184.

73. Akimov, A. V.; Neukirch, A. J.; Prezhdo, O. V., Theoretical insights into photoinduced charge transfer and catalysis at metal oxide surfaces. *Chem. Rev.* **2013,** *113*, 4496-4565.

74. Marcus, R. A., On the Theory of Electron-Transfer Reactions. VI. Unified Treatment for Homogeneous and Electrode Reactions. *J. Chem. Phys.* **1965,** *43*, 679-701.

75. Gerischer, H., Charge transfer processes at semiconductor-electrolyte interfaces in connection with problems of catalysis *Surf. Sci.* **1969,** *18*, 97-122.

76. Gerischer, H., Electrochemical Techniques for the Study of Photosensitization. *Photochem. Photobiol.* **1972,** *16*, 243-260.

77. Coalson, R. D.; Evans, D. G.; Nitzan, A., A nonequilibrium golden rule formula for electronic state populations in nonadiabatically coupled systems *J. Chem. Phys.* **1994,** *101*, 436-448.

78. Evans, D. G.; Coalson, R. D., Incorporating backflow into a relaxation theory treatment of the dynamics of nonequilibrium nonadiabatic transition processes *J. Chem. Phys.* **1995,** *102*, 5658-5668.

79. Golosov, A. A.; Reichman, D. R., Reference system master equation approaches to condensed phase charge transfer processes. I. General formulation *J. Chem. Phys.* **2001,** *115*, 9848-9861.

80. Golosov, A. A.; Reichman, D. R., Reference system master equation approaches to condensed phase charge transfer processes. II. Numerical tests and applications to the study of photoinduced charge transfer reactions *J. Chem. Phys.* **2001,** *115*, 9862-9870.

81. Egorova, D.; Thoss, M.; Domcke, W.; Wang, H., Modeling of ultrafast electron-transfer processes: Validity of multilevel Redfield theory *J. Chem. Phys.* **2003,** *119*, 2761-2773.

82. Kondov, I.; Thoss, M., Theoretical Study of Ultrafast Heterogeneous Electron Transfer Reactions at Dye−Semiconductor Interfaces: Coumarin 343 at Titanium Oxide. *J. Phys. Chem. A* **2006,** *110*, 1364-1374.

83. Liang, K.-K.; Lin, C.-K.; Chang, H.-C.; Hayashi, M.; Lin, S. H., Theoretical treatments of ultrafast electron transfer from adsorbed dye molecule to semiconductor nanocrystalline surface *J. Chem. Phys.* **2006,** *125*, 154706.

84. Welack, S.; Schreiber, M.; Kleinekathöfer, U., The influence of ultrafast laser pulses on electron transfer in molecular wires studied by a non-Markovian density-matrix approach *J. Chem. Phys.* **2006,** *124*, 044712.

85. Zhang, M.-L.; Ka, B. J.; Geva, E., Nonequilibrium quantum dynamics in the condensed phase via the generalized quantum master equation *J. Chem. Phys.* **2006,** *125*, 044106.

86. Jakubikova, E.; Snoeberger III, R. C.; Batista, V. S.; Batista, E. R., Interfacial electron transfer in $TiO_2$ surfaces sensitized with Ru(II)-polypyridine complexes. *J. Phys. Chem. A* **2009,** *113*, 12532-12540.

87. Mukamel, S., *Principles of Nonlinear Optical Spectroscopy*. Oxford University Press: New York, 1995.

88. Nitzan, A., *Chemical Dynamics in Condensed Phases*. Oxford University Press: Oxford, 2006.

89. Barbara, P. F.; Meyer, T. J.; Ratner, M. A., Contemporary Issues in Electron Transfer Research. *J. Phys. Chem.* **1996,** *100*, 13148-13168.

90. Lesheng, L.; Giokas, P. G.; Kanai, Y.; Moran, A. M., Modeling Time-Coincident Ultrafast Electron Transfer and Solvation Processes at Molecule-Semiconductor Interfaces. *J. Chem. Phys.* **2014,** *140*, 234109.

91. Vos, M. H.; Lambry, J.-C.; Robles, S. J.; Youvan, D. C.; Breton, J.; Martin, J.-L., Direct Observation of Vibrational Coherence in Bacterial Reaction Centers Using Femtosecond Absorption Spectroscopy. *Proc. Natl. Acad. Sci.* **1991,** *88*, 8885-8889.

92. Vos, M. H.; Rappaport, F.; Lambry, J.-C.; Breton, J.; Martin, J.-L., Visualization of Coherent Nuclear Motion in a Membrane Protein by Femtosecond Spectroscopy. *Nature* **1993,** *363*, 320-325.

93. Peteanu, L. A.; Schoenlein, R. W.; Wang, H.; Mathies, R. A.; Shank, C. V., The First Step in Vision Occurs in Femtoseconds: Complete Blue and Red Spectral Studies. *Proc. Natl. Acad. Sci.* **1993,** *90*, 11762-11766.

94. Banin, U.; Kosloff, R.; Ruhman, S., Femtosecond Chemical Dynamics in Solution: Photodissociation of $I_3^-$. *Isr. J. Chem.* **1993,** *33*, 141-156.

95. Zhu, L.; Sage, J. T.; Champion, P. M., Observation of Coherent Reaction Dynamics in Heme Proteins. *Science* **1994,** *266*, 629-632.

96. Wynne, K.; Reid, G. D.; Hochstrasser, R. M., Vibrational Coherence in Electron Transfer: The Tetracyanoethylene-Pyrene Complex. *J. Chem. Phys.* **1996,** *105*, 2287-2297.

97. Spörlein, S.; Zinth, W.; Wachtveitl, J., Vibrational Coherence in Photosynthetic Reaction Centers Observed in the Bacteriochlorophyll Anion Band. *J. Phys. Chem. B* **1998,** *102*, 7492-7496.

98. Arnett, D. C.; Moser, C. C.; Dutton, P. L.; Scherer, N. F., The First Events in Photosynthesis: Electronic Coupling and Energy Transfer Dynamics in the Photosynthetic Reaction Center from Rhodobacter sphaeroides. *J. Phys. Chem. B* **1999,** *103*, 2014-2032.

99. Lynch, M. S.; Van Kuiken, B. E.; Daifuku, S. L.; Khalil, M., On the Role of High-Frequency Intramolecular Vibrations in Ultrafast Back-Electron Transfer Reactions. *J. Phys. Chem. Lett.* **2011,** *2*, 2252-2257.

100. Fuller, F. D.; Pan, J.; Gelzinis, A.; Butkus, V.; Senlik, S. S.; Wilcox, D. E.; Yocum, C. F.; Valkunas, L.; Abramavicius, D.; Ogilvie, J. P., Vibronic Coherence in Oxygenic Photosynthesis. *Nat. Chem.* **2014,** *6*, 706-711.

101. Song, Y.; Clafton, S. N.; Pensack, R. D.; Kee, T. W.; Scholes, G. D., Vibrational Coherence Probes the Mechanism of Ultrafast Electron Transfer in Polymer–Fullerene Blends. *Nat. Commun.* **2014,** *5*, 4933.

102. Tisdale, W. A.; Williams, K. J.; Timp, B. A.; Norris, D. J.; Aydil, E. S.; Zhu, X.-Y., Hot-Electron Transfer from Semiconductor Nanocrystals. *Science* **2010,** *328*, 1543-1547.

103. Huber, R.; Dworak, L.; Moser, J. E.; Grätzel, J.; Wachtveitl, J., Beyond Vibrationally Mediated Electron Transfer: Coherent Phenomena Induced by Ultrafast Charge Separation. *J. Phys. Chem. C* **2016**, DOI: 10.1021/acs.jpcc.6b02012.

104. Valkunas, L.; Abramavicius, D.; Mančal, T., *Molecular Excitation Dynamics and Relaxation: Quantum Theory and Spectroscopy* Wiley-VCH: Weinheim, 2013.

105. Bixon, M.; Jortner, J., Vibrational Coherence in Nonadiabatic Dynamics. *J. Chem. Phys.* **1997,** *107*, 1470-1482.

106. Clarke, T. M.; Durrant, J. R., Charge Photogeneration in Organic Solar Cells. *Chem. Rev.* **2010,** *110*, 6736-6767.

107. Ross, R. T.; Nozik, A. J., Efficiency of Hot-Carrier Solar Energy Converters. *J. Appl. Phys.* **1982,** *53*, 3813-3818.

108. Jin, X.; Li, Y.; Chen, Z.; Wei, T.-H.; He, X.; Sun, W., Energy Level Control: Toward an Efficient Hot Electron Transport. *Sci. Rep.* **2014,** *4*, 5983.

109. Li, L.; Kanai, Y., Excited Electron Dynamics at Semiconductor–Molecule Type-II Heterojunction Interface: First-Principles Dynamics Simulation. *J. Phys. Chem. Lett.* **2016,** *7*, 1495-1500.

110. Borgias, B. A.; Cooper, S. R.; Koh, Y. B.; Raymond, K. N., Synthetic, Structural, and Physical Studies of Titanium Complexes of Catechol and 3,5-*tert*-butylcatechol. *Inorg. Chem.* **1984,** *23*, 1009-1016.

111. Wang, Y.; Hang, K.; Anderson, N. A.; Lian, T., Comparison of Electron Transfer Dynamics in Molecule-to-Nanoparticle and Intramolecular Charge Transfer Complexes. *J. Phys. Chem. B* **2003,** *107*, 9434-9440.

112. Hush, N. S., Homogeneous and Heterogeneous Optical and Thermal Electron Transfer. *Electrochimica Acta.* **1968,** *13*, 1005-1023.

113. Yan, Y. J.; Sparpaglione, M.; Mukamel, S., Solvation Dynamics in Electron-Transfer, Isomerization, and Nonlinear Optical Processes. A Unified Liouville-Space Theory. *J. Phys. Chem.* **1988,** *92*, 4842-4853.

114. Britt, B. M.; McHale, J. L.; Friedrich, D. M., Application of Time Dependent Raman Theory to Raman Excitation Profiles of Hexamethylbenzene: Tetracyanoethylene Electron Donor-Acceptor Complex. *J. Phys. Chem.* **1995,** *99*, 6347-6355.

115. Kelley, A. M., Resonance Raman Intensity Analysis of Vibrational and Solvent Reorganization in Photoinduced Charge Transfer. *J. Phys. Chem. A* **1999,** *103*, 6891-6903.

116. Hupp, J. T.; Williams, R. D., Using Resonance Raman Spectroscopy to Examine Vibrational Barriers to Electron Transfer and Electronic Delocalization. *Acc. Chem. Res.* **2001,** *34*, 808-817.

117. Jean, J. M.; Fleming, G. R., Competition Between Energy and Phase Relaxation in Electronic Curve Crossing Processes. *J. Chem. Phys.* **1995,** *103*, 2092-2101.

# CHAPTER 2: ELUCIDATION OF REACTIVE WAVEPACKETS BY TWO-DIMENSIONAL RESONANCE RAMAN SPECTROSCOPY[1]

## I. Introduction

Models used to describe photoinduced electronic relaxation mechanisms in condensed phases are often based on perturbative descriptions at the level of Fermi's Golden Rule (e.g., Marcus equation, Forster energy transfer).[1-3] Such second-order rate theories typically assume an equilibrium initial condition in the photoexcited state of the system prior to the non-radiative transition of interest. This assumption is generally poor when applied to processes that occur on a time scale faster than solvation and/or vibrational dephasing. Recent studies show that non-trivial quantum effects may emerge when electronic and nuclear relaxation processes become time-coincident.[4] For example, in charge transfer processes that are time-coincident with vibrational dephasing, bursts of population flow have been observed in polymer-fullerene blends,[5] photosynthetic complexes,[6] and at interfaces of semiconductors.[7,8] Transient coupling between electronic and vibrational degrees of freedom has also been implicated in sub-picosecond energy transfer transitions.[9-15] The two-dimensional resonance Raman (2DRR) techniques developed in this work are motivated by new insights into these types of non-equilibrium dynamics.

In this paper, the sensitivity of 2DRR spectroscopy to coherent reaction mechanisms is demonstrated with measurements conducted on the photodissociation process of triiodide. Two-color laser pulse configurations are used to selectively detect vibrational motions of the triiodide reactant and/or diiodide photoproduct in the two dimensions of the 2DRR spectrum. The unique

[1] This chapter previously appeared as an article in the Journal of Chemical Physics. The original citation is as follows: Guo, Z.; Molesky, B. M.; Cheshire, T. P.; Moran, A. M. J. Chem. Phys. 2015, 143, 124202.

power of the technique is ultimately realized using a pulse sequence, where vibrational resonances of triiodide and diiodide appear in separate dimensions. These "cross peaks" represent events in which a nuclear wavepacket transitions between reactant and product states without loss of coherence. Below we explore how 2DRR spectroscopy can be used to expose non-trivial correlations between the nonequilibrium geometry of the reactant and vibrational coherence frequency of the product. Such information cannot be derived from four-wave mixing spectroscopies, which possess only one "population time" in which nuclear wavepacket motions take place.

Ultrafast spectroscopic investigations of the photodissociation process in solvated triiodide are motivated by knowledge of the extraordinary reaction mechanism in this well-defined system.[16-23] Light absorption by triiodide in the ultraviolet spectral range induces photodissociation on a time-scale that is shorter than[16,19] or comparable to[22,24] the vibrational period of diiodide. Photodissociation of triiodide acts as an impulse that initiates vibrational coherence in the bond stretching coordinate of diiodide. Information about the geometry changes that transform the reactant to the photoproduct can be derived from oscillatory components of transient absorption signals. For example, earlier work has shown that the oscillatory amplitude reflects symmetry breaking in the excited state,[20] whereas the "chirp" in the waveform of the vibrational coherence represents time evolution of the bond strength during the reaction.[22] It has also been demonstrated that photodissociation yields distinct populations of free solvated diiodide and a contact fragment pair (diiodide and iodine).[25] Of relevance to the present 2DRR study, recent work suggests that the vibrational mode in free solvated diiodide dephases on a time scale that is longer than the 300-fs vibrational period, whereas overdamped vibrational motion tends to take place in the contact radical pair.[24]

We recently measured 2DRR spectra of triiodide using deep UV laser pulses.[26] This approach was sensitive to ground state wavepacket motions in the triiodide molecule, but did not convey detailed information about the photodissociation mechanism. Examination of this simple nonlinearity was motivated by the ability to compare experimental 2DRR spectra with those simulated using the Hamiltonian of triiodide determined in earlier spontaneous resonance Raman studies.[27-29] Together with a battery of control experiments, these simulations were essential for ruling out cascades of four-wave mixing signal fields, which are known to significantly challenge 2D Raman experiments conducted under off-resonant conditions.[30-34] We concluded that the desired 2DRR response will generally be dominant in systems with large excited state potential energy surface displacements. In effect, Franck-Condon activity obviates the selection rules that favor cascaded signal intensity under off-resonant conditions.

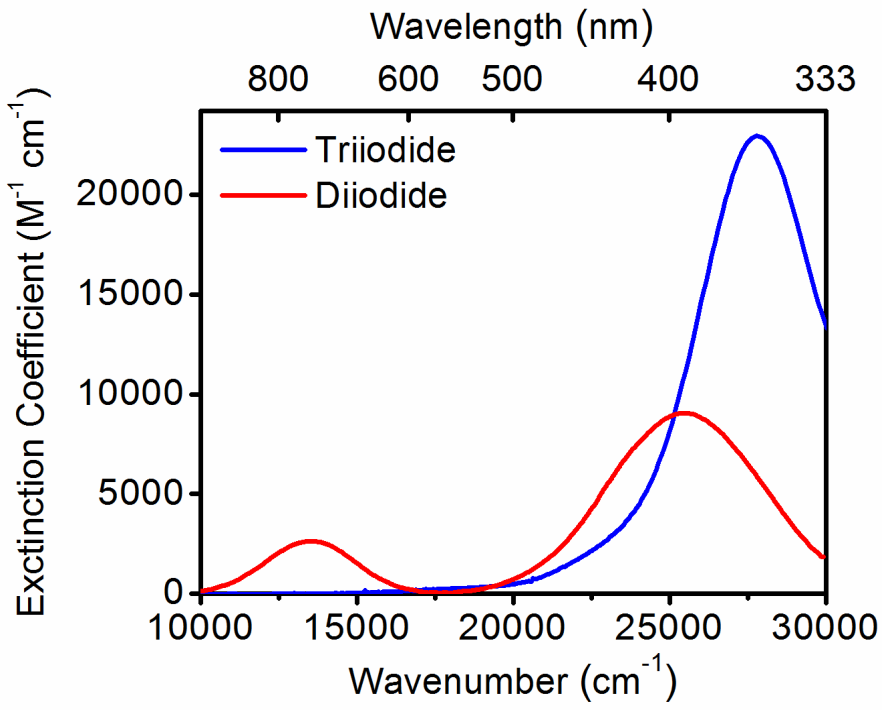


***Figure 2.1.*** *Linear absorbance spectra of triiodide and diiodide in ethanol. The absorbance spectrum of triiodide is directly measured, whereas that of diiodide is derived from Reference [35] because it is not stable in solution. Diiodide is probed on the picosecond time scale in the present work. The electronic resonance frequencies associated with this nonequilibrium state of diiodide are likely red-shifted from those displayed above.*

## II. 2DRR Spectra Simulated for a Reactive Model System

As implemented in this work, 2DRR spectroscopy is a fifth-order technique in which vibrational coherences are detected in two delay times between laser pulses. In contrast, vibrational coherences may be investigated during only one pulse delay time in a traditional third-order pump-probe spectroscopy. The goal of the model presented in this section is to establish spectroscopic signatures corresponding to particular classes of terms in the 2DRR response function. It is important to carry out such an analysis, because the 2DRR nonlinearity is more complicated than that associated with a traditional pump-probe experiment.[1]

Vibrational motions in the ground electronic state of triiodide were detected in our earlier all-UV 2DRR experiments.[26] Here, sensitivity to the diiodide photoproduct is derived by applying laser pulses in a spectral range that is electronically off-resonant with triiodide at equilibrium.[16-23] The patterns of 2DRR resonances associated with such two-color pulse sequences are explored with model calculations below.

### IIA. Model Hamiltonians

The electronic resonances relevant to the experiments conducted in this work are displayed in Figure 2.1. The resonance of triiodide centered near 27,800 $cm^{-1}$ is excited in all experiments. In a single experiment, either the lower (13,300 $cm^{-1}$) or higher-frequency (25,400 $cm^{-1}$) electronic resonance of diiodide is probed (i.e., the 2DRR experiments presented below are two-color rather than three-color). Therefore, the nonlinear optical response associated with all measurements presented below may be simulated using a Hamiltonian in which each molecule, triiodide and diiodide, is treated as an effective two-level electronic system. Explicit inclusion of additional off-resonant electronic states will have a negligible impact on these signals. The effective Hamiltonian for triiodide can be written as

$$H_{triiodide} = |r\rangle\langle r| \sum_{m=0}^{\infty} |m\rangle\langle m| \left[ E_r + E_m \right] + |r*\rangle\langle r*| \sum_{n=0}^{\infty} |n\rangle\langle n| \left[ E_{r*} + E_n \right] , \quad (2.1)$$

whereas that of diiodide is given by

$$H_{diiodide} = |p\rangle\langle p| \sum_{m=0}^{\infty} |m\rangle\langle m| \left[ E_p + E_m \right] + |p*\rangle\langle p*| \sum_{n=0}^{\infty} |n\rangle\langle n| \left[ E_{p*} + E_n \right] . \quad (2.2)$$

Here, $r$ and $p$ represent the ground electronic states of triiodide and diiodide, whereas an asterisk is used to denote the excited electronic state. The energies, $E_r$ and $E_r^*$ ($E_p$ and $E_p^*$), correspond to the ground and excited states, respectively. The dummy indices, $m$ and $n$, represent vibrational levels belonging to the ground and excited electronic states.

The transition energies of each system, $E_{r*} - E_r$ and $E_{p*} - E_p$, are readily derived from the absorbance spectra presented in Figure 2.1. The two potential energy surfaces that belong to each molecule must also be described in order to generate the vibrational energy levels, $E_m$ and $E_n$. The ground state potential energy surfaces must be modeled with a far greater level of detail than the excited state potential energy surfaces in order for the model to generate realistic spectroscopic signals. Insensitivity to the global excited state potential energy surfaces is taken into account when writing the summations over quantized vibrational levels for the dissociative excited states in $H_{triiodide}$ and $H_{diiodide}$. We next discuss the approximations made in the descriptions of the potential energy surfaces in a qualitative way. Further technical details about the parameterization of the potential energy surfaces are given in section VIA.

The summations over quantized levels for the ground states in $H_{triiodide}$ and $H_{diiodide}$ are clearly motivated. Previous literature can be used to guide decisions about parameters.[16,19,27] The vibrational motions of triiodide and diiodide detected in this work are known to occur in the electronic ground states, because the excited states of both systems are dissociative.[16,19]

Vibrational resonances in the ground electronic state of triiodide have been detected in both spontaneous and stimulated Raman experiments carried out with deep and near ultraviolet laser beams.[16,27] In this work, signals will be simulated using a harmonic ground-state potential for triiodide, because only the lowest-energy vibrational states contribute to the signals. Resonance Raman experiments suggest that the harmonic approximation is indeed reasonable for these energy levels.[27] In two-color transient absorption experiments (ultraviolet pump with visible and near-infrared probes), the relationship between the vibrational phase and detection wavelength was used to assign wavepacket motions to the electronic ground state in diiodide.[16,19] The ground state potential energy surface of diiodide is modeled using a cubic potential in this work, because higher-energy vibrational levels (near 12 quanta) are known to contribute to the response following photodissociation.[19] Introduction of the cubic potential is required to obtain agreement between theoretical and experimental vibrational frequencies, but does not impact the patterns of peaks in the 2DRR spectra.

The shapes of the excited state potentials require far less detail than those of the ground states, because the experiments presented here are sensitive only to the potential energy gradient near the Franck-Condon geometry.[36] This aspect of the response is made clear by the absence of vibronic progressions in the absorbance spectra shown in Figure 2.1. In the semiclassical perspective, this means that the wavepacket initiated on the excited state potential energy surface does not return to the Franck-Condon geometry before electronic dephasing is complete (i.e., electronic dephasing is on the order of 10-20 fs).[37] The excited state potential energy gradient near the Franck-Condon geometry primarily governs the amplitude of the wavepacket stimulated in the ground electronic state. Here, we use the cubic fitting parameters for the London-Eyring-Polanyi-Sato (LEPS) excited state potential energy surface of triiodide in ethanol.[18,27] Johnson

and Myers used a similar displaced oscillator model for triiodide to achieve reasonable agreement with spontaneous Raman spectra.[27] The gradient of the excited state potential energy surface of diiodide at the Franck-Condon geometry is approximated by displacing a replica of the cubic ground state potential energy surface. We have chosen a set of parameters that produces a gradient which is consistent with models used in other work (see section VIA).[24,25]

**IIB. Response Functions**

We consider three types of 2DRR nonlinearities: (i) both dimensions correspond to the triiodide reactant; (ii) both dimensions correspond to the diiodide photoproduct; (iii) the vibrational resonances of triiodide and diiodide appear in separate dimensions. As in section IIA, we use a notation where the indices $r$ and $r*$ represent the ground and lowest-energy excited electronic states of the triiodide reactant. Likewise, $p$ and $p*$ correspond to the ground and lowest-energy excited states of the diiodide photoproduct. Vibrational levels associated with these electronic states are specified by dummy indices ($m, n, j, k, l, u, v, w$). The Feynman diagrams presented in Figure 2.2 show that the vibrational coherences detected in 2DRR spectra evolve in the two time intervals with even indices ($t_2$ and $t_4$). Electronic (or vibronic) coherences, which dephase in 10's of fs for solvated triiodide, evolve in the time intervals that correspond to odd indices ($t_1$, $t_3$, and $t_5$). It is useful to consider that the experimentally controlled pulse delay times, $\tau_1$ and $\tau_2$, are good approximations to the time intervals between field-matter interactions, $t_2$ and $t_4$.

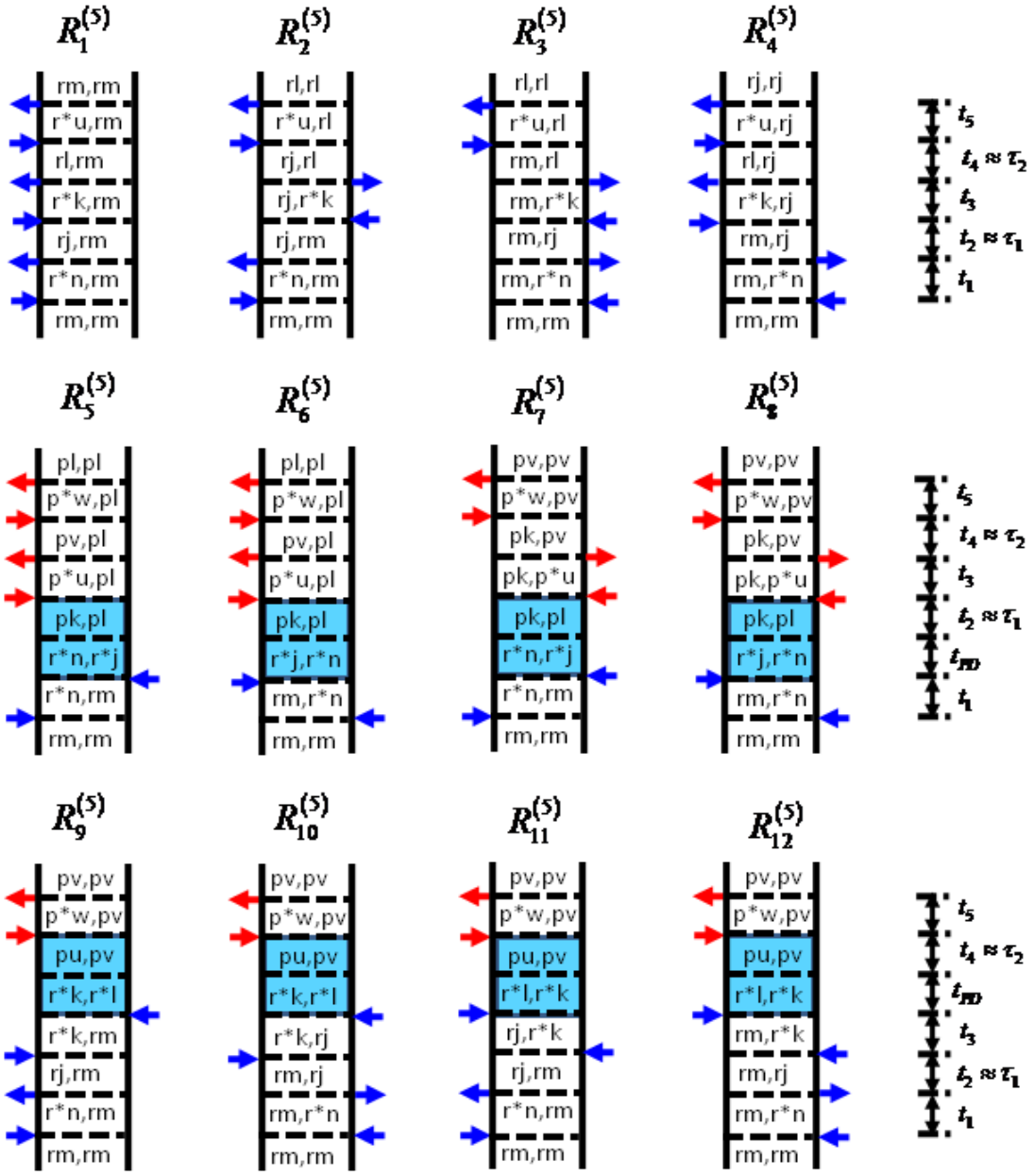


***Figure 2.2.*** *Feynman diagrams associated with dominant 2DRR nonlinearities. Blue and red arrows represent pulses resonant with triiodide and diiodide, respectively. The indices $r$ and $r^*$ represent the ground and excited electronic states of the triiodide reactant, whereas $p$ and $p^*$ correspond to the diiodide photoproduct. Vibrational levels associated with these electronic states are specified by dummy indices ($m, n, j, k, l, u, v, w$). Each row represents a different class of terms: (i) both dimensions correspond to triiodide in terms 1-4; (ii) both dimensions correspond to diiodide in terms 5-8; (iii) vibrational resonances of triiodide and diiodide appear in separate dimensions in terms 9-12. The intervals shaded in blue represent a non-radiative transfer of vibronic coherence from triiodide to diiodide.*

The first class of nonlinearities shown in Figure 2.2 (i.e., terms 1-4) involves vibrational motions of only the triiodide reactant.[26] In contrast to terms 1-4, the Feynman diagrams associated with the other two classes of response functions incorporate the photodissociation process as a transfer of vibronic coherence from triiodide to diiodide either before (terms 5-8) or after (terms 9-12) evolution of the vibrational coherence in $t_2$ (i.e., the delay time, $\tau_1$). In the present model, we assume that the reaction is faster than the 300-fs period of the symmetric stretching coordinate in triiodide. This separation in time scales is consistent with the finding of vibrational coherence in diiodide (i.e., vibrational motions in the ensemble can dephase if the reaction is not impulsive). It was understood in earlier studies that photodissociation is faster than the 300-fs vibrational period.[16,19] However, some later work suggests that the reaction takes place on nearly the same time scale as the vibrational period (i.e., a few hundred femtoseconds).[22,24] In any case, we consider the impulsive approximation to be reasonable here, because it does not impact the pattern of peaks in the 2DRR spectra.

As in Reference [26], response functions are written in the "snapshot" limit, where the laser pulses are short compared to the vibrational period but long compared to electronic dephasing.[1] Both approximations are appropriate for the experiments described below. We additionally take the finite bandwidths of the laser pulses into account in the expressions for the nuclear wavepackets. Under these approximations, the polarization components consist of products of Lorentzian functions (see Appendix 1 for derivation).[38] For example, the first term is given by

$$P_1^{(5)}(\omega_1,\omega_2) = -\frac{N\xi_{UV}^5\left|\mu_{r^*r}\right|^6}{\mathrm{h}^5}\sum_{mnjklu} B_m \langle n|m\rangle\langle n|j\rangle\langle k|j\rangle\langle k|l\rangle\langle u|l\rangle\langle u|m\rangle \times L_{r^*n,rm}(\omega_{UV}) D_{rj,rm}(\omega_1) L_{r^*k,rm}(\omega_{UV}) D_{rl,rm}(\omega_2) L_{r^*u,rm}(\omega_t), \quad (2.3)$$

where

$$L_{r^*n,rm}(\omega) = \frac{1}{\omega - \omega_{r^*r} - \omega_{nm} + i\Gamma_{r^*r}}, \tag{2.4}$$

and

$$D_{rk,rm}(\omega) = \frac{2\Gamma_{vib} + 4\Lambda_{UV}}{\omega_{km}^2 + (\Gamma_{vib} + 2\Lambda_{UV})^2}\left(\frac{1}{\omega - \omega_{km} + i\Gamma_{vib}}\right). \tag{2.5}$$

Here, $\langle n|m\rangle$ is a vibrational overlap integral, where the index on the left represents the vibrational level of the excited electronic state (i.e., the same notation is used in Reference [39]). The subscript of the electric field, *UV*, denotes an interaction with the lowest-energy electronic resonance of triiodide (VIS denotes an interaction with either electronic resonance of diiodide). The remaining 11 response functions are given in section VIB.

The parameters given in Table 2.1 are chosen to approximate the properties of triiodide and diiodide. The electronic and vibrational resonance frequencies of both systems have been determined in earlier studies.[16-23,26] We take the potential energy surface of the ground state of triiodide to be harmonic in agreement with spontaneous resonance Raman experiments.[27] The excited state potential energy surface of triiodide and both the ground and excited state potential energy surfaces of diiodide are expanded to the cubic term.[26] Cubic expansion coefficients of -1 $cm^{-1}$ (see Equation 2.8) approximate the LEPS surface of triiodide[17] and capture the 100-$cm^{-1}$ gap between successive energy levels in diiodide near 20 vibrational quanta.[19] Evaluation of the vibrational overlap integrals in the response function is accomplished by assuming a dimensionless displacement of 7.0 for both triiodide and diiodide. This value of the displacement is consistent with spontaneous Raman measurements[27] and our previous 2DRR study of triiodide.[26] A displacement of 7.0 also produces an excited state potential energy gradient in diiodide (225 eV/pm) that is identical to that associated with a commonly employed exponential surface at a displacement of only 9 pm from the Franck-Condon geometry.[24,25] As discussed in

section IIA, this gradient is the key quantity that must be reproduced by the present model, because electronic dephasing is fast compared to the vibrational period.

***Table 2.1.*** *Parameters of Model Used to Compute 2DRR Spectra*

| [a]Parameter | Value |
|---|---|
| $\omega_{r^*r}/2\pi c$ | 27,800 $cm^{-1}$ |
| [b] $\omega_{p^*p}/2\pi c$ | 13,300 $cm^{-1}$ & 25,400 $cm^{-1}$ |
| [c] $\omega_{r,vib}/2\pi c = \omega_{r^*,vib}/2\pi c$ | 111 $cm^{-1}$ |
| [c] $\omega_{p,vib}/2\pi c = \omega_{p^*,vib}/2\pi c$ | 114 $cm^{-1}$ |
| [c] $U_{3,r}/hc$ | 0 $cm^{-1}$ |
| [c] $U_{3,r^*}/hc = U_{3,p}/hc = U_{3,p^*}/hc$ | -1 $cm^{-1}$ |
| $\Gamma_{r,vib}/c = \Gamma_{r^*,vib}/c = \Gamma_{p,vib}/c = \Gamma_{p^*,vib}/c$ | 10 $cm^{-1}$ |
| $\Gamma_{r^*r}/c = \Gamma_{p^*p}/c$ | 2000 $cm^{-1}$ |
| [d] $\mu_{r^*r}$ | 2.3 D |
| [d] $\mu_{p^*p}$ | 1.0 D |
| [e] $\omega_{UV}/2\pi c$ | 29,400 & 25,000 $cm^{-1}$ |
| [f] $\omega_{VIS}/2\pi c$ | 14,705 & 18,900 $cm^{-1}$ |
| $\omega_t/2\pi c$ | $\omega_{VIS}/2\pi c$ |
| $\Lambda_{UV}/c = \Lambda_{VIS}/c$ | 500 $cm^{-1}$ |

[a] The indices $r$ and $p$ represent triiodide and diiodide, respectively. Asterisks indicate the lowest-energy excited electronic states of the molecules.
[b] The electronic resonance of diiodide that is probed depends on the particular experiment (see section III). In terms 1-4 and 9-12, the resonance is located at 25,400 $cm^{-1}$, whereas in terms 5-8 it is equal to 13,300 $cm^{-1}$.
[c] Parameters of Equation (2.7).
[d] Magnitudes of transition dipoles do not impact line shapes of simulated 2DRR spectra.
[e] In Figure 2.3, "pump" wavenumbers are: 25,000 $cm^{-1}$ for terms 1-4; 29,400 $cm^{-1}$ for terms 5-8; 25,000 $cm^{-1}$ for terms 9-12.
[f] In Figure 2.3, "probe" wavenumbers are 14,705 $cm^{-1}$ in terms 5-8 and 20,000 $cm^{-1}$ in terms 9-12, respectively.

## IIC. Calculated 2DRR Spectra

Figure 2.3 presents signals that are simulated for the three types of nonlinearities. Terms 1-4 yield resonances in only the upper right and lower left quadrants of Figure 2.3a because of interferences between components of the response function.[26] For terms 5-8 in Figure 2.3b, suppression of signal intensity in the upper left and lower right quadrants originates in the same

types of interferences found in terms 1-4. In terms 1-8, evolution of the system in the time intervals, $t_2$ and $t_4$, is always described by a pair of coherences in which only one of the vibrational indices is modified by the third and fourth field-matter interactions (e.g., $rj$ in terms 2 and 4 or $pl$ in terms 5 and 6). In contrast, calculations based on terms 9-12 yield peaks with equal intensities in all four quadrants in Figure 2.3c. *The unique pattern of resonances found in terms 9-12 reflects independence of the vibrational coherences that evolve during* $t_2$ and $t_4$. The key issue is that the photodissociaton process takes place *between* the $t_2$ and $t_4$ time intervals in terms 9-12 (see Figure 2.2). Therefore, the vibrational coherence in the time interval $t_4$ involves a sets of indices that are fully independent from those in $t_2$. In contrast, photodissociation occurs before vibrational coherences evolve in $t_2$ in terms 5-8, thereby placing constraints on the vibrational coherences that evolve in $t_2$ and $t_4$.

In summary, the model calculations presented in this section demonstrate that cross peaks between triiodide and diiodide appear in all four quadrants of the 2DRR spectrum. These 2DRR cross peaks may be induced with a pulse configuration in which UV pulses are employed before the $\tau_2$ delay time, and a visible pulse is applied afterwards (see terms 9-12). This particular signature of cross peaks will generalize to other systems in which vibrational coherences of the reactant and product evolve in the ground electronic states. For such systems, only cross peaks between the reactant and product will yield resonances in the upper left and lower right quadrants. The key issue is that the third and fourth field-matter interactions must take place with either the ket or bra in terms 1-8, thereby allowing a difference in only one of the indices that describes the coherences in $\tau_1$ and $\tau_2$ (see Figure 2.2).

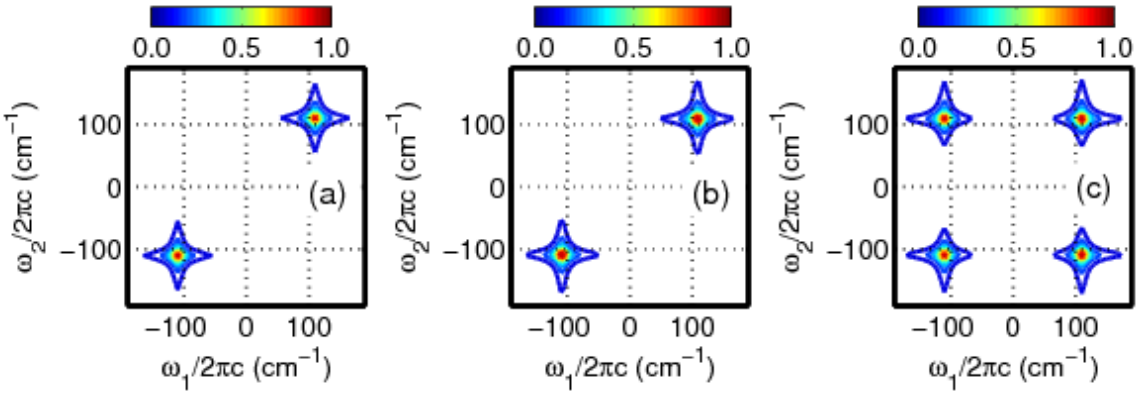


***Figure 2.3.*** *Absolute values of 2DRR spectra computed using (a) the sum of terms 1-4 in Equation (2.22), (b) the sum of terms 5-8 in Equation (2.23), and (c) the sum of terms 9-12 in Equation (2.24). The frequency dimensions,* $\omega_1$ *and* $\omega_2$*, are conjugate to the delay times,* $\tau_1$ *and* $\tau_2$ *(see Figure 2.2). Signal components of the type shown in panel (a) are generally detected in one-color experiments. Two-color 2DRR approaches are used to detect nonlinearities that correspond to panels (b) and (c) in this work. The peaks displayed in Figure 2.3c are unique in that resonances of the reactant and product are found in* $\omega_1$ *and* $\omega_2$*, respectively.*

## III. Experimental Methods

The 2DRR experiments conducted in this work utilize either five or three laser beams to obtain the fifth-order response. Measurements conducted in these geometries must contend with a background of residual laser light and/or lower-order nonlinearities, because fewer than six laser beams are employed.[26] In this section, we describe the two experimental setups and discuss how sources of background are dealt with.

### IIIA. Conducting 2DRR Spectroscopy with a Five-Beam Geometry

Detection of signal components described by terms 5-8 in Figure 2.2 is accomplished with a geometry of five laser beams. In Figure 2.4, it is shown that a 340-nm laser beam is simply added to an existing diffractive optic-based transient grating setup operational at 680 nm.[40] A slightly modified version of this interferometer has been described elsewhere.[41,42] Briefly, the 680-nm beams are focused on the diffractive optic with a 20-cm focal length spherical mirror and cross at 5.4º. The angle between the +1 and -1 diffraction orders is also 5.4º.

Thus, a square pattern of 680-nm beams appears on the 20-cm focal length spherical mirror. The spherical mirror is tilted off-axis by approximately 5º (i.e., the minimum amount) in order to image the spot from the diffractive optic onto the sample. Focusing conditions of the 340-nm beam are optimized to match the 200-μm FWHM spot sizes of the 680-nm beams.

The 340-nm and 680-nm laser beams are produced by focusing a 0.8-mJ, 60-fs laser beam at 800 nm into a 43-cm long hollow core fiber with a 250-μm inner diameter. The continuum produced in the fiber spans the full visible spectral range. A 4-uJ, 40-nm wide portion of the continuum centered at 680 nm is filtered in a fused silica prism compressor. Most of the 680-nm beam (65%) is used to generate 340-nm light in a 100-micron thick, Type I Beta Barium Borate (BBO) crystal. In order to minimize lossy reflections, the 340-nm beam is directly imaged from the BBO onto the sample using a 15-cm focal length spherical mirror placed 30-cm from the BBO. Residual 680-nm light is filtered using a 1-mm thick fused silica polarizer. A lossy second compression step is not required for the 340-nm beam because of precompensation for dispersion in the aforementioned prism compressor; the polarizer used to filter residual 680-nm light compensates for negative chirp in the 340-nm pulse.

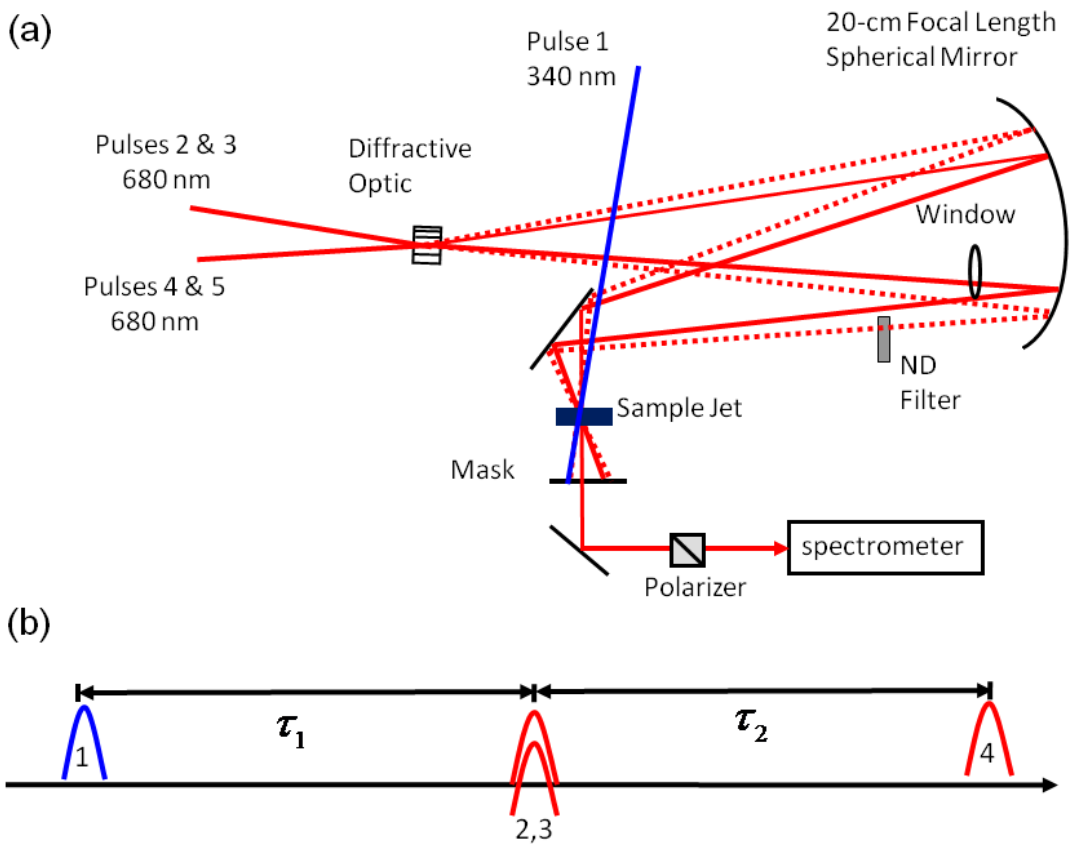


***Figure 2.4.*** *(a) Diffractive optic-based interferometer used to detect signal components described by terms 5-8 in Figure 2.2. Each of the two 680-nm beams is split into -1 and +1 diffraction orders with equal intensities at the diffractive optic. The signal is collinear with the reference field (pulse 5) used for interferometric signal detection. (b) The 340-nm pulse induces photodissociation and vibrational coherence in the diiodide photoproduct during the delay,* $\tau_1$*. The time-coincident 680-nm pulses, 2 and 3, reinitiate the vibrational coherence in diiodide during the delay,* $\tau_2$*.*

In this pulse sequence, the 40-fs, 340-nm pulse (pulse 1 in Figure 2.4) induces a photodissociation process that leaves the diiodide photoproduct in a vibrational coherence as suggested by terms 5-8 in Figure 2.2. A time-coincident pair of 25-fs, 680-nm laser pulses (pulses 2 and 3 in Figure 2.4) reinitiates the vibrational coherence in diiodide during the delay, $\tau_2$. The fourth pulse (also at 680 nm) induces signal emission. The fifth pulse, which is attenuated by a factor of 1000 before the sample, is used for heterodyne detection by spectral interferometry.[43,44] The signal phase can be determined using the method devised by Turner and

Scholes in this beam geometry,[45] because the 340-nm pulse does not factor into the phase calibration. Scherer and Blank have employed similar laser beam geometries and phasing schemes in related fifth-order experiments.[46-48]

An undesired four-wave mixing response may be radiated by the solvent in the same direction as the fifth-order signal in this geometry. However, because the sample is transparent at 680 nm, this four-wave mixing signal is approximately 50 times smaller than that associated with the solute at delay times greater than 80 fs. Moreover, the desired signal radiated by the solute exhibits a vibrational coherence with a period of 300 fs. Insensitivity of this setup to intramolecular vibrations of the solvent was confirmed by scanning the delay, $\tau_2$, with the 340 nm beam blocked. Thus, the assignment of the experimentally observed 112-$cm^{-1}$ vibrational resonance to the solute is unambiguous.[26] The 2DRR experiment may be conducted without chopping the 340-nm beam, because the desired fifth-order nonlinearity dominates the total response of the solution. Conducting the experiment without chopping the 340-nm beam greatly speeds up data acquisition and facilitates signal averaging.

Signals are detected using a back-illuminated CCD array (Princeton Instruments PIXIS 100B) mounted on a 0.3 meter spectrograph with a 600 g/mm grating. The signal generates roughly 80 counts/ms on the detector with 150-nJ, 340-nm pulses and 200-nJ, 680-nm pulses. All beams possess the same electric field polarization and are focused to 200 μm at the sample position. The two delay lines are scanned 20 times and averaged. The step sizes are 40 fs in both dimensions.

**IIIB. Conducting 2DRR Spectroscopy with a Three-Beam Geometry**

Signal components of the type described by terms 9-12 are detected using a three-pulse geometry (i.e., a standard pump-repump-probe experiment).[49] As shown in Figure 2.5, the first

two pulses that arrive at the sample are 25-fs, 400-nm pulses produced by self-phase modulation in a hollow core fiber,[50] whereas the third pulse is a visible continuum produced in a 3-mm thick sapphire plate. The 400-nm beams are focused onto the sample with a 30-cm focal length spherical mirror, whereas the continuum is relayed from the sapphire plate onto the sample using a single 5-cm focal length mirror (the continuum focuses 35 cm from the spherical mirror). The FWHM spot sizes of the 400-nm beams are 600 μm, whereas that of the continuum is 400 μm. Angles between the adjacent beams are 5°. Pulse energies of the 400-nm beams range from 150-300 nJ in various experiments, and we observe no differences in the vibrational lineshapes obtained within this range of pulse energies. The phases of the two chopper wheels, which are both operated at 250 Hz, are shifted by 90° to acquire signals under the four conditions needed to produce a pump-repump-probe signal ($\Delta\Delta A$).[49] Signal detection is accomplished with a CMOS array detector that is synchronized to the 1-kHz repetition rate of the laser system. The noise level of a pump-repump-probe signal is approximately 0.1 mOD in this setup. The delay lines are scanned 10 times with step sizes of 40 fs and averaged.

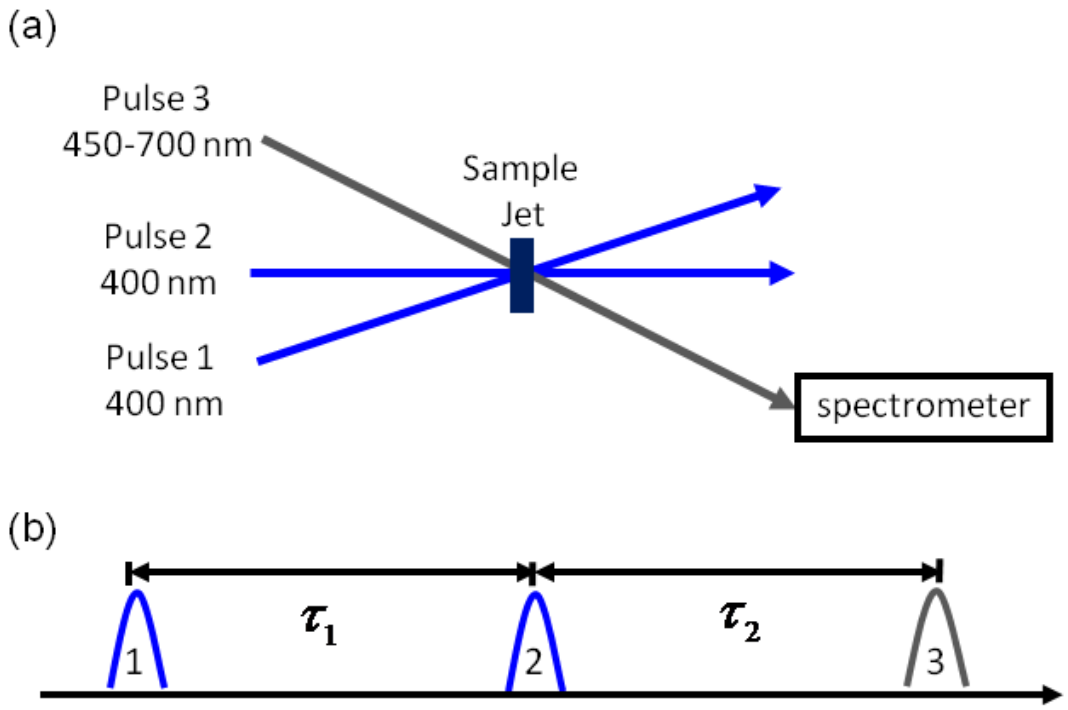


***Figure 2.5.*** *(a) Pump-repump-probe beam geometry used to detect signal components described by terms 9-12 in Figure 2.2. (b) The first 400-nm pulse promotes a stimulated Raman response in the ground electronic state of the triiodide reactant during the delay, $\tau_1$. The second pulse induces photodissociation of the non-equilibrium reactant, thereby giving rise to vibrational coherence in the diiodide photoproduct during the delay, $\tau_2$. Sensitivity to diiodide is enhanced by signal detection in the visible spectral range.*

Two field-matter interactions with triiodide occur with each of the 400-nm pump pulses in this experiment. The first pulse stimulates wavepacket motion in the ground electronic state of triiodide as indicated in terms 9-12. The application of a second 400-nm pulse ensures that the signals are primarily sensitive to vibrational coherences of triiodide during $\tau_1$ (i.e., signal contributions from diiodide are negligible during $\tau_1$). The key issue is that the transient electronic resonance of triiodide is dominant at 400 nm (i.e., the bleach of the ground state). The second 400-nm pulse induces photodissociation of triiodide and leaves the diiodide photoproduct in a vibrational coherence in $\tau_2$. Signal detection in the visible spectral range enhances sensitivity to the diiodide product in the delay, $\tau_2$.

### IIIC. Sample Preparation and Handling

Triiodide solutions are prepared by mixing solid $I_2$ (Aldrich) with 5-fold molar excess of KI (Aldrich) in ethanol (Decon Labs, 200 proof). The solutions are stirred for one hour to fully dissolve the solid. The absorbance of the solutions is equal to 0.5 at 400 nm in a 300-μm path length. The sample is flowed through a wire-guided jet with a thickness of 300 μm, where the volume of the reservoir is 50 mL.

## IV. Experimental Results

In this section, we present 2DRR signals obtained for triiodide using two-color pulse sequences. We begin by reviewing properties of the third-order pump-probe response to facilitate the subsequent discussion of 2DRR spectra.

### IVA. Third-Order Stimulated Raman Response

The pump-probe signals shown in Figure 2.6 illustrate several aspects of the stimulated Raman response of triiodide. Vibrational coherences are observed throughout the visible spectral range as in earlier work on this system.[16-23] The modulation depth of the oscillations is greatest in the range, 18,000-21,000 $cm^{-1}$ (475-555 nm). Coherences at detection wavenumbers below 20,000 $cm^{-1}$ (500 nm) are dominated by diiodide, whereas signals acquired at detection wavenumbers above 20,000 $cm^{-1}$ possess significant contributions from ground state wavepacket motions of triiodide. The vibrational coherences detected below 20,000 $cm^{-1}$ are similarly assigned to the ground electronic state of diiodide, because the excited state potential energy surface is dissociative.[51]

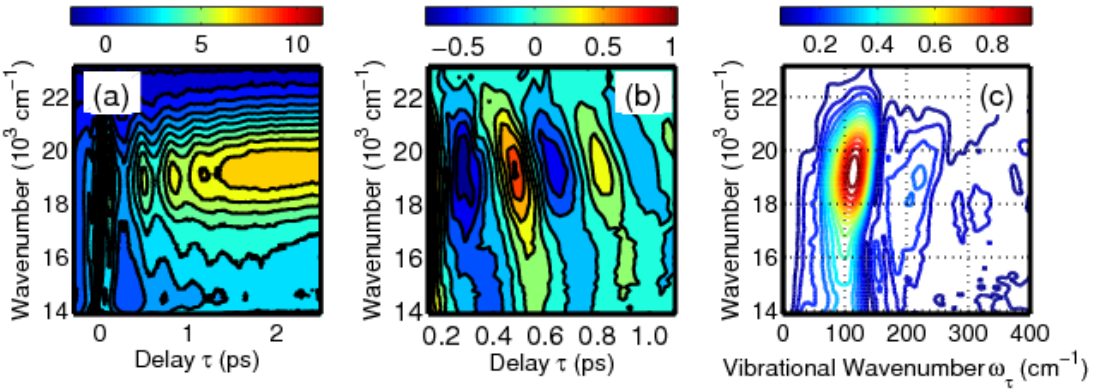


***Figure 2.6.*** *(a) Transient absorption signals (in mOD) obtained for triiodide with a 400-nm pump pulse and continuum probe pulse. (b) The coherent component of the signal is isolated by subtracting sums of 2 exponentials from the total signal presented in panel (a). (c) Fourier transformation of the signal between delay times of 0.1 and 2.5 ps shows that the vibrational frequency decreases as the detection wavenumber decreases. Dispersion in the vibrational frequency reflects sensitivity to high-energy quantum states in the anharmonic potential of diiodide.*[19]

The photodissociation process is known to cause the period of vibrational motion to evolve as the delay increases.[22] In Figure 2.6b, such "chirped" wavepacket dynamics are evidenced by time evolution in the orientations of the nodal contour lines of the signal. It has been established that the strength of the chemical bond weakens as the symmetry of triiodide breaks immediately following light absorption.[16-23] The reactive wavepacket departs from the Franck-Condon geometry as one of the bonds ruptures, thereby giving rise to the time dependence of the vibrational frequency observed in Figure 2.6b. The dependence of the vibrational period on the detection wavenumber reflects sensitivity to highly excited states in the anharmonic potential of the diiodide product. Kühne and Vöhringer determined that experiments with visible probe pulses are sensitive to states with 10-30 vibrational quanta.[19]

**IVB. 2DRR Response of the Diiodide Photoproduct**

The 2DRR response of the diiodide photoproduct is detected using the two-color approach described in Figure 2.4. The signals shown in Figure 2.7 are Fourier transformed to

reveal peaks in the upper right and lower left quadrants of the 2DRR spectrum. The resonances appear near 100 $cm^{-1}$ in both dimensions, which indicates that the experiment is sensitive to states of diiodide that possess roughly 20 vibrational quanta.[19] Vibrational resonances are not detected in the other two quadrants of the 2DRR spectrum as in our earlier study of ground state wavepacket motions in triiodide.[26] The locations of the peaks in the experimental 2DRR spectrum agree with the prediction made for terms 5-8 in Figure 2.3 (i.e., the terms this pulse sequence is designed to detect).

The data shown in Figure 2.7b indicate that the vibrational dephasing rate is slightly faster in $\tau_1$ than it is in $\tau_2$ (i.e., the line width is slightly larger in $\omega_1$ than it is in $\omega_2$). We attribute this difference in line widths to intramolecular relaxation and inertial solvation processes that occur following photodissociation in $\tau_1$. The photoproduct is likely far from equilibrium when the vibration fully damps near 2 ps; however, a significant amount of solute-to-solvent vibrational energy transfer may still take place on this time scale.[17] This view of the information carried by each dimension of the 2DRR signal is consistent with interpretations of related optical pump/Raman probe experiments.[46-48,52-54] That is, the relaxation processes detected in the first delay time, $\tau_1$, are related to those investigated with traditional pump-probe experiments (e.g., vibrational cooling).[16-23] Scanning the second delay time, $\tau_2$, essentially yields a snapshot of the vibrational spectrum as the system relaxes in $\tau_1$.[18]

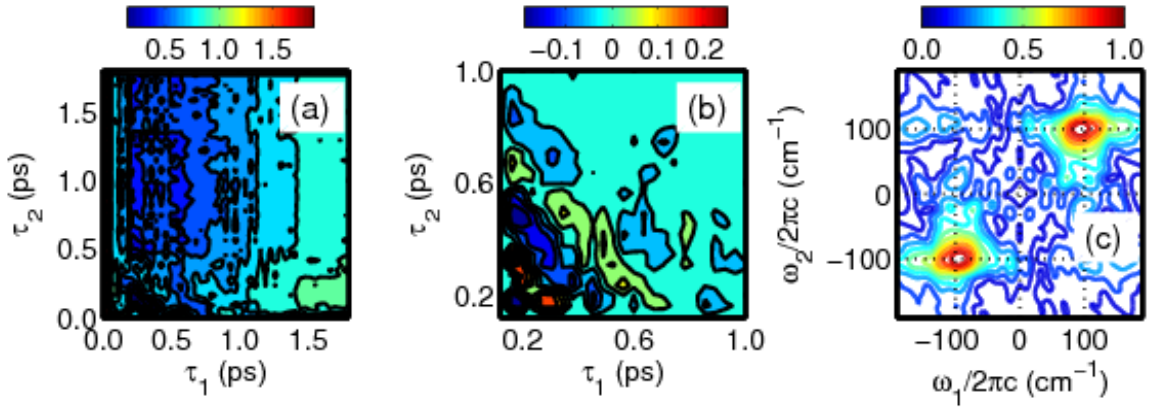


***Figure 2.7.*** *2DRR signals associated with terms 5-8 are obtained using the two-color approach described in Figure 2.4. (a) The total signal possesses both coherent and incoherent components. (b) The coherent (Raman) component of the signal is isolated by subtracting sums of two exponentials from the total signal presented in panel (a). (c) The two-dimensional Fourier transformation of the signal in panel (b) in delay ranges,* $\tau_1$ *and* $\tau_2$*, between 0.15 and 2.0 ps reveals resonances in the upper right and lower left quadrants. This pattern of 2DRR resonances is consistent with calculations based on terms 5-8 (see Figure 2.3), which this experiment is designed to detect.*

**IVC. 2DRR Cross Peaks Between Triiodide and Diiodide**

The 2DRR spectra theoretically predicted in Figure 2.3 are consistent with the experimental measurements shown in Figure 2.7 (terms 5-8) and our earlier all-UV 2DRR spectra (terms 1-4).[26] In both cases, peaks are found in only the upper right and lower left quadrants because of interferences between numerous terms in the response function. In this section, we test the prediction that signal components corresponding to terms 9-12 will give rise to resonances in all four quadrants of the 2DRR spectrum (see Figure 2.3c). This unique pattern of resonances signifies a process in which a vibrational wavepacket transitions between reactant and product states without loss of coherence.

The 2DRR data presented in Figure 2.8 are obtained using the experimental setup described in Figure 2.5. The pump-repump-probe signals exhibit oscillations in both dimensions, which may be Fourier transformed to produce 2DRR spectra. Signals acquired at several detection wavenumbers are displayed to illustrate a transition between regimes in which motions

of triiodide or diiodide dominate the second dimension, $\omega_2$. At a detection wavenumber of 22,500 $cm^{-1}$ (444 nm), where absorption of triiodide is dominant, the pattern of resonances is consistent with terms 1-4 (see Figure 2.3a). However, intensities of the vibrational resonances in the upper left and lower right quadrants of the 2DRR spectrum increase as the detection wavenumber is detuned from the absorption spectrum of triiodide. At detection wavenumbers less than 19,500 $cm^{-1}$ (513 nm), we observe peaks with equal intensities in all four quadrants, which is consistent with the prediction made for terms 9-12 in Figure 2.3c.

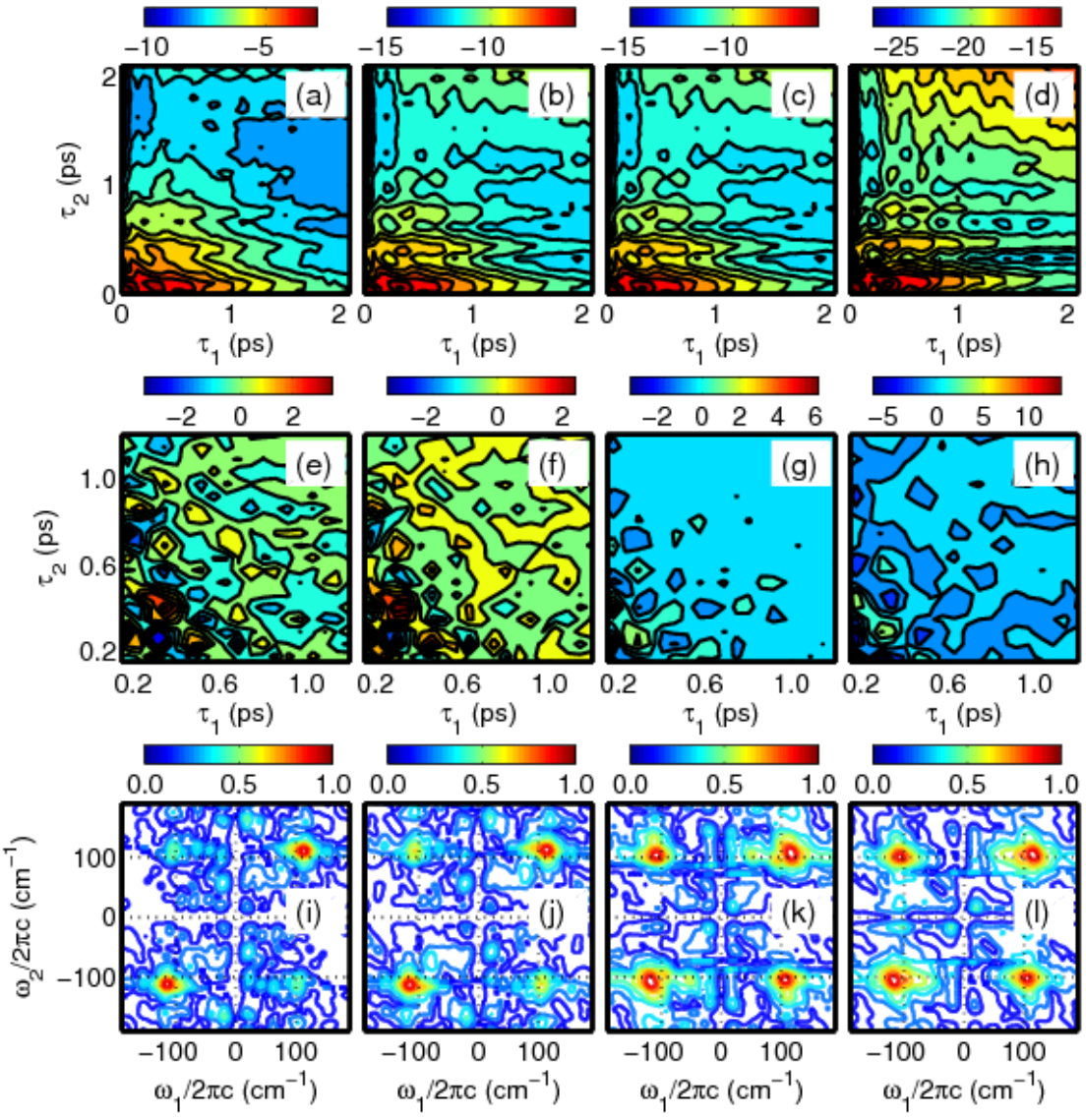


***Figure 2.8.*** *2DRR data are obtained using the two-color approach described in Figure 2.5. Each column corresponds to a different detection wavenumber: 22,500 cm$^{-1}$ (444 nm) in column 1; 21,000 cm$^{-1}$ (476 nm) in column 2; 19,500 cm$^{-1}$ (513 nm) in column 3; 18,000 cm$^{-1}$ (555 nm) in column 4. (a)-(d) Total pump-repump-probe signal in mOD. (e)-(h) Coherent parts of the pump-repump-probe signals displayed in the first row. (i)-(l) 2DRR spectra are generated by Fourier transforming the signals shown in the second row in delay ranges, $\tau_1$ and $\tau_2$, between 0.15 and 2.0 ps. The data show that peaks in the upper left and lower right quadrants emerge as the detection wavenumber becomes off-resonant with triiodide. Signals acquired at detection wavenumbers above 21,000 cm$^{-1}$ (476 nm) are dominated by stimulated Raman processes in the ground electronic state of triiodide (terms 1-4). In contrast, signals acquired at detection wavenumbers below 19,500 cm$^{-1}$ (513 nm) are consistent with terms 9-12, where vibrational resonances in $\omega_1$ and $\omega_2$ correspond to triiodide and diiodide, respectively.*

The detection of peaks with equal intensities in all four quadrants is consistent with nonlinearities of the type shown in terms 9-12. The peak positions are also consistent with this assignment. The 112-cm$^{-1}$ vibrational resonance in $\omega_1$ is notably independent of the detection wavenumber (as it should be for the reactant). In contrast, the frequency of the vibrational resonance in $\omega_2$ decreases as the detection wavenumber decreases. For example, we observe resonances in $\omega_2$ at 110 cm$^{-1}$ and 100 cm$^{-1}$ for detection wavenumbers of 22,500 cm$^{-1}$ (444 nm) and 18,000 cm$^{-1}$ (555 nm), respectively. As discussed in section IVA, correlation between the vibrational frequency and detection wavenumber is a signature that diiodide contributes to the signal (i.e., the origin of the response transitions from terms 1-4 to terms 9-12 as the detection frequency decreases).[51] At present, 2DRR spectra cannot be measured at detection wavenumbers below 18,000 cm$^{-1}$ (555 nm) in this setup, because of the substantial background that must be removed by chopping the pump and repump laser beams. Nonetheless, the transition between the two aforementioned regimes (i.e., terms 1-4 versus terms 9-12) is made sufficiently clear in the range of detection frequencies where adequate signal strength is obtained.

Cascades of four-wave mixing signal fields challenge the application of 2D Raman spectroscopy under off-resonant conditions. Cascades were ruled out in our previous all-UV 2DRR study of triiodide using control experiments based on the signal phase, concentration dependence of the signal intensity, and the relative phases of the vibrations detected in four and six-wave mixing signals.[26] The direct 2DRR response should be even more dominant in the present study, because lower-frequency laser beams are employed. Moreover, the direct response is favored in the present experiments for the same reasons discussed at length in Reference [26]. In the Appendix 1, we demonstrate that the sign of the 2DRR response is consistent with the direct fifth-order nonlinearity rather than a cascade.[38]

## IVD. Summary of 2DRR Signal Components

In this section, we summarize our attainment of 2DRR spectra associated with the three types of signal components d. Figure 2.9 displays the present results alongside the 2DRR spectrum for ground state wavepacket motions of triiodide obtained in earlier work.[26] As shown in 9a, the application of all-UV pulses yields a 2DRR spectrum in which the vibrational resonances of triiodide appear in both dimensions (i.e., terms 1-4 in Figure 2.2). Similarly, vibrational motions of diiodide dominate both dimensions in Figure 2.9b , because only the first pulse is resonant with equilibrium triiodide (i.e., terms 5-8 in Figure 2.2). Finally, vibrational motions of triiodide and diiodide are detected in separate dimensions in Figure 2.9c. Here, only the final pulse to arrive at the sample is electronically off-resonant with triiodide (i.e., terms 9-12 in Figure 2.2). This type of nonlinearity is unique in that it gives rise to 2DRR spectra in which peaks with equal intensities appear in all four quadrants. The terms in the response function responsible for these peaks reflect a sequence in which a wavepacket in the symmetric stretching coordinate of triiodide transforms into a wavepacket in the bond stretching mode of diiodide without loss of coherence. 2DRR spectroscopy is specially equipped for investigations of such coherent dynamics, because it possesses two electronic “population times”. In contrast, traditional third-order pump-probe experiments only have one population time.

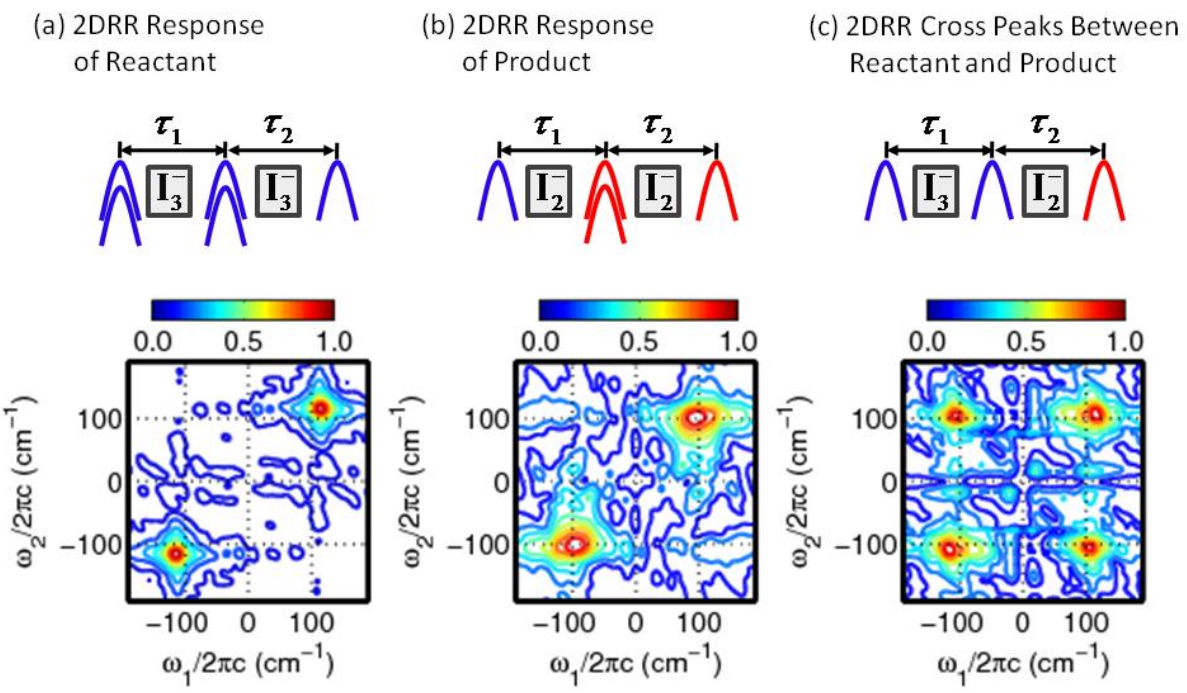


***Figure 2.9.*** *Summary of 2DRR experiments conducted on triiodide: (a) the response of triiodide was detected in both dimensions in Reference [26]; (b) the response of the diiodide photoproduct is detected in both dimensions (see Figure 2.7); (c) the response of triiodide and diiodide are detected in separate dimensions (see Figure2.8). Blue and red laser pulses represent wavelengths that are electronically resonant with triiodide and diiodide, respectively.*

The signature of cross peaks demonstrated in Figure 2.9 will not necessarily generalize to all systems. In the photodissociation process of triiodide, the key is that the wavepacket motions take place on the ground state potential energy surfaces of both the reactant and product. For signal components associated with terms 1-8, this means that both the third and fourth field-matter interactions occur with either the ket or bra (see Figure 2.2). In contrast, the constraints that suppress intensity in the upper left and lower right quadrants in Figures 2.9a and 2.9b may be lifted in systems with bound excited states, thereby yielding peaks in all four quadrants. Nonetheless, it is likely that strategies such as three-color pulse sequences can be used in systems with bound excited states to isolate the desired signal components.

## V. Nonequilibrium Correlation Between Reactants and Products

We have focused to this point on establishing signatures of cross peaks between triiodide and diiodide in 2DRR spectra (see Figure 2.9c). Of course, the vibrational resonance frequencies of both species can be determined by lower-order pump-probe experiments.[16,19-21] The information unique to 2DRR spectroscopy pertains to the correlated vibrational motions of the reactant and product. In this section, we explore a time-frequency representation of the signal that is well-suited for physical insight into the photodissociation process of triiodide.

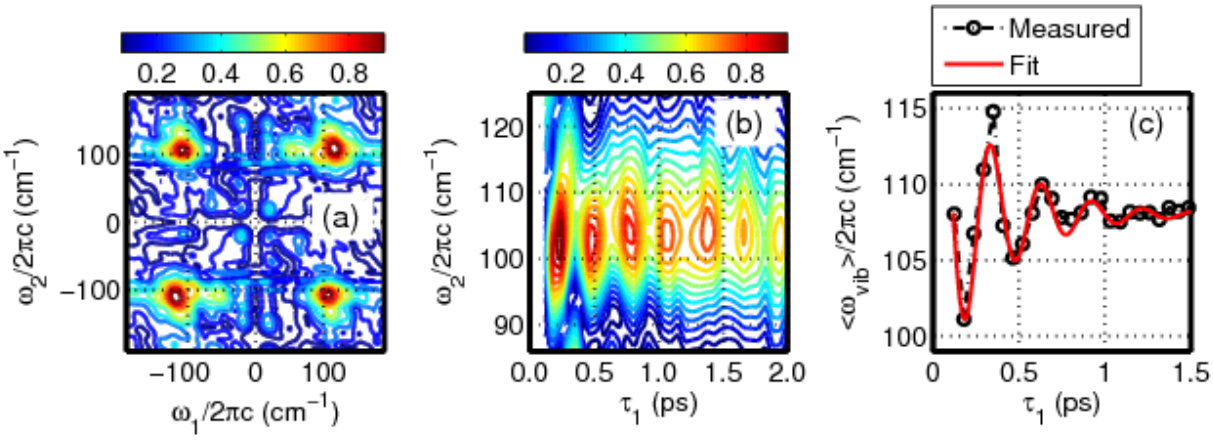


***Figure 2.10.*** *2DRR response of triiodide in ethanol with a detection wavenumber of 19,500 cm$^{-1}$ (513 nm). (a) Resonances in all four quadrants of the 2DRR spectrum signify cross peaks between triiodide (in $\omega_1$) and diiodide (in $\omega_2$). (b) Quantum beats in the Raman spectrum of diiodide are observed when the 2DRR spectrum in panel (a) is inverse Fourier transformed with respect to $\omega_1$. (c) Oscillations in the mean vibrational frequency are analyzed using Equation (2.6). Such oscillatory behavior suggests that the vibrational coherence frequency of diiodide is sensitive to vibrational motions of triiodide in the delay time, $\tau_1$.*

For the present system, it is our view that the frequency-domain representation of the 2DRR signal is primarily useful for confirming that the reactant and product dominate separate dimensions (see Figure 2.9). Once this is established, we suggest that the physical insight into the dissociation process is most clearly derived by leaving the first dimension in the time domain as displayed in Figure 2.10b. Here, the $\tau_1$ dimension represents wavepacket motion of triiodide in

its ground electronic state, whereas the vibrational spectrum of diiodide is displayed in the $\omega_2$ dimension. The mean vibrational frequency shown in Figure 2.10c is generated using the weighted average,

$$\left\langle \omega_{vib}(\tau_1) \right\rangle = \frac{\int d\omega_2 S(\tau_1, \omega_2)\omega_2}{\int d\omega_2 S(\tau_1, \omega_2)}, \tag{2.6}$$

where $S(\tau_1, \omega_2)$ denotes the signal displayed in Figure 2.10b. The oscillations in $\left\langle \omega_{vib}(\tau_1) \right\rangle$ indicate that the vibrational coherence frequency of diiodide depends on the time-evolving nonequilibrium geometry of triiodide in the delay time, $\tau_1$. The fit shown in Figure 2.10c reveals extrema in $\left\langle \omega_{vib}(\tau_1) \right\rangle$ of 99 and 111 $cm^{-1}$ near the turning points of the wavepacket at delay times of 170 and 325 fs, respectively.

The LEPS potential energy surface of triiodide in ethanol shown in Figure 2.11 facilitates a discussion of the signal generation mechanism in terms of a microscopic picture.[17,27] As suggested by Figure 2.11a, the first pulse induces an electronic coherence and initiates a wavepacket in the symmetric stretching mode on the ground state potential (i.e., a stimulated Raman process). The turning points of the wavepacket can be estimated using the 300-fs period of the vibration and approximate 0.6 Å bond length displacement between the ground and excited state potential energy minima (i.e., 0.6 Å is the projection of the symmetric stretching coordinate onto the individual bond lengths).[27] We estimate that the wavepacket is stimulated in the ground state at bond lengths, $R_{ab}$=$R_{bc}$, near 3.06 Å by assuming a 20-fs electronic dephasing time. Here, the turning point is computed by adding 20/75*0.6 Å to the equilibrium bond length of 2.9 Å (75 fs is 1/4 of the vibrational period and 20 fs is the electronic dephasing time).[18] In other words, we estimate that the wavepacket moves approximately 0.16 Å from the equilibrium

position of 2.9 Å during the electronic coherence induced by the first laser pulse before undergoing oscillations on the ground state potential energy surface in $\tau_1$. Notably, small changes in the numbers chosen for this analysis do not impact the physical interpretation of the experiment.

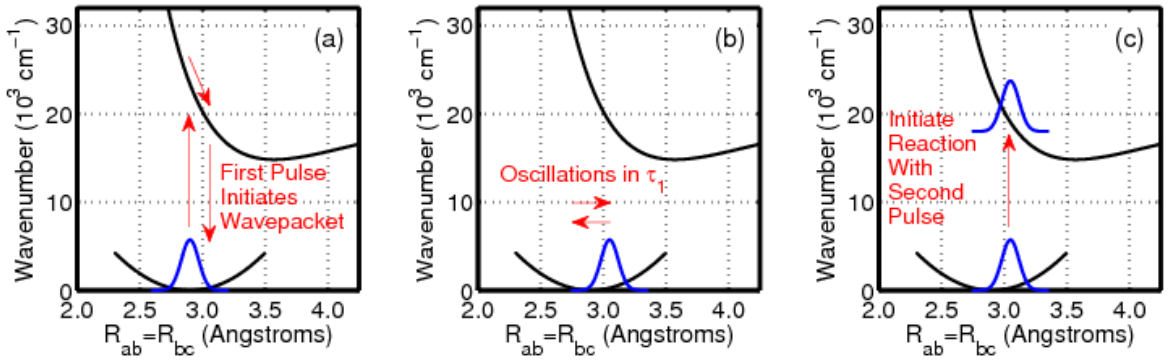


***Figure 2.11.*** *The sequence of events associated with the 2DRR signals shown in Figure 2.10. $R_{ab}$ and $R_{bc}$ denote the two bond lengths in triiodide. (a) The first pulse initiates a ground state wavepacket in the symmetric stretching coordinate. Force is accumulated when both bond lengths increase during the electronic coherence induced by the first laser pulse. (b) Wavepacket motion on the ground state potential energy surface is detected in the delay between the pump and repump laser pulses, $\tau_1$. (c) Photodissociation of triioide is initiated from a nonequilibrium geometry by the repump laser pulse. The Raman spectrum of diiodide may then be detected by scanning the delay of a probe pulse, $\tau_2$.*

Following ground state wavepacket initiation by the pump pulse, the application of a repump laser pulse promotes the vibrational wavepacket in triiodide to the excited state potential energy surface, where asymmetric motion induces dissociation of the molecule (see Figures 2.11b and 2.11c). The 20-fs pump and repump laser pulses are much shorter than the 300-fs vibrational period, and the wavepacket moves very little along the symmetric stretching coordinate before photodissociation.[20] For these reasons, the geometry of triiodide from which the reaction commences is sensitive to the delay time, $\tau_1$. By contrast, in a traditional (third-order) transient absorption spectroscopy, the reactive wavepacket must always be promoted onto

the excited state potential energy surface from the equilibrium geometry (i.e., bond lengths of approximately 2.9 Å).

Correlation between the wavepacket in the symmetric stretching coordinate of triiodide and the vibrational coherence frequency of diiodide can be visualized by converting the delay time, $\tau_1$, into the position of the wavepacket in the symmetric stretching coordinate (i.e., the bond lengths in triiodide, $R_{ab}$=$R_{bc}$). In Figure 2.12, the inner and outer turning points of the wavepacket are taken to correspond to the minima and maxima in $\langle \omega_{vib}(\tau_1) \rangle$ shown in Figure 2.10c. Translation between the delay, $\tau_1$, and the bond lengths is achieved by applying the model described above to $\langle \omega_{vib}(\tau_1) \rangle$. That is, we estimate that the wavepacket is located at 2.74 and 3.06 Å at delay times, $\tau_1$, of 170 and 325 fs, respectively. Each revolution of the spiral in Figure 2.12 represents one period of vibrational motion in $\tau_1$. The spiral focuses inward towards the equilibrium bond length because of damping in $\langle \omega_{vib}(\tau_1) \rangle$. The orientation of the spiral during the first cycle of the wavepacket suggests that bond length displacements of approximately 0.1 Å in triiodide produce a 6.8-cm$^{-1}$ shift in the vibrational coherence frequency of diiodide.

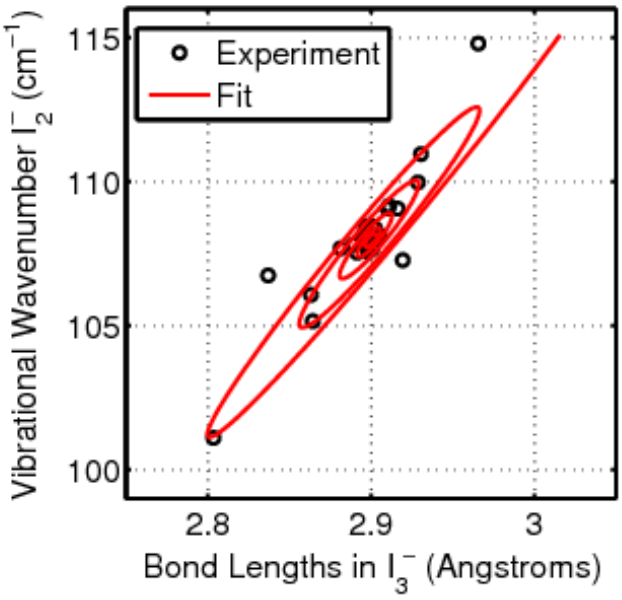


***Figure 2.12.*** *Correlation between the vibrational wavenumber of the diiodide photoproduct and the pair of bond lengths in the triiodide reactant, $R_{ab}$=$R_{bc}$, is illustrated by analyzing the dynamics in the mean vibrational coherence frequency, $\langle \omega_{vib}(\tau_1) \rangle$, shown in Figure 2.10c. The delay time, $\tau_1$, is converted into the position of the wavepacket in the symmetric stretching coordinate using the model presented in Figure 2.11. Each revolution of the spiral corresponds to 300 fs. The wavepacket oscillates around the equilibrium bond length until vibrational dephasing is complete. The diagonal slant in the spiral suggests that a bond length displacement of 0.1 Å in triiodide induces a shift of 6.8 $cm^{-1}$ in the vibrational coherence frequency of diiodide.*

The primary goal of the analysis presented in this section is to demonstrate the type of information that 2DRR spectroscopy can provide about nonequilibrium dynamics. Although our data suggests correlation between triiodide and diiodide, further theoretical work will be needed to draw firm conclusions about the relationship established in Figure 2.12. We have considered two possibilities. First, the geometry of the triiodide from which the reaction is initiated may influence the distribution of vibrational quanta in diiodide through a straightforward Franck-Condon mechanism as discussed in earlier work on triiodide in the gas phase.[55] Indeed, a second-order perturbative theory for photodissociation processes suggests that the populations of the vibrational states in a product may be weighted by overlap integrals involving the nuclear coordinates of the reactant.[56] Of course, the vibrational coherence frequency of diiodide is

known to be sensitive to the distribution of vibrational quanta because of anharmonicity.[19] A second possibility is that the correlation displayed in Figure 2.12 reflects interactions between dissociated fragments. Small inter-fragment distances have been suggested to influence vibrational coherence frequencies in solution on short time scales (i.e., fragment recoil).[19] Ruhman and co-workers have also recently discovered the presence of contact fragment pairs in solution (i.e., fragments in close proximity).[25] It is not yet clear if contributions from distinct relaxation channels are relevant to the present observations. Nishiyama et al. found evidence that vibrational dephasing may be faster than or comparable to the vibrational period in contact ion pairs, which suggests that 2DRR spectroscopy may be insensitive to these species.[24]

## VI. Supplemental Information

### VIA. Vibrational Hamiltonians

The present model assumes that both triiodide and diiodide possess two electronic levels and one nuclear coordinate whose potential energy minimum is displaced between the ground and excited electronic states. The rationale behind the model is discussed in section IIA. The anharmonic vibrational wavefunctions for the Franck-Condon active bond stretching mode of diiodide and the symmetric stretching coordinate of triiodide are generated using a Hamiltonian with the following form[60]

$$H_\alpha = \frac{\mathrm{h}\omega_{\alpha,vib}}{2}\left(2a^\dagger a + 1\right) + U_{3,\alpha}\left[a^\dagger a^\dagger a^\dagger + 3a^\dagger a^\dagger a + 3a^\dagger aa + aaa + 3a^\dagger + 3a\right], \tag{2.7}$$

where

$$U_{3,\alpha} = \frac{1}{3!\sqrt{2^3 m^3 \omega^3 \mathrm{h}^{-3}}}\left(\frac{d^3V}{dq^3}\right)_0. \tag{2.8}$$

The wavefunctions are obtained by diagonalizing this Hamiltonian in a basis set of harmonic oscillators that includes states with up to the 40 vibrational quanta. Parameters of the vibrational

Hamiltonian are given in Table 2.1. We use a notation in which $\alpha$ represents the molecule ($r$ for triiodide or $p$ for diiodide) and an asterisk indicates an electronically excited state.

The vibrational overlap integrals used to evaluate the response functions of diiodide are obtained using

$$\langle n|m\rangle = \sum_{jk} \varphi_{nk}\varphi_{mj} \langle k|j\rangle, \tag{2.9}$$

where $\varphi_{nk}$ is the expansion coefficient for harmonic basis vector, $k$, and the anharmonic excited state vibrational wavefunction, $n$. Vibrational overlap integrals of triiodide are given by a different formula,

$$\langle n|m\rangle = \sum_{k} \varphi_{nk} \langle k|m\rangle, \tag{2.10}$$

because the ground and excited states are taken to be harmonic and anharmonic, respectively (see discussion in section II). In order to evaluate the overlap integrals, we assume a dimensionless displacement of 7.0 based on spontaneous Raman measurements for triiodide[27] and our earlier 2DRR study.[26] A displacement of 7.0 also produces an excited state potential energy gradient of 225 eV/pm in diiodide which is identical to that associated with a previously employed exponential surface at a displacement of only 9 pm from the Franck-Condon geometry.[24,25] As discussed in section IIA, this gradient is the key quantity that must be reproduced by the present model, because electronic dephasing is fast compared to the vibrational period.[36] For this reason, the spectroscopic signals investigated in this work are insensitive to features of the excited state potential energy surface that are displaced from the Franck-Condon geometry.

**VIB. Two-Dimensional Resonance Raman Signal Components**

The Feynman diagrams presented in Figure 2.2 include dummy indices for vibrational levels ($m, n, j, k, l, u, v, w$) associated with the ground and excited electronic states ($r$ and $r*$ for triiodide, $p$ and $p*$ for diiodide). Response functions are written in the Condon approximation, where the integral over electronic and nuclear degrees of freedom in the transition dipole is separated into a product of two integrals. For example, an interaction that couples vibrational level $m$ in the ground electronic state of the reactant and vibrational level $n$ in the excited electronic state of the reactant contributes the product, $\mu_{r*r}\langle n|m\rangle$, to the response function, where $\mu_{r*r}$ is the electronic transition dipole and $\langle n|m\rangle$ is a vibrational overlap integral. We use a notation in which the excited state vibrational energy level is always written in the bra.[39]

The first polarization component is given in Equation (2.3). The remaining 11 polarization components, which are derived in the Appendix 1,[38] are given by

$$P_2^{(5)}(\omega_1,\omega_2) = -\frac{N\xi_{UV}^5\left|\mu_{r*r}\right|^6}{\mathrm{h}^5}\sum_{mnjklu} B_m \langle n|m\rangle\langle n|j\rangle\langle k|m\rangle\langle k|l\rangle\langle u|j\rangle\langle u|l\rangle \times L_{r*n,rm}(\omega_{UV})D_{rj,rm}(\omega_1)L_{rj,r*k}(-\omega_{UV})D_{rj,rl}(\omega_2)L_{r*u,rl}(\omega_t), \quad (2.11)$$

$$P_3^{(5)}(\omega_1,\omega_2) = -\frac{N\xi_{UV}^5\left|\mu_{r*r}\right|^6}{\mathrm{h}^5}\sum_{mnjklu} B_m \langle n|m\rangle\langle n|j\rangle\langle k|j\rangle\langle k|l\rangle\langle u|m\rangle\langle u|l\rangle \times L_{rm,r*n}(-\omega_{UV})D_{rm,rj}(\omega_1)L_{rm,r*k}(-\omega_{UV})D_{rm,rl}(\omega_2)L_{r*u,rl}(\omega_t), \quad (2.12)$$

$$P_4^{(5)}(\omega_1,\omega_2) = -\frac{N\xi_{UV}^5\left|\mu_{r*r}\right|^6}{\mathrm{h}^5}\sum_{mnjklu} B_m \langle n|m\rangle\langle n|j\rangle\langle k|m\rangle\langle k|l\rangle\langle u|l\rangle\langle u|j\rangle \times L_{rm,r*n}(-\omega_{UV})D_{rm,rj}(\omega_1)L_{r*k,rj}(\omega_{UV})D_{rl,rj}(\omega_2)L_{r*u,rj}(\omega_t), \quad (2.13)$$

$$P_5^{(5)}(\omega_1,\omega_2) = -\frac{N\xi_{UV}^2\xi_{VIS}^3\left|\mu_{r^*r}\right|^2\left|\mu_{p^*p}\right|^4}{\mathrm{h}^5}\sum_{mnjkluvw} B_m\langle n|m\rangle\langle j|m\rangle\langle u|k\rangle\langle u|v\rangle\langle w|v\rangle\langle w|l\rangle, \quad (2.14)$$
$$\times L_{r^*n,rm}(\omega_{UV})D_{pk,pl}(\omega_1)L_{p^*u,pl}(\omega_{VIS})D_{pv,pl}(\omega_2)L_{p^*w,pl}(\omega_t)$$

$$P_6^{(5)}(\omega_1,\omega_2) = -\frac{N\xi_{UV}^2\xi_{VIS}^3\left|\mu_{r^*r}\right|^2\left|\mu_{p^*p}\right|^4}{\mathrm{h}^5}\sum_{mnjkluvw} B_m\langle n|m\rangle\langle j|m\rangle\langle u|k\rangle\langle u|v\rangle\langle w|v\rangle\langle w|l\rangle, \quad (2.15)$$
$$\times L_{rm,r^*n}(-\omega_{UV})D_{pk,pl}(\omega_1)L_{p^*u,pl}(\omega_{VIS})D_{pv,pl}(\omega_2)L_{p^*w,pl}(\omega_t)$$

$$P_7^{(5)}(\omega_1,\omega_2) = -\frac{N\xi_{UV}^2\xi_{VIS}^3\left|\mu_{r^*r}\right|^2\left|\mu_{p^*p}\right|^4}{\mathrm{h}^5}\sum_{mnjkluvw} B_m\langle n|m\rangle\langle j|m\rangle\langle u|l\rangle\langle u|v\rangle\langle w|k\rangle\langle w|v\rangle, \quad (2.16)$$
$$\times L_{r^*n,rm}(\omega_{UV})D_{pk,pl}(\omega_1)L_{pk,p^*u}(-\omega_{VIS})D_{pk,pv}(\omega_2)L_{p^*w,pv}(\omega_t)$$

$$P_8^{(5)}(\omega_1,\omega_2) = -\frac{N\xi_{UV}^2\xi_{VIS}^3\left|\mu_{r^*r}\right|^2\left|\mu_{p^*p}\right|^4}{\mathrm{h}^5}\sum_{mnjkluvw} B_m\langle n|m\rangle\langle j|m\rangle\langle u|l\rangle\langle u|v\rangle\langle w|k\rangle\langle w|v\rangle, \quad (2.17)$$
$$\times L_{rm,r^*n}(-\omega_{UV})D_{pk,pl}(\omega_1)L_{pk,p^*u}(-\omega_{VIS})D_{pk,pv}(\omega_2)L_{p^*w,pv}(\omega_t)$$

$$P_9^{(5)}(\omega_1,\omega_2) = -\frac{N\xi_{UV}^4\xi_{VIS}\left|\mu_{r^*r}\right|^4\left|\mu_{p^*p}\right|^2}{\mathrm{h}^5}\sum_{mnjkluvw} B_m\langle n|m\rangle\langle n|j\rangle\langle k|j\rangle\langle l|m\rangle\langle w|u\rangle\langle w|v\rangle, \quad (2.18)$$
$$\times L_{r^*n,rm}(\omega_{UV})D_{rj,rm}(\omega_1)L_{r^*k,rm}(\omega_{UV})D_{pu,pv}(\omega_2)L_{p^*w,pv}(\omega_t)$$

$$P_{10}^{(5)}(\omega_1,\omega_2) = -\frac{N\xi_{UV}^4\xi_{VIS}\left|\mu_{r^*r}\right|^4\left|\mu_{p^*p}\right|^2}{\mathrm{h}^5}\sum_{mnjkluvw} B_m\langle n|m\rangle\langle n|j\rangle\langle k|m\rangle\langle l|j\rangle\langle w|u\rangle\langle w|v\rangle,$$
$$\times L_{rm,r^*n}(-\omega_{UV})D_{rm,rj}(\omega_1)L_{r^*k,rj}(\omega_{UV})D_{pu,pv}(\omega_2)L_{p^*w,pv}(\omega_t)$$

(2.19)

$$P_{11}^{(5)}(\omega_1,\omega_2) = -\frac{N\xi_{UV}^4\xi_{VIS}\left|\mu_{r^*r}\right|^4\left|\mu_{p^*p}\right|^2}{\mathrm{h}^5}\sum_{mnjkluvw} B_m\langle n|m\rangle\langle n|j\rangle\langle k|m\rangle\langle l|j\rangle\langle w|u\rangle\langle w|v\rangle, \quad (2.20)$$
$$\times L_{r^*n,rm}(\omega_{UV})D_{rj,rm}(\omega_1)L_{rj,r^*k}(-\omega_{UV})D_{pu,pv}(\omega_2)L_{p^*w,pv}(\omega_t)$$

$$P_{12}^{(5)}(\omega_1,\omega_2) = -\frac{N\xi_{UV}^4\xi_{VIS}\left|\mu_{r^*r}\right|^4\left|\mu_{p^*p}\right|^2}{\mathrm{h}^5}\sum_{mnjkluvw} B_m\langle n|m\rangle\langle n|j\rangle\langle k|j\rangle\langle l|m\rangle\langle w|u\rangle\langle w|v\rangle. \quad (2.21)$$
$$\times L_{rm,r^*n}(-\omega_{UV})D_{rm,rj}(\omega_1)L_{rm,r^*k}(-\omega_{UV})D_{pu,pv}(\omega_2)L_{p^*w,pv}(\omega_t)$$

In the above polarization components, laser pulses with the subscripts *UV* and *VIS* are taken to interact with triiodide and diiodide, respectively.

For convenience, we further group the terms into three classes of signal fields under the assumption of perfect phase-matching conditions

$$E_{r,r}^{(5)}(\omega_1,\omega_2)=\left(\frac{i\omega_t l}{2\varepsilon_0 n(\omega_t)c}\right)\sum_{m=1}^{4}P_m^{(5)}(\omega_1,\omega_2)\,, \tag{2.22}$$

$$E_{p,p}^{(5)}(\omega_1,\omega_2)=\left(\frac{i\omega_t l}{2\varepsilon_0 n(\omega_t)c}\right)\sum_{m=5}^{8}P_m^{(5)}(\omega_1,\omega_2)\,, \tag{2.23}$$

and

$$E_{r,p}^{(5)}(\omega_1,\omega_2)=\left(\frac{i\omega_t l}{2\varepsilon_0 n(\omega_t)c}\right)\sum_{m=9}^{12}P_m^{(5)}(\omega_1,\omega_2)\,. \tag{2.24}$$

Here, the two subscripts of the signal fields represent sensitivity to the triiodide reactant (subscript $r$) and diiodide product (subscript $p$) in the two frequency dimensions, $\omega_1$ and $\omega_2$.

**VII. Concluding Remarks**

In summary, we have demonstrated that 2DRR spectra carry unique signatures of vibronic coherence transfer in triiodide. The patterns of resonances associated with three different types of nonlinearities are summarized in Figure 2.9. The unique pattern of resonances associated with cross peaks between triiodide and diiodide facilitates insights into the reaction mechanism. Moreover, cross peaks between triiodide and diiodide provide information about nonequilibrium behavior that cannot be derived from traditional pump-probe experiments, where reactants are always photo-initiated from the equilibrium geometry of the ground state. The present experiments suggest positive correlation between the bond lengths of the triiodide reactant and the vibrational coherence frequency of the diiodide photoproduct (see Figure 2.12).

We suggest that correlation between these variables can be explained by Franck-Condon activity and/or by sensitivity to interfragment interactions.[24,25,56]

2DRR spectroscopy may reveal coherent reaction dynamics in any system where a light-activated non-radiative transition is fast compared to the period of vibrational motion. A non-radiative transition, rather than the direct action of laser pulses, serves as an impulse that initiates vibrational coherence in such systems. Triiodide has long been recognized as a well-defined model system for reaction-induced wavepacket motions; however, these types of dynamics may also be detected in larger systems that possess numerous Franck-Condon active coordinates. For example, the photodissociation process of myoglobin is known to exhibit reaction-induced vibrational coherences in both the doming and iron-histidine stretching coordinates.[57] Champion and co-workers uncovered these dynamics with a sophisticated modulation scheme in third-order stimulated Raman experiments.[58] New physical insights can be derived at fifth-order, because the photodissociation reaction can be initiated from a well-defined nonequilibrium geometry of the heme moiety. Fast non-radiative transitions also initiate vibrational coherences in bulk-heterojunction systems,[5] photosynthetic complexes,[9-13,59] and molecule-semiconductor interfaces.[7,8] These systems may also be well-suited to 2DRR investigations.

## REFERENCES


1. S. Mukamel, *Principles of Nonlinear Optical Spectroscopy*. (Oxford University Press, New York, 1995).

2. A. Nitzan, *Chemical Dynamics in Condensed Phases*. (Oxford University Press, Oxford, 2006).

3. L. Valkunas, D. Abramavicius, and T. Mančal, *Molecular Excitation Dynamics and Relaxation: Quantum Theory and Spectroscopy* (Wiley-VCH, Weinheim, 2013).

4. *Quantum Effects in Biology*, edited by M. Mohseni, Y. Omar, G. S. Engel, and M. B. Plenio (Cambridge University Press, Cambridge, 2014).

5. Y. Song, S. N. Clafton, R. D. Pensack, T. W. Kee, and G. D. Scholes, Nat. Commun. **5**, 4933 (2014).

6. F. D. Fuller, J. Pan, A. Gelzinis, V. Butkus, S. S. Senlik, D. E. Wilcox, C. F. Yocum, L. Valkunas, D. Abramavicius, and J. P. Ogilvie, Nature Chemistry **6**, 706 (2014).

7. W. A. Tisdale, K. J. Williams, B. A. Timp, D. J. Norris, E. S. Aydil, and X.-Y. Zhu, Science **328**, 1543 (2010).

8. C. Zimmerman, F. Willig, S. Ramakrishna, B. Burfeindt, B. Pettinger, R. Eichenberger, and W. Storck, J. Phys. Chem. B **105**, 9245 (2001).

9. J. M. Womick and A. M. Moran, J. Phys. Chem. B **115**, 1347 (2011).

10. N. Christensson, H. F. Kauffmann, T. Pullerits, and T. Mančal, J. Phys. Chem. B **116**, 7449 (2011).

11. A. Kolli, E. J. O'Reilly, G. D. Scholes, and A. Olaya-Castro, J. Chem. Phys. **137**, 174109 (2012).

12. A. W. Chin, J. Prior, R. Rosenbach, F. Caycedo-Soler, S. F. Huelga, and M. B. Plenio, Nature Phys. **9**, 113 (2013).

13. Y. Fujihashi, G. R. Fleming, and A. Ishizaki, J. Chem. Phys. **142**, 212403 (2015).

14. S. Jun, C. Yang, M. Isaji, H. Tamiaki, J. Kim, and H. Ihee, J. Phys. Chem. Lett. **5**, 1386 (2014).

15. V. Perlík, J. Seibt, L. J. Cranston, R. J. Cogdell, C. N. Lincoln, J. Savolainen, F. Šanda, T. Mančal, and J. Hauer, J. Chem. Phys. **142**, 212434 (2015).

16. U. Banin, R. Kosloff, and S. Ruhman, Isr. J. Chem. **33**, 141 (1993).

17. I. Benjamin, U. Banin, and S. Ruhman, J. Chem. Phys. **98**, 8337 (1993).

18. U. Banin, R. Kosloff, and S. Ruhman, Chem. Phys. **183**, 289 (1994).

19. T. Kühne and P. Vöhringer, J. Chem. Phys. **105**, 10788 (1996).

20. E. Gershgoren, E. Gordon, and S. Ruhman, J. Chem. Phys. **106**, 4806 (1997).

21. T. Kühne, R. Küster, and P. Vöhringer, Chem. Phys. **233**, 161 (1998).

22. S. Hess, H. Bürsing, and P. Vöhringer, J. Chem. Phys. **111**, 5461 (1999).

23. T.-S. Yang, M.-S. Chang, M. Hayashi, S. H. Lin, P. Vöhringer, W. Dietz, and N. F. Scherer, J. Chem. Phys. **110**, 12070 (1999).

24. Y. Nishiyama, M. Terazima, and Y. Kimura, J. Phys. Chem. B **116**, 9023 (2012).

25. A. Baratz and S. Ruhman, Chem. Phys. Lett. **461**, 211 (2008).

26. B. P. Molesky, P. G. Giokas, Z. Guo, and A. M. Moran, J. Chem. Phys. **114**, 114202 (2014).

27. A. E. Johnson and A. B. Myers, J. Chem. Phys. **104**, 3519 (1995).

28. A. E. Johnson and A. B. Myers, J. Phys. Chem. **100**, 7778 (1996).

29. A. E. Johnson and A. B. Myers, J. Chem. Phys. **104**, 2497 (1996).

30. J. E. Ivanecky III and J. C. Wright, Chem. Phys. Lett. **206**, 437 (1993).

31. D. J. Ulness, J. C. Kirkwood, and A. C. Albrecht, J. Chem. Phys. **108**, 3897 (1998).

32. D. A. Blank, L. J. Kaufman, and G. R. Fleming, J. Chem. Phys. **111**, 3105 (1999).

33. K. J. Kubarych, C. J. Milne, S. Lin, V. Astinov, and R. J. D. Miller, J. Chem. Phys. **116**, 2016 (2002).

34. K. C. Wilson, B. Lyons, R. Mehlenbacher, R. Sabatini, and D. W. McCamant, J. Chem. Phys. **131**, 214502 (2009).

35. V. Herrmann and P. Krebs, J. Phys. Chem. **99**, 6794 (1995).

36. A. B. Myers, in *Laser Techniques in Chemistry*, edited by A. B. Myers and T. R. Rizzo (John Wiley & Sons, New York, 1995), Vol. 23, pp. 325.

37. E. J. Heller, Acc. Chem. Res. **14**, 368 (1981).

38. AIP, See Supplementary Material Document No._____ for derivation of the response functions presented in Appendix B and an experimental test used to rule out cascades.

39. A. B. Myers, R. A. Mathies, D. J. Tannor, and E. J. Heller, J. Chem. Phys. **77**, 3857 (1982).

40. G. D. Goodno, G. Dadusc, and R. J. D. Miller, J. Opt. Soc. Am. B **15**, 1791 (1998).

41. B. A. West, J. M. Womick, and A. M. Moran, J. Phys. Chem. A **115**, 8630 (2011).

42. B. A. West, J. M. Womick, and A. M. Moran, J. Phys. Chem. A **117**, 5865 (2013).

43. L. Lepetit, G. Chériaux, and M. Joffre, J. Opt. Soc. Am. B **12**, 2467 (1995).

44. S. M. Gallagher, A. W. Albrecht, J. D. Hybl, B. L. Landin, B. Rajaram, and D. M. Jonas, J. Opt. Soc. Am. B **15**, 2338 (1998).

45. D. B. Turner, K. E. Wilk, P. M. G. Curmi, and G. D. Scholes, J. Phys. Chem. Lett. **2**, 1904 (2011).

46. D. F. Underwood and D. A. Blank, J. Phys. Chem. A **109**, 3295 (2005).

47. A. M. Moran, R. A. Nome, and N. F. Scherer, J. Chem. Phys. **127**, 184505:1 (2007).

48. S. Park, J. Kim, and N. F. Scherer, Phys. Chem. Chem. Phys. **14**, 8116 (2012).

49. E. Busby, E. C. Carroll, E. M. Chinn, L. Chang, A. J. Moulé, and D. S. Larsen, J. Phys. Chem. Lett. **2**, 2764 (2011).

50. B. P. Molesky, Z. Guo, and A. M. Moran, J. Chem. Phys. **142**, 212405 (2015).

51. E. C. M. Chen and W. E. Wentworth, J. Phys. Chem. **89**, 4099 (1985).

52. M. S. Marek, T. Buckup, and M. Motzkus, J. Phys. Chem. B **115**, 8328 (2011).

53. D. T. Valley, D. P. Hoffman, and R. A. Mathies, Phys. Chem. Chem. Phys. **17**, 9231 (2015).

54. P. Kukura, D. W. McCamant, and R. A. Mathies, Annu. Rev. Phys. Chem. **58**, 461 (2007).

55. M. T. Zanni, J. Greenblatt, A. V. Davis, and D. M. Neumark, J. Chem. Phys. **111**, 2991 (1999).

56. Y. B. Band and K. F. Freed, J. Chem. Phys. **67**, 1462 (1977).

57. P. M. Champion, F. Rosca, D. Ionascu, W. Cao, and X. Ye, Faraday. Discuss. **127**, 123 (2004).

58. A. T. N. Kumar, F. Rosca, A. Widom, and P. M. Champion, J. Chem. Phys. **114**, 701 (2001).

59. F. D. Fuller, J. Pan, A. Gelzinis, V. Butkus, S. S. Senlik, D. E. Wilcox, C. F. Yocum, L. Valkunas, D. Abramavicius, and J. P. Ogilvie, Nature Chem. **6**, 706 (2014).

60. A. M. Moran, J. Dreyer, and S. Mukamel, J. Chem. Phys. **118**, 1347 (2003).

# CHAPTER 3: TWO-DIMENSIONAL RESONANCE RAMAN SIGNATURES OF VIBRONIC COHERENCE TRANSFER IN CHEMICAL REACTIONS[2]

## I. Introduction

Time-coincidence between chemical reactions and relaxation processes such as solvation and vibrational dephasing gives rise to interesting physical effects. Assumptions made in traditional kinetic models based on an equilibrium version of Fermi's golden rule often break down in the ultrafast regime [1-3]. For example, early femtosecond pump-probe experiments investigated the importance of coherent vibrational motions in electron transfer [4-5], isomerization [6], and photodissociation [7-10] reactions. It was shown that recurrences of a photoexcited reactant at the transition state can give rise to periodic "bursts" in product formation [4-5, 10-14]. Recent 2D photon echo studies have renewed interest in coherent photochemical reactions and inspired deeper thought about the significance of coherence in biological function [14-16]. To date, most studies of coherent reaction mechanisms have been conducted with pump-probe or 2D photon echo techniques [17-18]. These methods possess a single delay time between laser pulses (i.e., a population time) in which the vibrational coherences of interest evolve. With only one population time, it is not possible to establish correlations between separate chemical species in a reaction that is initiated by light absorption; however, if laser pulses (and population times) are added to a traditional three-pulse experiment, then vibrational resonances of reactants and products can be displayed in separate dimensions of a 2D spectrum [19-21].

[2] This chapter previously appeared as an article in the Journal of Chemical Physics. The original citation is as follows: Z. Guo, B.P. Molesky, T.P. Cheshire, A.M. Moran, Top Curr Chem (Z) (2017) 375:87.

In this chapter, we discuss our development of two-dimensional resonance Raman (2DRR) spectroscopy and describe how it can be used to elucidate vibronic coherence transfer processes [22-26]. Our focus will be on ultrafast chemical reactions where 2DRR reveals non-trivial information; however, this is not the only way that 2DRR can be employed. For example, 2DRR can be used to uncover line broadening mechanisms in non-reactive systems in the same manner as any other 2D vibrational spectroscopies. To begin, the basic sequence of events associated with a 2DRR experiment is outlined in Figure 3.1. The experiment begins when a laser pulse initiates coherent vibrational motion on the ground state potential of a reactant by way of a stimulated Raman transition (these motions correspond to dimension #1). The second laser pulse promotes the system to the excited electronic state of the reactant which then undergoes an ultrafast transition to the product state. Most generally, the product can also exhibit coherent vibrational motion if the transition is fast compared to the vibrational period(s) of the system (these motions are displayed in dimension #2). The sequence outlined in Figure 3.1 can be applied to a variety of ultrafast transitions (e.g., electron transfer, energy transfer, isomerization).

We use the term 2DRR to refer to a specific component of the fifth-order response in which the system evolves in a purely vibrational coherence in each of the two electronic population times. Of course, our implementation of 2DRR is preceded by a variety of other time-resolved vibrational spectroscopies which can be adapted to provide similar information. The techniques most closely related to 2DRR are described at fifth-order in perturbation theory. Examples include Femtosecond Stimulated Raman Spectroscopy (FSRS)[27-28] and resonant pump degenerate four-wave mixing (RP-D4WM) [29-30]. These two techniques isolate the same components of the fifth-order response function but differ in how vibrational spectra are obtained. For example, data acquisition is generally faster in FSRS because only one delay time

is scanned due to its use of frequency-domain detection. FSRS and RP-D4WM are usually conducted in a manner wherein one-dimensional vibrational spectra of a product are measured with respect to a variable population time. Vibrational coherences in two dimensions have been reported in recent FSRS applications (this is the same nonlinearity detected with 2DRR) [31-32]. In addition, Harel and co-workers have developed a new fifth-order, four-dimensional experiment that, like our version of 2DRR, yields a 2D vibrational spectrum for Raman active modes; however, this technique also possesses two dimensions associated with electronic resonance frequencies [33-35].

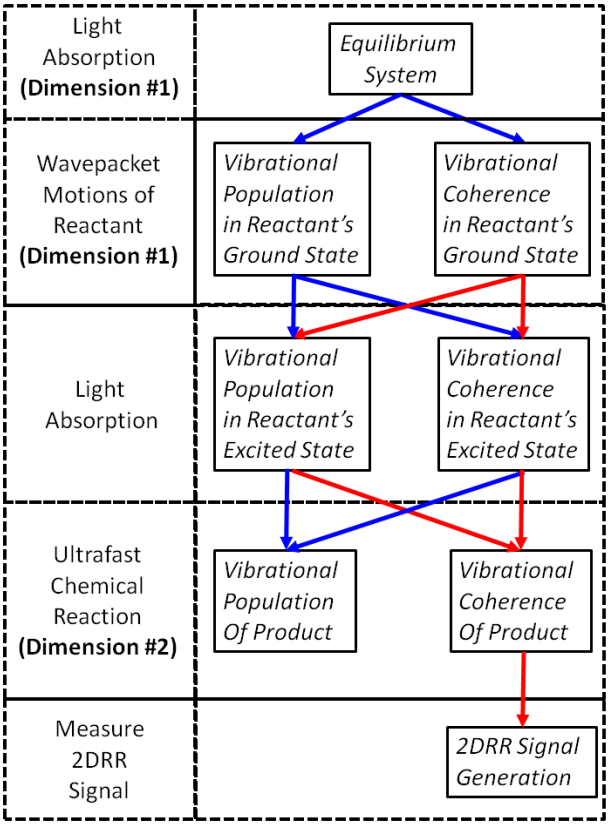


***Figure 3.1.*** *The 2DRR technique can be used to detect correlations between reactants and products in ultrafast chemical reactions. The first dimension represents coherent vibrational motion of the reactant, whereas the second dimension corresponds to coherent vibrational motion of the product. This scheme applies to reactions in which the transition from the reactant to product is faster than the vibrational periods of the system. The 2DRR method effectively isolates the paths traced with red arrows, thereby facilitating study of reaction mechanisms involving vibronic coherence transfer.*

The information provided by 2DRR spectroscopy differs from that obtained in a traditional pump-probe measurement in that the reaction is initiated from a nonequilibrium state. That is, a system is usually at equilibrium before the (single) pump pulse is absorbed in a traditional pump-probe experiment. In the 2DRR technique, the chemical reaction is initiated by a second pump pulse, which arrives while the reactant is undergoing coherent vibrational motions. Such wavepacket motions correspond to Franck-Condon active modes for the optical transition, whereas the vibrational motions in dimension #2 are Franck-Condon active for the non-radiative transition (i.e., the chemical reaction). Notably, the most prominent vibrational modes must also be Franck-Condon active for light absorption of the product in order for the final laser pulse to induce signal emission. For this reason, 2DRR spectroscopy can be used to distinguish modes that project onto the reaction coordinate from so-called "spectator modes" which are Franck-Condon active only for light absorption. Physically interesting effects are revealed when wavepacket motions along the reaction coordinate in dimension #1 affect properties of the product in dimension #2. For example, the application to the photodissociation reaction of triiodide that we focus on in this chapter will show that coherent motion of the reactant in dimension #1 directly influences the distribution of vibrational quanta in the product [22-23].

The extraordinary photodissociation mechanism of triiodide has motivated numerous ultrafast spectroscopic studies [7-8, 36-41]. Light absorption in the ultraviolet spectral range induces photodissociation on a time-scale that is shorter than [7, 37] or comparable to [40, 42] the ~300-fs vibrational period of the symmetric stretching mode. Therefore, the photodissociation process acts as an impulse that initiates vibrational coherence in the bond stretching coordinate of the diiodide product. Earlier work has shown that the oscillatory transient absorption response of this

system reflects symmetry breaking in the excited state [38], whereas the "chirp" in the waveform of the vibrational coherence represents time evolution of the bond strength during the reaction [40]. It should be noted that the reaction is more complex than originally thought; relatively recent work shows that distinct populations of free solvated diiodide and a contact fragment pair (diiodide and iodine) are produced by photodissociation [43]. 2DRR spectroscopy is notably insensitive to the contact radical pair because its vibrational motion is known to be overdamped [42].

This chapter is organized as follows. In section II, we discuss theoretical aspects of the 2DRR response. Experimental approaches are detailed in section III. Our application to the photodissociation reaction of triiodide is then reviewed in section IV. Finally, we conclude by summarizing key findings and discussing future directions in section V.

## II. 2DRR Signal Generation Mechanism for a Photoinduced Reaction

The 2DRR response function possesses a large number of components that can be selectively enhanced by tuning laser pulses into the electronic resonances of the reactant and/or product. Reaction mechanisms, line broadening dynamics, and/or anharmonicities can be probed depending on the laser pulse sequence [26]. In this section, we define signal components associated with a system in which the reactant and product absorb light in separate spectral regions. The 2DRR response is discussed in the context of the photodissociation reaction of triiodide to facilitate discussion of the measurements presented below; however, the principles generalize to other ultrafast reactions such as energy and electron transfer.

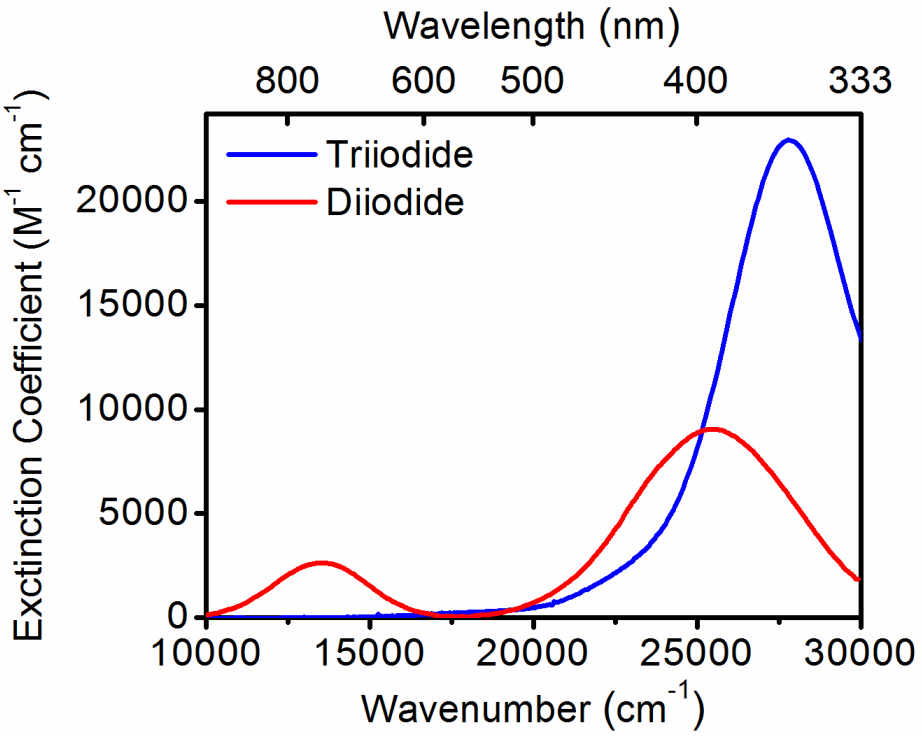


***Figure 3.2.*** *Linear absorbance spectra of triiodide and diiodide in ethanol. The absorbance spectrum of triiodide is directly measured, whereas that of diiodide is derived from Reference 44 because it is not stable in solution. The electronic resonance frequencies associated with this nonequilibrium state of diiodide are likely red-shifted from those displayed above. Displacement of the absorbance spectra of triiodide and diiodide facilitates detection of the pathway defined in Figure 3.1. Reproduced from Z. Guo, B. M. Molesky, T. P. Cheshire, A. M. Moran, J. Chem. Phys. 143, 124202 (2015), with the permission of AIP Publishing.*

**IIA. 2DRR Response Function for the Photodissociation Reaction of Triiodide**

Photodissociation of triiodide is initiated by light absorption in the UV spectral range; however, as shown in Figure 3.2, light absorption by diiodide dominates the visible region of the spectrum. A relative shift betweeen the electronic resonances of triiodide and diiodide is convenient, because this means that the two species are readily distinguished in a two-color 2DRR experiment. This will be shown by the model developed in this section. The electronic resonance frequencies extracted from the absorbance spectra can be used to parameterize effective Hamiltonians for triiodide [23],

$$H_{triiodide} = |r\rangle\langle r| \sum_{m=0}^{\infty} |m\rangle\langle m| \left[ E_r + E_m \right] + |r*\rangle\langle r*| \sum_{n=0}^{\infty} |n\rangle\langle n| \left[ E_{r*} + E_n \right] , \quad (3.1)$$

and diiodide,

$$H_{diiodide} = |p\rangle\langle p| \sum_{m=0}^{\infty} |m\rangle\langle m| \left[ E_p + E_m \right] + |p*\rangle\langle p*| \sum_{n=0}^{\infty} |n\rangle\langle n| \left[ E_{p*} + E_n \right] . \quad (3.2)$$

The indices $r$ and $p$ represent the ground electronic states of triiodide and diiodide, whereas an asterisk is used to denote the excited electronic state. The energies, $E_r$ and $E_r^*$ ($E_p$ and $E_p^*$), correspond to the ground and excited states, respectively. The energy gaps, $E_r^* - E_r$ and $E_p^* - E_p$, govern the optical response and can be parameterized based on the linear absorbance spectrum in Figure 3.2. The dummy indices, $m$ and $n$, represent vibrational levels associated with the ground and excited electronic states.

The vibrational energy levels of the ground electronic state are described in the harmonic limit based on earlier spontaneous resonance Raman measurements [45]. The excited state potentials of both triiodide and diiodide are dissociative [8, 37]; however, the optical response is only sensitive to the gradient of the excited state potential at the Franck-Condon geometry. This is a general property of systems whose absorbance spectra do not exhibit vibronic progressions because of line broadening [46]. In the semiclassical perspective, this means that the wavepacket initiated on the excited state potential energy surface does not return to the Franck-Condon geometry before electronic dephasing is complete (i.e., electronic dephasing is on the order of 10-20 fs in triiodide) [47]. Therefore, wavepacket motions on the ground state potentials can be accurately simulated by introducing a bound excited state potential with a realistic slope at the Franck-Condon geometry. In Reference [23], we used the cubic fitting parameters for the London-Eyring-Polanyi-Sato (LEPS) excited state potential energy surface of triiodide in ethanol [36, 45].

The potential energy minima of the excited state potentials (both triiodide and diiodide) are displaced to produce gradients consistent with models used in other work (see section VIA) [42-43].

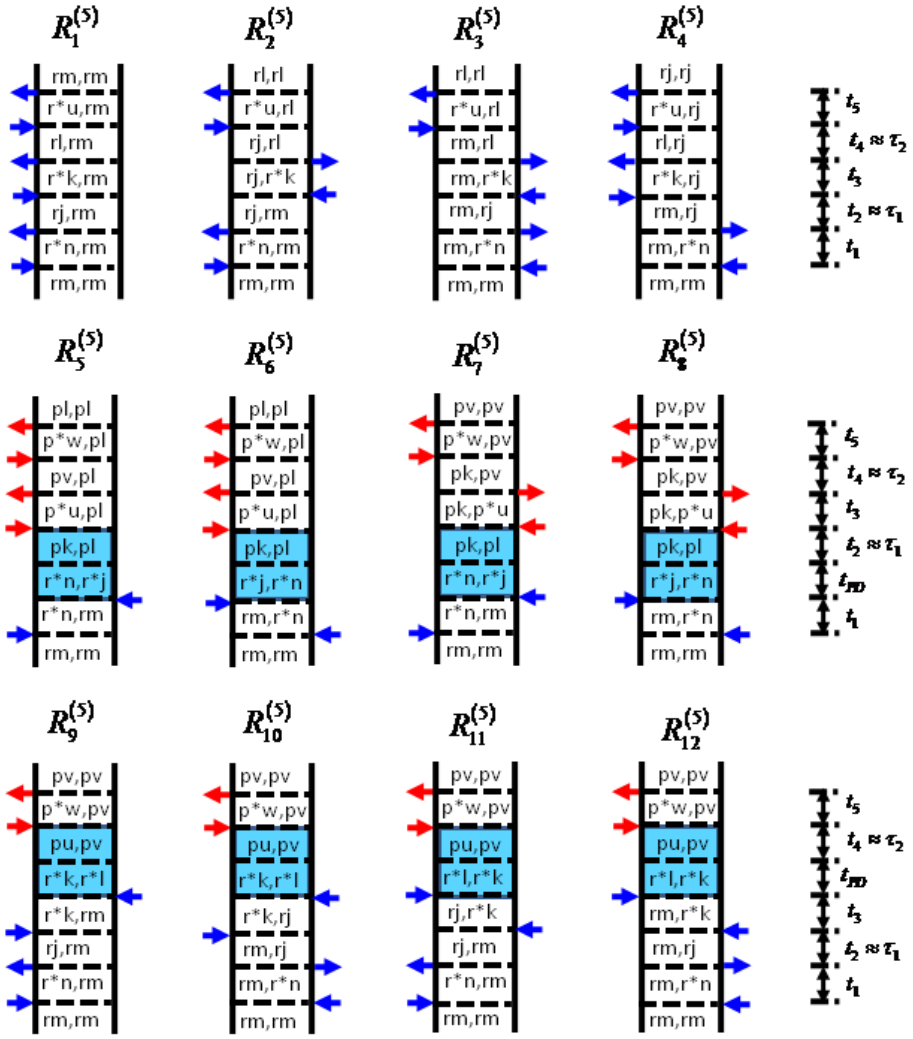


***Figure 3.3.*** *Feynman diagrams associated with dominant 2DRR nonlinearities. Blue and red arrows represent pulses resonant with triiodide and diiodide, respectively (see Figure 3.2). The indices $r$ and $r*$ represent the ground and excited electronic states of the triiodide reactant, whereas $p$ and $p*$ correspond to the diiodide photoproduct. Vibrational levels associated with these electronic states are specified by dummy indices ($m, n, j, k, l, u, v, w$). Each row represents a different class of terms: (i) both dimensions correspond to triiodide in terms 1-4; (ii) both dimensions correspond to diiodide in terms 5-8; (iii) vibrational resonances of triiodide and diiodide appear in separate dimensions in terms 9-12. The intervals shaded in blue represent a non-radiative transfer of vibronic coherence from triiodide to diiodide. Reproduced from Z. Guo, B. M. Molesky, T. P. Cheshire, A. M. Moran, J. Chem. Phys. 143, 124202 (2015), with the permission of AIP Publishing.*

Three types of 2DRR nonlinearities must be considered for signal interpretation: (i) both dimensions correspond to the triiodide reactant; (ii) both dimensions correspond to the diiodide product; (iii) the vibrational resonances of triiodide and diiodide appear in separate dimensions. These components of the response are understood by considering classes of terms in the fifth-order response function [1]. The Feynman diagrams presented in Figure 3.3 show that the vibrational coherences detected in 2DRR spectra evolve in the two time intervals with even indices ($t_2$ and $t_4$). Vibrational levels associated with the electronic states ($r$, $r^*$, $p$, $p^*$) are specified by dummy indices ($m$, $n$, $j$, $k$, $l$, $u$, $v$, $w$). It is useful to consider that the experimentally controlled pulse delay times, $\tau_1$ and $\tau_2$, are good approximations to the time intervals between field-matter interactions, $t_2$ and $t_4$ (these time intervals are limited by vibrational dephasing). Electronic (or vibronic) coherences, which evolve in the intervals with odd indices ($t_1$, $t_3$, and $t_5$), dephase in 10-20 fs for solvated triiodide.

The first class of nonlinearities shown in Figure 3.3 (terms 1-4) correspond to one-color (ultraviolet) experimental conditions and involve vibrational motions of only triiodide [22]. In Figure 3.4, we illustrate how the Feynman diagram for term 1 can be viewed in an energy level representation. The Feynman diagrams associated with the other two classes of response functions incorporate both ultraviolet and visible laser pulses, thereby enabling observation of vibrational coherences in the diiodide product. The key point is that the photodissociation process transfers vibronic coherence from triiodide to diiodide either before (terms 5-8) or after (terms 9-12) evolution of the vibrational coherence in $t_2$ (i.e., the delay time, $\tau_1$). Most notably, vibrational resonances of triiodide and diiodide appear in separate dimensions of the 2DRR spectrum in terms 9-12; this is the pathway defined in Figure 3.1.

In previous work [22-23], response functions were written under the assumption that the laser pulses are short compared to the vibrational period but long compared to electronic dephasing (i.e., the snapshot limit) [23]. Both approximations are appropriate for the experiments we have conducted on triiodide. In these limits, the components of the fifth-order polarization consist of products of Lorentzian functions. Fourier transformation with respect to the experimentally controlled delay times, $\tau_1$ and $\tau_2$, yields a 2D spectrum in the conjugate dimensions, $\omega_1$ and $\omega_2$. For example, the response function associated with the first term in Figure 3.3 is given by

$$\begin{aligned} P_1^{(5)}(\omega_1,\omega_2) = -\frac{N\xi_{UV}^5 \left|\mu_{r^*r}\right|^6}{\mathrm{h}^5} \sum_{mnjklu} B_m \langle n|m\rangle\langle n|j\rangle\langle k|j\rangle\langle k|l\rangle\langle u|l\rangle\langle u|m\rangle \\ \times L_{r^*n,rm}(\omega_{UV}) D_{rj,rm}(\omega_1) L_{r^*k,rm}(\omega_{UV}) D_{rl,rm}(\omega_2) L_{r^*u,rm}(\omega_t) \end{aligned}, \tag{3.3}$$

where

$$L_{r^*n,rm}(\omega) = \frac{1}{\omega - \omega_{r^*r} - \omega_{nm} + i\Gamma_{r^*r}}, \tag{3.4}$$

and

$$D_{rk,rm}(\omega) = \frac{2\Gamma_{vib} + 4\Lambda_{UV}}{\omega_{km}^2 + \left(\Gamma_{vib} + 2\Lambda_{UV}\right)^2}\left(\frac{1}{\omega - \omega_{km} + i\Gamma_{vib}}\right). \tag{3.5}$$

The subscript of the electric field, *UV*, denotes an interaction with triiodide (VIS denotes an interaction with diiodide). The parameter $N$ is the number density, $B_m$ is a Boltzmann population, $\xi_{UV}$ is the electric field amplitude, $\Lambda_{UV}$ is the UV pulse width, $\mu_{r^*r}$ is an electronic transition dipole for triiodide, $\omega_{r^*r}$ is the electronic resonance frequency for triiodide, $\Gamma_{r^*r}$ is the electronic line width for triiodide, $\Gamma_{vib}$ is the vibrational line width. The inner-product, $\langle n|m\rangle$, represents a vibrational overlap integral, where the index on the left (right) represents the

vibrational level of the excited (ground) electronic state [48]. The remaining 11 response functions are given in section VIB.

The physical picture associated with the signal component of interest is illustrated in Figure 3.5. The potential energy surfaces and wavepacket widths in Figure 3.5 are based on earlier work [36, 45]. The experiment begins when a laser pulse initiates vibrational motion in the ground electronic state of the triiodide reactant. This wavepacket corresponds to the first dimension of the 2DRR spectrum. The second pulse promotes the wavepacket to the excited state potential where asymmetric motion induces bond rupture. The photodissociation process is shorter than [7, 37] or comparable to [40, 42] the ~300-fs vibrational period of the bond stretching mode of diiodide. Therefore, the reaction initiates coherent wavepacket motion in diiodide which can be detected in the second dimension of the 2DRR spectrum.

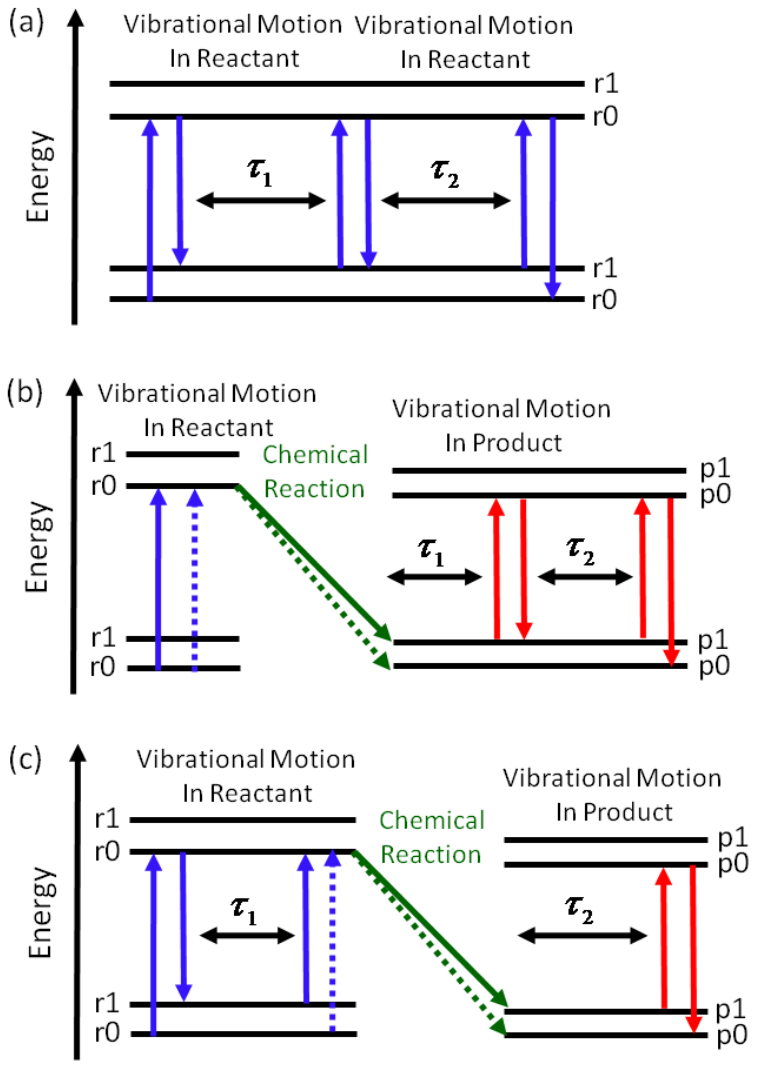


***Figure 3.4.*** *Energy level representations associated with individual pathways in (a) term 1, (b) term 5, and (c) term 9. It is assumed that the chemical reaction is fast compared to the vibrational periods of the reactants and products. Solid and dashed arrows correspond to field-matter interactions with the ket and bra in the Feynman diagrams presented in Figure 3.3.*

The possibility of observing vibrational resonances of reactants and products in separate dimensions of a 2DRR spectrum is the most interesting aspect of the model presented in this section. The ultrafast time-scale of the reaction is the main pre-requisite for observing correlations between reactants and products with 2DRR spectroscopy. The nonradiative transition (i.e., chemical reaction) can then impulsively excite vibrational motions in the product.

In the language of a density matrix, the Feynman diagrams in Figure 3.3 indicate that impulsive excitation transfers vibronic coherence from triiodide to diiodide (vibronic coherence transfer is highlighted in blue in Figure 3.3). For example, in term 9, the density matrix element, $\rho_{r^*k,r^*l}$, is transformed into $\rho_{pu,pv}$ by the photodissociation process. Terms in the summation in which $u \neq v$ represent vibrational coherences of diiodide and appear in the second dimension of the 2DRR spectrum. Similarly, vibrational coherences of triiodide, $\rho_{rj,rm}$ ($j \neq m$), appear in the first dimension of the 2DRR spectrum. To further illustrate this point, we present an energy level representation associated with term 9 in Figure 3.4.

Another unique aspect of terms 9-12 is that the third and fourth field-matter interactions occur on opposite sides of the density operator (see Figure 3.3). Consequently, unlike terms 1-8, the two indices of the vibronic states in $\tau_2$ differ from the two indices in $\tau_1$. For example, in term 9, vibronic coherences associated with the first and second dimensions are $\rho_{rj,rm}$ ($j \neq m$) and $\rho_{pu,pv}$ ($u \neq v$), respectively. In contrast, the vibronic coherences associated with the first and second dimensions in term 1 are $\rho_{rj,rm}$ ($j \neq m$) and $\rho_{rl,rm}$ ($l \neq m$), respectively. Similarly, in term 5, the vibronic coherences associated with the first and second dimensions are $\rho_{pk,pl}$ ($k \neq l$) and $\rho_{pv,pl}$ ($v \neq l$), respectively. One index must remain unchanged in terms 1-8. The measurements and model calculations in section IV will show that retention of the indices $m$ and $l$ in terms 1 and 5 limits the vibrational resonances to two quadrants of the 2DRR spectrum. On the other hand, resonances can appear in all quadrants of the 2DRR spectrum for terms 9-12 because the vibronic indices associated with the two dimensions are independent. This is a convenient spectroscopic signature with which to establish vibronic coherence transfer.

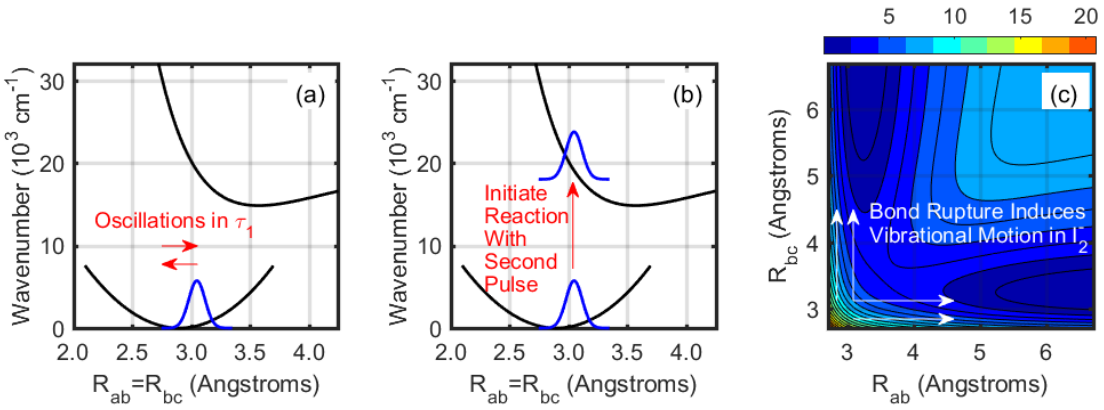


***Figure 3.5.*** *The sequence of events associated with terms 9-12 and the pathway in Figure 3.1. $R_{ab}$ and $R_{bc}$ denote the two bond lengths in triiodide and must be equal because wavepacket motion in $\tau_1$ occurs in the symmetric stretching coordinate. (a) The first pulse initiates a ground state wavepacket in the symmetric stretching coordinate. Wavepacket motion on the ground state potential energy surface is detected in the delay between the pump and repump laser pulses, $\tau_1$. (b) Photodissociation of triioide is initiated from a nonequilibrium geometry by the repump laser pulse, which separates the $\tau_1$ and $\tau_2$ delay times. The Raman spectrum of diiodide may then be detected by scanning the delay of the probe pulse, $\tau_2$. (c) The repump pulse promotes the wavepacket in triiodide to a steep portion of the excited state potential energy surface. Diiodide is produced by asymmetric motion on the excited state potential energy surface. Adapted from Z. Guo, B. M. Molesky, T. P. Cheshire, A. M. Moran, J. Chem. Phys. 143, 124202 (2015), with the permission of AIP Publishing.*

**IIB. Susceptibility to Third-Order Cascades**

Cascades of third-order signals have been recognized as a serious experimental complication in off-resonant fifth-order Raman experiments conducted on pure liquids [49-54]. As indicated in Figure 3.6, this artifact represents a process in which the four-wave mixing response on one molecule radiates a signal field that drives a four-wave mixing process on a second molecule. The second four-wave mixing signal (i.e., the cascaded signal) is radiated in the same direction as the desired fifth-order response and carries many of the same spectroscopic signatures. In contrast, all five field-matter interactions take place with an individual molecule in a genuine six-wave mixing process, thereby yielding a direct fifth-order signal field. Under off-resonant conditions, the cascaded response can be many orders of magnitude larger than the

fifth-order 2D Raman signal. Success in measuring the off-resonant 2D Raman spectrum of $CS_2$ was finally achieved in 2002 when clever experimental geometries and detection schemes were developed to suppress the cascaded signal intensity [53, 55]. The possibility of conducting 2DRR spectroscopy without contributions from cascaded artifacts was first studied by our group in 2014 [22]. Cascades were more recently shown to be negligible in a related fifth-order method [33]. These investigations suggest potential for even higher-order nonlinear spectroscopies such as the Raman echo [19, 56].

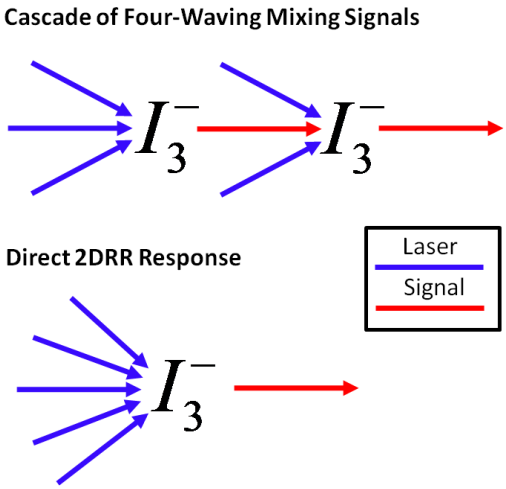


***Figure 3.6.*** *Cascades of four-wave mixing signals generally dominate in off-resonant 2D Raman experiments. In the desired 'direct' process, all 6 field-matter interactions take place with an individual molecule. The cascaded response is generally negligible in 2DRR spectroscopy because it involves 8 field-matter interactions, whereas the direct process only requires 6. Both types of nonlinearities are subject to the same selection rules under electronically resonant conditions.*

In our initial efforts, we ruled out cascaded signals with control experiments based on the signal phases, concentration dependence, and variation of the beam geometry [22, 24]. Our model calculations suggest that cascades dominate off-resonant experiments because the 2D Raman and cascaded responses are respectively forbidden and allowed for harmonic systems (i.e., they are subject to different selection rules). Of course, this is also why off-resonant 2D Raman experiments are useful for investigating anharmonicities in pure liquids [20]. The problem is that

the cascaded signal is more intense because it relies on lower-order terms in the potential energy and/or polarizability. Tuning laser pulses into electronic resonance obviates such selection rules. Vibrational modes contribute to the 2DRR signals if they are Franck-Condon active (i.e., whether they are harmonic or not). Moreover, the 2DRR signal intensity is larger than that associated with cascades because cascades involve two more field-matter interactions (i.e., the cascade is higher-order in this sense). This can be proven by summing the interactions in Figure 3.6.

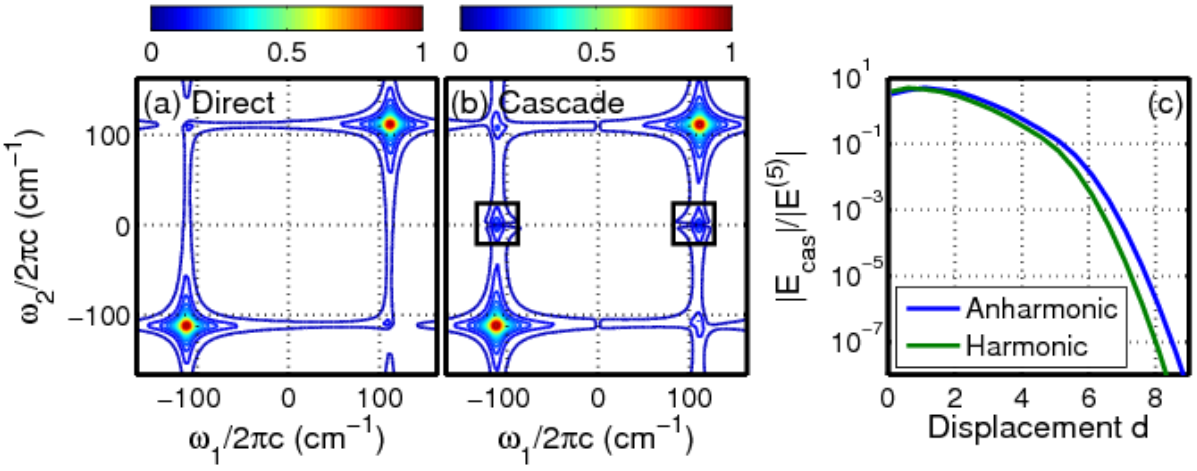


***Figure 3.7.*** *Absolute values of the (a) direct fifth-order and (b) cascaded third-order signal magnitudes of triiodide at* $\omega_1 = \omega_2 = \pm 112$ *cm*$^{-1}$ *are computed with an empirical anharmonic excited state potential energy surface (see section VIA). The ratio,* $\left|E_{cas}(\omega_1,\omega_2)\right| / \left|E^{(5)}(\omega_1,\omega_2)\right|$*, is computed using (blue) an empirical anharmonic model and (green) a harmonic model with equal ground and excited state frequencies (112 cm*$^{-1}$*)* [45]*. The features at* $\omega_2 = 0$ *cm*$^{-1}$ *(enclosed in boxes) in the cascaded signal spectrum represent imperfect subtraction of the non-oscillatory component of the signal (these are not vibrational resonances). Reproduced from B. M. Molesky, P. G. Giokas, Z. Guo, and A. M. Moran J. Chem. Phys. 141, 114202 (2014), with the permission of AIP Publishing.*

While 2DRR spectroscopy is less susceptible to cascades than is off-resonant 2D Raman spectroscopy, the calculations presented in Figure 3.7 suggest that it is still important to keep the optical density low (but not so low that the solvent response becomes comparable to that of the solute). Our model predicts that the 2DRR response will generally dominate in transmissive

beam geometries; however, optically thick systems like molecular crystals, where a reflective geometry is required, will certainly be problematic. In Figure 3.7, we present the ratio between the cascaded and 2DRR signal field magnitudes, $\left|E_{cas}\left(\omega_1,\omega_2\right)\right|/\left|E^{(5)}\left(\omega_1,\omega_2\right)\right|$, versus the dimensionless mode displacement, $d$, for the resonance at the fundamental frequency of the vibration. For our experimental conditions, the ratio is close to unity when the displacement is less than one but is extremely small for a displacement consistent with triiodide ($d$ =7.0). Reasons for this were discussed in Reference [22]. The dependence on $d$ is important to consider because Franck-Condon active modes in many larger molecules possess displacements that are much less than 1.0. Fortunately, the ratio, $\left|E_{cas}\left(\omega_1,\omega_2\right)\right|/\left|E^{(5)}\left(\omega_1,\omega_2\right)\right|$, also decreases linearly with the signal emission frequency.

The calculation in Figure 3.7 employs a fairly large 1-mM concentration and deep ultraviolet detection wavelength of 267 nm. It is not necessary to carefully tune experimental parameters in triiodide because of its enormous displacement, $d$; Figure 3.7c shows that the direct response dominates for displacements >2. Larger polyatomic molecules generally possess much smaller displacements. Fortunately, it is usually possible to detect signal emission at longer wavelengths for larger molecules, particularly for conjugated systems. For example, control experiments and model calculations show contributions from cascades to be negligible in 2DRR experiments conducted on myoglobin with a 0.2-mM concentration and 400-nm detection [24]. Harel and co-workers similarly found negligible contributions from cascades in a related 2D Raman experiment in which one of the pulses is pre-resonant with an electronic transition [34]. Our model calculations suggest that the cascaded signal intensity can reach and potentially exceed 10% of the total signal strength in a three-beam geometry with small crossing angles. For this reason, we recommend conducting control experiments based on the signal phase and sample

concentration to rule out cascades when new systems are studied. Specialized beam geometries can be employed for challenging cases [53].

## III. Experimental Methods

Approaches that we have used to conduct 2DRR spectroscopy differ in the bandwidths, frequencies, and geometries of the laser beams [22, 24, 57]. In this section, we describe how these aspects of a 2DRR pulse sequence can be used to selectively detect the three signal components defined in section IIA.

### IIIA. Pulse Sequences

In Figure 3.8, we present pulse sequences that have been used to isolate each of the three signal components discussed in section IIA. The nonlinearity associated with terms 1-4 can be probed with a degenerate six-wave mixing configuration in which all pulses are resonant with the triiodide reactant. A resonant pump degenerate four-wave mixing approach is used to enhance signal components corresponding to terms 5-8. Finally, we find that terms 9-12 are most conveniently detected with a traditional pump-repump-probe setup. It should be noted that the fifth-order 2DRR nonlinearity is detected in each case even though the approaches differ in the number of laser pulses (i.e., more than one field-matter interaction can occur with each pulse).

Suppression of third-order cascades in electronically off-resonant 2D Raman experiments was achieved using carefully designed laser beam geometries in which phase-mismatch was induced in third-order signals [53, 55]. In contrast, the choice of 2DRR beam geometry is primarily governed by convenience because of negligible cascaded signal intensity. We conduct degenerate six-wave mixing 2DRR measurements using an interferometer originally developed by Mark Berg for a different type of experiment (see Figures 3.8a and 3.9a) [58-59]. In this approach, the first and second pulse-pairs, which are electronically resonant with triiodide,

initiate vibrational coherences on the ground state potential which evolve in the delay times, $\tau_1$ and $\tau_2$. The advantage of the six-wave mixing geometry is that one field-matter interaction occurs with each of the incident beams. Therefore, the signal is generated in a background-free direction when the fifth pulse is diffracted from the holographic grating prepared by the first four pulses. The signal is weak but can be interferometrically detected using the sixth pulse as a reference field [60]. Experiments that take several hours can be conducted with the passive phase stabilization afforded by the diffractive optics approach [61].

The pump degenerate four-wave mixing pulse sequence is most convenient when the final four field-matter interactions are electronically resonant with the diiodide product (see Figure 3.8b) [29-30]. With inspiration from Scherer and Blank [62-64], we have added a resonant pump to a third-order, diffractive optic-based transient grating setup (see Figure 3.9b) [61, 65]. Interferometric detection is readily implemented in this design because the direction in which the signal is radiated is independent of the color of the pump pulse (pulse 1 in Figure 3.8b) [60]. Because two field-matter interactions occur with pulse 1, a four-wave mixing background is produced by the three visible beams (beams 2-4 in Figure 3.9b). Fortunately, this third-order background is negligible when product of the reaction possesses a large extinction coefficient and the equilibrium sample is transparent at the detection wavelength. Fortunately, triiodide does not absorb light in the visible spectral range at equilibrium; whereas diiodide possesses a significant extinction coefficient (see Figure 3.2). Therefore, the 2DRR signal strength is at least an order of magnitude larger than the four-wave mixing background produced by the ethanol solvent when the visible pulses are tuned to wavelengths longer than 460 nm [23]. The experiment can therefore be conducted without a time-consuming differencing scheme.

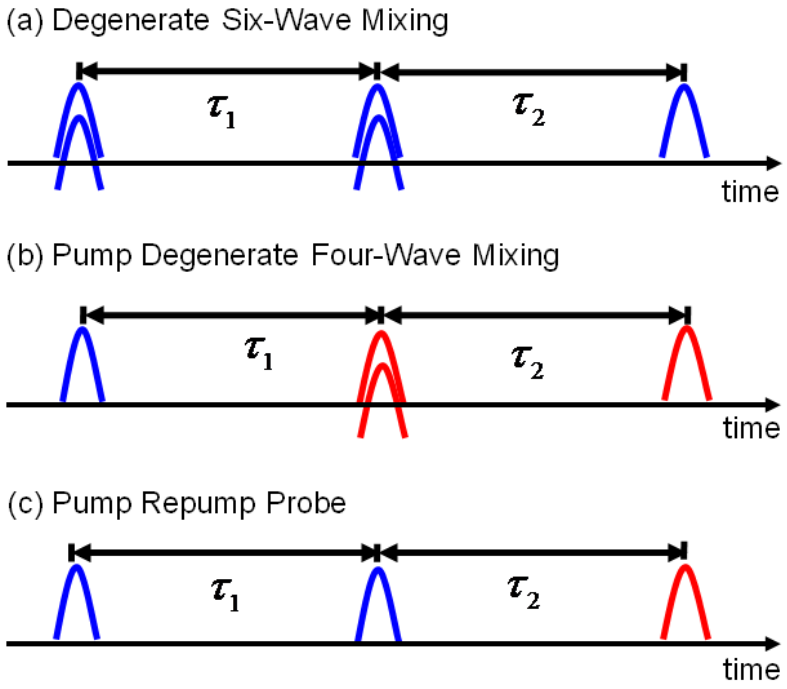


***Figure 3.8.*** *Pulse sequences used to probe terms (a) 1-4, (b) 5-8, and (c) 9-12 in Figure 3.3. In all cases, the signal is Fourier transformed with respect to the delays, $\tau_1$ and $\tau_2$, to generate a 2D spectrum. Blue (deep or near ultraviolet) and red (visible) laser pulses represent resonance with triiodide and diiodide, respectively.*

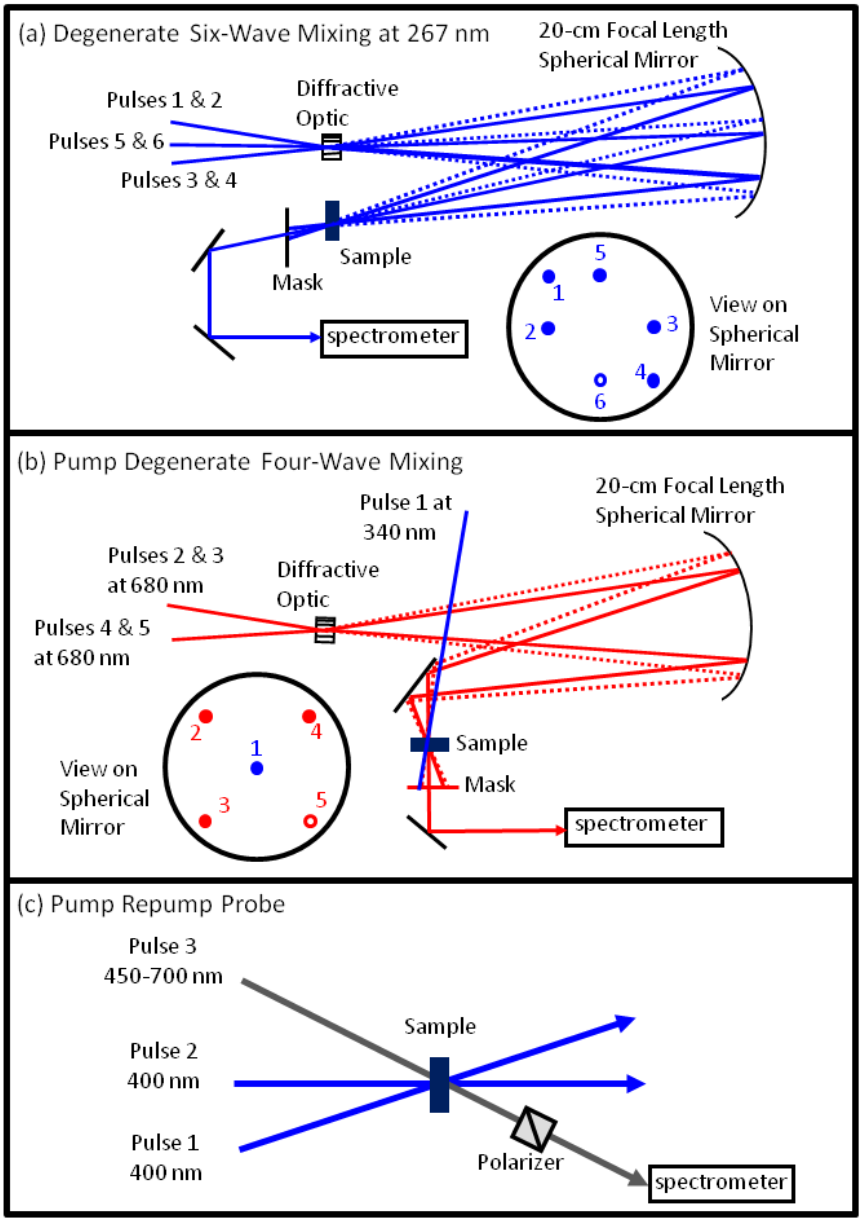


***Figure 3.9.*** *Diffractive optic-based interferometers used for (a) degenerate six-wave mixing (with 267-nm beams) and (b) pump (340 nm) degenerate four-wave mixing (680 nm). The signal is radiated in the direction* $\boldsymbol{k_s = k_1-k_2+k_3-k_4+k_5}$ *in panel (a). The wavevector of the signal is* $\boldsymbol{k_s=k_2-k_3+k_4}$ *in panel (b) (i.e., the signal wave vector is independent of the direction and color of the 340-nm pump beam). In both cases, the passively phase-stabilized signal field is interferometrically detected using a local oscillator beam (beams 6 and 5 in panels (a) and (b), respectively). (c) Differential transmission of a probe pulse is detected in a pump-repump-probe geometry. The experimental setups in (a) (b), and (c) are used to implement the pulse sequences shown in Figures3.8a, 3.8b, and 3.8c, respectively. Adapted from Z. Guo, B. M. Molesky, T. P. Cheshire, A. M. Moran, J. Chem. Phys. 143, 124202 (2015) and B. M. Molesky, P. G. Giokas, Z. Guo, and A. M. Moran J. Chem. Phys. 141, 114202 (2014), with the permission of AIP Publishing.*

Finally, we find that the traditional pump-repump-probe geometry shown in Figure 3.9c is most convenient when the first four field-matter interactions are resonant with triiodide and the final two are resonant with diiodide (terms 9-12 in Figure 3.3) [66]. The change in transmission of the continuum probe pulse induced by absorption of the pump and repump pulses is detected in this scheme. Both the pump and repump pulses must be chopped on a shot-to-shot basis to subtract a large background in this geometry, which makes this a fairly time consuming approach. Fortunately, the vibrational resonances of triiodide and diiodide are near 112 $cm^{-1}$, so a high density of points is not required. The 2D spectra in our published works were obtained by sampling a 40 by 40 grid of points with step sizes ranging from 60 to 75 fs [22-23].

**IV. Application to the Photodissociation Reaction of Triiodide**

Experiments conducted on the photodissociation reaction of triiodide show that it is indeed possible to isolate the three classes of nonlinearities defined in section II [22, 57]. Triiodide is in many ways an ideal system with which to demonstrate such a decomposition of the response function. As discussed above, the electronic resonances of the reactant and product are well-separated and the photodissociation reaction is faster than or comparable to the vibrational periods of the systems. In addition, the Franck-Condon active modes in the reactant and product possess extremely large displacements between ground and excited state potential energy minima. As a result, the 2DRR response dominates over the portion of the fifth-order nonlinearity associated with vibrational populations.

In Figure 3.10, we present 2DRR spectra acquired using each of the three pulse sequences defined in Figure 3.8. The all-UV pulse configuration yields vibrational resonances of triiodide in both dimensions, whereas the response of only diiodide is observed with the second pulse sequence. The 2DRR spectra in Figures 3.10a and 3.10b differ slightly in both the resonance frequencies and line widths. At equilibrium, the vibrational mode frequencies of

triiodide and diiodide differ by only a few wavenumbers [7]; however, the resonance frequencies of diiodide detected by 2DRR reflect a highly nonequilibrium distribution of vibrational quanta. For this reason, the vibrational coherence frequency also depends on the detection wavelength due to anharmonicity [37]. A 2DRR spectrum in which resonances of triiodide and diiodide are displayed in separate dimensions is shown in Figure 3.10c. The resonances are slightly off-diagonal at the 500-nm detection wavelength where we obtain the best signal-to-noise ratio. In agreement with earlier literature [37], we have also confirmed that the vibrational coherence frequency of diiodide decreases in $\omega_2$ as the detection wavelength increases (i.e., the peaks move further off-diagonal at longer detection wavelengths) [23].

The measurement displayed in Figure 3.10c is distinct from the other two in that resonances with equal intensities appear in all four quadrants of the 2DRR spectrum. The model calculations presented below the corresponding measurements in Figure 3.10 suggest that this pattern of resonances originates in the sequences of field-matter interactions discussed in section IIA. Consider that the third and fourth field-matter interactions occur on the same sides of the Feynman diagrams in terms 1-8. Therefore, as discussed in section IIA, either the bra or ket must have the same vibrational state index in both $\tau_1$ and $\tau_2$. This constraint causes intensity to accumulate in the upper right and lower left quadrants of the spectrum [22-23]. In contrast, the third and fourth field-matter interactions occur on opposite sides of the Feynman diagrams in terms 9-12; vibronic coherence transfer from triiodide to diiodide produces a coherence in $\tau_2$ that is fully independent from that in $\tau_1$. Consequently, peaks with equal intensities appear in all four quadrants. This unambiguous signature of vibronic coherence transfer should generalize to other photoinduced processes in which vibrational coherences are detected on the ground state potentials [23].

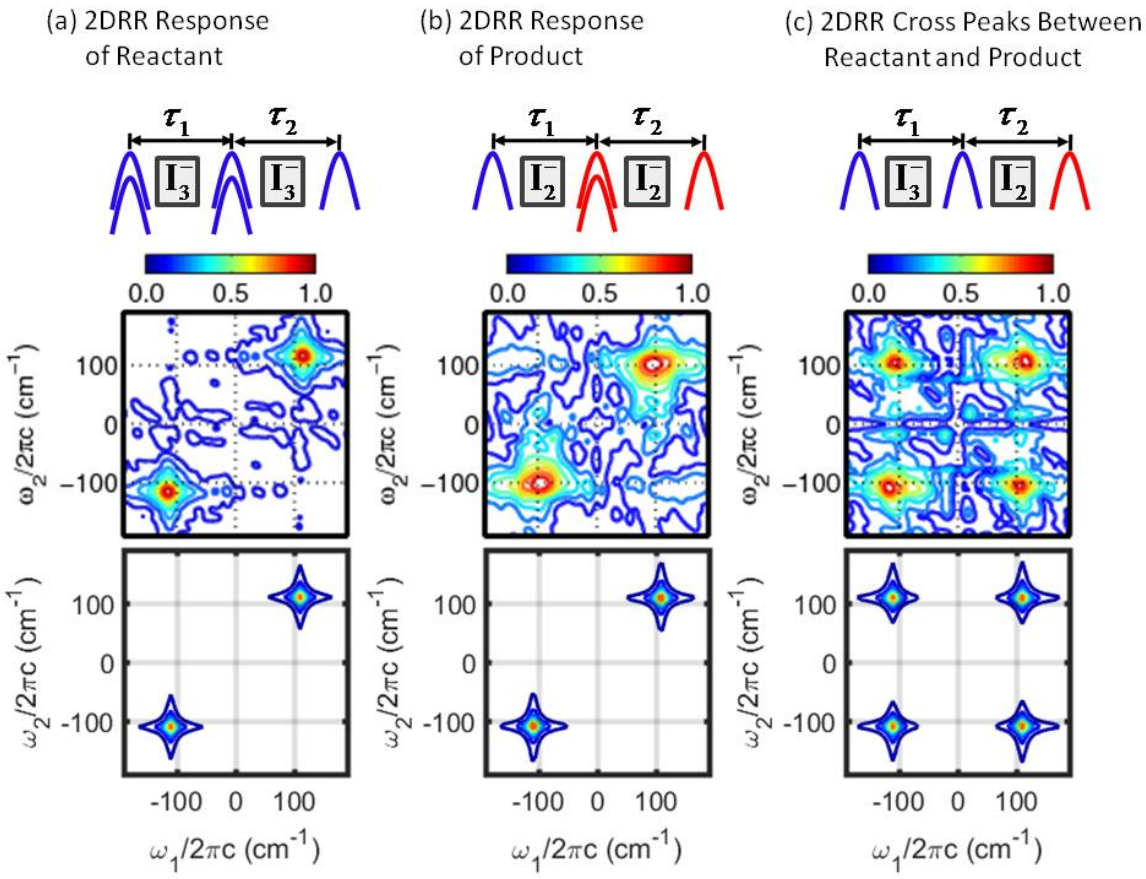


***Figure 3.10.*** *Summary of 2DRR experiments conducted on triiodide: (a) the response of triiodide is detected in both dimensions (terms 1-4 in Figure 3.3); (b) the response of the diiodide photoproduct is detected in both dimensions (terms 5-8 in Figure 3.3); (c) the response of triiodide and diiodide are detected in separate dimensions (terms 9-12 in Figure 3.3). Experimental and theoretical 2DRR spectra are presented in the second and third rows, respectively. Calculations in panels (a), (b), and (c) employ Equations (3.22), (3.23), and (3.24). Blue and red laser pulses represent wavelengths that are electronically resonant with triiodide and diiodide, respectively. Adapted from Z. Guo, B. M. Molesky, T. P. Cheshire, A. M. Moran, J. Chem. Phys. 143, 124202 (2015), with the permission of AIP Publishing.*

The observation of peaks in all four quadrants in Figure 3.10c confirms that the process of interest has been isolated (i.e., the pathway defined in Figure 3.1). We find that Fourier transforming the signal with respect to only $\tau_2$ facilitates signal interpretation (see Figure 3.11a) [23]. In this representation, oscillations of the signal in $\tau_1$ represent recurrences of a vibrational wavepacket on the ground state potential energy surface of the triiodide reactant, whereas the

vibrational spectrum of diiodide is displayed in $\omega_2$. The average vibrational frequency of diiodide is computed at each delay point using

$$\left\langle \omega_{vib}(\tau_1) \right\rangle = \frac{\int d\omega_2 S(\tau_1, \omega_2)\omega_2}{\int d\omega_2 S(\tau_1, \omega_2)}, \tag{3.6}$$

where $S(\tau_1, \omega_2)$ represents the absolute value of the signal displayed in Figure 3.11a. The recurrences in $\left\langle \omega_{vib}(\tau_1) \right\rangle$ shown in Figure 3.11b indicate that the frequency of wavepacket motion of diiodide depends on the geometry of the triiodide at the "instant" the reaction is initiated by the repump laser pulse. Notably, this analysis is insensitive to the signal phase because it is carried out on the absolute value of the signal. Based on earlier work [37], we suggest that the nonequilibrium distribution of vibrational quanta in the diiodide product governs the vibrational coherence frequency of this anharmonic system.

***Table 3.1.*** *Parameters of Model Used to Compute 2DRR Spectra*

| [a]Parameter | Value |
|---|---|
| $\omega_{r^*r} / 2\pi c$ | 27,800 $cm^{-1}$ |
| [b] $\omega_{p^*p} / 2\pi c$ | 13,300 $cm^{-1}$ & 25,400 $cm^{-1}$ |
| [c] $\omega_{r,vib} / 2\pi c = \omega_{r^*,vib} / 2\pi c$ | 111 $cm^{-1}$ |
| [c] $\omega_{p,vib} / 2\pi c = \omega_{p^*,vib} / 2\pi c$ | 114 $cm^{-1}$ |
| [c] $U_{3,r} / hc$ | 0 $cm^{-1}$ |
| [c] $U_{3,r^*} / hc = U_{3,p} / hc = U_{3,p^*} / hc$ | -1 $cm^{-1}$ |
| $\Gamma_{r,vib} / c = \Gamma_{r^*,vib} / c = \Gamma_{p,vib} / c = \Gamma_{p^*,vib} / c$ | 10 $cm^{-1}$ |
| $\Gamma_{r^*r} / c = \Gamma_{p^*p} / c$ | 2000 $cm^{-1}$ |
| [d] $\mu_{r^*r}$ | 2.3 D |
| [d] $\mu_{p^*p}$ | 1.0 D |
| [e] $\omega_{UV} / 2\pi c$ | 29,400 & 25,000 $cm^{-1}$ |
| [f] $\omega_{VIS} / 2\pi c$ | 14,705 & 18,900 $cm^{-1}$ |
| $\omega_t / 2\pi c$ | $\omega_{VIS} / 2\pi c$ |
| $\Lambda_{UV} / c = \Lambda_{VIS} / c$ | 500 $cm^{-1}$ |

[a] The indices $r$ and $p$ represent triiodide and diiodide, respectively. Asterisks indicate the lowest-energy excited electronic states of the molecules.
[b] The electronic resonance of diiodide that is probed depends on the experiment (see section III). In terms 1-4 and 9-12, the resonance is located at 25,400 $cm^{-1}$, whereas in terms 5-8 it is equal to 13,300 $cm^{-1}$.
[c] Parameters of Equation (3.7).
[d] Magnitudes of transition dipoles do not impact line shapes of simulated 2DRR spectra.
[e] In Figure 3.3, "pump" wavenumbers are: 25,000 $cm^{-1}$ for terms 1-4; 29,400 $cm^{-1}$ for terms 5-8; 25,000 $cm^{-1}$ for terms 9-12.
[f] In Figure 3.3, "probe" wavenumbers are 14,705 $cm^{-1}$ in terms 5-8 and 20,000 $cm^{-1}$ in terms 9-12, respectively.

Further insight is obtained by converting the delay time, $\tau_1$, into the classical bond length of triiodide. This calculation makes use of the equilibrium bond length, the electronic dephasing time, the vibrational period of the symmetric stretching vibration, and the London-Eyring-Polanyi-Sato excited state potential energy surface of triiodide in ethanol [36, 45]. A classical view of the wavepacket is justified by heterogeneity of the molecular geometry in the condensed phase environment. Wavepacket dynamics can often be successfully described by solving Schrödinger's equation using a Gaussian *ansatz* under such conditions [46-47]. The

trajectory shown in Figure 3.11c indicates that turning points along triiodide's symmetric stretching coordinate are reached near delay times of 170 and 325 fs. Each revolution of the spiral represents a cycle of the symmetric stretching mode of triiodide, which possesses a 300-fs period. Vibrational dephasing causes the spiral to focus inward as time increases. Most importantly, the orientation of the spiral reflects positive correlation between the bond lengths of triiodide and the vibrational coherence frequency of diiodide.

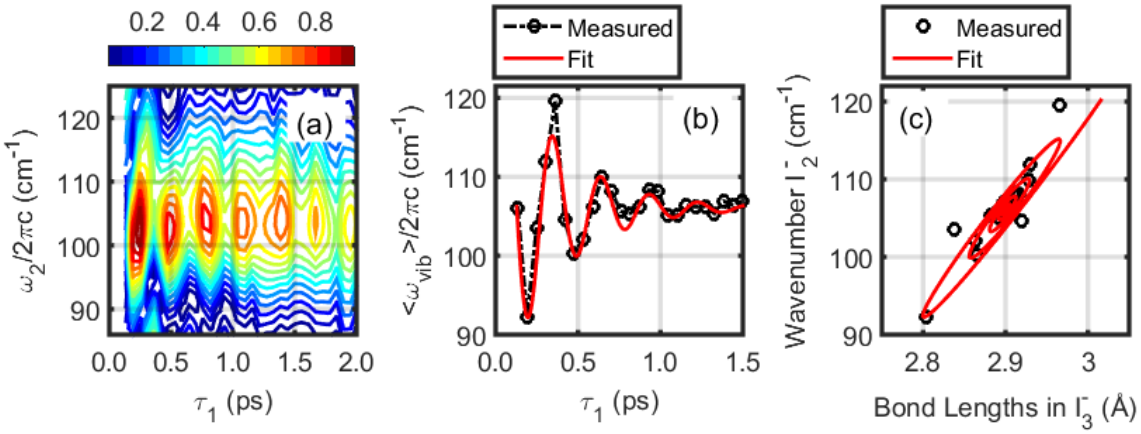


***Figure 3.11.*** *(a) Fourier transforming the 2DRR signal with respect to only $\tau_2$ reveals quantum beats of triiodide in the delay time, $\tau_1$. (b) The average vibrational frequency of diiodide is computed at each delay point using the signal displayed in panel (a). (c) The delay, $\tau_1$, is translated into the bond lengths of triiodide. The diagonal slant of the spiral suggests that a bond length displacement of 0.1 Å in triiodide induces a shift of approximately 6.8 cm$^{-1}$ in the vibrational coherence frequency of diiodide. Adapted from Z. Guo, B. M. Molesky, T. P. Cheshire, A. M. Moran, J. Chem. Phys. 143, 124202 (2015), with the permission of AIP Publishing.*

The information provided by the 2DRR experiments is illustrated in Figure 3.12. We conclude that the distribution of vibrational quanta in diiodide (as reflected by the vibrational coherence frequency) [37] depends on the bond lengths of triiodide at the "instant" the repump pulse induces photodissociation. Correlation between these two quantities can be understood within the framework of a traditional perturbative model in which vibrational overlap integrals weight state-specific paths from the initial (triiodide) to final (diiodide) states in the reaction [67].

In this perspective, the relative weights of the photodissociation channels are modulated by periodic changes in the bond lengths of the reactant in $\tau_1$. That is, the distribution of vibrational quanta in diiodide reflects correlation between the amplitudes of state-specific photodissociation channels and the bond lengths of triiodide. 2DRR spectroscopy is specially equipped to provide such information about nonequilibrium processes because it possesses two electronic population times. In contrast, traditional third-order experiments such at transient absorption and photon echo spectroscopy must initiate reactions from equilibrium geometries [1].

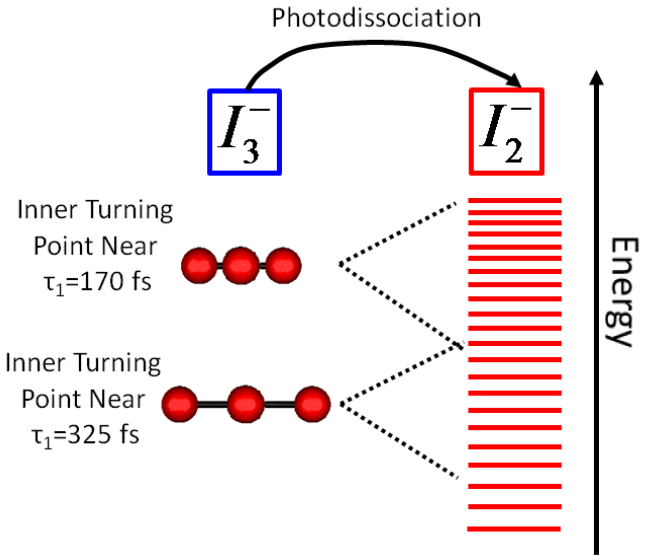


***Figure 3.12.*** *2DRR experiments suggest correlation between the geometry of the wavepacket in triiodide at the time of photodissociation and the distribution of vibrational quanta in the diiodide product. The vibrational coherence frequency of diiodide is smallest when the wavepacket is at the inner turning point of the symmetric stretching mode. This information cannot be obtained from traditional pump-probe experiments where the reaction must be initiated from the equilibrium geometry of the system.*

## V. General Applicability and Limitations of 2DRR Spectroscopy

The 2DRR signatures of vibronic coherence transfer discussed in this chapter are subject to several constraints. Firstly, the photoinduced reaction should generally be faster than the vibrational period (i.e., impulsive regime). It may be possible for a vibronic coherence transfer mechanism to promote phase coherence in an ensemble of systems where the reaction time is

greater than or equal to the vibrational period; however, the prevalence of such mechanisms in chemical systems is not presently clear. Secondly, it is desirable to have reactants and products with non-overlapping electronic transitions. This constraint can be relaxed if the vibrational resonances of the reactant and product are well-separated and known beforehand, thereby allowing signal components to be assigned. Thirdly, the 2DRR method is sensitive to Franck-Condon active modes regardless of anharmonicity. Fourthly, the 2DRR method is limited to systems with modest optical densities because of the possibility of cascades. Optical densities less than 1.0 will usually be fine based on our calculations [25]. However, optically thick systems like molecular crystals will be problematic.

The constraints listed above are specific to studies of vibronic coherence transfer. In fact, 2DRR signals can be detected for any system with Franck-Condon active modes with relatively few constraints. Of course, cascades should be ruled out with control experiments as in any other fifth-order vibrational spectroscopy. Beyond that, the challenge is simply a matter of generating adequate signal strength. 2DRR experiments conducted on non-reactive systems yield information about line broadening mechanisms. As in other 2D vibrational spectroscopies, the 2DRR vibrational line shapes elongate with respect to the diagonal axis for inhomogeneously broadened transitions. We have observed such elongated 2DRR line shapes in the low-frequency vibrational modes of myoglobin [25-26]. It should be noted that such 2DRR experiments are relatively insensitive to anharmonic couplings because Franck-Condon active modes contribute whether the modes are harmonic or not. In recent work, Harel predicts that sensitivity to anharmonic couplings can be achieved if the first pulse is pre-resonant with the electronic transition for a related 2D Raman technique [35].

The signatures of vibronic coherence transfer identified in this work generalize to any ultrafast process that can be photoinduced (e.g., energy or electron transfer). We suggest that electron transfer may be easier to study with 2DRR than is energy transfer. The reason is that one of the key requirements for fast energy transfer is spectral overlap between the donor's emission spectrum and the acceptor's absorption spectrum. It will not be possible to distinguish donor and acceptor modes by tuning incident laser beams in this situation, particularly if extremely broadband pulses are employed. Nonetheless, 2DRR studies of vibrational coherence transfer in systems like light harvesting proteins may be possible if the donor and acceptor possess readily distinguished vibrational mode frequencies. In contrast, applications to electron transfer reactions will be straightforward if the oxidized and/or reduced species have intense electronic transitions. For such systems, electron transfer can be investigated with an approach similar to that described here.

## VI. Supplemental Information

### VIA. Vibrational Hamiltonians

The present model assumes that both triiodide and diiodide possess two electronic levels and one nuclear coordinate with displaced ground and excited state potential energy minima. The anharmonic vibrational wavefunctions for the Franck-Condon active bond stretching mode of diiodide and the symmetric stretching coordinate of triiodide are generated using a Hamiltonian with the following form [74]

$$H_\alpha = \frac{\mathrm{h}\omega_{\alpha,vib}}{2}\left(2a^\dagger a + 1\right) + U_{3,\alpha}\left[a^\dagger a^\dagger a^\dagger + 3a^\dagger a^\dagger a + 3a^\dagger aa + aaa + 3a^\dagger + 3a\right], \tag{3.7}$$

where

$$U_{3,\alpha} = \frac{1}{3!\sqrt{2^3 m^3 \omega^3 \mathrm{h}^{-3}}}\left(\frac{d^3V}{dq^3}\right)_0. \tag{3.8}$$

The wavefunctions are obtained by diagonalizing this Hamiltonian in a basis set of harmonic oscillators that includes states with up to the 40 vibrational quanta. Parameters of the vibrational Hamiltonian are given in Table 3.1. We use a notation in which $\alpha$ represents the molecule ($r$ for triiodide or $p$ for diiodide) and an asterisk indicates an electronically excited state.

The vibrational overlap integrals used to evaluate the response functions of diiodide are obtained using

$$\langle n|m\rangle = \sum_{jk} \varphi_{nk}\varphi_{mj} \langle k|j\rangle, \tag{3.9}$$

where $\varphi_{nk}$ is the expansion coefficient for harmonic basis vector, $k$, and the anharmonic excited state vibrational wavefunction, $n$. Vibrational overlap integrals of triiodide are given by a different formula,

$$\langle n|m\rangle = \sum_{k} \varphi_{nk} \langle k|m\rangle, \tag{3.10}$$

because the ground and excited states are taken to be harmonic and anharmonic, respectively (see discussion in section II). In order to evaluate the overlap integrals, we assume a dimensionless displacement of 7.0 based on spontaneous Raman measurements for triiodide [45] and our earlier 2DRR study.[22] A displacement of 7.0 produces an excited state potential energy gradient of 225 eV/pm in diiodide which is identical to that associated with a previously employed exponential surface [42-43].

**VIB. Two-Dimensional Resonance Raman Signal Components**

The Feynman diagrams presented in Figure 3.3 include dummy indices for vibrational levels ($m, n, j, k, l, u, v, w$) associated with the ground and excited electronic states ($r$ and $r*$ for triiodide, $p$ and $p*$ for diiodide). Transition dipoles are written as product of integrals over electronic and nuclear degrees of freedom based on the Condon approximation. For example, an

interaction that couples vibrational level $m$ in the ground electronic state of the reactant and vibrational level $n$ in the excited electronic state of the reactant contributes the product, $\mu_{r^*r}\langle n|m\rangle$, to the response function, where $\mu_{r^*r}$ is the electronic transition dipole and $\langle n|m\rangle$ is a vibrational overlap integral. We use a notation in which the excited state vibrational energy level is always written in the bra [48].

The first polarization component is given in Equation (3.3). The remaining 11 polarization components are given by

$$P_2^{(5)}(\omega_1,\omega_2) = -\frac{N\xi_{UV}^5\left|\mu_{r^*r}\right|^6}{\mathrm{h}^5}\sum_{mnjklu} B_m \langle n|m\rangle\langle n|j\rangle\langle k|m\rangle\langle k|l\rangle\langle u|j\rangle\langle u|l\rangle \times L_{r^*n,rm}(\omega_{UV})D_{rj,rm}(\omega_1)L_{rj,r^*k}(-\omega_{UV})D_{rj,rl}(\omega_2)L_{r^*u,rl}(\omega_t), \quad (3.11)$$

$$P_3^{(5)}(\omega_1,\omega_2) = -\frac{N\xi_{UV}^5\left|\mu_{r^*r}\right|^6}{\mathrm{h}^5}\sum_{mnjklu} B_m \langle n|m\rangle\langle n|j\rangle\langle k|j\rangle\langle k|l\rangle\langle u|m\rangle\langle u|l\rangle \times L_{rm,r^*n}(-\omega_{UV})D_{rm,rj}(\omega_1)L_{rm,r^*k}(-\omega_{UV})D_{rm,rl}(\omega_2)L_{r^*u,rl}(\omega_t), \quad (3.12)$$

$$P_4^{(5)}(\omega_1,\omega_2) = -\frac{N\xi_{UV}^5\left|\mu_{r^*r}\right|^6}{\mathrm{h}^5}\sum_{mnjklu} B_m \langle n|m\rangle\langle n|j\rangle\langle k|m\rangle\langle k|l\rangle\langle u|l\rangle\langle u|j\rangle \times L_{rm,r^*n}(-\omega_{UV})D_{rm,rj}(\omega_1)L_{r^*k,rj}(\omega_{UV})D_{rl,rj}(\omega_2)L_{r^*u,rj}(\omega_t), \quad (3.13)$$

$$P_5^{(5)}(\omega_1,\omega_2) = -\frac{N\xi_{UV}^2\xi_{VIS}^3\left|\mu_{r^*r}\right|^2\left|\mu_{p^*p}\right|^4}{\mathrm{h}^5}\sum_{mnjkluvw} B_m \langle n|m\rangle\langle j|m\rangle\langle u|k\rangle\langle u|v\rangle\langle w|v\rangle\langle w|l\rangle \times L_{r^*n,rm}(\omega_{UV})D_{pk,pl}(\omega_1)L_{p^*u,pl}(\omega_{VIS})D_{pv,pl}(\omega_2)L_{p^*w,pl}(\omega_t), \quad (3.14)$$

$$P_6^{(5)}(\omega_1,\omega_2) = -\frac{N\xi_{UV}^2\xi_{VIS}^3\left|\mu_{r^*r}\right|^2\left|\mu_{p^*p}\right|^4}{\mathrm{h}^5}\sum_{mnjkluvw} B_m \langle n|m\rangle\langle j|m\rangle\langle u|k\rangle\langle u|v\rangle\langle w|v\rangle\langle w|l\rangle \times L_{rm,r^*n}(-\omega_{UV})D_{pk,pl}(\omega_1)L_{p^*u,pl}(\omega_{VIS})D_{pv,pl}(\omega_2)L_{p^*w,pl}(\omega_t), \quad (3.15)$$

$$P_7^{(5)}(\omega_1,\omega_2) = -\frac{N\xi_{UV}^2\xi_{VIS}^3\left|\mu_{r^*r}\right|^2\left|\mu_{p^*p}\right|^4}{\mathrm{h}^5}\sum_{mnjkluvw} B_m \langle n|m\rangle\langle j|m\rangle\langle u|l\rangle\langle u|v\rangle\langle w|k\rangle\langle w|v\rangle \times L_{r^*n,rm}(\omega_{UV})D_{pk,pl}(\omega_1)L_{pk,p^*u}(-\omega_{VIS})D_{pk,pv}(\omega_2)L_{p^*w,pv}(\omega_t), \quad (3.16)$$

$$P_8^{(5)}(\omega_1,\omega_2) = -\frac{N\xi_{UV}^2\xi_{VIS}^3\left|\mu_{r^*r}\right|^2\left|\mu_{p^*p}\right|^4}{\mathrm{h}^5}\sum_{mnjkluvw} B_m\langle n|m\rangle\langle j|m\rangle\langle u|l\rangle\langle u|v\rangle\langle w|k\rangle\langle w|v\rangle, \quad (3.17)$$
$$\times L_{rm,r^*n}(-\omega_{UV})D_{pk,pl}(\omega_1)L_{pk,p^*u}(-\omega_{VIS})D_{pk,pv}(\omega_2)L_{p^*w,pv}(\omega_t)$$

$$P_9^{(5)}(\omega_1,\omega_2) = -\frac{N\xi_{UV}^4\xi_{VIS}\left|\mu_{r^*r}\right|^4\left|\mu_{p^*p}\right|^2}{\mathrm{h}^5}\sum_{mnjkluvw} B_m\langle n|m\rangle\langle n|j\rangle\langle k|j\rangle\langle l|m\rangle\langle w|u\rangle\langle w|v\rangle, \quad (3.18)$$
$$\times L_{r^*n,rm}(\omega_{UV})D_{rj,rm}(\omega_1)L_{r^*k,rm}(\omega_{UV})D_{pu,pv}(\omega_2)L_{p^*w,pv}(\omega_t)$$

$$P_{10}^{(5)}(\omega_1,\omega_2) = -\frac{N\xi_{UV}^4\xi_{VIS}\left|\mu_{r^*r}\right|^4\left|\mu_{p^*p}\right|^2}{\mathrm{h}^5}\sum_{mnjkluvw} B_m\langle n|m\rangle\langle n|j\rangle\langle k|m\rangle\langle l|j\rangle\langle w|u\rangle\langle w|v\rangle, \quad (3.19)$$
$$\times L_{rm,r^*n}(-\omega_{UV})D_{rm,rj}(\omega_1)L_{r^*k,rj}(\omega_{UV})D_{pu,pv}(\omega_2)L_{p^*w,pv}(\omega_t)$$

$$P_{11}^{(5)}(\omega_1,\omega_2) = -\frac{N\xi_{UV}^4\xi_{VIS}\left|\mu_{r^*r}\right|^4\left|\mu_{p^*p}\right|^2}{\mathrm{h}^5}\sum_{mnjkluvw} B_m\langle n|m\rangle\langle n|j\rangle\langle k|m\rangle\langle l|j\rangle\langle w|u\rangle\langle w|v\rangle, \quad (3.20)$$
$$\times L_{r^*n,rm}(\omega_{UV})D_{rj,rm}(\omega_1)L_{rj,r^*k}(-\omega_{UV})D_{pu,pv}(\omega_2)L_{p^*w,pv}(\omega_t)$$

$$P_{12}^{(5)}(\omega_1,\omega_2) = -\frac{N\xi_{UV}^4\xi_{VIS}\left|\mu_{r^*r}\right|^4\left|\mu_{p^*p}\right|^2}{\mathrm{h}^5}\sum_{mnjkluvw} B_m\langle n|m\rangle\langle n|j\rangle\langle k|j\rangle\langle l|m\rangle\langle w|u\rangle\langle w|v\rangle. \quad (3.21)$$
$$\times L_{rm,r^*n}(-\omega_{UV})D_{rm,rj}(\omega_1)L_{rm,r^*k}(-\omega_{UV})D_{pu,pv}(\omega_2)L_{p^*w,pv}(\omega_t)$$

In the above polarization components, laser pulses with the subscripts *UV* and *VIS* are taken to interact with triiodide and diiodide, respectively.

For convenience, we further group the terms into three classes of signal fields under the assumption of perfect phase-matching conditions

$$E_{r,r}^{(5)}(\omega_1,\omega_2) = \left(\frac{i\omega_t l}{2\varepsilon_0 n(\omega_t)c}\right)\sum_{m=1}^{4} P_m^{(5)}(\omega_1,\omega_2), \quad (3.22)$$

$$E_{p,p}^{(5)}(\omega_1,\omega_2) = \left(\frac{i\omega_t l}{2\varepsilon_0 n(\omega_t)c}\right)\sum_{m=5}^{8} P_m^{(5)}(\omega_1,\omega_2), \quad (3.23)$$

and

$$E_{r,p}^{(5)}(\omega_1,\omega_2)=\left(\frac{i\omega_t l}{2\varepsilon_0 n(\omega_t)c}\right)\sum_{m=9}^{12}P_m^{(5)}(\omega_1,\omega_2)\ . \qquad (3.24)$$

Here, the two subscripts of the signal fields represent sensitivity to the triiodide reactant (subscript $r$) and diiodide product (subscript $p$) in the two frequency dimensions, $\omega_1$ and $\omega_2$.

**VI. Concluding Remarks**

In summary, 2DRR spectroscopy can be used to expose correlations between reactants and products in ultrafast photochemistries. These types of correlations cannot be revealed by traditional third-order methods such as transient absorption and photon echo spectroscopy in which reactions must be initiated from equilibrium conditions. Experimental tests show that 2DRR signals will generally be larger than cascaded nonlinearities for solutions with optical densities less than 1.0 [22, 24]. Model calculations suggest that Franck-Condon activity obviates the selection rules that promote artifacts under electronically off-resonant conditions [22]. Our experimental investigation of the photodissociation reaction of triiodide demonstrates that that the information content of a 2DRR spectrum can be controlled by varying laser beam geometries and the colors of the pulses in the sequence. Results summarized in this article suggest that the bond length of the triiodide reactant is correlated to the distribution of vibrational quanta in the diiodide product [23].

The 2DRR technique can be used to probe the general vibronic coherence transfer process defined in Figure 3.1 provided that the photoinduced reaction is faster than or comparable to the vibrational period(s). Thus, the 2DRR method can also be applied to vibronic coherence transfer in ultrafast energy and electron transfer transitions. For example, it may be interesting to apply 2DRR spectroscopy to ultrafast energy transfer processes in light harvesting proteins [14-16]. In these systems, the role vibronic effects in Frenkel exciton delocalization and

energy transport has generated significant interest in recent years and some issues remain unsettled [14, 68-73]. Notably, Harel and co-workers are making significant steps in this direction with a multidimensional method that is related to 2DRR spectroscopy [33-34]. Electron transfer processes offer practical advantages that will facilitate decomposition of the 2DRR nonlinearity. Most importantly, the oxidized and/or reduced species in an electron transfer reaction often absorb light in different regions of the spectrum. Therefore, for some systems, the pathway defined in Figure 3.1 may be readily isolated with multi-color pulse sequences (i.e., the same approach that we have taken for triiodide). In contrast, the electronic resonances of the donor and acceptor in an energy transfer transition usually possess significant overlap, thereby challenging an approach in which pathways are distinguished by tuning the wavelength of the laser pulses.

## REFERENCES


1. Mukamel, S., *Principles of Nonlinear Optical Spectroscopy*. Oxford University Press: New York, 1995.

2. Nitzan, A., *Chemical Dynamics in Condensed Phases*. Oxford University Press: Oxford, 2006.

3. Valkunas, L.; Abramavicius, D.; Mančal, T., *Molecular Excitation Dynamics and Relaxation: Quantum Theory and Spectroscopy* Wiley-VCH: Weinheim, 2013.

4. Vos, M. H.; Lambry, J.-C.; Robles, S. J.; Youvan, D. C.; Breton, J.; Martin, J.-L., Direct Observation of Vibrational Coherence in Bacterial Reaction Centers Using Femtosecond Absorption Spectroscopy. *Proc. Natl. Acad. Sci.* **1991,** *88*, 8885-8889.

5. Vos, M. H.; Rappaport, F.; Lambry, J.-C.; Breton, J.; Martin, J.-L., Visualization of Coherent Nuclear Motion in a Membrane Protein by Femtosecond Spectroscopy. *Nature* **1993,** *363*, 320-325.

6. Peteanu, L. A.; Schoenlein, R. W.; Wang, H.; Mathies, R. A.; Shank, C. V., The First Step in Vision Occurs in Femtoseconds: Complete Blue and Red Spectral Studies. *Proc. Natl. Acad. Sci.* **1993,** *90*, 11762-11766.

7. Banin, U.; Kosloff, R.; Ruhman, S., Femtosecond Chemical Dynamics in Solution: Photodissociation of $I_3^-$. *Isr. J. Chem.* **1993,** *33*, 141-156.

8. Benjamin, I.; Banin, U.; Ruhman, S., Ultrafast photodissociation of I3 in ethanol: A molecular dynamics study. *J. Chem. Phys.* **1993,** *98*, 8337-8340.

9. Zhu, L.; Sage, J. T.; Champion, P. M., Observation of Coherent Reaction Dynamics in Heme Proteins. *Science* **1994,** *266*, 629-632.

10. Zewail, A. H., Femtochemistry: Atomic-Scale Dynamics of the Chemical Bond. *J. Phys. Chem. A* **2000,** *104*, 5560-5694.

11. Bixon, M.; Jortner, J., Vibrational Coherence in Nonadiabatic Dynamics. *J. Chem. Phys.* **1997,** *107*, 1470-1482.

12. Wynne, K.; Reid, G. D.; Hochstrasser, R. M., Vibrational Coherence in Electron Transfer: The Tetracyanoethylene-Pyrene Complex. *J. Chem. Phys.* **1996,** *105*, 2287-2297.

13. Song, Y.; Clafton, S. N.; Pensack, R. D.; Kee, T. W.; Scholes, G. D., Vibrational Coherence Probes the Mechanism of Ultrafast Electron Transfer in Polymer–Fullerene Blends. *Nat. Commun.* **2014,** *5*, 4933.

14. Fuller, F. D.; Pan, J.; Gelzinis, A.; Butkus, V.; Senlik, S. S.; Wilcox, D. E.; Yocum, C. F.; Valkunas, L.; Abramavicius, D.; Ogilvie, J. P., Vibronic Coherence in Oxygenic Photosynthesis. *Nat. Chem.* **2014,** *6*, 706-711.

15. Mohseni, M.; Omar, Y.; Engel, G. S.; Plenio, M. B., *Quantum Effects in Biology*. Cambridge University Press: Cambridge, 2014.

16. Chenu, A.; Scholes, G. D., Coherence in Energy Transfer and Photosynthesis. *Annu. Rev. Phys. Chem.* **2015,** *66*, 69-96.

17. Jonas, D. M., Two-Dimensional Femtosecond Spectroscopy. *Annu. Rev. Phys. Chem.* **2003,** *54*, 425-463.

18. Ogilvie, J. P.; Kubarych, K. J., Multidimensional Electronic and Vibrational Spectroscopy: An Ultrafast Probe of Molecular Relaxation and Reaction Dynamics *Adv. At. Mol. Opt. Phys.* **2009,** *57*, 249-321.

19. Loring, R. F.; Mukamel, S., Selectivity in Coherent Transient Raman Measurements of Vibrational Dephasing in Liquids. *J. Chem. Phys.* **1985,** *83*, 2116-2126.

20. Tanimura, Y.; Mukamel, S., Two-Dimensional Femtosecond Vibrational Spectroscopy of Liquids. *J. Chem. Phys.* **1993,** *99*, 9496-9511.

21. Tanimura, Y.; Okumura, K., First-, Third-, and Fifth-Order Resonant Spectroscopy of an Anharmonic Displaced Oscillators System in the Condensed Phase. *J. Chem. Phys.* **1996,** *106*, 2078-2095.

22. Molesky, B. P.; Giokas, P. G.; Guo, Z.; Moran, A. M., Multidimensional Resonance Raman Spectroscopy by Six-Wave Mixing in the Deep UV. *J. Chem. Phys.* **2014,** *114*, 114202.

23. Guo, Z.; Molesky, B. P.; Cheshire, T. P.; Moran, A. M., Elucidation of Reactive Wavepackets by Two-Dimensional Resonance Raman Spectroscopy. *J. Chem. Phys.* **2015,** *143*, 124202.

24. Molesky, B. M.; Guo, Z.; Moran, A. M., Femtosecond Stimulated Raman Spectroscopy by Six-Wave Mixing. *J. Chem. Phys.* **2015,** *142*, 212405.

25. Molesky, B. M.; Guo, Z.; Cheshire, T. P.; Moran, A. M., Two-Dimensional Resonance Raman Spectroscopy of Oxygen- and Water-Ligated Myoglobin. *J. Chem. Phys.* **2016,** *145*, 034203.

26. Molesky, B. M.; Guo, Z.; Cheshire, T. P.; Moran, A. M., Perspective: Two-Dimensional Resonance Raman Spectroscopy *J. Chem. Phys.* **2016,** *145*, 180901.

27. McCamant, D. W.; Kukura, P.; Yoon, S.; Mathies, R. A., Femtosecond Broadband Stimulated Raman Spectroscopy: Apparatus and Methods *Rev. Sci. Instrum.* **2004,** *75*, 4971-4980.

28. Kukura, P.; McCamant, D. W.; Mathies, R. A., Femtosecond stimulated Raman spectroscopy. *Annu. Rev. Phys. Chem.* **2007,** *58*, 461-488.

29. Takeuchi, S.; Ruhman, S.; Tsuneda, T.; Chiba, M.; Taketsugu, T.; Tahara, T., Spectroscopic Tracking of Structural Evolution in Ultrafast Stilbene Photoisomerization *Science* **2008,** *322*, 1073-1077.

30. Kraack, J. P.; Wand, A.; Buckup, T.; Motzkus, M.; Ruhman, S., Mapping Multidimensional Excited State Dynamics Using Pump-Impulsive-Vibrational-Spectroscopy and Pump-Degenerate-Four-Wave-Mixing. *Phys. Chem. Chem. Phys.* **2013,** *15*, 14487-14501.

31. Wang, Y.; Liu, W.; Tang, L.; Oscar, B.; Han, F.; Fang, C., Early-Time Excited-State Structural Evolution of Pyranine in Methanol Revealed by Femtosecond Stimulated Raman Spectroscopy. *J. Phys. Chem. A* **2013,** *117*, 6024-6042.

32. Hoffman, D. P.; Mathies, R. A., Femtosecond Stimulated Raman Exposes the Role of Vibrational Coherence in Condensed-Phase Photoreactivity. *Acc. Chem. Res.* **2016,** *49*, 616-625.

33. Hutson, W. O.; Spencer, A. P.; Harel, E., Isolated Ground-State Coherence Measured by Fifth-Order Single-Shot Two-Dimensional Electronic Spectroscopy. *J. Phys. Chem. Lett.* **2016,** *7*, 3636-3640.

34. Spencer, A. P.; Hutson, W. O.; Harel, E., Quantum Coherence Selective 2D Raman-Electronic Spectroscopy. *Nat. Commun.* **2017,** *8*, 14732.

35. Harel, E., Four-Dimensional Coherent Electronic Raman Spectroscopy *J. Chem. Phys.* **2017,** *146*, 154201.

36. Banin, U.; Kosloff, R.; Ruhman, S., Vibrational Relaxation of Nascent Diiodide Ions Studied by Femtosecond Transient Resonance Impulsive Stimulated Raman Scattering (TRISRS); Experiment and Simulation. *Chem. Phys.* **1994,** *183*, 289-307.

37. Kühne, T.; Vöhringer, P., Vibrational Relaxation and Geminate Recombination in the Femtosecond Photodissociation of Triiodide in Solution. *J. Chem. Phys.* **1996,** *105*, 10788-10802.

38. Gershgoren, E.; Gordon, E.; Ruhman, S., Effect of symmetry breaking on vibrational coherence transfer in impulsive photolysis of trihalide ions. *J. Chem. Phys.* **1997,** *106*, 4806-4809.

39. Kühne, T.; Küster, R.; Vöhringer, P., Femtosecond photodissociation of triiodide in solution: Excitation energy dependence and transition state dynamics. *Chem. Phys.* **1998,** *233*, 161-178.

40. Hess, S.; Bürsing, H.; Vöhringer, P., Dynamics of fragment recoil in the femtosecond photodissociation of triiodide ions in liquid solution *J. Chem. Phys.* **1999,** *111*, 5461-5473.

41. Yang, T.-S.; Chang, M.-S.; Hayashi, M.; Lin, S. H.; Vöhringer, P.; Dietz, W.; Scherer, N. F., Femtosecond pump-probe study of molecular vibronic structures and dynamics of a cyanine dye in solution. *J. Chem. Phys.* **1999,** *110*, 12070-12081.

42. Nishiyama, Y.; Terazima, M.; Kimura, Y., Ultrafast Relaxation and Reaction of Diiodide Anion after Photodissociation of Triiodide in Room-Temperature Ionic Liquids. *J. Phys. Chem. B* **2012,** *116*, 9023-9032.

43. Baratz, A.; Ruhman, S., UV Photolysis of $I_3^-$ in solution - Multiple Product Channels Detected by Transient Hyperspectral Probing. *Chem. Phys. Lett.* **2008,** *461*, 211-217.

44. Herrmann, V.; Krebs, P., Temperature Dependence of Optical Absorption Spectra of Solvated Electrons in $CD_3OD$ for $T \leq Tc$. *J. Phys. Chem.* **1995,** *99*, 6794-6800.

45. Johnson, A. E.; Myers, A. B., Emission cross sections and line shapes for photodissociating triiodide in ethanol: Experimental and computational studies. *J. Chem. Phys.* **1995,** *104*, 3519-3533.

46. Myers, A. B., Excited Electronic State Properties From Ground-State Resonance Raman Intensities. In *Laser Techniques in Chemistry*, Myers, A. B.; Rizzo, T. R., Eds. John Wiley & Sons: New York, 1995; Vol. 23, pp 325-384.

47. Heller, E. J., The semiclassical way to molecular spectroscopy. *Acc. Chem. Res.* **1981,** *14*, 368-375.

48. Myers, A. B.; Mathies, R. A.; Tannor, D. J.; Heller, E. J., Excited State Geometry Changes from Preresonance Raman Intensities: Isoprene and Hexatriene. *J. Chem. Phys.* **1982,** *77*, 3857-3866.

49. Ivanecky III, J. E.; Wright, J. C., An investigation of the origins and efficiencies of higher-order nonlinear spectroscopic processes *Chem. Phys. Lett.* **1993,** *206*, 437-444.

50. Ulness, D. J.; Kirkwood, J. C.; Albrecht, A. C., Competitive Events in Fifth Order Time Resolved Coherent Raman Scattering: Direct Versus Sequential Processes. *J. Chem. Phys.* **1998,** *108*, 3897-3902.

51. Jansen, T. I. C.; Snijders, J. G.; Duppen, K., Interaction induced effects in the nonlinear Raman response of liquidCS 2 : A finite field nonequilibrium molecular dynamics approach *J. Chem. Phys.* **2001,** *114*, 109210-10921.

52. Blank, D. A.; Kaufman, L. J.; Fleming, G. R., Fifth-order two-dimensional Raman spectra ofCS 2 are dominated by third-order cascades *J. Chem. Phys.* **1999,** *111*, 3105-3114.

53. Kubarych, K. J.; Milne, C. J.; Lin, S.; Astinov, V.; Miller, R. J. D., Diffractive optics-based six-wave mixing:Heterodyne detection of the full $\chi^{(5)}$ tensor of liquid $CS_2$. *J. Chem. Phys.* **2002,** *116*, 2016-2042.

54. Mehlenbacher, R.; Lyons, B.; Wilson, K. C.; Du, Y.; McCamant, D. W., Theoretical analysis of anharmonic coupling and cascading Raman signals observed with femtosecond stimulated Raman spectroscopy *J. Chem. Phys.* **2009,** *131*, 244512.

55. Kaufman, L. J.; Heo, J.; Ziegler, L. D.; Fleming, G. R., Heterodyne-Detected Fifth-Order Nonresonant Raman Scattering from Room Temperature CS2. *Phys. Rev. Lett.* **2002,** *88*, 207402:1-4.

56. Berg, M.; Vanden Bout, D. A., Ultrafast Raman Echo Measurements of Vibrational Dephasing and the Nature of Solvent−Solute Interactions. *Acc. Chem. Res.* **1997,** *30*, 65-71.

57. Guo, Z.; Molesky, B. M.; Cheshire, T. P.; Moran, A. M., Elucidation of Reactive Wavepackets by Two-Dimensional Resonance Raman Spectroscopy. *J. Chem. Phys.* **2015,** *143*, 124202.

58. van Veldhoven, E.; Khurmi, C.; Zhang, X.; Berg, M. A., Time-Resolved Optical Spectroscopy with Multiple Population Dimensions: A General Method for Resolving Dynamic Heterogeneity. *ChemPhysChem* **2007,** *8*, 1761-1765.

59. Berg, M. A., Multidimensional Incoherent Time-Resolved Spectroscopy and Complex Kinetics. *Adv. Chem. Phys.* **2012,** *150*, 1-102.

60. Lepetit, L.; Chériaux, G.; Joffre, M., Linear techniques of phase measurement by femtosecond spectral interferometry for applications in spectroscopy. *J. Opt. Soc. Am. B* **1995,** *12*, 2467-2474.

61. Goodno, G. D.; Dadusc, G.; Miller, R. J. D., Ultrafast Heterodyne-Detected Transient-Grating Spectroscopy Using Diffractive Optics. *J. Opt. Soc. Am. B* **1998,** *15*, 1791-1794.

62. Underwood, D. F.; Blank, D. A., Measuring the Change in the Intermolecular Raman Spectrum during Dipolar Solvation. *J. Phys. Chem. A* **2005,** *109*, 3295-3306.

63. Moran, A. M.; Nome, R. A.; Scherer, N. F., Field-resolved measurement of reaction-induced spectral densities by polarizability response spectroscopy. *J. Chem. Phys.* **2007,** *127*, 184505:1-13.

64. Park, S.; Kim, J.; Scherer, N. F., Two-dimensional measurements of the solvent structural relaxation dynamics in dipolar solvation. *Phys. Chem. Chem. Phys.* **2012,** *14*, 8116-8122.

65. Moran, A. M.; Maddox, J. B.; Hong, J. W.; Kim, J.; Nome, R. A.; Bazan, G. C.; Mukamel, S.; Scherer, N. F., Optical coherence and theoretical study of the excitation dynamics of a highly symmetric cyclophane-linked oligophenylenevinylene dimer. *J. Chem. Phys.* **2006,** *124*, 194904:1-15.

66. Busby, E.; Carroll, E. C.; Chinn, E. M.; Chang, L.; Moulé, A. J.; Larsen, D. S., Excited-State Self-Trapping and Ground-State Relaxation Dynamics in Poly(3-hexylthiophene) Resolved with Broadband Pump–Dump–Probe Spectroscopy. *J. Phys. Chem. Lett.* **2011,** *2*, 2764-2769.

67. Band, Y. B.; Freed, K. F., Energy Distribution in Selected Fragment Vibrations in Dissociation Processes in Polyatomic Molecules. *J. Chem. Phys.* **1977,** *67*, 1462-1472.

68. Hennebicq, E.; Beljonne, D.; Curutchet, C.; Scholes, G. D.; Silbey, R. J., Shared-mode assisted resonant energy transfer in the weak coupling regime. *J. Chem. Phys.* **2009,** *130*, 214505:1-6.

69. Roden, J.; Schulz, G.; Eisfeld, A.; Briggs, J., Electronic energy transfer on a vibronically coupled quantum aggregate. *J. Chem. Phys.* **2009,** *131*, 044909.

70. Womick, J. M.; Moran, A. M., Vibronic Enhancement of Exciton Sizes and Energy Transport in Photosynthetic Complexes. *J. Phys. Chem. B* **2011,** *115*, 1347-1356.

71. Chenu, A.; Chrisensson, N.; Kauffmann, H. F.; Mančal, T., Enhancement of Vibronic and Ground-State Vibrational Coherences in 2D Spectra of Photosynthetic Complexes. *Sci. Rep.* **2013,** *3*, 2029.

72. O'Reilly, E. J.; Olaya-Castro, A., Non-Classicality of the Molecular Vibrations Assisting Exciton Energy Transfer at Room Temperature. *Nat. Commun.* **2014,** *5*, 3012.

73. Singh, V. P.; Westberg, M.; Wang, C.; Dahlberg, P. D.; Gellen, T.; Gardiner, A. T.; Cogdell, R. J.; Engel, G. S., Towards Quantification of Vibronic Coupling in Photosynthetic Antenna Complexes *J. Chem. Phys.* **2015,** *142*, 212446.

74. Moran, A. M.; Dreyer, J.; Mukamel, S., Ab initio simulation of the two-dimensional vibrational spectrum of dicarbonylacetylacetonato rhodium(I). *J. Chem. Phys.* **2003,** *118*, 1347-1355.

## CHAPTER 4: TWO-DIMENSIONAL RESONANCE RAMAN SPECTROSCOPY OF OXYGEN- AND WATER-LIGATED MYOGLOBIN[3]

### I. Introduction

Once the specialization of a small number of experimental groups, multidimensional laser spectroscopies have become fairly widespread in the past 20 years with applications spanning the traditional disciplines of chemistry, biology, and physics.[1-10] The development of multi-dimensional techniques is rooted in the picosecond coherent Raman spectroscopies of the late 1970's and early 1980's.[11-14] At the time, it was unclear whether or not traditional (one-dimensional) coherent Raman measurements could distinguish between homogeneous and inhomogeneous line broadening mechanisms.[15-17] Theoretical work showed that higher-order (multidimensional) methods were indeed required to obtain such information,[18-20] and early success was achieved in Raman echo experiments (i.e., eight-wave mixing).[21] Several experimental groups took up the challenge of conducting six-wave mixing experiments in the mid-1990's but met substantial technical challenges.[22-27] Success in six-wave mixing measurements was achieved after years of exhaustive efforts.[27,28] Difficulties encountered in these pioneering works significantly slowed further development of multidimensional Raman techniques. However, interest in this class of experiments has been reinitiated by related methods that are used to study molecular photochemistries.[29-40]

In this paper, we present two-dimensional resonance Raman (2DRR) measurements that blend different types of higher-order Raman spectroscopies. The multi-beam aspect of the

[3] This chapter previously appeared as an article in the Journal of Chemical Physics. The original citation is as follows: B. P. Molesky, Z. Guo, T. P. Cheshire, A. M. Moran, J. Chem. Phys., 145, .034203 (2016).

experiment illustrated in Figure 4.1 is similar in nature to earlier off-resonant 2D Raman work,[27,28] whereas the combination of narrowband and broadband pulses is inspired by Femtosecond Stimulated Raman Spectroscopy (FSRS).[30,32] As depicted in Figure 4.1, the experiment begins when an actinic pump pulse initiates vibrational motion of the system in the variable delay, $\tau_1$. Fourier transformation with respect to $\tau_1$ constitutes the first dimension of the 2DRR spectrum. Vibrational motion is reinitiated by time-coincident Raman pump and Stokes pulses before a second Raman pump pulse induces signal emission. The second dimension of the 2DRR spectrum is obtained by dispersing the signal pulse on an array detector. The approach is distinct from traditional three-pulse FSRS in that (i) residual laser light does not travel in the same direction as the signal beam and (ii) a fixed delay, $\tau_2$, is used to suppress the intense broadband pump-repump-probe response.[41] The data acquisition rate and sensitivity of our method facilitate detection of the 2DRR response, which is generally less that 5% of the total fifth-order signal. Traditional three-beam FSRS offers other advantages such as automatic heterodyne detection and straightforward implementation of two-color experiments.[30]

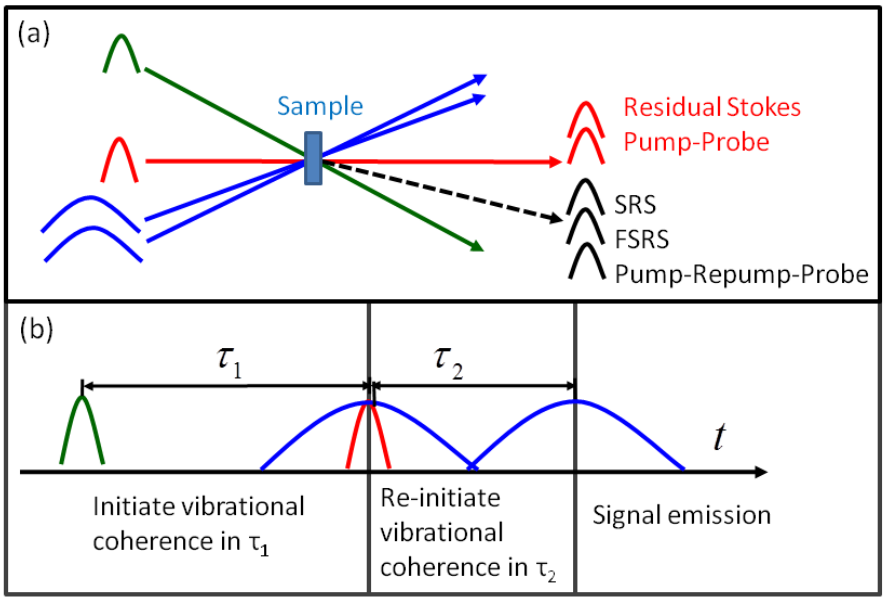


***Figure 4.1.*** *(a) A four-beam FSRS geometry is used in this work to eliminate the portion of the background associated with residual Stokes light and a pump-probe response. The color code is as follows: the actinic pump is green, the Raman pump is blue, and the Stokes pulse is red. (b) Vibrational coherences in* $\tau_1$ *are resolved by numerically Fourier transforming the signal with respect to the delay time. Time-coincident Raman pump and Stokes pulses then initiate a second set of vibrational coherences, which are resolved by dispersing the signal pulse on an array detector. The fixed time delay,* $\tau_2$ *, is used to suppress the broadband pump-repump-probe response of the solution.*

Measurements and model calculations are conducted for both metmyoglobin (metMb) and oxymyoglobin ($MbO_2$) in order to establish signatures of inhomogeneous line broadening and anharmonic coupling in 2DRR spectra. The charge of the iron atom is +3 (ferric) and +2 (ferrous) in metMb and $MbO_2$, respectively. Of course, the two systems also differ in whether water (metMb) or oxygen ($MbO_2$) is coordinated on the distal side of the heme group. Sub-100-fs photodissociation of oxygen is induced following photoexcitation in the visible spectral range in $MbO_2$, whereas metMb relaxes to the ground electronic state by way of non-radiative processes on the picosecond time scale.[42-47] In analogy with other 2D methods, the present 2DRR measurements reveal heterogeneity within the ensembles for the two systems. The 220-$cm^{-1}$ iron-histidine stretching mode is of particular interest because of its prominence in $MbO_2$, where the

heme moiety transitions from a planar to non-planar geometry following photodissociation.[48] In addition, vibrational modes associated with the propionic acid side chains may provide insight into energy exchange between the heme and aqueous solvent.[49-52] Line broadening mechanisms of these modes are intimately connected to such vibrational energy exchange, because they reflect fluctuations in the geometries of the side chains.

The present work builds upon a variety of experimental approaches that we have developed for conducting 2DRR experiments in recent years.[41,53,54] An earlier report of the technique employed in this work focused primarily on experimental issues.[41] Control experiments were used to show that the response of metMb exhibits the anticipated (correct) dependence on sample concentration and on the intensities of the incoming beams. The susceptibility of the experiment to cascaded four-wave mixing responses was an issue of primary concern, because these undesired nonlinearities present significant challenges in off-resonant 2D Raman experiments.[26-28,55,56] It was also shown that cascades of four-wave mixing signals are negligible under our experimental conditions. Calculations suggest the selection rules that enhance cascaded signal intensity under electronically off-resonant conditions are obviated when all pulses are electronically resonant with the system. In effect, the direct and cascaded signals compete on the same footing when all laser beams are tuned into electronic resonance. The cascaded signal is weaker than the direct response with optical densities of metMb less than 1.0, because it involves two more field-matter interactions (i.e., it is a higher-order process in this respect). Our analysis suggests that the direct response of myoglobin will also dominate in a conventional three-beam FSRS geometry. That is, it may generally be possible to conduct 2DRR spectroscopy without beam geometries cleverly designed to induce phase mismatch in third-order nonlinearities.

## II. Experimental Methods

### IIA. Sample Preparation

Myoglobin from horse skeletal muscle (Sigma-Aldrich) is dissolved in 0.1-M sodium phosphate buffer at a pH of 7.0. The metMb solutions are centrifuged at 6000 revolutions per minute for 15 minutes before each experiment to optimize the optical quality. To convert metMb to $MbO_2$, 10-fold molar excess of sodium hydrosulfite is added to reduce metMb. Air is then bubbled through the solution for 15 minutes until it is bright red in color. Attainment of a high quality $MbO_2$ sample is confirmed by comparison of the sample's linear absorption to the known spectrum of $MbO_2$. The primary metric is the peak position of the Soret band, which is located at 409 and 418 nm for metMb and $MbO_2$, respectively.[57] Spontaneous Raman spectra are also used to confirm the position of the most intense in-plane bond stretching vibration (i.e., an oxidation state marker band). The vibrational frequencies of this mode are close to 1373 and 1356 $cm^{-1}$ for metMb and $MbO_2$ , respectively.[58,59] In all experiments, the 0.2-mM sample of myoglobin is flowed through a wire-guided jet with a thickness of 220 μm, where the reservoir volume is 50 mL.[60] Absorbance spectra are measured before and after experiments to confirm the absence of sample degradation.

### IIB. Spectroscopic Measurements

In this section, we summarize key aspects of the experimental approach, which is described at length in Reference [41]. As in earlier work, we employ laser pulses which are resonant with the Soret bands of metMb and $MbO_2$ (see Figure 4.2). The narrowband Raman pump pulses are generated by sending 70-fs, 410-nm second harmonic pulses through a 4F spectral filter consisting of two 2400-g/mm gratings and two 25-cm focal length lenses. Pulses with spectral widths of 50 $cm^{-1}$ are obtained by placing a slit with a 890-μm width at the 2F plane. Broadband actinic pump and Stokes pulses are produced by focusing a 90-μJ, 410-nm

second harmonic beam into a 75-cm long hollow core fiber filled with 1.0 atm of argon gas. The spectrally broadened output of the fiber is compressed using fused-silica prisms separated by 50 cm to achieve an instrument response of 20 fs over the spectral range corresponding to Raman shifts of 200-1500 $cm^{-1}$ (413-437 nm)

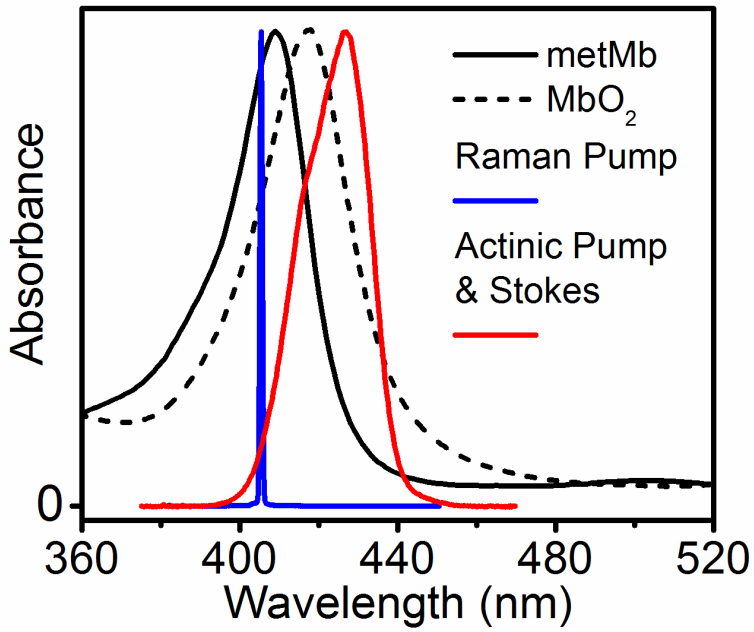


***Figure 4.2.*** *Laser spectra are overlaid on the linear absorbance spectra of (a) metMb and (b) $MbO_2$ in aqueous buffer solution at pH=7.0.*

Experiments are conducted with the diffractive optic-based interferometer shown in Figure 4.3. All beams are focused onto the diffractive optic with a 50-cm focal length spherical mirror. Approximately 25% of each incident beam is diffracted into each of the three diffraction orders (0 and +/-1). The 20-cm focal length imaging mirror is rotated off-axis by approximately 5º (i.e., the minimum amount). The actinic pump and Raman pump beams cross at approximately 6.9º in the diffractive optic and are bisected by the Stokes beam. The angle between the +1 and -1 diffraction orders of the Raman pump beams is 6.9º. The angle between +1 and -1 diffraction orders of the actinic pump and Stokes beams is 7.2º; the actinic pump and Stokes pulses have the same spectrum (see Figure 4.2). Pulse energies of the actinic pump and Stokes pulses are 100 nJ

each. The energy of each Raman pump pulse is 150 nJ. The FWHM spot sizes of all laser beams are 200 μm at the sample position.

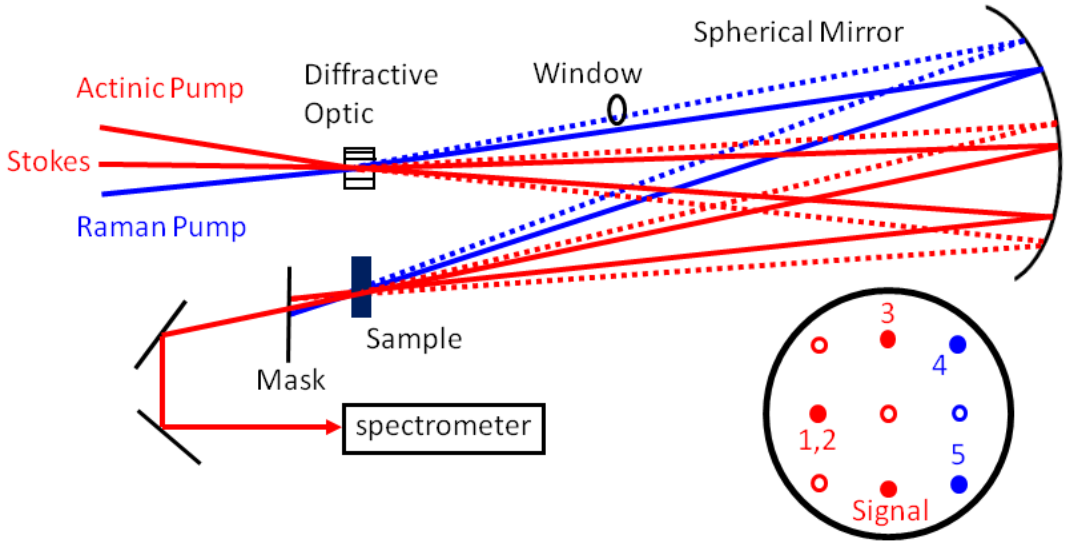


***Figure 4.3.*** *Diffractive optic-based interferometer used for 2DRR measurements. The transparent fused silica window delays pulse 5 by 290 fs with respect to pulse 4 (delay* $\tau_2$ *in Figure 4.1). A four-beam geometry is used to detect the signal radiated in the direction,* $\boldsymbol{k}_1$-$\boldsymbol{k}_2$+$\boldsymbol{k}_3$-$\boldsymbol{k}_4$+$\boldsymbol{k}_5$*; the wavevectors* $\boldsymbol{k}_1$ *and* $\boldsymbol{k}_2$ *cancel each other. The 2DRR signal is obtained by measuring differences with and without the actinic pump (beam 1,2). The indices represent the desired order of field-matter interactions. Beams represented with solid circles reach the sample, whereas those represented with open circles are blocked with a mask.*

We employ a four-beam geometry in which the signal is associated with the difference produced by the actinic pump beam.[41] The four-wave mixing background generated by the Raman pump and Stokes pulses is not difficult to subtract, because it is only 10-20 times larger than the desired fifth-order response. We find that the background is most effectively removed by subtracting spectra acquired at negative delay times (far from the rise of the FSRS signal near $\tau_1$ =-10 ps). An alternate approach in which the actinic pump beam is chopped at every delay point results in poor signal quality because of the longer data acquisition time. Despite its smaller background, we opt not to use the five-beam geometry described in Reference [41], because it is more difficult to maintain alignment day-to-day. In addition, color-tunable actinic pump beams

may be employed in the four-beam geometry, and such experiments are presently being pursued with the same experimental setup.[54]

Signals are detected using a back-illuminated CCD array (Princeton Instruments PIXIS 100B) mounted on a 0.3-meter spectrograph with a 1200-g/mm grating. The signal beam is focused to a spot size of 100 μm at the entrance to the spectrograph to obtain hardware-limited spectral resolution of approximately 10 $cm^{-1}$. Ultimately, the resolution of the measurement is limited by the 50-$cm^{-1}$ spectral width of the Raman pump beam. The total FSRS response produces roughly 1000 counts on the detector at each delay point with an integration time of 100 ms. The vibrational coherences associated with the 2DRR component of the response are all less than 5% of the total signal. The delay, $\tau_1$, of the actinic pump is scanned 100 times, and the signal is averaged to optimize the data quality. 2DRR spectra were acquired with different step sizes in the dimension, $\tau_1$, to rule out artifacts. Such control experiments are important in Fourier transform spectroscopy, because motion of the stage (if not aligned properly) or sample can potentially give rise to spurious peaks. This is one major advantage to conducting experiments in a jet.

**III. Simulations of 2DRR Spectra**

The development of 2DRR spectroscopy is still at an early stage despite a long history of off-resonant 2D Raman work. As mentioned above, signal generation is allowed and forbidden for harmonic systems in resonant and off-resonant experiments, respectively. The implications of this difference in selection rules for information content have not yet been established. To this end, we begin this section by examining signatures of inhomogeneous broadening and anharmonicity in 2DRR spectra for a pair of vibrational modes. The 2DRR spectrum of myoglobin is then simulated using parameters derived from earlier spontaneous resonance

Raman experiments. Insights gained from these calculations will be used to interpret experimental signals in section IV.

**IIIA. Signatures of Inhomogeneous Broadening in 2DRR Spectra**

The ability to distinguish inhomogeneous and homogeneous line broadening mechanisms motivated the first multidimensional Raman experiments conducted in the late 1980's and early 1990's.[18,21] The spectroscopic signatures are much like those associated with 2D photon echo experiments, where heterogeneity gives rise to a difference between the diagonal and anti-diagonal widths.[1,8,61,62] That is, inhomogeneous line broadening is a signature of correlation between the resonance frequencies detected in the two frequency dimensions.[63,64] Unlike Raman echo experiments,[21] the present (fifth-order) 2DRR experiments do not yield the time scale at which correlation decays, because an intermediate "waiting time" cannot be scanned.[18] Rather, we are only able to detect the amount of correlation present in the system on the time-scale of the inverse of the vibrational line width.

Spectroscopic signatures are most easily established with calculations based on two vibrational modes and a single electronic resonance. The model developed in Reference [41] can be adapted for this purpose (see section VA). We take the mode frequencies to be 400 $cm^{-1}$ and 1100 $cm^{-1}$ in order to produce well-resolved vibrational resonances. Resolution of the various 2DRR peaks also requires that the two mode frequencies and their overtones are well-separated. For example, the overtone of the 400-$cm^{-1}$ mode (at 800 $cm^{-1}$) must be well-separated from the fundamental mode frequency at 1100 $cm^{-1}$. The dimensionless displacement of each mode is set equal to 0.75 so that all key resonances can be observed on the same linear scale for the signal magnitude.

Heterogeneity is introduced by convoluting the signal field defined in section VA with a Gaussian function,

$$S(\omega_1,\omega_2)=\int_{-\infty}^{\infty}\int_{-\infty}^{\infty}G(\eta_a,\eta_b)E_{2DRR}^{(5)}(\omega_1,\omega_2)d\eta_a d\eta_b \ , \tag{4.1}$$

where

$$G(\eta_a,\eta_b)=\frac{1}{2\pi\sigma_a\sigma_b\sqrt{1-\rho^2}}\times$$
$$\exp\left\{-\frac{1}{2(1-\rho^2)}\left[\frac{(\varpi_a+\eta_a)^2}{\sigma_a^2}-2\rho\frac{(\varpi_a+\eta_a)(\varpi_b+\eta_b)}{\sigma_a\sigma_b}+\frac{(\varpi_b+\eta_b)^2}{\sigma_b^2}\right]\right\} . \tag{4.2}$$

Here, $\eta_a$ is the deviation of the harmonic mode frequency, $a$ ,from its mean value, $\varpi_a$ (in $cm^{-1}$), whereas $\sigma_a$ is the width of the inhomogeneous distribution. The inter-mode correlation parameter, $\rho$, ranges from the fully anti-correlated (-1) to fully correlated (+1) limits.[63,64] The signal field depends on $\varpi_a$ and $\varpi_b$ through the vibrational Hamiltonian of the system (see section VB).

The calculations in Figure 4.4 are conducted in the anti-correlated ( $\rho$ =-0.75), uncorrelated ( $\rho$ =0), and correlated ( $\rho$ =+0.75) regimes. Of course, the diagonal peaks exhibit correlated line shapes for all cases, because the inhomogeneous widths, $\sigma_a$ and $\sigma_b$, are nonzero. Notably, this signature of inhomogeneous line broadening cannot be derived from one-dimensional Raman spectroscopy (e.g., third-order stimulated Raman and spontaneous Raman measurements). For diagonal 2DRR peaks, the anti-diagonal width is related to homogeneous broadening, whereas the diagonal width represents the combination of homogeneous and inhomogeneous broadening mechanisms. Unlike the diagonal peaks, the orientations and relative intensities of the cross peaks depend on the correlation parameter, $\rho$; the cross peaks possess an anti-diagonal and diagonal slant when the correlation parameter is negative (Figure 4.4a) and positive (Figure 4.4c), respectively. The cross peaks exhibit a fairly “round” line shape for the uncorrelated limit in Figure 4.4b. These spectroscopic signatures are much like those established

in 2D infrared experiments.[1,8,61,62] The relative intensities of the cross peaks are largest when $\rho$ is positive because of cancellations between terms with opposite signs in $G(\eta_a, \eta_b)$.

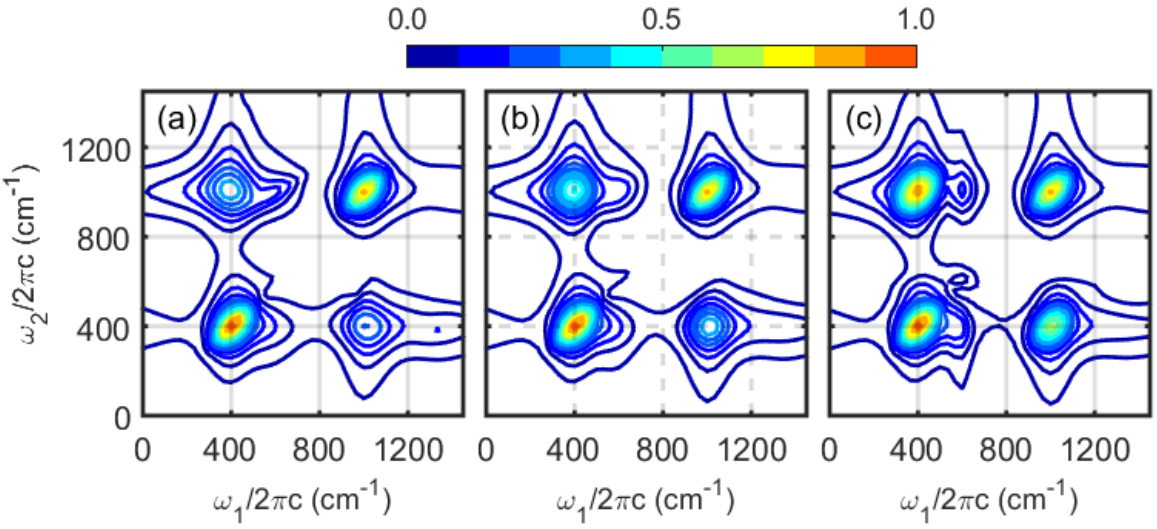


***Figure 4.4.*** *2DRR spectra computed for a pair of harmonic oscillators with inhomogeneous line broadening. The spectra are computed by combining Equations (4.1) and (4.23) with the parameters given in Table 4.1. The correlation parameter, $\rho$, is set equal to (a) -0.75, (b) 0.0, and (c) 0.75. The diagonal peaks always exhibit correlated line shapes when the inhomogeneous widths are nonzero, whereas the orientations and intensities of the off-diagonal peaks depend on the correlation parameter, $\rho$.*

***Table 4.1.*** *Parameters of Theoretical Model for System with Two Vibrational Modes*

| [a]Parameter | Value |
|---|---|
| $\omega_{eg}/2\pi c$ | 23250 $cm^{-1}$ |
| $\omega_{AP}$ & $\omega_{RP}$ | set equal to $\omega_{eg}$ |
| [b] $\varpi_a$ | 400 $cm^{-1}$ |
| [b] $\varpi_b$ | 1100 $cm^{-1}$ |
| [c] $d_a$ | 0.75 |
| [c] $d_b$ | 0.75 |
| $\Gamma_{vib}/c$ | 10 $cm^{-1}$ |
| $\Gamma_{eg}/c$ | 750 $cm^{-1}$ |
| $\mu_{eg}$ | 8.8 D |
| [d] $\sigma_a$ & $\sigma_b$ | 35 $cm^{-1}$ |

[a] The number density ( $N$ ), refractive index ( $n(\omega_t)$ ), and path length ( $l$ ) do not affect these results because normalized intensities are displayed (see section VA).

[b] The parameter, $\varpi_j$, is the wavenumber for mode $j$, $\varpi_j = \omega_j/2\pi c$.

[c] The parameter, $d_j$, is the dimensionless potential energy minimum displacement for mode $j$.

[d] Inhomogeneous line broadening is included only for the calculations shown in Figure 4.5 (see Equations (4.1) and (4.2)).

### IIIB. Signatures of Anharmonicity in 2DRR Spectra

Signal generation is allowed in off-resonant 2D Raman experiments only if the modes are anharmonic or the polarizability scales nonlinearly with the vibrational coordinates.[19,20] Thus, success in detecting the signal constitutes unambiguous evidence of a non-trivial behavior. Of course, this aspect of the off-resonant nonlinearity also means that the signal will generally be small and that artifacts such as cascades can readily contaminate the signals.[27,28] As noted in our previous work, 2DRR spectroscopy is "easier" to conduct than off-resonant 2D Raman experiments, because signal generation is allowed for harmonic modes. Unfortunately, this also means that any pair of harmonic Franck-Condon active modes will generate a 2DRR cross peak, thereby complicating signal interpretation. We investigate signatures of anharmonicity in 2DRR spectra in this section.

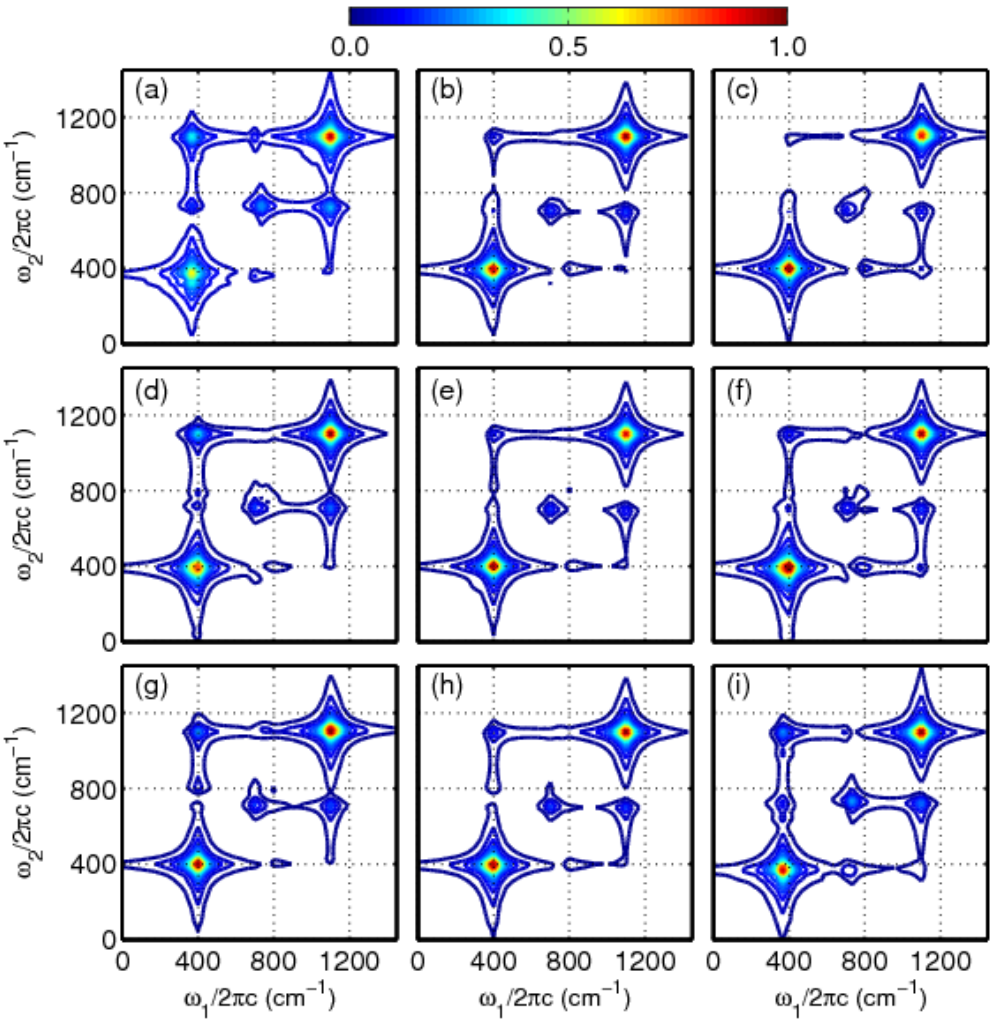


***Figure 4.5.*** *2DRR spectra computed with the anharmonic vibrational Hamiltonian described in section VB and the parameters in Table 4.1. The diagonal cubic expansion coefficients are set equal to -5 (first row), 0 (second row), and 5 cm$^{-1}$ (third row). The off-diagonal expansion coefficients are set equal to -5 (first column), 0 (second column), and 5 cm$^{-1}$ (third column). The response of a harmonic system is shown in panel (e). These calculations suggest that anharmonic coupling promotes intensity borrowing effects via the transformation of Franck-Condon overlap integrals from the harmonic to anharmonic basis set (see Equation (4.26)). For many of the parameter sets, anharmonicity causes the intensity of the cross peak above the diagonal to increase relative to that of the cross peak below the diagonal. This effect is most pronounced in the left column.*

As in section IIIA, calculations are conducted for a pair of vibrational modes and a single electronic resonance. We treat only homogeneous line broadening in this section in order to focus on the effects of anharmonicity. Cubic force constants are added to a harmonic vibrational Hamiltonian as described in section VB. The two normal modes mix through cubic force

constants that depend on two coordinates. These "off-diagonal" cubic expansion coefficients are denoted as $U_{122}$, $U_{212}$, $U_{221}$, $U_{211}$, $U_{121}$, and $U_{112}$. In contrast, the "diagonal" cubic expansion coefficients, $U_{111}$ and $U_{222}$, primarily shift the resonances to lower frequencies.

In Figure 4.5, the off-diagonal expansion coefficients are all set equal to three values (-5, 0, and 5 $cm^{-1}$) to illustrate the effects that these terms have on 2DRR spectra. New resonances are not generated; however, the peak intensities are influenced by an intensity borrowing effect that originates in the transformation of Franck-Condon overlap integrals from the harmonic to anharmonic basis sets (see Equation (4.26)). Calculations are also carried out for three values of the diagonal expansion coefficients (-5, 0, and 5 $cm^{-1}$). The cross peak intensity above the diagonal increases relative to the intensities of the diagonal peaks for some of the anharmonic systems (Figures 4.5a, 4.5d, 4.5g, and 4.5i). We consider the 2DRR spectra for the other anharmonic systems (Figures 4.5b,4. 5c, 4.5h, and 4.5f) to be experimentally indistinguishable from that of the harmonic system (Figure 4.5e). Unlike 2D infrared spectroscopy, spectral shifts in the peak positions do not necessarily yield clear signatures of anharmonicity because of the variety of coherences that contribute to a particular peak as a result of Franck-Condon activity. For example, a coherence between the ground and singly excited vibrational levels can contribute in both dimensions; a coherence between the singly and doubly excited vibrational levels is only one possibility in the second dimension. Overall, these factors suggest limited potential of the 2DRR technique to reveal anharmonic couplings in the present quasi-degenerate (one-color) configuration.

For FSRS signals represented in the traditional way ($\tau_1$ and $\omega_2$ in our notation), it has been shown that anharmonic coupling between modes may cause the vibrational resonance frequencies in $\omega_2$ to oscillate with respect to $\tau_1$ in ring-opening[65] and proton photodissociation[66]

reactions. The present model does not predict such dynamics, because the non-oscillatory component of the signal dominates the response under one-color conditions. In previous 2DRR studies of the photodissociation reaction of triiodide, we similarly observed anharmonicity-induced oscillations in the vibrational resonance frequencies under two-color conditions.[53,54] Although signatures of anharmonicity are more readily derived from two-color 2DRR experiments, it will still be true that cross peaks are generated for all pairs of Franck-Condon active modes (whether they are harmonic or not).

**IIIC. Predicted 2DRR Spectrum of Myoglobin**

Calculations presented in sections IIIA and IIIB provide basic insights into 2DRR signal interpretation. The simulations suggest that signatures of inhomogeneous line broadening will be fairly obvious, whereas unambiguous evidence of anharmonicity will be difficult to derive from experimental data (particularly in one-color experiments). It will be useful to "estimate" how the 2DRR spectrum of myoglobin will appear based on earlier work. To this end, the parameters needed to simulate the 2DRR spectrum for a one-color experiment can be obtained from earlier fits to the spontaneous Raman excitation profiles for the Soret band.[67] Notably, these fits are carried out in a basis of harmonic modes.

In Figure 4.6, we present a 2DRR spectrum computed in the homogeneous limit of line broadening using the parameters given in Table 4.2. The four most dominant vibrational modes are included in the model. A peak associated with each mode appears on the diagonal. The most intense cross peak is found at $\omega_1 / 2\pi c$ =220 cm$^{-1}$ (iron-histidine stretch) and $\omega_2 / 2\pi c$ =1356 cm$^{-1}$ (in-plane stretch of heme); the cross peak intensity above the diagonal is greater than that associated with the corresponding cross peak below the diagonal. The model additionally suggests that the intensity of the cross peak above the diagonal increases with respect to the cross

peak intensity below the diagonal as the dimensionless displacements increase. The spectrum in Figure 4.6 exhibits weak off-diagonal peaks that are shifted down the $\omega_2$ axis from the 674-cm$^{-1}$ and 1356-cm$^{-1}$ diagonal peaks by 220 cm$^{-1}$. These off-diagonal peaks represent sequences in which the system evolves in coherences at the fundamental mode frequencies in $\tau_1$ and an inter-mode coherences in $\tau_2$. Finally, we remark that the calculations presented in Figure 4.6, which employ large mode displacements, exhibit a peak associated with an inter-mode vibrational coherence on the diagonal (at $\omega_1 / 2\pi c = \omega_2 / 2\pi c$ =454 cm$^{-1}$). Detection of this type of resonance requires two modes with significant displacements.

***Table 4.2.*** *Parameters of Model Based on Empirical Fit of Spontaneous Raman Signals*

| [a]Parameter | Value |
|---|---|
| $\omega_{eg} / 2\pi c$ | 23250 cm$^{-1}$ |
| $\omega_{AP}$ & $\omega_{RP}$ | set equal to $\omega_{eg}$ |
| [b] $\varpi_1$ | 220 cm$^{-1}$ |
| [b] $\varpi_2$ | 370 cm$^{-1}$ |
| [b] $\varpi_3$ | 674 cm$^{-1}$ |
| [b] $\varpi_4$ | 1356 cm$^{-1}$ |
| [c] $d_1$ | 0.47 |
| [c] $d_2$ | 0.20 |
| [c] $d_3$ | 0.26 |
| [c] $d_4$ | 0.34 |
| $\Gamma_{vib} / c$ | 10 cm$^{-1}$ |
| $\Gamma_{eg} / c$ | 750 cm$^{-1}$ |
| $\mu_{eg}$ | 8.8 D |

[a] The number density ( $N$ ), refractive index ( $n(\omega_t)$ ), and path length ( $l$ ) do not affect these results because normalized intensities are displayed (see section VA).

[b] The parameter, $\varpi_j$, is the wavenumber for mode $j$, $\varpi_j = \omega_j / 2\pi c$.

[c] The parameter, $d_j$, is the dimensionless potential energy minimum displacement for mode $j$.

Overall, the calculations presented in Figures 4.4-4.6 suggest that line broadening mechanisms will be the primary information to be derived from 2DRR spectra for myoglobin. Signatures of anharmonicity are likely to be ambiguous in the present quasi-degenerate (one-color) experiments, because the response is allowed for harmonic modes. Moreover, the fairly small potential energy surface displacements found in myoglobin should make most cross peaks difficult to detect.[67]

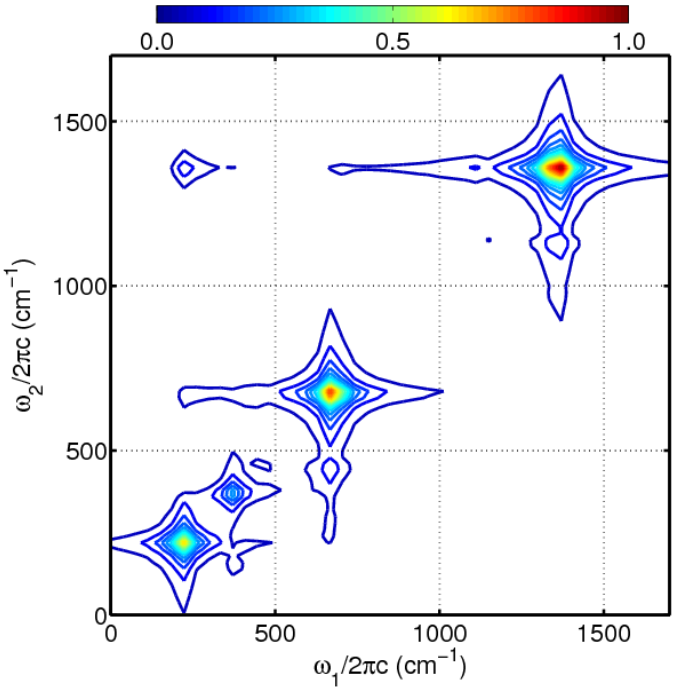


***Figure 4.6.*** *2DRR spectrum of myoglobin computed using parameters obtained by fitting spontaneous resonance Raman excitation profiles.[67] The spectrum is dominated by resonances on the diagonal. The most dominant cross peak is associated with the iron-histidine stretch ($\omega_1 / 2\pi c = 220\ cm^{-1}$) and in-plane stretching mode ($\omega_2 / 2\pi c = 1356\ cm^{-1}$). The spectra are computed by combining (A20) with the parameters in Table 4.2.*

## IV. Results and Discussion

### IVA. Isolation of 2DRR Signal Components

In this section, we show how the 2DRR response is extracted from the total signal. The procedure used to obtain the FSRS-like representation of the signal at various delay times, $\tau_1$, was described at length in earlier work.[41] Examples of such FSRS-like signals are shown in

Figures 4.7a and 4.7d. The novel aspect of this study is that we carry out a Fourier transformation with respect to $\tau_1$ to generate a 2DRR spectrum. The main challenge in doing so is that the 2DRR signal component must be separated from a much larger incoherent fifth-order response. Below, we discuss issues particular to this aspect of the data analysis.

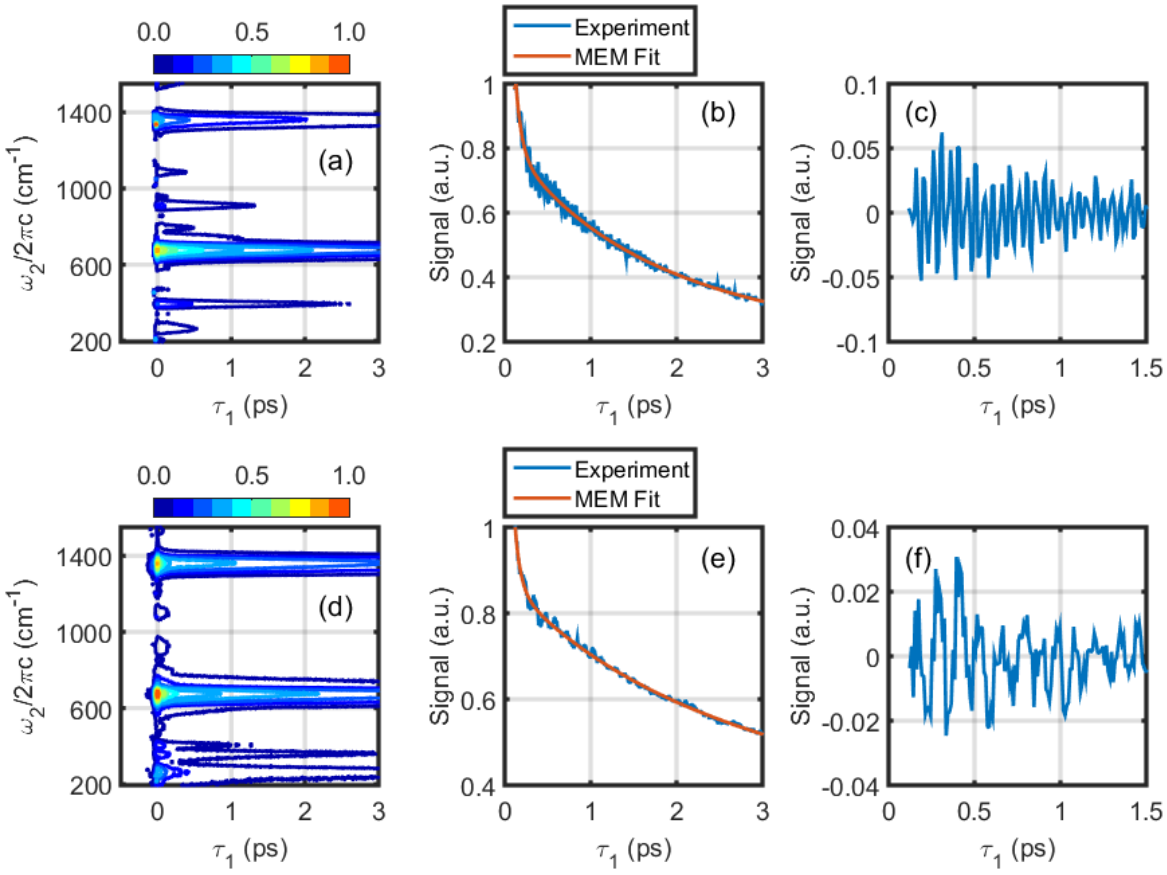


***Figure 4.7.*** *Signals obtained for (a) metMb and (d) $MbO_2$ in a FSRS-like representation. At each point in $\omega_2$, the incoherent baseline is generated using the maximum entropy method. Shown here are slices of the signals for (b) the 670-cm$^{-1}$ mode of metMb and (e) the 370-cm$^{-1}$ mode of $MbO_2$. Coherent residuals are obtained by subtracting incoherent MEM baselines from the total signals for (b) metMb and (e) $MbO_2$. The coherent residuals are presented for (c) metMb and (f) $MbO_2$.*

To illustrate the method of data analysis, we begin by examining time-dependent Raman spectra obtained for both metMb and $MbO_2$ in Figure 4.7. In both cases, peaks are observed near 220 cm$^{-1}$, 370 cm$^{-1}$, 670 cm$^{-1}$, and 1356 cm$^{-1}$. The 220-cm$^{-1}$ mode corresponds to the iron-

histidine stretch on the proximal side of the heme group. The intensity of the resonance at 220-$cm^{-1}$ varies significantly between systems, because photodissociation is initiated only in $MbO_2$. That is, there is a significant excited state potential energy gradient for the iron-histidine stretch in $MbO_2$, because the iron moves out of plane following photodissociation. The 370-$cm^{-1}$ mode represents methylene deformation local to the propionic acid side chains (see Figure 4.8). The 670-$cm^{-1}$ mode corresponds to deformation of the tetrapyrrole moiety. The vibrational wavenumber of the in-plane bond stretching mode, which is a useful marker for the oxidation state of the heme, is 1356 $cm^{-1}$ in $MbO_2$ and 1373 $cm^{-1}$ in metMB.[59]

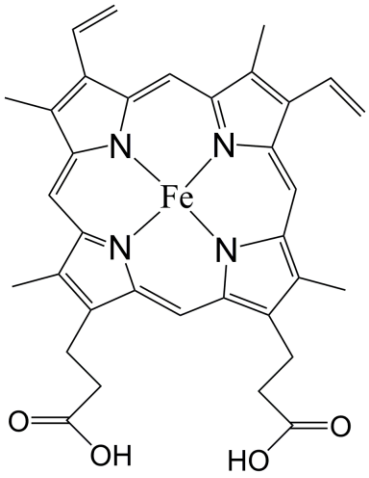


***Figure 4.8.*** *Molecular structure of iron protoporphyrin-IX.*

Oscillatory signal components in $\tau_1$ are isolated by subtracting incoherent baselines generated using the maximum entropy method (MEM), which suppresses low-frequency artifacts that may arise when baselines are produced using a small number of exponential functions.[68] In Figures 4.7b and 4.7e, we overlay example MEM fits with signals obtained for both metMb and $MbO_2$; residuals are plotted in Figures 4.7c and 4.7f. The analysis is carried out beginning at a delay time of 0.1 ps in $\tau_1$ to remove contributions from the region of pulse overlap. The 2DRR

spectra shown in Figure 4.9 are obtained by repeating this procedure at every point in $\omega_2$ (i.e., every pixel on the CCD array), then carrying out a Fourier transformation with respect to $\tau_1$,

$$S(\omega_1,\omega_2)=\int S(\tau_1,\omega_2)\exp(i\omega_1\tau_1-\alpha\tau_1)\,d\tau_1, \tag{4.3}$$

where $S(\tau_1,\omega_2)$ is the baseline-subtracted signal, $S(\omega_1,\omega_2)$ is the 2DRR spectrum, and $\alpha$ is a constant used to suppress contributions from delay times at which the oscillations have decayed below the noise level. In the present work we set $\alpha$ equal to 1.4 ps$^{-1}$.

The 2DRR spectra of both systems shown in Figure 4.9 exhibit diagonal peaks near 220 cm$^{-1}$, 370 cm$^{-1}$, 674 cm$^{-1}$, and 1356 cm$^{-1}$ (close to 1373 cm$^{-1}$ in metMb).[59,67] The peaks near 1356 cm$^{-1}$ are relatively weak, because the 24-fs period of this mode is slightly larger than the 19-fs instrument response width at this particular value of the Raman shift. Two cross peaks are located above the diagonal. The cross peaks at $\omega_1/2\pi c$=50 cm$^{-1}$ and $\omega_2/2\pi c$=674 cm$^{-1}$ reflect motion along the doming coordinate in $\tau_1$. Cross peaks are also located near $\omega_1/2\pi c$=370 cm$^{-1}$ and $\omega_2/2\pi c$=1356 cm$^{-1}$. It is interesting that only one cross peak is found in the slices of the 2D spectra near $\omega_2/2\pi c$=1356 cm$^{-1}$; cross peaks near $\omega_1/2\pi c$=674 cm$^{-1}$ and $\omega_2/2\pi c$=1356 cm$^{-1}$ are below the detection threshold despite the significant intensities of the diagonal peaks at 674 cm$^{-1}$. This aspect of the experimental spectra is consistent with the simulation for myoglobin in Figure 4.6. In this calculation, an intense cross peak is generated above the diagonal near $\omega_1/2\pi c$=220 cm$^{-1}$ and $\omega_2/2\pi c$=1356 cm$^{-1}$, but not at $\omega_1/2\pi c$=674 cm$^{-1}$ and $\omega_2/2\pi c$=1356 cm$^{-1}$.

The measurements in Figure 4.9 differs from the prediction in Figure 4.6 in that off-diagonal peaks are not detected 220 cm$^{-1}$ below diagonal peaks in the $\omega_2$ dimension (e.g., at $\omega_1/2\pi c$=674 cm$^{-1}$ and $\omega_2/2\pi c$=454 cm$^{-1}$). In the calculation, the off-diagonal peaks originate

from multiple pathways and do not necessarily require thermal population in the 220-$cm^{-1}$ mode. For example, terms 13-17 in section VA can give rise to such off-diagonal peaks if one of the first two field-matter interactions photoexcites a combination band between the 220- and 674-$cm^{-1}$ modes. It is possible that terms 1-4 dominate the experimental signals, because of the short lifetime of the excited electronic state (i.e., the excited electronic state is populated in $\omega_1$, $\omega_2$, or both dimensions in terms 5-16). In other words, differences between Figures 4.6 and 4.9 may be attributed to overestimated contributions from terms 5-16.

Cross peaks are detected below the diagonal near $\omega_1 / 2\pi c$ =990 $cm^{-1}$ and $\omega_2 / 2\pi c$ =674 $cm^{-1}$. We tentatively suggest that a Franck-Condon active vinyl wagging mode is responsible for the 990-$cm^{-1}$ location of this peak in the first dimension.[59] The absence of a diagonal peak at $\omega_1 / 2\pi c = \omega_2 / 2\pi c$ =990 $cm^{-1}$ can be explained by the weak Franck-Condon activity of this mode. That is, the cross peak at $\omega_1 / 2\pi c$ =990 $cm^{-1}$ and $\omega_2 / 2\pi c$ =674 $cm^{-1}$ derives strength from the 674-$cm^{-1}$ mode, which has a large displacement. In contrast, a diagonal peak at $\omega_1 / 2\pi c = \omega_2 / 2\pi c$ =990 $cm^{-1}$ must possess a weak intensity, because it depends exclusively on the small displacement of this mode. Moreover, modes that give rise to relatively weak transitions in spontaneous Raman spectroscopy are further attenuated in 2DRR because of its higher order. It is unclear why a cross peak is not also detected at $\omega_1 / 2\pi c$ =674 $cm^{-1}$ and $\omega_2 / 2\pi c$ =990 $cm^{-1}$. One possibility is that anharmonicity redistributes intensities among cross peaks as demonstrated in Figure 4.5. *The calculation presented in Figure 4.6 captures many aspects of the measured 2DRR spectra in Figure 4.9; however, knowledge of the anharmonic couplings may be the key to precisely reproducing peak intensities.*

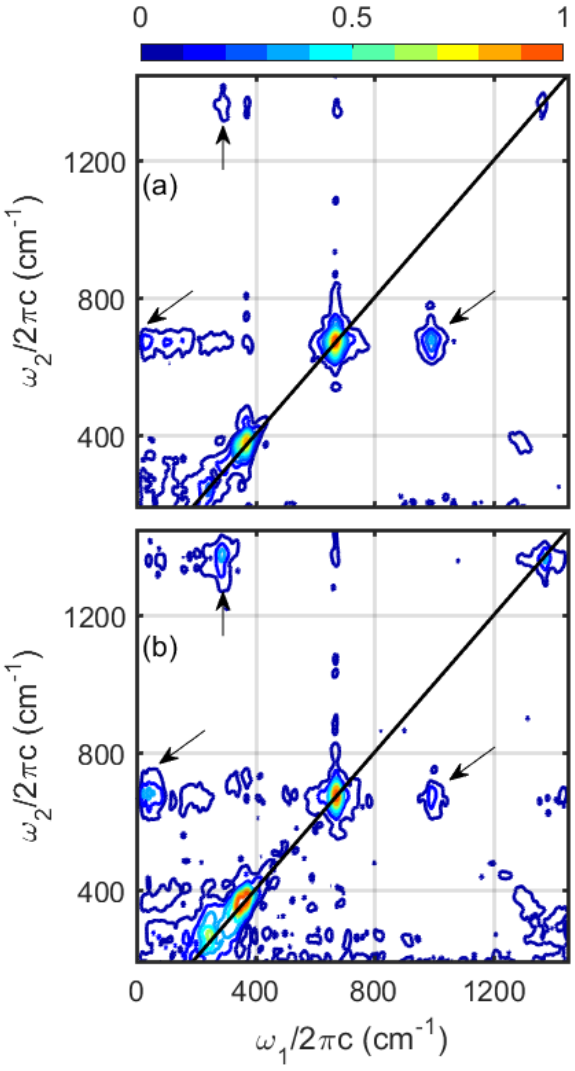


***Figure 4.9.*** *Experimental 2DRR spectra for (a) metMb and (b) $MbO_2$ are generated by Fourier transforming the coherent residuals with respect to $\tau_1$ at each point in $\omega_2$ (i.e., at each pixel on the CCD detector). For both systems, diagonal peaks are detected near 220, 370, 674, and 1356 cm$^{-1}$ (close to 1373 cm$^{-1}$ in metMb). Arrows are used to identify cross peaks.*

**IVB. Analysis of Spectral Line Shapes**

The ability to distinguish inhomogeneous and homogeneous line broadening mechanisms motivated the first multidimensional Raman experiments.[18,21] As in 2D infrared spectroscopy, information about the line broadening mechanism can be read directly from the line shape. Inhomogenous broadening will cause peaks to elongate on the diagonal of the 2DRR spectrum; the diagonal width will then be greater than the anti-diagonal width. Correlated line shapes may

be observed when spectral diffusion of a vibrational resonance frequency is much slower than the time-scale of the inverse line width (roughly 1 ps). In this section, we characterize the 2DRR line shapes shown in Figure 4.9. The present analysis is limited to the region of the spectrum between 200 and 800 $cm^{-1}$ in both dimensions, because we find no evidence of inhomogeneous line broadening elsewhere.

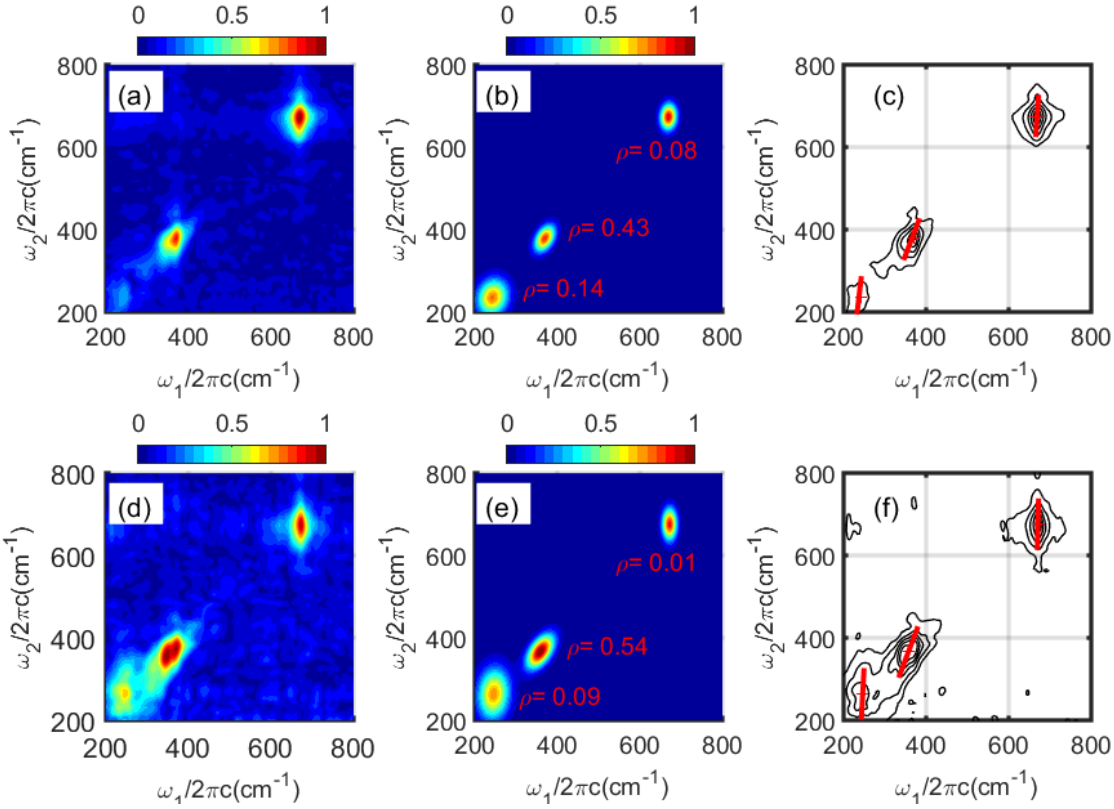


***Figure 4.10.*** *Line shapes of diagonal peaks are examined in lower-frequency regions of 2DRR spectra obtained for (a) metMb and (b) $MbO_2$. Peaks are fit to two-dimensional Gaussians with correlation parameters given in panels (c) and (d) (see Equation (4.2)). The parameter, $\rho$, ranges between the uncorrelated ($\rho$ =0) and fully correlated ($\rho$ =1) limits for diagonal peaks. A correlation parameter greater than 0 is a signature of inhomogeneous line broadening. In panels (e) and (f), a straight line consistent with each correlation parameter is overlaid on the experimental data. For both systems, the 370-$cm^{-1}$ methylene deformation mode local to the propionic acid side chains exhibits the greatest amount of heterogeneity.*

In Figure 4.10, all peaks are fit to two-dimensional Gaussian line shapes of the form given in Equation (4.2). This form of the 2D Gaussian function notably takes into account the

difference in frequency resolution associated with the two dimensions. The correlation parameter, $\rho$, generally ranges from the fully anti-correlated ($\rho$=-1) to fully correlated ($\rho$=+1) limits; however, $\rho$ should not be less than zero for diagonal peaks. The correlation parameters are equal to zero if the line broadening mechanisms are fully homogeneous. With inspiration from 2D infrared spectroscopy, lines obtained with a linear regression analysis are overlaid on various peaks in Figures 4.10c and 4.10f.

The iron-histidine stretching mode near 220-$cm^{-1}$ exhibits a small amount of heterogeneity; the correlation parameter is 0.14 in metMb and 0.09 in $MbO_2$. For both systems, the greatest amount of heterogeneity is associated with the 370-$cm^{-1}$ methylene deformation mode local to the propionic acid groups. The correlation parameter for this mode is 0.43 in metMb and 0.54 in $MbO_2$. We hypothesize that such heterogeneity originates in fluctuations of the "floppy" propionic acid side chains. That is, the 2DRR data suggest that rigidity of the macrocycle suppresses heterogeneity in higher frequency modes such as the in-plane deformation mode near 674 $cm^{-1}$.

**IVC. Computational Analysis of Line Broadening Mechanism**

In this section, computational models are used to explore the effects that motions of the propionic acid side chains have on the vibrational frequency of the 370-$cm^{-1}$ methylene deformation mode. In particular, we are interested in how the magnitudes of the fluctuations compare to characteristic frequencies in the spectral densities (i.e., spectra of vibrational frequency fluctuations), because such comparisons will provide insights into the line broadening mechanisms. It is relatively straightforward to model fluctuations in the geometries of the proteins with classical molecular dynamics (MD) simulations; however, the vibrational frequencies should be calculated at a higher level of theory. Here, we use *ab initio* maps to

parameterize the vibrational frequencies associated with side chain geometries extracted from MD simulations. Similar approaches have been used to interpret 2D infrared experiments conducted on proteins and pure liquids.[69-72]

Fluctuations in the geometries of the proteins are modeled with MD simulations based on the GROMACS96 force field[73-75] To prepare the systems, heavy atoms in the proteins were restrained and an energy minimization (steepest descent method) was implemented to relax the solvent around the protein. This was followed by two equilibration steps in the isothermal-isochoric and isothermal-isobaric ensembles for a total of 400 ps. Simulations were run for 1 ns with 2 fs steps. The *ab initio* maps are constructed by first optimizing the geometries of the isolated hemes at the B3LYP/6-311G(2d,3p) level.[76] The optimized dihedral angles associated with the propionic acid side chains are $\Phi_L$ =81.3° and $\Phi_R$ =81.1° for metMb and $\Phi_L$ =94.4° and $\Phi_R$ =109° for $MbO_2$ (see Figure 4.11). The *ab initio* maps are produced by varying the two dihedral angles (in steps of 5°) over the full ranges covered by the MD simulations while holding all other coordinates fixed at the values corresponding to the optimized geometries. In doing so, it is assumed that the frequency of the methylene deformation mode local to the propionic acid side chains is primarily affected by the "floppy" coordinates of the side chain. The vibrational modes are computed at each geometry, and the methylene deformation mode is identified by (i) large-amplitude motion of the methylene bonds near the propionic acid side chains and (ii) the scalar product with the normal mode calculated at the optimized geometry. The resulting maps of vibrational frequencies are presented in Figures 4.11b and 4.11e. With these maps, vibrational frequencies are readily generated at each step in the MD trajectory by extracting the two dihedral angles. Segments of the trajectories are presented in Figures 4.11c and 4.11f. Scatter plots of the

dihedral angles suggest that fluctuations in these coordinates are fairly evenly distributed about the equilibrium geometry (see Appendix 3).[77]

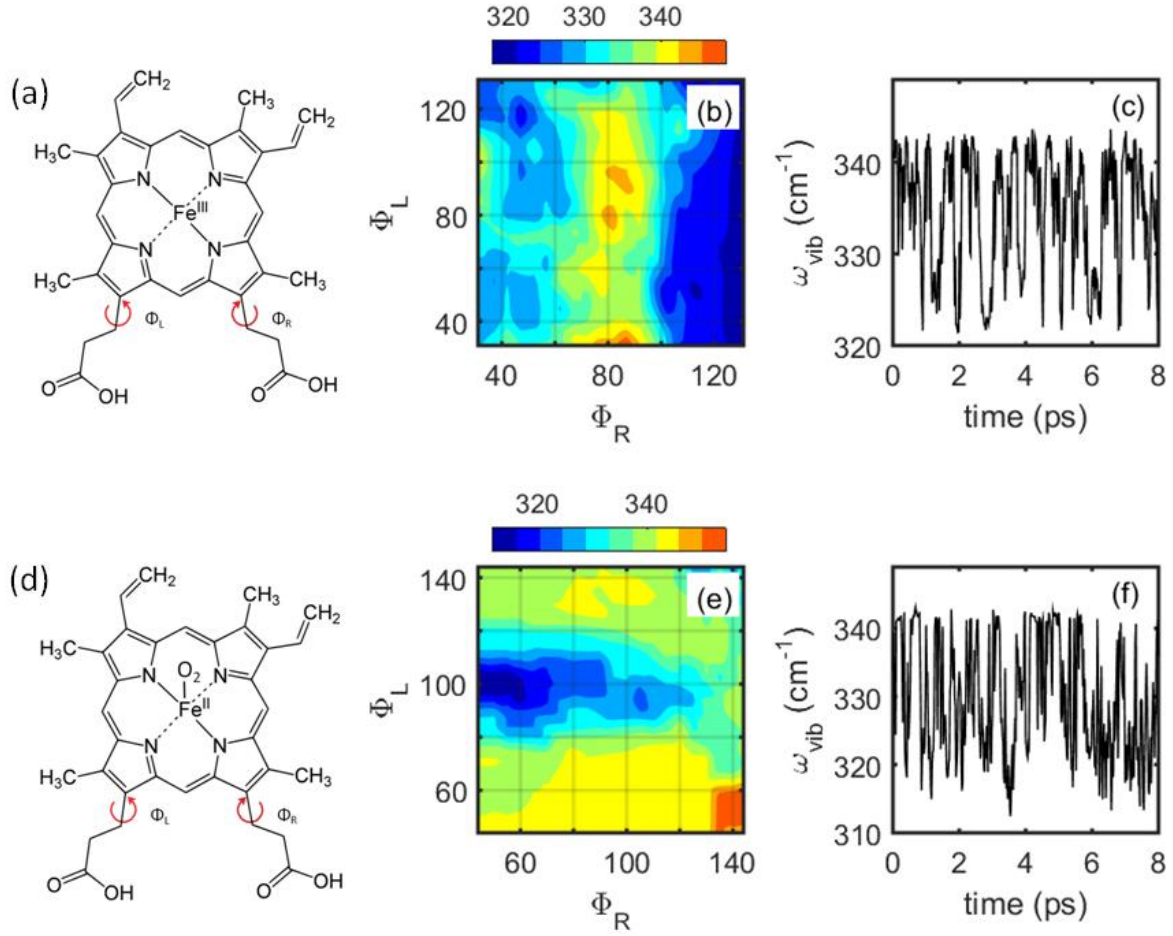


***Figure 4.11.*** *Dihedral angles associated with the propionic acid chains are defined for the heme in (a) metMb and (d) $MbO_2$. The vibrational frequency of the methylene deformation mode local to the propionic acid side chains is computed as a function of the two dihedral angles for (b) metMb and (e) $MbO_2$. These ab initio maps are used to parameterize the vibrational frequencies associated with molecular dynamics simulations. Segments of molecular dynamics trajectories for the vibrational frequencies are shown for (c) metMb and (f) $MbO_2$.*

MD trajectories of vibrational frequencies for metMb and $MbO_2$ yield standard deviations of 5.9 and 7.0 cm$^{-1}$, respectively. These standard deviations correspond to FWHM line widths of 13.9 and 16.5 cm$^{-1}$ under the assumption of Gaussian line shapes. These line widths are smaller than those found in the 2DRR measurements shown in Figure 4.9 because of finite spectral resolution.

In order to obtain further insight into the line broadening mechanism, time-correlation functions associated with the MD trajectories are Fourier transformed to produce the spectral densities shown in Figure 4.12.[78,79] The spectral densities show how the fluctuation amplitudes are distributed in the frequency domain. The simulations suggest that the fluctuations in the vibrational frequencies are dominated by thermal motion below 10 $cm^{-1}$; however, higher-frequency components with magnitudes up to 10% of the maximum value are found in both systems.

The line broadening mechanism can be interpreted by comparing the fluctuation amplitudes (5.9 $cm^{-1}$ in metMb and 7.0 $cm^{-1}$ in $MbO_2$) to the characteristic frequencies of thermal motion (i.e., dominant part of spectral density). In the homogeneous limit, the fluctuation amplitude must be small compared to the characteristic frequency, whereas the opposite applies in the inhomogeneous limit.[78] The spectral densities decay to roughly 50% of their maximum values at frequencies corresponding to the fluctuation amplitudes computed for metMb and $MbO_2$. Thus, the calculations suggest that the line broadening mechanisms of both systems reside between the homogeneous and inhomogeneous limits. The correlation parameters of 0.43 and 0.54 determined from experimental data for metMb and $MbO_2$ are also consistent with an intermediate line broadening regime (see Figure 4.10).

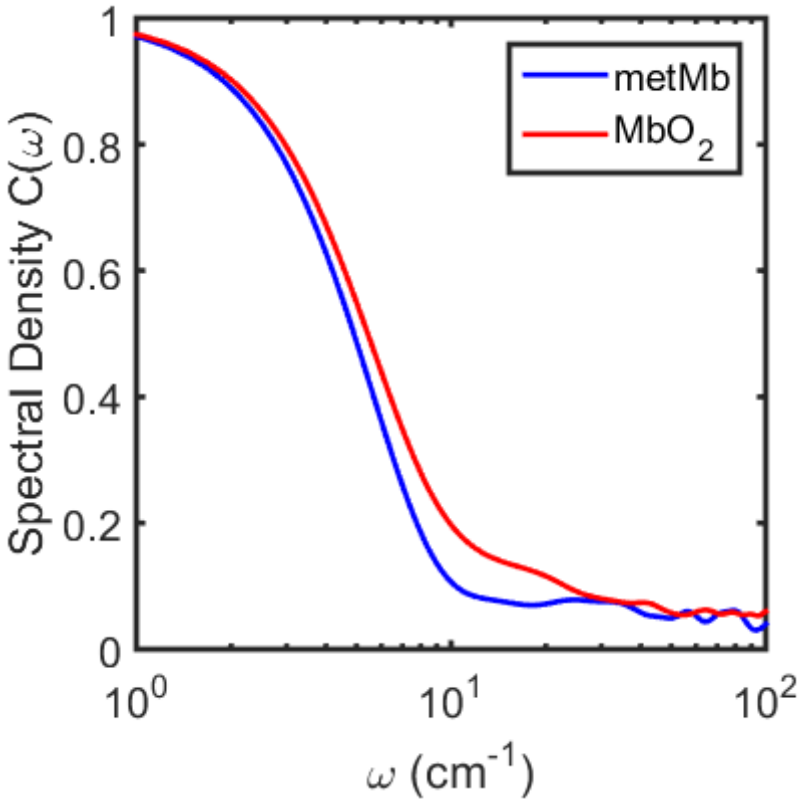


***Figure 4.12.*** *Spectral densities of the methylene deformation modes obtained from molecular dynamics simulations. The spectral densities decay to less than 50% of the maximum values at frequencies corresponding to the fluctuation amplitudes (5.9 and 7.0 $cm^{-1}$ for metMb and $MbO_2$). These calculations are consistent with an intermediate line broadening regime.*

**IVD. Implications for the Vibrational Cooling Mechanism**

The propionic acid groups are known to dominate vibrational energy exchange of the heme with its surrounding environment. Hochstrasser first proposed this mechanism in 1994, and MD simulations contributed further support several years later.[49-51] In 2006, the role of the propionic acid groups was finally confirmed by a direct experimental test in which vibrational cooling rates were compared for the native protein and a mutant.[52] These earlier works suggest that the propionic acid side chains are an effective gateway for vibrational energy transfer, because they hydrogen bond with the aqueous solvent. In contrast, the porphyrin macrocycle is enclosed in a hydrophobic pocket devoid of solvent. The surrounding protein matrix is less effective than the solvent in exchanging vibrational energy with the porphyrin despite close to 90

van der Waals contacts.[80] This behavior underscores the important role of hydrogen bonds in accelerating solute-to-solvent vibrational energy transfer.[81]

The experimental data and computational simulations presented in Figures 4.10-4.12 suggest that the 2DRR line shapes of the methylene deformation modes reflect heterogeneity in the geometries of the side chains. It is interesting to consider whether or not heterogeneity in the structure translates into heterogeneity in the vibrational cooling rate. This issue cannot be directly addressed with 2DRR spectroscopy. However, Berg and co-workers have shown that such information about incoherent dynamics can be derived from six-wave mixing experiments.[82,83] We are presently using a related pump-repump-probe approach to examine heterogeneity in the vibrational cooling rates of heme proteins.

## V. Supplemental Information

### VA. Components of Nonlinear Polarization

The fifth-order polarization possesses 16 components when a single electronic resonance dominates the optical response.[41] The 2DRR spectra in this work are calculated by Fourier transforming the polarization components presented in Reference [41] with respect to the delay time, $\tau_1$. The frequency dimension, $\omega_2$, is equal to the difference between the detection frequency, $\omega_t$, and the frequency of the narrowband Raman pump, $\omega_{RP}$. The summations below are restricted to eliminate population terms from the dimensions, $\omega_1$ and $\omega_2$. The 16 polarization components are

$$P_1^{(5)}(\omega_1,\omega_2) = -\frac{N\xi_{AP}^2\xi_{RP}^2\xi_{St}\left|\mu_{eg}\right|^6}{\mathrm{h}^5}\sum_{\substack{mnkluv \\ k\neq m,u\neq m}} B_m \langle n|m\rangle\langle n|k\rangle\langle l|k\rangle\langle l|u\rangle\langle v|u\rangle\langle v|m\rangle \times L_{en,gm}(\omega_{AP})D_{gk,gm}(\omega_1)L_{el,gm}(\omega_t)J_{gu,gm}(\omega_2)L_{ev,gm}(\omega_t), \quad (4.4)$$

$$P_2^{(5)}(\omega_1,\omega_2) = -\frac{N\xi_{AP}^2\xi_{RP}^2\xi_{St}\left|\mu_{eg}\right|^6}{\mathrm{h}^5}\sum_{\substack{mnkluv\\ k\neq m,u\neq k}} B_m\langle n|m\rangle\langle n|k\rangle\langle l|m\rangle\langle l|u\rangle\langle v|k\rangle\langle v|u\rangle, \tag{4.5}$$
$$\times L_{en,gm}(\omega_{AP})D_{gk,gm}(\omega_1)L_{gk,el}(-\omega_{RP})J_{gk,gu}(\omega_2)L_{ev,gu}(\omega_t)$$

$$P_3^{(5)}(\omega_1,\omega_2) = -\frac{N\xi_{AP}^2\xi_{RP}^2\xi_{St}\left|\mu_{eg}\right|^6}{\mathrm{h}^5}\sum_{\substack{mnkluv\\ k\neq m,u\neq m}} B_m\langle n|m\rangle\langle n|k\rangle\langle l|k\rangle\langle l|u\rangle\langle v|m\rangle\langle v|u\rangle, \tag{4.6}$$
$$\times L_{gm,en}(-\omega_{AP})D_{gm,gk}(\omega_1)L_{gm,el}(-\omega_{RP})J_{gm,gu}(\omega_2)L_{ev,gu}(\omega_t)$$

$$P_4^{(5)}(\omega_1,\omega_2) = -\frac{N\xi_{AP}^2\xi_{RP}^2\xi_{St}\left|\mu_{eg}\right|^6}{\mathrm{h}^5}\sum_{\substack{mnkluv\\ k\neq m,u\neq k}} B_m\langle n|m\rangle\langle n|k\rangle\langle l|m\rangle\langle l|u\rangle\langle v|u\rangle\langle v|k\rangle, \tag{4.7}$$
$$\times L_{gm,en}(-\omega_{AP})D_{gm,gk}(\omega_1)L_{el,gk}(\omega_t)J_{gu,gk}(\omega_2)L_{ev,gk}(\omega_t)$$

$$P_5^{(5)}(\omega_1,\omega_2) = -\frac{N\xi_{AP}^2\xi_{RP}^2\xi_{St}\left|\mu_{eg}\right|^6}{\mathrm{h}^5}\sum_{\substack{mnkluv\\ k\neq n,u\neq k}} B_m\langle n|m\rangle\langle k|m\rangle\langle n|l\rangle\langle u|l\rangle\langle k|v\rangle\langle u|v\rangle, \tag{4.8}$$
$$\times L_{en,gm}(\omega_{AP})D_{en,ek}(\omega_1)L_{gl,ek}(-\omega_{RP})J_{eu,ek}(\omega_2)L_{eu,gv}(\omega_t)$$

$$P_6^{(5)}(\omega_1,\omega_2) = -\frac{N\xi_{AP}^2\xi_{RP}^2\xi_{St}\left|\mu_{eg}\right|^6}{\mathrm{h}^5}\sum_{\substack{mnkluv\\ k\neq n,u\neq n}} B_m\langle n|m\rangle\langle k|m\rangle\langle k|l\rangle\langle u|l\rangle\langle u|v\rangle\langle n|v\rangle, \tag{4.9}$$
$$\times L_{en,gm}(\omega_{AP})D_{en,ek}(\omega_1)L_{en,gl}(\omega_t)J_{en,eu}(\omega_2)L_{en,gv}(\omega_t)$$

$$P_7^{(5)}(\omega_1,\omega_2) = -\frac{N\xi_{AP}^2\xi_{RP}^2\xi_{St}\left|\mu_{eg}\right|^6}{\mathrm{h}^5}\sum_{\substack{mnkluv\\ k\neq n,u\neq n}} B_m\langle n|m\rangle\langle k|m\rangle\langle k|l\rangle\langle u|l\rangle\langle n|v\rangle\langle u|v\rangle, \tag{4.10}$$
$$\times L_{gm,en}(-\omega_{AP})D_{ek,en}(\omega_1)L_{gl,en}(-\omega_{RP})J_{eu,en}(\omega_2)L_{eu,gv}(\omega_t)$$

$$P_8^{(5)}(\omega_1,\omega_2) = -\frac{N\xi_{AP}^2\xi_{RP}^2\xi_{St}\left|\mu_{eg}\right|^6}{\mathrm{h}^5}\sum_{\substack{mnkluv\\ k\neq n,u\neq k}} B_m\langle n|m\rangle\langle k|m\rangle\langle n|l\rangle\langle u|l\rangle\langle u|v\rangle\langle k|v\rangle, \tag{4.11}$$
$$\times L_{gm,en}(-\omega_{AP})D_{ek,en}(\omega_1)L_{ek,gl}(\omega_t)J_{ek,eu}(\omega_2)L_{ek,gv}(\omega_t)$$

$$P_9^{(5)}(\omega_1,\omega_2) = -\frac{N\xi_{AP}^2\xi_{RP}^2\xi_{St}\left|\mu_{eg}\right|^6}{\mathrm{h}^5}\sum_{\substack{mnkluv\\ k\neq m,u\neq l}} B_m \langle n|m\rangle\langle n|k\rangle\langle l|k\rangle\langle u|m\rangle\langle u|v\rangle\langle l|v\rangle, \quad (4.12)$$
$$\times L_{en,gm}(\omega_{AP}) D_{gk,gm}(\omega_1) L_{el,gm}(\omega_t) J_{el,eu}(\omega_2) L_{el,gv}(\omega_t)$$

$$P_{10}^{(5)}(\omega_1,\omega_2) = -\frac{N\xi_{AP}^2\xi_{RP}^2\xi_{St}\left|\mu_{eg}\right|^6}{\mathrm{h}^5}\sum_{\substack{mnkluv\\ k\neq m,u\neq l}} B_m \langle n|m\rangle\langle n|k\rangle\langle l|m\rangle\langle u|k\rangle\langle l|v\rangle\langle u|v\rangle, \quad (4.13)$$
$$\times L_{en,gm}(\omega_{AP}) D_{gk,gm}(\omega_1) L_{gk,el}(-\omega_{RP}) J_{eu,el}(\omega_2) L_{eu,gv}(\omega_t)$$

$$P_{11}^{(5)}(\omega_1,\omega_2) = -\frac{N\xi_{AP}^2\xi_{RP}^2\xi_{St}\left|\mu_{eg}\right|^6}{\mathrm{h}^5}\sum_{\substack{mnkluv\\ k\neq m,u\neq l}} B_m \langle n|m\rangle\langle n|k\rangle\langle l|m\rangle\langle u|k\rangle\langle u|v\rangle\langle l|v\rangle, \quad (4.14)$$
$$\times L_{gm,en}(-\omega_{AP}) D_{gm,gk}(\omega_1) L_{el,gk}(\omega_t) J_{el,eu}(\omega_2) L_{el,gv}(\omega_t)$$

$$P_{12}^{(5)}(\omega_1,\omega_2) = -\frac{N\xi_{AP}^2\xi_{RP}^2\xi_{St}\left|\mu_{eg}\right|^6}{\mathrm{h}^5}\sum_{\substack{mnkluv\\ k\neq m,u\neq l}} B_m \langle n|m\rangle\langle n|k\rangle\langle l|k\rangle\langle u|m\rangle\langle l|v\rangle\langle u|v\rangle, \quad (4.15)$$
$$\times L_{gm,en}(-\omega_{AP}) D_{gm,gk}(\omega_1) L_{gm,el}(-\omega_{RP}) J_{eu,el}(\omega_2) L_{eu,gv}(\omega_t)$$

$$P_{13}^{(5)}(\omega_1,\omega_2) = -\frac{N\xi_{AP}^2\xi_{RP}^2\xi_{St}\left|\mu_{eg}\right|^6}{\mathrm{h}^5}\sum_{\substack{mnkluv\\ k\neq n,u\neq l}} B_m \langle n|m\rangle\langle k|m\rangle\langle n|l\rangle\langle k|u\rangle\langle v|l\rangle\langle v|u\rangle, \quad (4.16)$$
$$\times L_{en,gm}(\omega_{AP}) D_{en,ek}(\omega_1) L_{gl,ek}(-\omega_{RP}) J_{gl,gu}(\omega_2) L_{ev,gu}(\omega_t)$$

$$P_{14}^{(5)}(\omega_1,\omega_2) = -\frac{N\xi_{AP}^2\xi_{RP}^2\xi_{St}\left|\mu_{eg}\right|^6}{\mathrm{h}^5}\sum_{\substack{mnkluv\\ k\neq n,u\neq l}} B_m \langle n|m\rangle\langle k|m\rangle\langle k|l\rangle\langle n|u\rangle\langle v|u\rangle\langle v|l\rangle, \quad (4.17)$$
$$\times L_{en,gm}(\omega_{AP}) D_{en,ek}(\omega_1) L_{en,gl}(\omega_t) J_{gu,gl}(\omega_2) L_{ev,gl}(\omega_t)$$

$$P_{15}^{(5)}(\omega_1,\omega_2) = -\frac{N\xi_{AP}^2\xi_{RP}^2\xi_{St}\left|\mu_{eg}\right|^6}{\mathrm{h}^5}\sum_{\substack{mnkluv\\ k\neq n,u\neq l}} B_m \langle n|m\rangle\langle k|m\rangle\langle k|l\rangle\langle n|u\rangle\langle v|l\rangle\langle v|u\rangle, \quad (4.18)$$
$$\times L_{gm,en}(-\omega_{AP}) D_{ek,en}(\omega_1) L_{gl,en}(-\omega_{RP}) J_{gl,gu}(\omega_2) L_{ev,gu}(\omega_t)$$

$$P_{16}^{(5)}(\omega_1,\omega_2) = -\frac{N\xi_{AP}^2\xi_{RP}^2\xi_{St}\left|\mu_{eg}\right|^6}{\mathrm{h}^5}\sum_{\substack{mnkluv\\ k\neq n,u\neq l}} B_m \langle n|m\rangle\langle k|m\rangle\langle n|l\rangle\langle k|u\rangle\langle v|u\rangle\langle v|l\rangle \cdot \tag{4.19}$$
$$\times L_{gm,en}(-\omega_{AP}) D_{ek,en}(\omega_1) L_{ek,gl}(\omega_t) J_{gu,gl}(\omega_2) L_{ev,gl}(\omega_t)$$

The electronic line shape function, $L_{en,gm}(\omega)$, is written as

$$L_{en,gm}(\omega) = \frac{1}{\omega - \omega_{eg} - \omega_{nm} + i\Gamma_{eg}} . \tag{4.20}$$

The vibrational line shape functions, $D_{gk,gm}(\omega_1)$ and $J_{gu,gm}(\omega_2)$, are given by

$$D_{gk,gm}(\omega_1) = \frac{2\Lambda_{AP}}{\omega_{km}^2 + \Lambda_{AP}^2}\cdot\frac{1}{(\omega_1 - \omega_{km}) + i\Gamma_{vib}} \tag{4.21}$$

and

$$J_{gu,gm}(\omega_2) = \frac{\exp[i\omega\tau_2 - \Lambda_{RP}\tau_2]}{(\omega_2 - \omega_{um}) + i(\Gamma_{vib} - \Lambda_{RP})} . \tag{4.22}$$

The fifth-order 2DRR signal field is expressed in terms of these polarization components as

$$E_{2DRR}^{(5)}(\omega_1,\omega_2) = \frac{1}{7}\left(\frac{i\omega_t l}{2\varepsilon_0 n(\omega_t) c}\right)\sum_{j=1}^{16} P_j^{(5)}(\omega_1,\omega_2) , \tag{4.23}$$

where perfect phase-matching has been assumed and the factor of 1/7 represents the orientational average for all-parallel electric field polarizations.[84]

**VB. Anharmonic Vibrational Hamiltonian**

All calculations conducted in this work are based on the following vibrational Hamiltonian,[85]

$$H = \sum_j \left[ \frac{\mathrm{h}\omega_j}{2}\left(2a_j^\dagger a_j + 1\right) + U_{jjj}\left(3a_j^\dagger + 3a_j\right)\right] + \sum_{jkl} U_{jkl}\left(a_j^\dagger a_k^\dagger a_l^\dagger + 3a_j^\dagger a_k^\dagger a_l + 3a_j^\dagger a_k a_l + a_j a_k a_l\right), \quad (4.24)$$

where the cubic expansion coefficients are given by

$$U_{jkl} = \frac{1}{3!\sqrt{2^3 m^3 \omega^3 \mathrm{h}^{-3}}}\left(\frac{\partial^3 V}{\partial q_j \partial q_k \partial q_l}\right)_0 . \quad (4.25)$$

The basis set is taken to be uncoupled at second-order for this Hamiltonian. Therefore, normal modes are recovered if the cubic expansion coefficients are set equal to zero. This is the most natural basis set for the present study, because the calculations in section III make use of fitting parameters obtained in a basis of normal modes.[67] Vibrational wavefunctions are obtained by diagonalizing the Hamiltonian in a basis of harmonic oscillators (up to 20 vibrational quanta in each mode results in good convergence).

The vibrational overlap integrals needed to evaluate the response functions are written as

$$\langle n | m \rangle = \sum_{\alpha\beta} \varphi_{n\alpha} \varphi_{m\beta} \langle \alpha | \beta \rangle , \quad (4.26)$$

where $\varphi_{n\alpha}$ is the expansion coefficient for harmonic basis function $\alpha$ and the anharmonic vibrational wavefunction, $n$.

**VI. Concluding Remarks**

In summary, we have conducted quasi-degenerate (one-color) 2DRR spectroscopy experiments on oxygen- and water-ligated myoglobin. The experimental technique developed in Reference [41] has been leveraged to produce a 2D resonance Raman spectra. For both systems, we find that the greatest amount of heterogeneity is associated with the methylene deformation

mode local to the propionic acid side chains. The computational model presented in section IVC yields distributions with standard deviations of 5.9 and 7.0 $cm^{-1}$ for metMb and $MbO_2$, respectively. It is interesting to consider whether or not the vibrational cooling rate of the heme varies as a consequence of heterogeneity in the propionic acid groups. This issue will be addressed in future work using pump-repump-probe spectroscopy.

The calculations in section III suggest that two key points that must be considered when interpreting 2DRR signals. First, 2DRR experiments do not necessarily yield information about anharmonic mode couplings, because the signal is allowed for harmonic systems. The absence of a signal for harmonic systems is one of the primary motivations for conducting electronically off-resonant 2D Raman experiments.[19,27,28,55,56] Thus, a tradeoff between information content and susceptibility to experimental artifacts is made when 2D Raman experiments are conducted under electronically resonant conditions. A two-color implementation of 2DRR spectroscopy may expand the range of scientific questions that can be addressed, but does not change this essential aspect of the signal generation mechanism.[54] Second, 2DRR experiments can be used to characterize vibrational line broadening mechanisms in a straightforward way. As in 2D infrared experiments, inhomogeneous line broadening is made clear by inspection of the 2DRR signal. Notably, the line broadening mechanism cannot be directly determined from traditional (third-order) coherent Raman or spontaneous Raman spectroscopies.[18]

## REFERENCES


1. M. C. Asplund, M. T. Zanni, and R. M. Hochstrasser, Proc. Natl. Acad. Sci. **97**, 8219-8224 (2000).

2. O. Golonzka, M. Khalil, N. Demirdöven, and A. Tokmakoff, Phys. Rev. Lett. **86**, 2154-2157 (2000).

3. D. M. Jonas, Annu. Rev. Phys. Chem. **54**, 425-463 (2003).

4. T. Brixner, T. Mancal, I. V. Stiopkin, and G. R. Fleming, J. Chem. Phys. **121**, 4221-4236 (2004).

5. M. L. Cowan, J. P. Ogilvie, and R. J. D. Miller, Chem. Phys. Lett. **386**, 184-189 (2004).

6. J. P. Ogilvie and K. J. Kubarych, Adv. At. Mol. Opt. Phys. **57**, 249-321 (2009).

7. A. V. Pakoulev, S. B. Block, L. A. Yurs, N. A. Mathew, K. M. Kornau, and J. C. Wright, J. Phys. Chem. Lett. **1**, 822-828 (2010).

8. P. Hamm and M. T. Zanni, *Concepts and Methods of 2D Infrared Spectroscopy*. (Cambridge University Press, Cambridge, 2011).

9. J. C. Wright, Annu. Rev. Phys. Chem. **62**, 209-230 (2011).

10. K. M. Slenkamp, M. S. Lynch, B. E. Van Kuiken, J. F. Brookes, C. C. Bannan, S. L. Daifuku, and M. Khalil, J. Chem. Phys. **140**, 084505 (2014).

11. A. Laubereau and W. Kaiser, Rev. Mod. Phys. **50**, 607-665 (1978).

12. B. H. Hesp and D. A. Wiersma, Chem. Phys. Lett. **75**, 423-426 (1980).

13. S. Velsko, J. Trout, and R. M. Hochstrasser, J. Chem. Phys. **79**, 2114-2120 (1983).

14. C. L. Schosser and D. D. Dlott, J. Chem. Phys. **80**, 1394-1406 (1984).

15. A. Laubereau, G. Wochner, and W. Kaiser, Phys. Rev. A **13**, 2212-2225 (1976).

16. D. W. Oxtoby, J. Chem. Phys. **74**, 5371- (1981).

17. S. M. George, A. L. Harris, M. Berg, and C. B. Harris, J. Chem. Phys. **80**, 83-94 (1984).

18. R. F. Loring and S. Mukamel, J. Chem. Phys. **83**, 2116-2126 (1985).

19. Y. Tanimura and S. Mukamel, J. Chem. Phys. **99**, 9496-9511 (1993).

20. T. I. C. Jansen, J. G. Snijders, and K. Duppen, J. Chem. Phys. **114**, 109210-110921 (2001).

21. M. Berg and D. A. Vanden Bout, Acc. Chem. Res. **30**, 65-71 (1997).

22. J. E. Ivanecky III and J. C. Wright, Chem. Phys. Lett. **206**, 437-444 (1993).

23. K. Tominaga and K. Yoshihara, J. Chem. Phys. **104**, 4419-4426 (1996).

24. T. Steffen and K. Duppen, J. Chem. Phys. **106**, 3854-3864 (1997).

25. A. Tokmakoff, M. J. Lang, D. S. Larsen, G. R. Fleming, V. Chernyak, and S. Mukamel, Phys. Rev. Lett. **79**, 2702-2705 (1997).

26. D. A. Blank, L. J. Kaufman, and G. R. Fleming, J. Chem. Phys. **111**, 3105-3114 (1999).

27. K. J. Kubarych, C. J. Milne, S. Lin, V. Astinov, and R. J. D. Miller, J. Chem. Phys. **116**, 2016-2042 (2002).

28. L. J. Kaufman, J. Heo, L. D. Ziegler, and G. R. Fleming, Phys. Rev. Lett. **88**, 207402:207401-207404 (2002).

29. S. Fujiyoshi, S. Takeuchi, and T. Tahara, J. Phys. Chem. A **107**, 494-500 (2003).

30. D. W. McCamant, P. Kukura, S. Yoon, and R. A. Mathies, Rev. Sci. Instrum. **75**, 4971-4980 (2004).

31. D. F. Underwood and D. A. Blank, J. Phys. Chem. A **109**, 3295-3306 (2005).

32. P. Kukura, D. W. McCamant, and R. A. Mathies, Annu. Rev. Phys. Chem. **58**, 461-488 (2007).

33. A. M. Moran, R. A. Nome, and N. F. Scherer, J. Chem. Phys. **127**, 184505:184501-184513 (2007).

34. M. S. Marek, T. Buckup, and M. Motzkus, J. Phys. Chem. B **115**, 8328-8337 (2011).

35. J. P. Kraack, A. Wand, T. Buckup, M. Motzkus, and S. Ruhman, Phys. Chem. Chem. Phys. **15**, 14487-14501 (2013).

36. A. Weigel, A. Dobryakov, B. Klaumünzer, M. Sajadi, P. Saalfrank, and N. P. Ernsting, J. Phys. Chem. B **115**, 3656-3680 (2011).

37. W. Yu, J. Zhou, and A. E. Bragg, J. Phys. Chem. Lett. **3**, 1321-1328 (2012).

38. S. Park, J. Kim, and N. F. Scherer, Phys. Chem. Chem. Phys. **14**, 8116-8122 (2012).

39. E. M. Grumstrup, Z. Chen, R. P. Vary, A. M. Moran, K. S. Schanze, and J. P. Papanikolas, J. Phys. Chem. B **117**, 8245-8255 (2013).

40. W. R. Silva and R. R. Frontiera, Phys. Chem. Chem. Phys., DOI: 10.1039/C1035CP06195D (2016).

41. B. M. Molesky, Z. Guo, and A. M. Moran, J. Chem. Phys. **142**, 212405 (2015).

42. J. W. Petrich, C. Poyart, and J.-L. Martin, Biochemistry **27**, 4049-4060 (1988).

43. S. Franzen, L. Kiger, C. Poyart, and J.-L. Martin, Biophys. J. **80**, 2372-2385 (2001).

44. X. Ye, A. Demidov, F. Rosca, W. Wang, A. Kumar, D. Ionascu, L. Zhu, D. Barrick, D. Wharton, and P. M. Champion, J. Phys. Chem. A **107**, 8156-8165 (2003).

45. J.-L. Martin and M. H. Vos, Annu. Rev. Biophys. Biomol. Struct. **21**, 199-222 (2006).

46. M. H. Vos, Biochim. Biophys. Acta **1777**, 15-31 (2008).

47. C. Consani, G. Auböck, O. Bräm, F. van Mourik, and M. Chergui, J. Chem. Phys. **140**, 025103 (2014).

48. P. M. Champion, F. Rosca, D. Ionascu, W. Cao, and X. Ye, Faraday. Discuss. **127**, 123-135 (2004).

49. T. Tian, B. Locke, Y. Kholodenko, and R. M. Hochstrasser, J. Phys. Chem. **98**, 11648-11656 (1994).

50. D. E. Sagnella and J. E. Straub, J. Phys. Chem. B **105**, 7057-7063 (2001).

51. L. Bu and J. E. Straub, J. Phys. Chem. B **107**, 10634-10639 (2003).

52. Y. Gao, M. Koyama, S. El-Mashtoly, T. Hayashi, K. Harada, Y. Mizutani, and T. Kitagawa, Chem. Phys. Lett. **429**, 239-243 (2006).

53. B. P. Molesky, P. G. Giokas, Z. Guo, and A. M. Moran, J. Chem. Phys. **114**, 114202 (2014).

54. Z. Guo, B. M. Molesky, T. P. Cheshire, and A. M. Moran, J. Chem. Phys. **143**, 124202 (2015).

55. K. C. Wilson, B. Lyons, R. Mehlenbacher, R. Sabatini, and D. W. McCamant, J. Chem. Phys. **131**, 214502 (2009).

56. R. Mehlenbacher, B. Lyons, K. C. Wilson, Y. Du, and D. W. McCamant, J. Chem. Phys. **131**, 244512 (2009).

57. X. Ye, A. Demidov, and P. M. Champion, J. Am. Chem. Soc. **124**, 5914-5924 (2002).

58. D. Morikis, J. T. Sage, A. K. Rizos, and P. M. Champion, J. Am. Chem. Soc. **110**, 6341-6342 (1988).

59. S. Hu, K. M. Smith, and T. G. Spiro, J. Am. Chem. Soc. **118**, 12638-12646 (1996).

60. M. J. Tauber, R. A. Mathies, X. Chen, and S. E. Bradforth, Rev. Sci. Instrum. **74**, 4958-4960 (2003).

61. M. Cho, Chem. Rev. **108**, 1331-1418 (2008).

62. M. D. Fayer, Annu. Rev. Phys. Chem. **60**, 21-38 (2009).

63. N. Demirdöven, M. Khalil, O. Golonzka, and A. Tokmakoff, J. Phys. Chem. A **105**, 8025-8030 (2001).

64. R. Venkatramani and S. Mukamel, J. Chem. Phys. **117**, 11089-11101 (2002).

65. D. T. Valley, D. P. Hoffman, and R. A. Mathies, Phys. Chem. Chem. Phys. **17**, 9231-9240 (2015).

66. Y. Wang, W. Liu, L. Tang, B. Oscar, F. Han, and C. Fang, J. Phys. Chem. A **117**, 6024-6042 (2013).

67. O. Bangcharoenpaurpong, K. T. Schomacker, and P. M. Champion, J. Am. Chem. Soc. **106**, 5688-5698 (1984).

68. A. T. N. Kumar, L. Zhu, J. F. Christian, A. Demidov, and P. M. Champion, J. Phys. Chem. B **105**, 7847-7856 (2001).

69. S. A. Corcelli, C. P. Lawrence, and J. L. Skinner, J. Chem. Phys. **120**, 8107-8117 (2004).

70. T. Hayashi, T. I. C. Jansen, W. Zhuang, and S. Mukamel, J. Phys. Chem. A **109**, 64-82 (2005).

71. T. I. C. Jansen and J. Knoester, J. Chem. Phys. **124**, 044502 (2006).

72. J. Wang, W. Zhuang, S. Mukamel, and R. M. Hochstrasser, J. Phys. Chem. B **112**, 5930-5937 (2008).

73. D. van der Spoel, E. Lindahl, B. Hess, G. Groenhof, A. E. Mark, and H. J. C. Berendsen, J. Comp. Chem. **26**, 1701-1718 (2005).

74. S. Pronk, S. Pall, R. Schulz, P. Larsson, P. Bjelkmar, R. Apostolov, M. R. Shirts, J. C. Smith, P. M. Kasson, D. van der Spoel, B. Hess, and E. Lindahl, Bioinformatics **29**, 845-854 (2013).

75. K. Vanommeslaeghe, E. Hatcher, C. Acharya, S. Kundu, S. Zhong, J. Shim, E. Darian, O. Guvench, P. Lopes, I. Vorobyov, and A. D. MacKerell, J. Comp. Chem. **31**, 671-690 (2010).

76 M. J. Frisch, G. W. Trucks, H. B. Schlegel, G. E. Scuseria, M. A. Robb, J. R. Cheeseman, G. Scalmani, V. Barone, B. Mennucci, G. A. Petersson, H. Nakatsuji, M. Caricato, X. Li, H. P. Hratchian, A. F. Izmaylov, J. Bloino, G. Zheng, J. L. Sonnenberg, M. Hada, M. Ehara, K. Toyota, R. Fukuda, J. Hasegawa, M. Ishida, T. Nakajima, Y. Honda, O. Kitao, H. Nakai, T. Vreven, J. A. Montgomery, Jr., J. E. Peralta, F. Ogliaro, M. Bearpark, J. J. Heyd, E. Brothers, K. N. Kudin, V. N. Staroverov, R. Kobayashi, J. Normand, K. Raghavachari, A. Rendell, J. C. Burant, S. S. Iyengar, J. Tomasi, M. Cossi, N. Rega, J. M. Millam, M. Klene, J. E. Knox, J. B. Cross, V. Bakken, C. Adamo, J. Jaramillo, R. Gomperts, R. E. Stratmann, O. Yazyev, A. J. Austin, R. Cammi, C. Pomelli, J. W. Ochterski, R. L. Martin, K. Morokuma, V. G. Zakrzewski, G. A. Voth, P. Salvador, J. J. Dannenberg, S. Dapprich, A. D. Daniels, Ö. Farkas, J. B. Foresman, J. V. Ortiz, J. Cioslowski, and D. J. Fox, Gaussian 09 (Wallingford,CT, 2009).

77 AIP, See Supplementary Material Document No._____ for further discussion of signatures of anharmonicity in 2DRR spectra and additional output of the molecular dynamics simulations. .

78 S. Mukamel, *Principles of Nonlinear Optical Spectroscopy*. (Oxford University Press, New York, 1995).

79 A. Nitzan, *Chemical Dynamics in Condensed Phases*. (Oxford University Press, Oxford, 2006).

80 R. J. D. Miller, Annu. Rev. Phys. Chem. **42**, 581-614 (1991).

81 C. T. Middleton, B. Cohen, and B. Kohler, J. Phys. Chem. A **111**, 10460-10467 (2007).

82 E. van Veldhoven, C. Khurmi, X. Zhang, and M. A. Berg, ChemPhysChem **8**, 1761-1765 (2007).

83 C. Khurmi and M. A. Berg, J. Chem. Phys. **129**, 064504 (2008).

84 F. Ding, E. C. Fulmer, and M. T. Zanni, J. Chem. Phys. **123**, 094502 (2005).

85 A. M. Moran, J. Dreyer, and S. Mukamel, J. Chem. Phys. **118**, 1347-1355 (2003).

# CHAPTER 5: CONTRIBUTIONS OF CASCADED NONLINEARITIES TO MULTI-DIMENSIONAL RESONANCE RAMAN SPECTROSCOPIES

## I. Introduction

Spectroscopists began to consider whether or not a one-dimensional coherent Raman experiment (i.e., four-wave mixing) could be used to distinguish between line broadening mechanisms in the late 1970's. [1-4] Loring and Mukamel settled this question in 1985 by showing that higher-order methods are necessary to differentiate homogeneous and inhomogeneous broadening.[5-6] They proposed an analogue of the spin-echo technique referred to as a Raman echo experiment (i.e., eight-wave mixing).[7] The Raman echo experiment was very difficult to implement and success was achieved by a small number of researchers. Tanimura and Mukamel achieved a breakthrough in 1993 by showing that six-wave mixing techniques may also be used to reveal line broadening mechanisms and anharmonicities in pure liquids.[6] Many experimental groups accepted the challenge of implementing the six-wave mixing approach; however, major technical challenges were encountered.[8-12] Success in conducing the six-wave mixing experiment was achieved by Fleming and Miller after almost 10 years of exhaustive efforts.[12-13]

The difficulty associated with 2D Raman experiments is related to the "order" of the nonlinearity (i.e., number of field-matter interactions).[14] Fifth-order spectroscopies involve five field-matter interactions with the incident laser pulses (see Figure 5.1a). Inherent to such high-order nonlinearities are small signal strengths and the possibility of artifacts known as lower-order signal cascades.[11, 15] As shown in Figures 5.1b and 5.1c, a cascade is a process in which the four-wave mixing signal radiated by one molecule induces a four-wave mixing response in a second molecule. The molecules can be either solute, solvent, or one of each as indicated in

Figure 5.1. Cascades are insidious because they are radiated in the same direction as the desired signal field and may possess comparable intensity. In addition, the cascades generally possess many of the same spectroscopic features as the desired response, which makes them difficult to identify experimentally.

For over two decades, third-order cascades have been known as a potential artifact in electronically off-resonant 2D Raman experiments.[8, 11-12, 15-17] For electronically off-resonant conditions, the key issue is that the cascades are allowed for harmonic systems whereas the desired fifth-order signal is not. In 2002, the off-resonant 2D Raman spectrum of $CS_2$ was successful measured by suppressing the third-order cascades through clever experimental geometries and detection schemes.[12-13] Our group first investigated the susceptibility of electronically resonant 2D Raman spectroscopies to cascades 2014.[18] We showed that the selection rules that plague off-resonant 2D Raman experiments are obviated under electronically resonant conditions. Electronically resonant 2D Raman signals are allowed for all Franck-Condon active modes whether they are harmonic or not. The desired response and cascades therefore compete on the same footing under electronically resonant conditions; the desired response will generally outcompete cascades because it requires fewer field-matter interactions (i.e., it is lower-order in this respect). More recently, Harel and co-workers showed that cascades can be negligible in a related fifth-order experiment.[19]

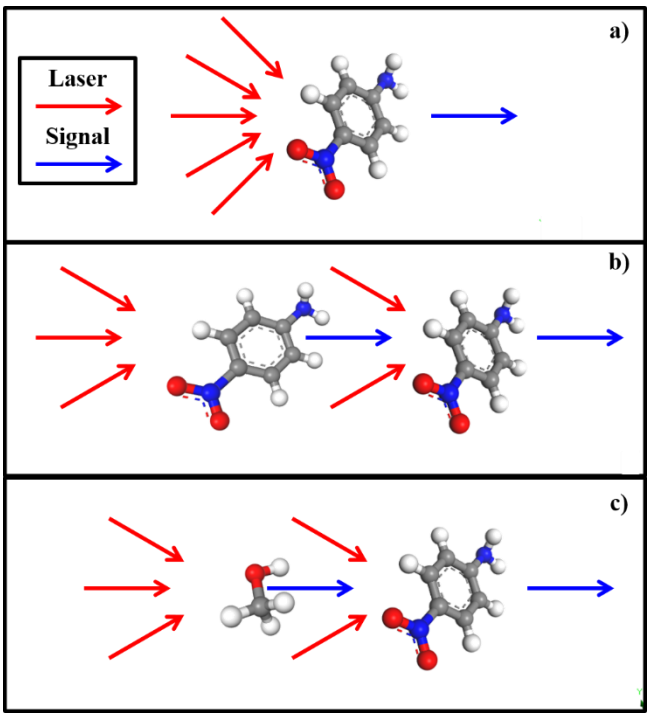


***Figure 5.1.*** *a) Six-wave mixing process for p-nitroaniline. Cascade of four-wave mixing responses between b) two p-nitroaniline molecules and c) methanol and p-nitroaniline.*

Under electronically resonant conditions, a small number of systems have been shown to be less susceptible to such undesirable signal contaminants; however, our group has shown that without well-considered precautions (e.g. sample concentration, beam geometry) cascades can readily exceed 20% of the measured signal. Although it is less susceptible to artifacts than off-resonant 2D Raman spectroscopy, a generalized study of the susceptibility of electronically resonant 2D Raman to cascading signals that treats both the solute and solvent has not been conducted (see Figures 5.1b and 5.1c). Electronic resonance enhancement will generally boost signal intensity by approximately 4-6 orders of magnitude; however, this does not mean that the solvent response can be taken as negligible because the solvent concentration is typically 5 orders of magnitude larger than that of the solute. Therefore, the two contributions to the signal strength are often offset, thereby allowing the solvent response to match or exceed that of the solute.

In this chapter, we simulate contributions of different classes of cascades in higher-order resonance Raman spectroscopies. Cascades that involve solute and solvent molecules are considered in addition to cascades that involve only the solute. To our knowledge, such solvent-solute cascades have not been addressed in any previous work. Fourier transform 2D resonance Raman experiments are considered because this technique is typically thought to be most susceptible to cascaded nonlinearities. Our work shows that this assumption should be questioned under electronically resonant conditions due to the irrelevance of the selection rules that promote cascades for pure liquids (i.e., off-resonance). For this reason, we also simulate signal cascades for the FSRS technique to gauge the importance of whether or not vibrational coherences evolve in one or two dimensions.

## II. Model Calculations

The direct fifth-order signal for a molecule with two electronic states has 16 terms in the fifth-order polarization. These terms were derived in the snapshot limit[14] for both the FSRS and 2DRR experiments in previous work.[20-24] We will review the classes of terms in the following subsections.

### IIA. Hamiltonians for Solute and Solvent

The Hamiltonian for the solute can be approximated to have two electronic states when the experimental conditions are electronically resonant. In Equation 5.1, $g$ and $e$ are the ground and excited electronic states of the solute, respectively, with energies $E_g$ and $E_e$. Vibrational modes and the corresponding energies are identified by the dummy indices $m$ and $n$ for the ground and excited electronic states, respectively. The solute will have the set of indices $\{m,k,u\}$ and $\{n,l,v\}$ associated with the ground and excited electronic states throughout this chapter. In this notation, the system Hamiltonian of the solute is written as

$$H_{Solute} = |g\rangle\langle g|\sum_m |m\rangle\langle m|\left(E_g + E_m\right) + |e\rangle\langle e|\sum_n |n\rangle\langle n|\left(E_e + E_n\right) \tag{5.1}$$

The Hamiltonian for the solvent must incorporate a large number of electronic states if field-matter interactions will be off-resonant. In Equation 5.2, the index $g$ represents the ground electronic state of the solvent with energy $E_g$. The excited electronic states of the solvent possess the energy $E_e$ and are denoted by the dummy index $e$. Vibrational modes and the corresponding energies are identified by the dummy indices $m$ and $n$ for the ground and excited electronic states, respectively. For the solvent the set of indices $\{m,k,u\}$ and $\{n,l,v\}$ will be associated with the ground and excited electronic states throughout this chapter.

$$H_{Solvent} = |g\rangle\langle g|\sum_m |m\rangle\langle m|\left(E_g + E_m\right) + \sum_e |e\rangle\langle e|\sum_n |n\rangle\langle n|\left(E_e + E_n\right) \tag{5.2}$$

**IIB. Response Function for FSRS and 2DRR Spectroscopies**

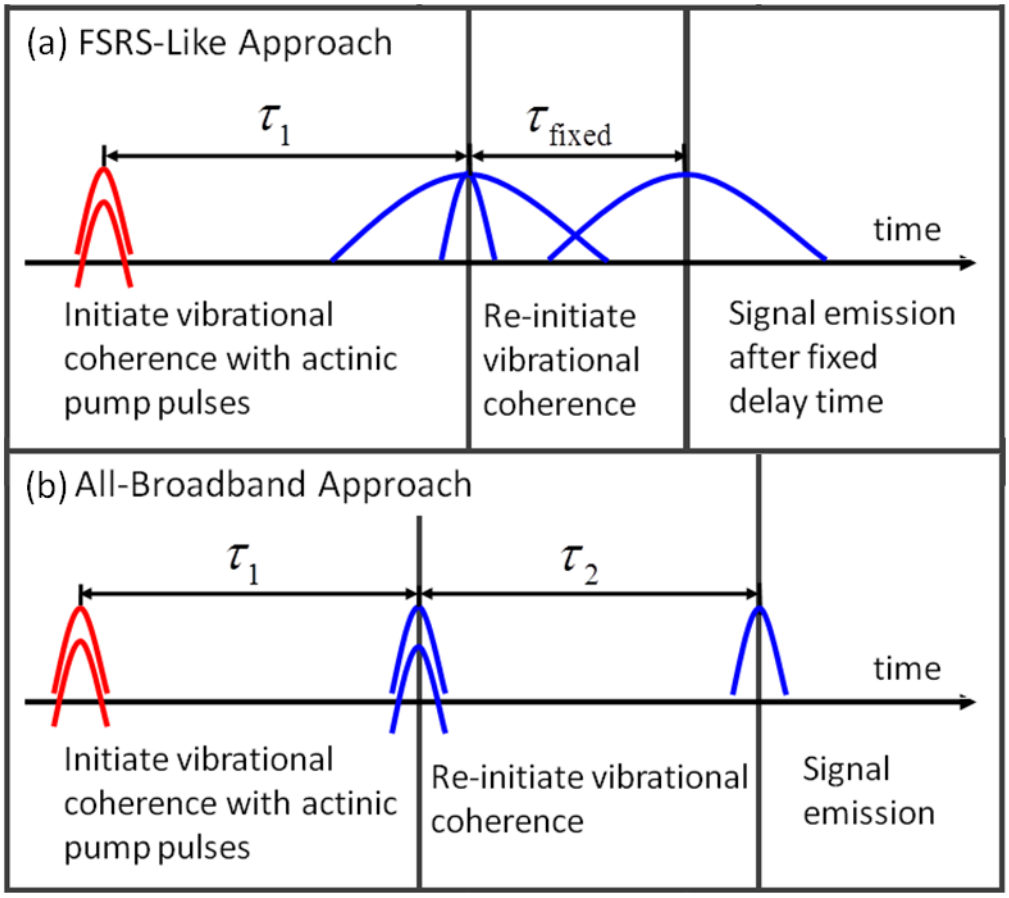


***Figure 5.2.*** *(a) Pulse sequence used in FSRS-like approach in which only one delay time, $\tau_1$, is scanned. A fixed delay $\tau_{fixed}$ is introduced to suppress undesired pump-repump-probe nonlinearities. (b) Pulse sequence used in all-broadband approach in which two experimentally controlled delay times, $\tau_1$ and $\tau_2$, are scanned. The 2DRR spectrum is obtained by 2D Fourier transformation of the signal.*

In this section, we define the sample terms of the FSRS and 2DRR polarizations used to compute the respective signal responses. Schematics of the FSRS and 2DRR pulse sequences are provided in Figure 5.2a and 5.2b respectively. In FSRS, following the coincident pair of actinic pulses, a delay time $\tau_1$ is scanned before introducing the first of the Raman pulses and the Stokes pulse. The second Raman pulse is delayed by a fixed duration to suppress a pump-repump-probe response; in contrast, the 2DRR experiment is an all broadband approach in which two delay times are scanned over periods of electronic population. Illustrated in Figure 5.2b, each delay is

preceded by a pair of coincident pulses. After the second delay $\tau_2$ , the Stokes pulse initiates an electronic coherence before signal emission.

Equation 5.3 is one of the 16 terms in the fifth-order polarization for FSRS, which was derived previously.[21] The remaining 15 terms can be found in section IVA with the associated two-sided Feynman diagrams.

$$P^{(5)}_{FSRS,1}(\omega_t) = iN_{Solute}\frac{\xi^2_{AP}\xi^2_{RP}\xi_{St}\left|\mu_{eg}\right|^6}{\mathrm{h}^5}\sum_{mnkluv} B_m \langle n|m\rangle\langle n|k\rangle\langle l|k\rangle\langle l|u\rangle\langle v|u\rangle\langle v|m\rangle \\ \times L_{en,gm}(\omega_{AP})D_{gk,gm}(\tau_1)L_{el,gm}(\omega_t)J_{gu,gm}(\omega_t-\omega_{RP})L_{ev,gm}(\omega_t) \tag{5.3}$$

where $\xi_j$ are the electric field amplitudes associated with the three types of laser pulses (actinic pump, Raman pump, Stokes), $N$ is the number density, $\mu_{eg}$ is the electronic transition dipole for the Soret band, $B_m$ is the Boltzmann population of level $m$ , $\langle n|m\rangle$ is a vibrational overlap integral (with excited state index in the bra),[25] and the summation is carried out with respect to dummy indices for vibrational energy levels.

The functions, $L_{en,gm}(\omega)$, are Lorentzian line shapes associated with resonances between vibronic levels in electronic states $g$ and $e$ ,

$$L_{ek,gm}(\omega_L) = \frac{1}{\omega_L - \omega_{eg} - \omega_{km} + i\Gamma_{eg}} , \tag{5.4}$$

whereas vibrational wavepacket motion induced by the actinic pump pulses is described by

$$D_{gk,gm}(\tau_1) = \exp(-i\omega_{km}\tau_1 - \Gamma_{vib}\tau_1)\frac{2\Lambda_{AP}}{\omega^2_{km} + \Lambda^2_{AP}} . \tag{5.5}$$

The function,

$$J_{gk,gm}(\omega_t - \omega_{RP}) = \frac{\exp\left[i(\omega_{RP} - \omega_t)\tau_2 - \Lambda_{RP}\tau_t\right]}{(\omega_t - \omega_{RP} - \omega_{km}) + i(\Gamma_{vib} - \Lambda_{RP})} , \tag{5.6}$$

provides insight into an advantage associated with the present approach. In particular, the denominator suggests that the line width of the resonance is reduced by introducing a time delay between Raman pump pulses (i.e., $\Gamma_{vib}$ and $\Lambda_{RP}$ have opposite signs). This prediction of the model is consistent with the experimental data.[21]

The first of 16 terms for the 2DRR fifth-order polarization is given in Equation 5.7, derived previously.[20] The remaining 15 terms can be found in section IVB with the associated two-sided Feynman diagrams. The line shape function for electronic population is given by Equation 5.8 and the electronic coherence line shape function is the same used for the FSRS polarization.

$$P^{(5)}_{2DRR,1}(\omega_t) = -N\left(\frac{\xi_L}{\mathrm{h}}\right)^5 \left|\mu_{eg}\right|^6 \sum_{mnkluv} B_m \langle n|m\rangle\langle n|k\rangle\langle l|k\rangle\langle l|u\rangle\langle v|u\rangle\langle v|m\rangle \times L_{en,gm}(\omega_L) L_{gk,gm}(\omega_t) L_{el,gm}(\omega_L) L_{gu,gm}(\omega_t) L_{ev,gm}(\omega_L) \tag{5.7}$$

$$L_{gk,gm}(\omega_t) = \frac{1}{\omega_t - \omega_{km} + i\Gamma_{vib}}\ , \tag{5.8}$$

where the quantities are defined in the same way as those in $P^{(5)}_{FSRS,1}(\omega_t)$.

**IIC. Polarizability**

Terms for the FSRS and 2DRR response functions can be found in the previous section and sections IVA and IVB. These equations as well as the solute-solute cascades in sections IVC and IVD are derived for resonant field-matter interactions. Polarization terms for off-resonant field-matter interactions need to be computed to account for the solvent contribution to solute-solvent cascades. Off-resonant four wave mixing signals can be reduced to a linear response with the approximation that electronic coherence times are short compared to pulse duration for off-resonant conditions. The linear susceptibility of the solvent,[14]

$$\chi_{\alpha\alpha}(\mathrm{t}) = \frac{\mathrm{i}}{\mathrm{h}}\langle\alpha(\mathrm{t})|\alpha(0)\rangle, \tag{5.9}$$

depends on the square of the polarizability, which can be written as

$$\alpha^2 = \frac{1}{\mathrm{h}^2}\sum_e\sum_k \langle gm|\hat{\mu}\hat{\mu}|gk\rangle\langle gk|\hat{\mu}\hat{\mu}|gm\rangle L^2_{e,g}(\omega_L)\ . \tag{5.10}$$

The polarizability can be related to the Raman cross-section as in Equation (5.11), [26]

$$\frac{\partial\sigma_R}{\partial\Omega} = \frac{\omega^4}{16\pi^2\varepsilon_0^2\mathrm{h}^2c^4}|\alpha(\omega)|^2. \tag{5.11}$$

## III. Simulations

In this section, simulations of cascades and the direct fifth-order signals from FSRS and 2DRR are used to compare the relative signal strengths. The model employs parameters derived from a resonance Raman study of p-nitroaniline, a 'push-pull' chromophore, in various solvents (acetonitrile, methanol, and dichloromethane).[27] The parameters used in the calculations are given in Table 5.I. The solute concentration, C, and path length, $l$, are chosen to match values in commonly performed experiments.

***Table 5.1.*** *Parameters for spectroscopic models of FSRS, 6 wave mixing, and the associated cascaded signals for p-nitroaniline in acetonitrile, methanol, and dichloromethane.*

| Parameter | Value | | | | | |
|---|---|---|---|---|---|---|
| | Solute-Solute (Acetonitrile) | | Solute-Solvent (Methanol) | | Full (Dichloromethane) | |
| | FSRS | 2DRR | FSRS | 2DRR | FSRS | 2DRR |
| $\omega_{eg} / 2\pi c$ (Solute) | 22720 $cm^{-1}$ | 22720 $cm^{-1}$ | 23800 $cm^{-1}$ | 23800 $cm^{-1}$ | 23490 $cm^{-1}$ | 23490 $cm^{-1}$ |
| $\omega_{eg} / 2\pi c$ (Solvent) | — | — | 153100 $cm^{-1}$ | 153100 $cm^{-1}$ | 126900 $cm^{-1}$ | 126900 $cm^{-1}$ |
| $\omega_{vib} / 2\pi c$ (Solute) | 861 $cm^{-1}$, 1326 $cm^{-1}$ | 861 $cm^{-1}$, 1326 $cm^{-1}$ | 861 $cm^{-1}$, 1328 $cm^{-1}$ | 861 $cm^{-1}$, 1328 $cm^{-1}$ | 862 $cm^{-1}$, 1326 $cm^{-1}$ | 862 $cm^{-1}$, 1326 $cm^{-1}$ |
| $\omega_{vib} / 2\pi c$ (Solvent) | — | — | 1035 $cm^{-1}$ | 1035 $cm^{-1}$ | 702 $cm^{-1}$ | 702 $cm^{-1}$ |
| *d (Solute)* | 0.84, 0.98 | 0.84, 0.98 | 1.46, 1.45 | 1.46, 1.45 | 1.05, 1.18 | 1.05, 1.18 |
| $\lvert\alpha\rvert^2 / \varepsilon_0^2$ (Solvent) | — | — | 2500 Å$^2$ | 2500 Å$^2$ | 14378 Å$^2$ | 14378 Å$^2$ |
| $\Gamma_{eg} / 2\pi c$ | 3092 $cm^{-1}$ | 3092 $cm^{-1}$ | 1413 $cm^{-1}$ | 1413 $cm^{-1}$ | 2896 $cm^{-1}$ | 2896 $cm^{-1}$ |
| $\Gamma_{vib} / 2\pi c$ | 20 $cm^{-1}$ | 20 $cm^{-1}$ | 20 $cm^{-1}$ | 20 $cm^{-1}$ | 20 $cm^{-1}$ | 20 $cm^{-1}$ |
| $\mu_{eg}$ (Solute) | 5.76 D | 5.76 D | 5.97 D | 5.97 D | 5.63 D | 5.63 D |
| $n(\omega_t)$ | 1.34 | 1.34 | 1.33 | 1.33 | 1.42 | 1.42 |
| C (Solute) | 0.200 mM | 0.200 mM | 0.200 mM | 0.200 mM | 0.200 mM | 0.200 mM |
| C (Solvent) | — | — | 24.7 M | 24.7 M | 15.6 M | 15.6 M |
| $l$ | 0.22 mm | 0.22 mm | 0.22 mm | 0.22 mm | 0.22 mm | 0.22 mm |
| $\frac{(\omega_L - \omega_{eg})}{2\pi c}$ | — | varied | — | varied | — | varied |
| $\frac{(\omega_{AP} - \omega_{eg})}{2\pi c}$ | varied | — | varied | — | varied | — |
| $\omega_{RP}$ | $\omega_{AP}$ | — | $\omega_{AP}$ | — | $\omega_{AP}$ | — |
| $\Lambda_{AP} / 2\pi c$ | 210 $cm^{-1}$ | — | 210 $cm^{-1}$ | — | 210 $cm^{-1}$ | — |
| $\Lambda_{RP} / 2\pi c$ | 40 $cm^{-1}$ | — | 40 $cm^{-1}$ | — | 40 $cm^{-1}$ | — |

### IIIA. Simulations of FSRS Signals and Cascaded Nonlinearities

Signals were calculated for p-nitroaniline in acetonitrile to deduce the effect of solute-solute interactions on the measured spectra under perfect phase matching conditions with all laser pulses being electronically resonant. Both direct (FSRS) and cascaded responses are shown in Figure 5.2. The largest features are associated with the $NO_2$ bending and stretching motions at 861 $cm^{-1}$ and 1326 $cm^{-1}$, respectively. Resonances at the fundamental frequencies dominate the response; however, various combination bands contribute to up to 25% of the maximum signal intensity. Notably, the cascades, which are roughly 10 times less intense than the FSRS response, have a clear effect on the combined signal in panel (c).

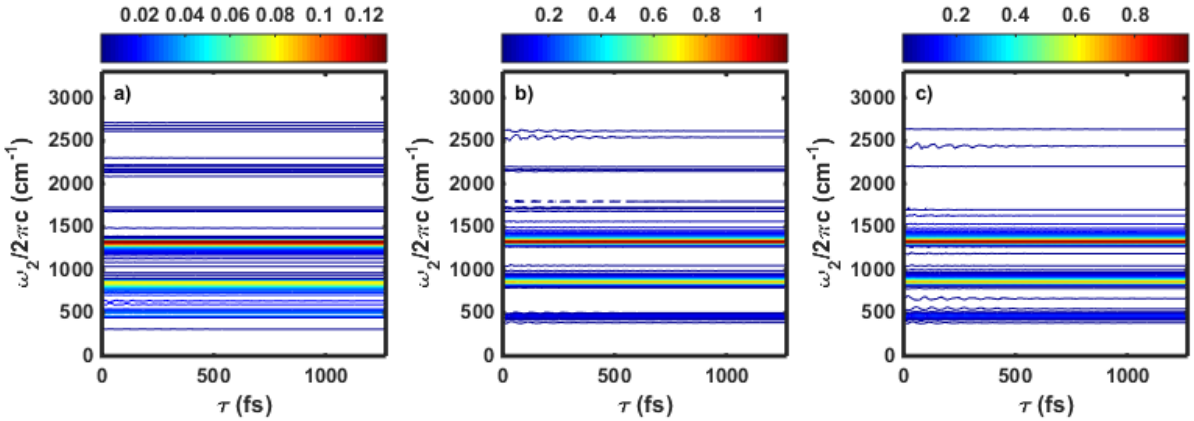


***Figure 5.3.*** *FSRS signals for p-nitroaniline in acetonitrile were computed using the parameters in Table 5.1. (a) Cascades from solute-solute interactions, (b) direct FSRS response, and (c) the total FSRS signals are simulated under the conditions of* $\omega_{AP} = \omega_{RP} = \omega_{eg}$ .

To further these results, we conducted simulations in which the laser frequency was detuned from the electronic resonance of the solute. In Figure 5.3, the first and second rows of panels are associated with signal detection at 861 $cm^{-1}$ and 1326 $cm^{-1}$, respectively. The cascades, direct response, and the logarithm of the ratio of signals are all displayed in Figure 5.3. Along the vertical axes, linear scaling factors are applied to the mode displacements listed in Table 5.1. Variation of the scaling factor provides insight into how the behaviors predicted for p-

nitroaniline would apply to molecules with smaller or larger mode displacements. In particular, our previous work suggests that cascades will be most problematic for systems with mode displacements that are less than unity.

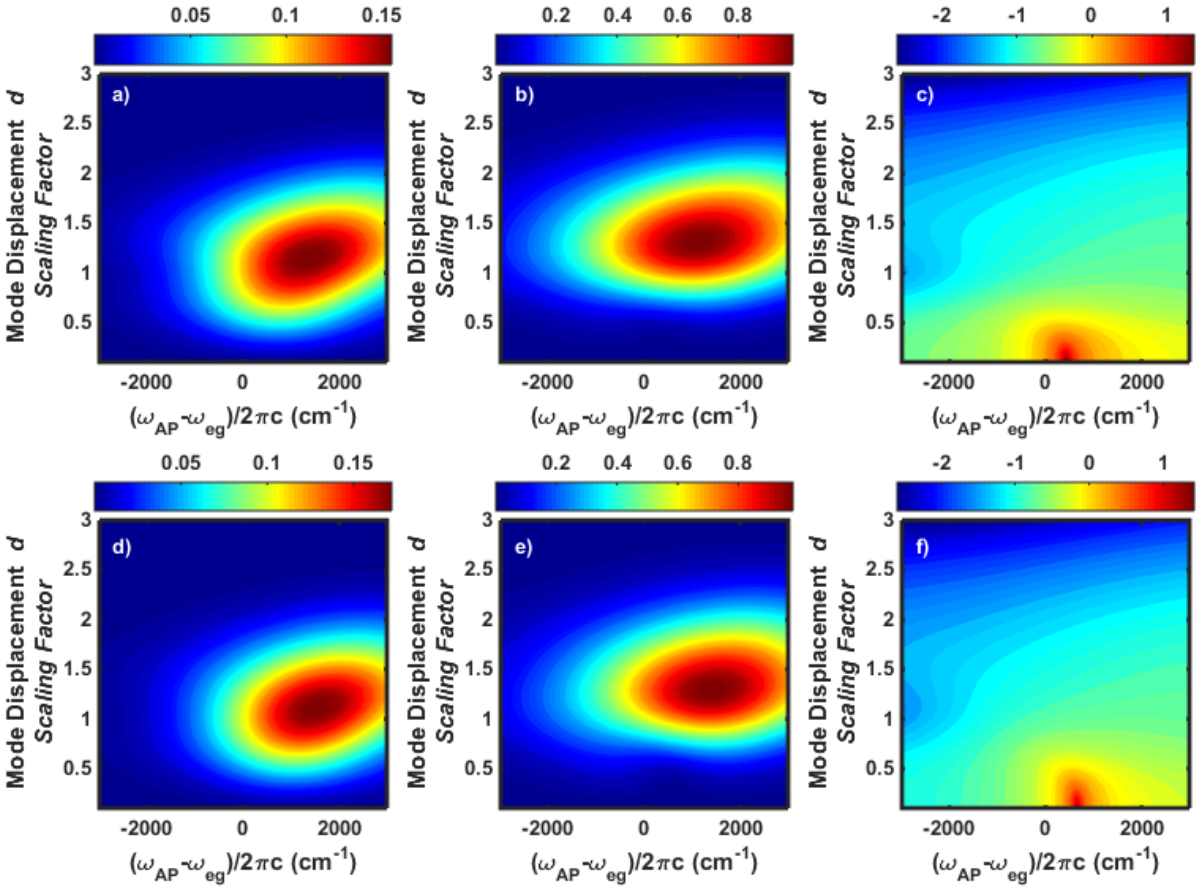


***Figure 5.4.*** *Raman shift for p-nitroaniline in acetonitrile at 861 cm$^{-1}$ (top) and 1326 cm$^{-1}$ (bottom). (a) & (d) Cascaded response of the solute, (b) & (e) the direct FSRS signal, and (e) & (f) the logarithm of the ratio of the signal fields* $\log_{10}\left(\left|E^{(3)}_{Solute-Solute,Cas}\right| / \left|E^{(5)}_{FSRS}\right|\right)$ *are computed using the parameters in Table 5.1. The horizontal axis represents the detuning of the actinic and Raman pump beams from the electronic resonance frequency. The linear scaling factor for the mode displacements is given on the vertical axis. The unscaled dimensionless mode displacements are 1.5 for both the 861 cm$^{-1}$ (top) and 1326 cm$^{-1}$ mode (bottom).*

Figure 5.3 demonstrates that the signal intensities maximize when the actinic and Raman pumps are tuned to the vibronic resonance (to the right of $\omega_{AP} - \omega_{eg} = 0$). Notably, the direct FSRS signal is somewhat broader with respect to the detuning axis and peaks at a larger value of

the scaling factor. The increase in signal intensity at larger mode displacements derives from the inflated number of nonlinear optical "pathways" that lead to appreciable signal strength. In contrast, cascaded signals peak at a smaller value of the scaling factor because of fewer available pathways. In addition, the cascaded signal is proportional to a product of six Lorentzian line shape functions, rather than five in the direct FSRS response, which causes an overall narrower line shape (see section IVC).

The concentration of a solvent in a solution is generally many orders of magnitude greater than that of the solute. The intensity of the solvent response increases with the number density and Raman cross-section. Therefore, the negligibility of cascades involving both a solute and solvent molecule should not be assumed. We next calculate such signals for p-nitroaniline under the same conditions as the previous simulations with the exception of using methanol parameters in place of acetonitrile. Methanol is chosen instead of acetonitrile because it also has proximal solute and solvent vibrational frequencies and a larger Raman cross-section.

The direct FSRS signal, shown in Figure 5.4, exhibits a pattern of peaks that is similar to that associated with p-nitroaniline in acetonitrile. However, cascades involving the solvent contain only the fundamental mode frequencies of the solute (i.e., the combination bands are too weak to assign). Cascades that involve both a solute and solvent molecule have the same phase as the direct signal, whereas cascades that originate from two solute molecules possess a $\pi$ phase shift. Therefore, constructive interference between the direct and cascaded response is computed for the total FSRS signal. Resonances of the solute dominate the total response; however, the cascades are detectable and of comparable intensity to the overtones and combination bands of the solute.

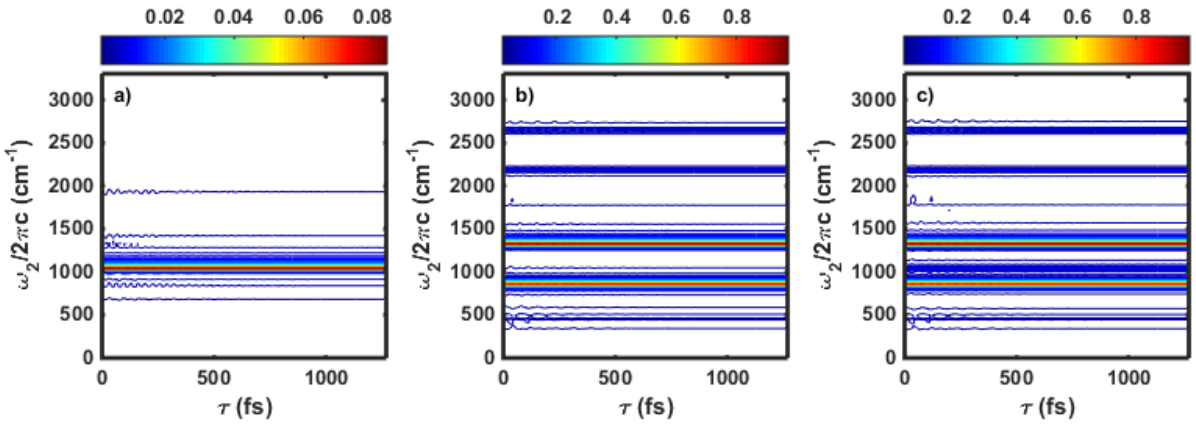


***Figure 5.5.*** *Spectra for p-nitroaniline in methanol computed using the parameters in Table 5.1. Cascades from solute-solvent interactions (a), direct fifth-order (b), and the total FSRS (c) signals are simulated under the condition* $\omega_{\mathrm{AP}} = \omega_{\mathrm{RP}} = \omega_{\mathrm{eg}}$.

The calculations in Figure 5.5 suggest that cascaded artifacts are generally negligible for signal detected near vibronic resonances of the solute for a wide range of small displacements. However, the resonances of the solute will be significantly affected when the mode displacements exceed 3. The mode of methanol at 1035 cm$^{-1}$ is between the two modes of p-nitroaniline used in our simulations. To highlight this effect, the mode frequency of the solvent was varied in Figure 5.6 and the ratios were computed at the Raman shifts 861 cm$^{-1}$ and 1328 cm$^{-1}$. One-dimensional slices of the ratio are from $\omega_{\mathrm{AP}} - \omega_{\mathrm{eg}} = 0$, and the inset shows the full range of detuning $\omega_{\mathrm{AP}} - \omega_{\mathrm{eg}}$. The cascaded signal intensity spikes when vibrational frequencies are in proximity to each other. This effect is slightly more pronounced for the 861-cm$^{-1}$ mode versus the mode at 1328 cm$^{-1}$.

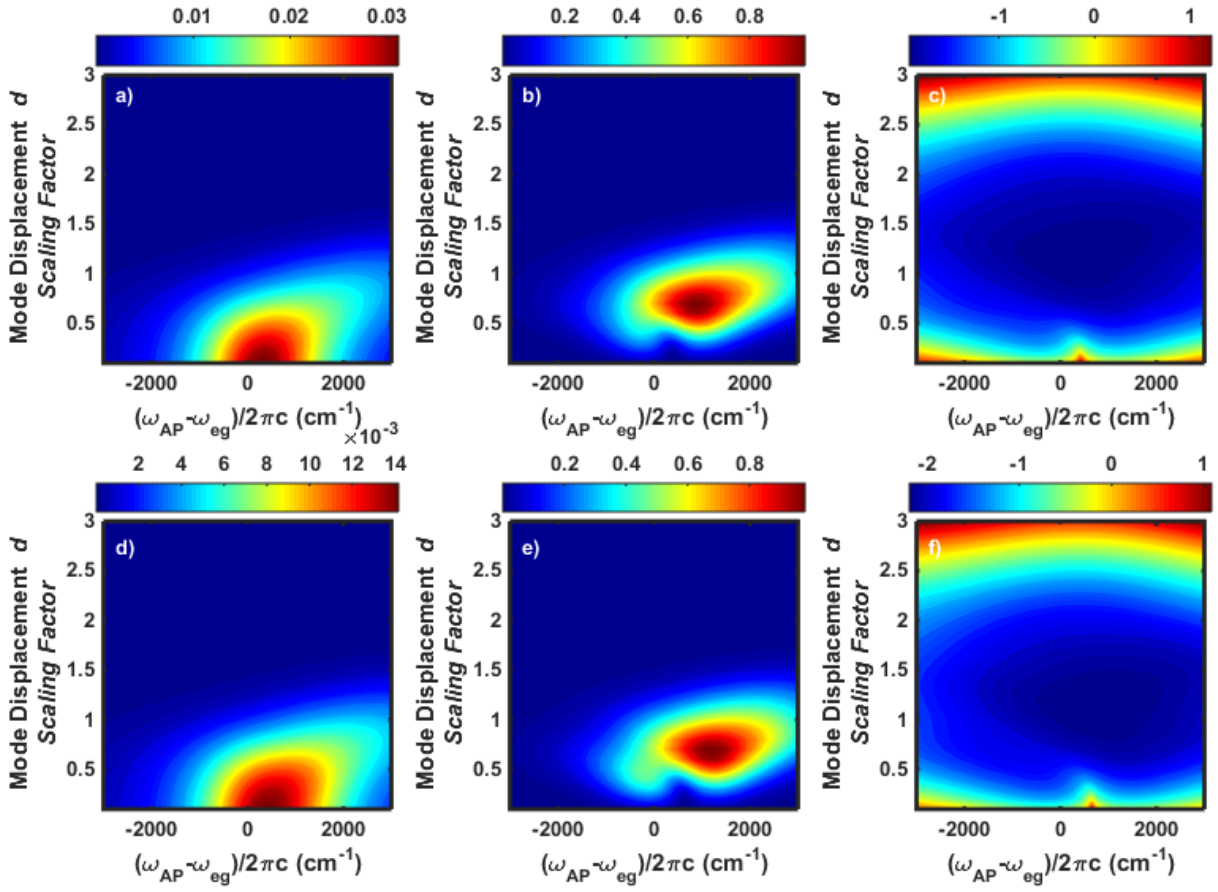


***Figure 5.6.*** *Raman shift for p-nitroaniline in methanol at 861 cm$^{-1}$ (top) and 1328 cm$^{-1}$ (bottom). (a) & (d) Cascaded response of the solvent, (b) & (e) the direct FSRS signal, and (e) & (f) the logarithm of the ratio of the signal fields* $\log_{10}\left(\left|E^{(3)}_{Solute-Solvent,Cas}\right|/\left|E^{(5)}_{FSRS}\right|\right)$ *are computed using the parameters in Table 5.1. The horizontal axis represents the detuning of the actinic and Raman pump beams from the electronic resonance frequency. The linear scaling factor for the mode displacements is given on the vertical axis. The unscaled dimensionless mode displacements are 1.5 for both the 861 cm$^{-1}$ (top) and 1326 cm$^{-1}$ mode (bottom).*

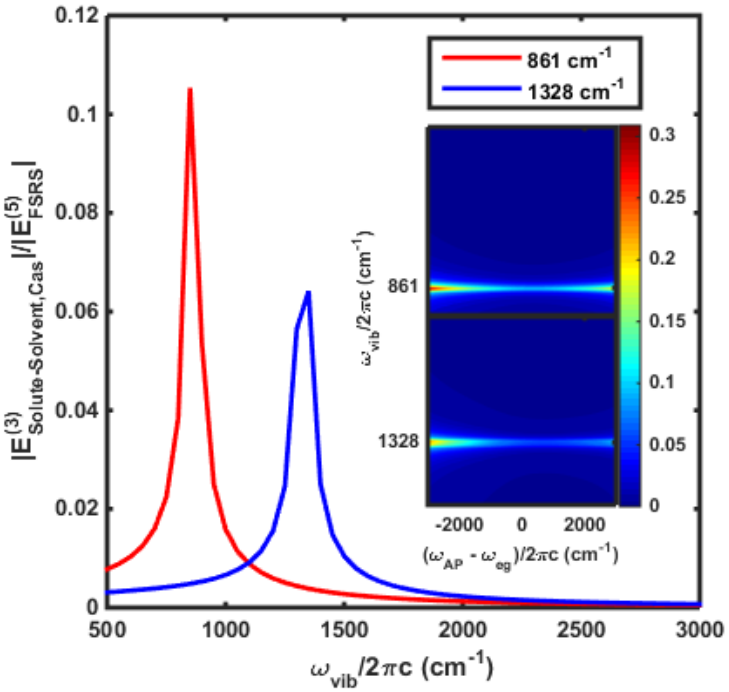


***Figure 5.7.*** *The ratio of the electric fields* $\left|E^{(3)}_{Solute-Solvent,Cas}\right| / \left|E^{(5)}_{FSRS}\right|$ *were computed for the Raman shift of p-nitroaniline at 861 cm*$^{-1}$ *(red, top inset) and 1328 cm*$^{-1}$ *(blue, bottom inset) using the methanol parameters in Table 5.1 and varying the solvent vibrational mode. The horizontal axis (vertical axis of the inset) represents the solvent mode. The detuning of the actinic and Raman pumps from the electronic resonance is set to 0 cm*$^{-1}$ *in the parent Figure and varies along the horizontal axes for the inset. The vertical axis (colorbar of the inset) gives values of the electric fields ratio.*

***Combined Cascades***

We combine separate components together to illustrate the pronounced effect artifacts can have on the FSRS spectra by simulating p-nitroaniline in dichloromethane with the actinic and Raman pulses equal to the electronic energy gap. The sum of the solute-solute and solute-solvent cascades is given in Figure 5.7a. P-nitroaniline has peaks of 862 cm$^{-1}$ and 1326 cm$^{-1}$ with displacements of 1.05 and 1.18 in dichloromethane, which has a 702 cm$^{-1}$ mode. Comparing to Figure 5.7b, the solute-solute cascades are less significant than the solute-solvent and the undesired signal is almost as large as the direct fifth-order signal. The direct and total spectra exhibit the fundamental Raman peaks, first overtone bands, and combinations bands. Longer

lived oscillations, solvent bands, and solute-solvent combination bands are noteworthy artifacts in the full spectrum. It is equally important to acknowledge the overall intensity in Figure 5.7c is lower than the pure FSRS signal.

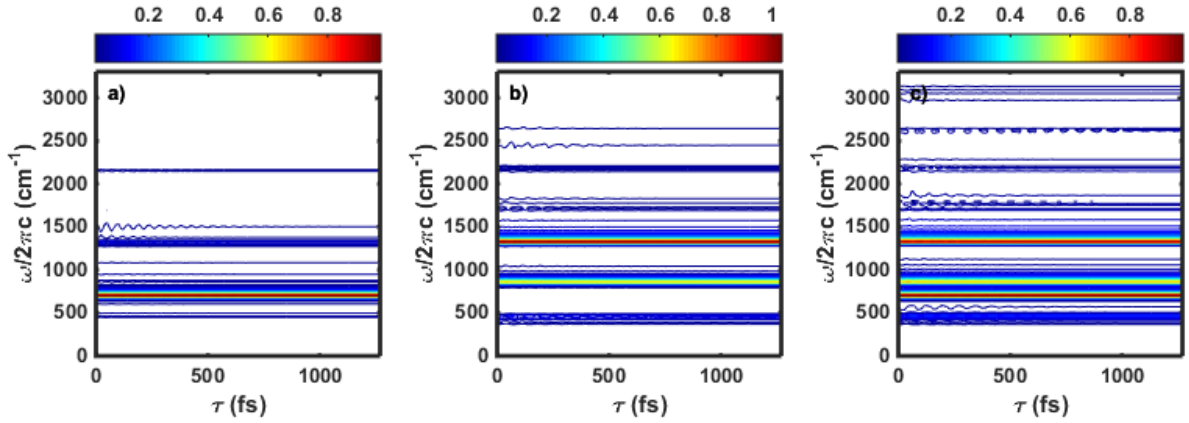


***Figure 5.8. S****pectra for p-nitroaniline in dichloromethane were computed using the parameters in Table 5.1. Cascades from solute-solute and solute-solvent interactions (a), direct fifth-order (b), and the total FSRS (c) signals are simulated under the condition* $\omega_{AP} = \omega_{RP} = \omega_{eg}$ .

**IIIB. Simulations of the 2DRR Spectra and Cascaded Nonlinearities**

In this section, we compute 2DRR spectra for the p-nitroniline molecule. As in section IIA, various types of cascaded four-wave mixing responses are considered. To begin, the 2DRR spectrum in Figure 5.8c reveals the resonances of *p*-nitroaniline in acetonitrile. All calculations in this figure employ electronically resonant laser pulses. The diagonal peaks at 861 $cm^{-1}$ and 1326 $cm^{-1}$ are the largest features in the spectrum (i.e., $NO_2$ bending and symmetric stretching). The diagonal peak at 465 $cm^{-1}$ represents the difference in frequencies for the two modes; both modes evolve as coherences during the two experimentally controlled delay times. The same resonances are found in the cascaded signal, although the diagonal peaks possess weaker intensities than the cross peaks (see Figure 5.8a). The total spectrum in 8c is lower in intensity than the purely direct 2DRR signal in Figure 5.8b and reveals subtle differences that arise from cascaded nonlinearities.

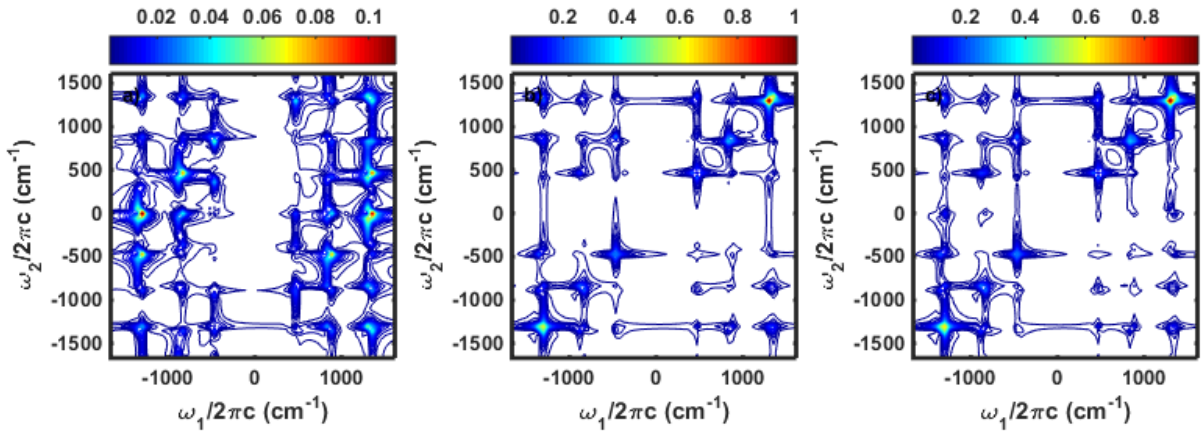


***Figure 5.9. S****pectra for p-nitroaniline in acetonitrile were computed using the parameters in Table 5.1. Cascades from solute-solute interactions (a), direct fifth-order (b), and the total 2DRR (c) signals are simulated under the condition* $\omega_L = \omega_{eg}$ .

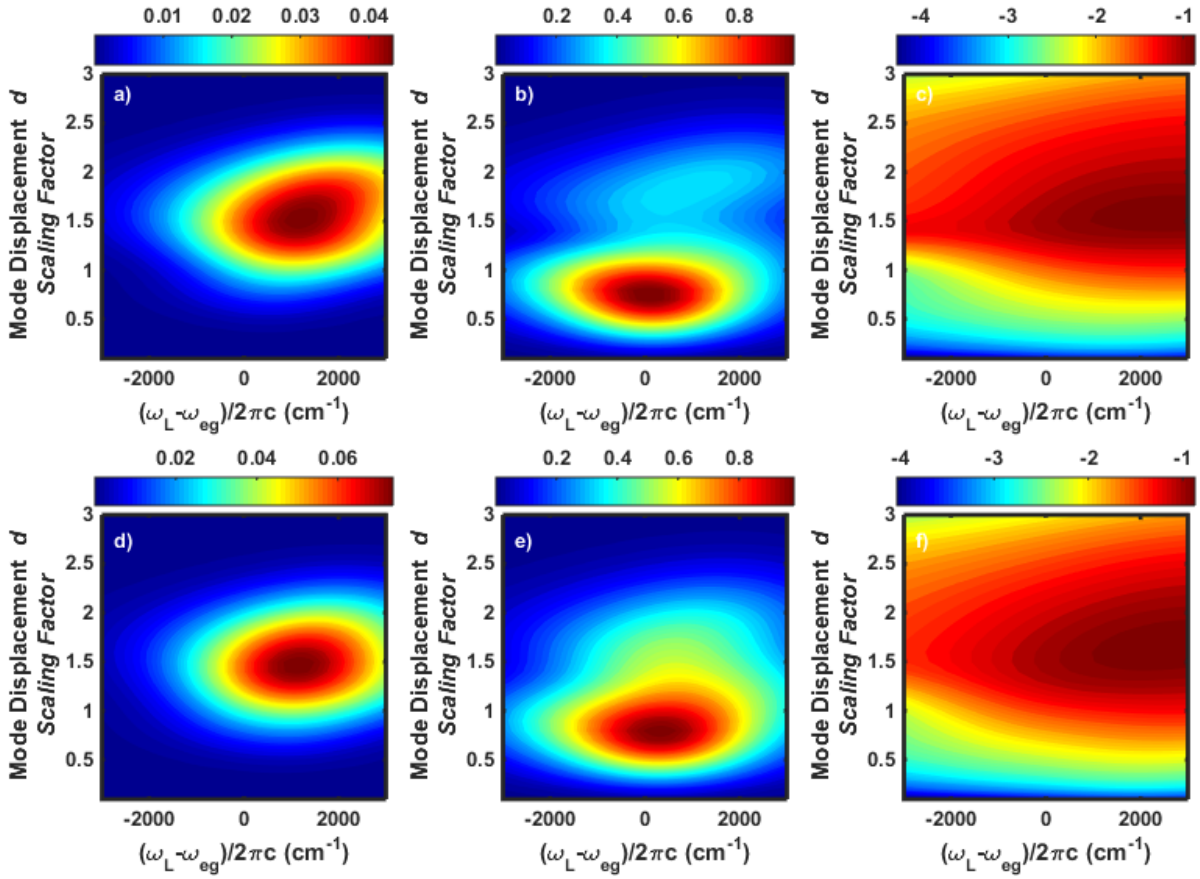


***Figure 5.10.*** *Raman shift for p-nitroaniline in acetonitrile at 861 cm$^{-1}$ (top) and 1326 cm$^{-1}$ (bottom). (a) & (d) Cascaded response of the solute, (b) & (e) the direct 2DRR signal, and (e) & (f) the logarithm of the ratio of the signal fields* $\log_{10}\left(\left|E^{(3)}_{Solute-Solute,Cas}\right| / \left|E^{(5)}_{2DRR}\right|\right)$ *are computed using the parameters in Table 5.1. The horizontal axis represents the detuning of the impinging laser pulses from the electronic resonance. The linear scaling factor for the mode displacements is given on the vertical axis. The unscaled dimensionless mode displacements are 0.84 and 0.98 for the 861 cm$^{-1}$ (top) and 1326 cm$^{-1}$ mode (bottom).*

In Figure 5.9, we present signal magnitudes for both the direct 2DRR responses and cascades. Much like the artifacts in the FSRS simulations, the cascaded signals in Figures 5.9a and 9d are most intense with mode displacements scaled by 1-1.5 times the values in Table 5.1 (d=1.5-2.25). Panels 9b and 9d show that the 2DRR signal intensities maximize at smaller displacements as compared to the cascades. This behavior originates in the much larger number of "pathways" available to the 2DRR process (32 times number of states to 5$^{th}$ power) as compared to the cascade (32 times number of states to 3$^{rd}$ power). Overall, the ratios of direct

responses to cascades are similar for both 2DRR and FSRS experiments, which may come as a surprise considering the reputation of 2D Raman techniques. Lastly, we find that the 2DRR signal becomes dominant as the mode displacement becomes very large or the laser detuning shifts far to the red.

The 2DRR spectrum in Figure 5.10b has the same pattern of diagonal and off-diagonal resonances with a notable reduction in signal intensity at 465 $cm^{-1}$ and the associated cross-peaks. Compared to the solute-solute cascades in Figure 5.8a, the spectrum for solute-solvent signal cascades in Figure 5.10a exhibits greater relative signal intensity, particularly in the cross peaks. Artifacts from the solvent are most noticeable in $\omega_2$ of the total signal shown in Figure 5.10c, although signal intensity can be observed in both dimensions at the solute-solvent cross peaks.

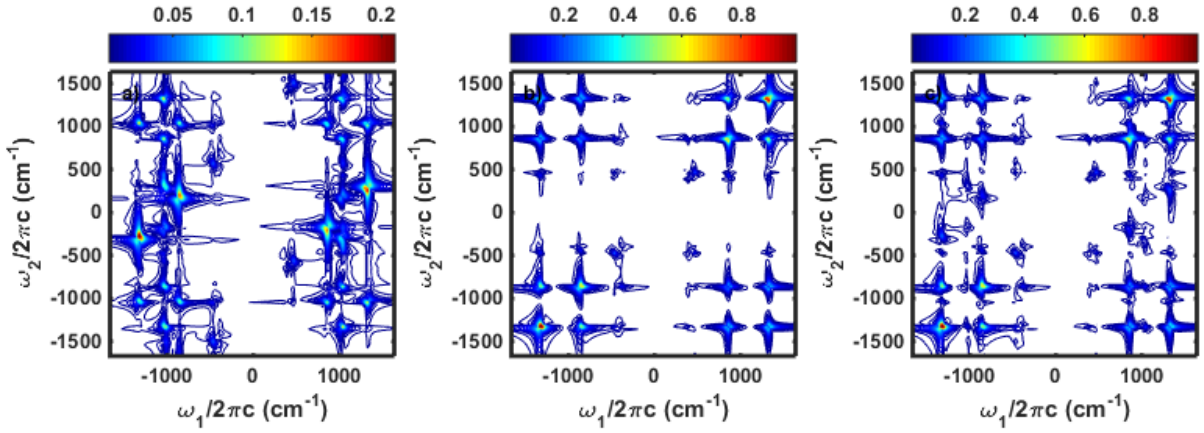


***Figure 5.11.*** *Spectra for p-nitroaniline in methanol were computed using the parameters in Table 5.1. (a) Cascades from solute-solvent interactions, (b) direct fifth-order, and (c) the total 2DRR, all simulated under the condition* $\omega_L = \omega_{eg}$ .

Figures 5.11c and 5.11f show that the direct 2DRR signal intensity is dominant in the region of parameter space in which the spectra in Figure 5.10 were calculated. The ratios were computed at diagonal peak wavenumbers of 861 $cm^{-1}$ and 1328 $cm^{-1}$. The logarithms of the ratios of signal fields suggest that the 2DRR responses are most dominant at a detuning of 0 $cm^{-1}$

when the mode displacements are small. Figures 5.11a and 5.11f show cascades from solute-solvent molecules generally yield weaker signals than those of the solute-solute cascades described in Figure 5.9. Figure 5.12 demonstrates that the magnitude of the cascaded response maximimizes when its vibrational frequency is close to that of the solute. Unlike FSRS, the cascades generated by a combination of solute and solvent molecules are greater than 10% of the pure 2DRR response.

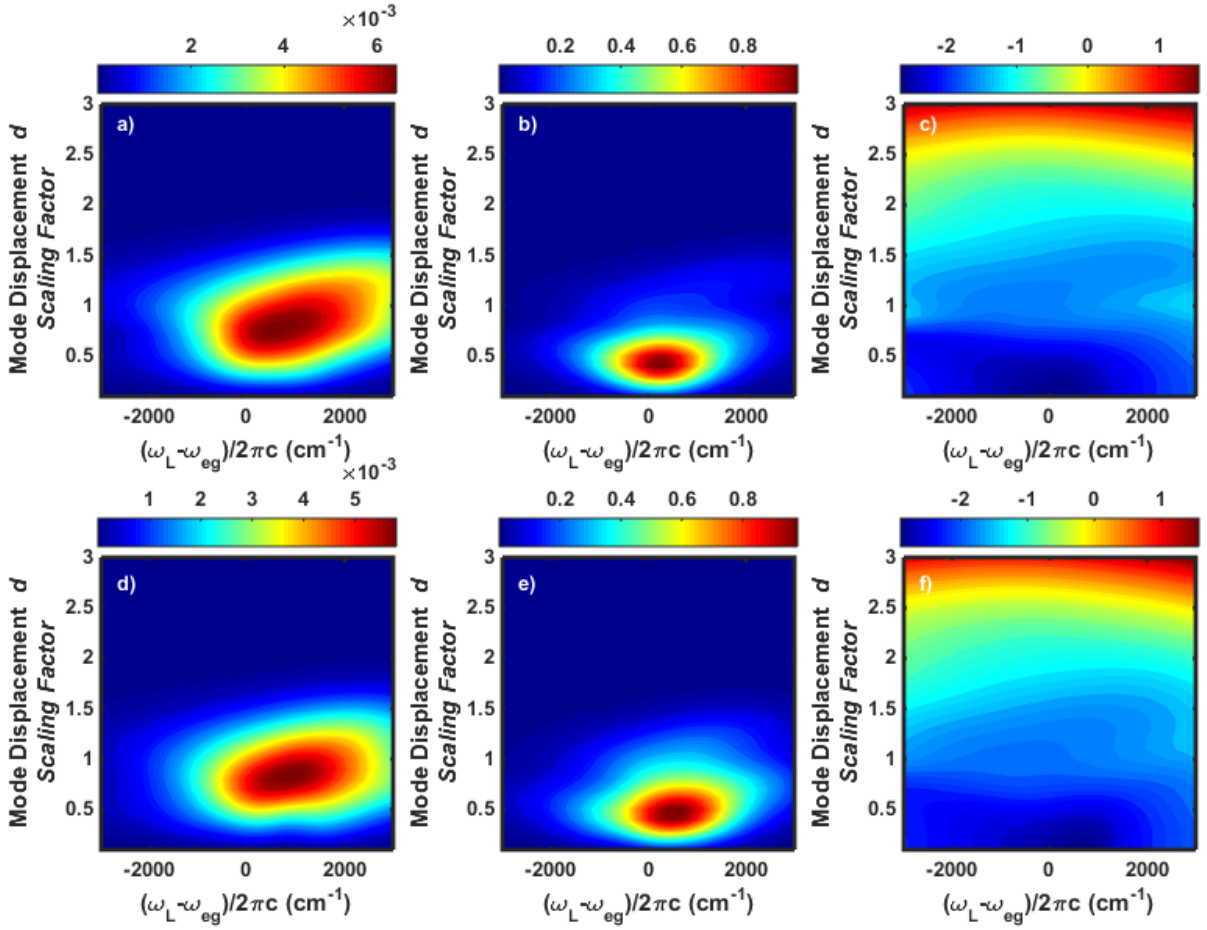


***Figure 5.12.*** *Raman shift for p-nitroaniline in methanol at 861 cm$^{-1}$ (top) and 1326 cm$^{-1}$ (bottom). (a) & (d) Cascaded response of the solvent, (b) & (e) the direct 2DRR signal, and (e) & (f) the logarithm of the ratio of the signal fields* $\log_{10}\left(\left|E^{(3)}_{Solute-Solvent,Cas}\right| / \left|E^{(5)}_{2DRR}\right|\right)$ *are computed using the parameters in Table 5.1. The horizontal axis represents the detuning of the impinging laser pulse from the electronic resonance. The linear scaling factor for the mode displacements is given on the vertical axis. The unscaled dimensionless mode displacements are 1.5 for both the 861 cm$^{-1}$ (top) and 1326 cm$^{-1}$ mode (bottom).*

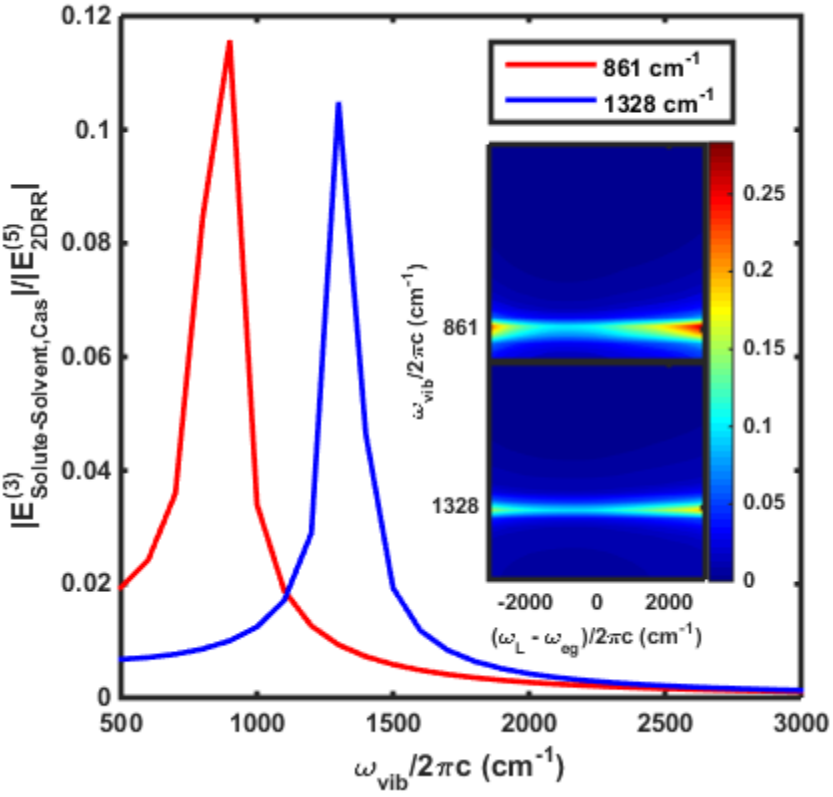


***Figure 5.13.*** *The ratio of the electric fields* $\left|E^{(3)}_{Solute-Solvent,Cas}\right| / \left|E^{(5)}_{2dRR}\right|$ *were computed for the Raman shift of p-nitroaniline at 861 cm*$^{-1}$ *(red, top inset) and 1328 cm*$^{-1}$ *(blue, bottom inset) using the methanol parameters in Table 5.1 and varying the solvent vibrational mode. The horizontal axis (vertical axis of the inset) represents the solvent mode. The detuning of the incident laser pulses from the electronic resonance is set to 0 cm*$^{-1}$ *in the parent Figure and varies along the horizontal axes for the inset. The vertical axis (colorbar of the inset) gives values of the electric fields ratio.*

In Figure 5.13, the 2D spectra for p-nitroaniline in dichloromethane illustrate the potential for solute and solvent molecules to cooperate in a cascade. The 2DRR spectrum of the system shown in Figure 5.13b is weaker in this solvent than is the cascades signal spectrum in Figure 5.13a. The diagonal peaks of the 2DRR spectrum are less than $50\%$ of the total signal displayed in 5.13c. Destructive interference between the 2DRR response and the cascade reduces the magnitudes of the diagonal 2DRR peaks in the total signal shown in Figure 5.13c.

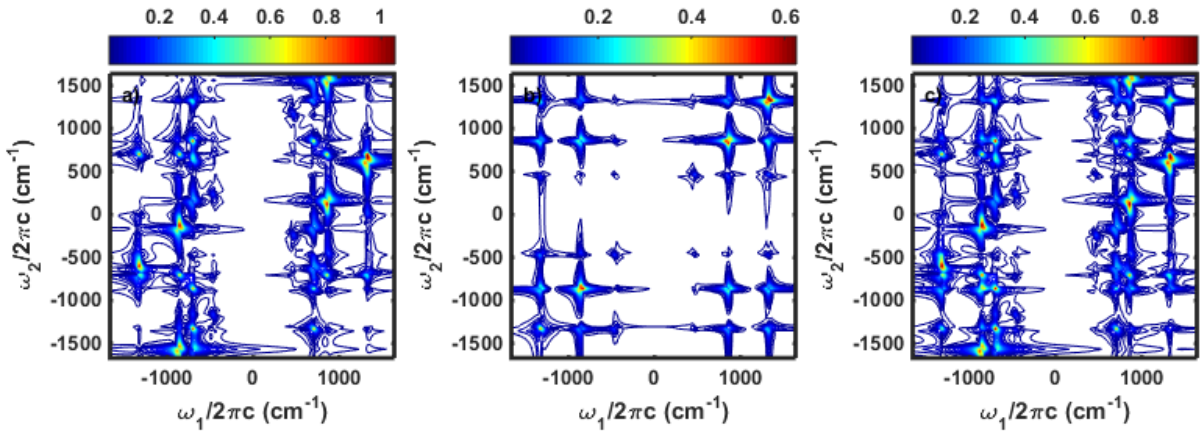


***Figure 5.14.*** *Spectra for p-nitroaniline in dichloromethane were computed using the parameters in Table 5.1. Cascades from solute-solute and solute-solvent interactions (a), direct 2DRR (b), and the total 2DRR (c) signals are simulated under the condition* $\omega_L = \omega_{eg}$ .

## IV. Supplemental Information

### IVA. Response Functions for FSRS Spectroscopy

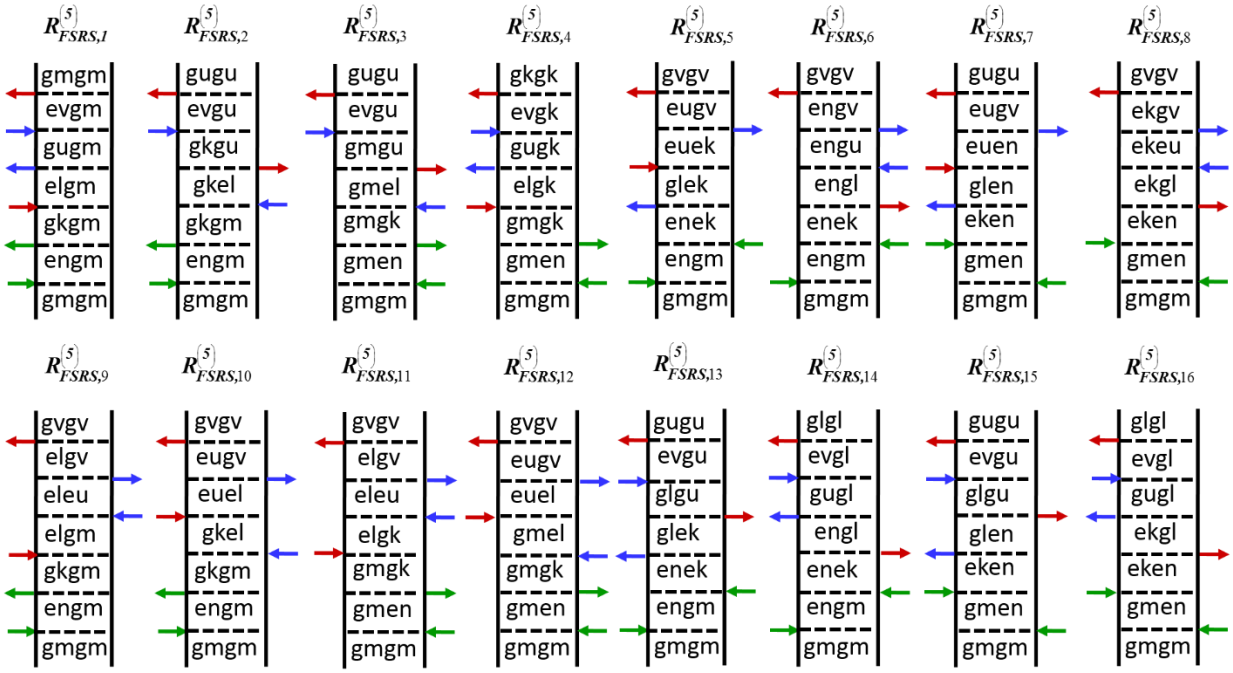


***Figure 5.15.*** *Feynman diagrams associated with the direct fifth-order response. The indices,* $g$ *and* $e$ *, represent the ground and excited electronic states, whereas dummy indices (*$m$ *,*$n$ *,*$k$ *,*$l$ *,*$u$ *, and* $v$ *) denote vibrational levels. Green, blue, and red arrows represent the actinic pump, Raman pump, and Stokes pulses, respectively.*

The direct fifth-order polarization possesses 16 components when a single electronic resonance dominates the optical response. The first FSRS polarization component, $P^{(5)}_{FSRS,1}(\omega_t)$, is given in Equation (5.3). The remaining 15 polarization components are

$$P^{(5)}_{FSRS,2}(\omega_t) = i\frac{N\xi^2_{AP}\xi^2_{RP}\xi_{St}\left|\mu_{eg}\right|^6}{\mathrm{h}^5}\sum_{mnkluv} B_m \langle n|m\rangle\langle n|k\rangle\langle l|m\rangle\langle l|u\rangle\langle v|k\rangle\langle v|u\rangle \times L_{en,gm}(\omega_{AP}) D_{gk,gm}(\tau_1) L_{gk,el}(-\omega_{RP}) J_{gk,gu}(\omega_t - \omega_{RP}) L_{ev,gu}(\omega_t) \tag{5.12}$$

$$P^{(5)}_{FSRS,3}(\omega_t) = i\frac{N\xi^2_{AP}\xi^2_{RP}\xi_{St}\left|\mu_{eg}\right|^6}{\mathrm{h}^5}\sum_{mnkluv} B_m \langle n|m\rangle\langle n|k\rangle\langle l|k\rangle\langle l|u\rangle\langle v|m\rangle\langle v|u\rangle \times L_{gm,en}(-\omega_{AP}) D_{gm,gk}(\tau_1) L_{gm,el}(-\omega_{RP}) J_{gm,gu}(\omega_t - \omega_{RP}) L_{ev,gu}(\omega_t) \tag{5.13}$$

$$P^{(5)}_{FSRS,4}(\omega_t) = i\frac{N\xi^2_{AP}\xi^2_{RP}\xi_{St}\left|\mu_{eg}\right|^6}{\mathrm{h}^5}\sum_{mnkluv} B_m \langle n|m\rangle\langle n|k\rangle\langle l|m\rangle\langle l|u\rangle\langle v|u\rangle\langle v|k\rangle \times L_{gm,en}(-\omega_{AP}) D_{gm,gk}(\tau_1) L_{el,gk}(\omega_t) J_{gu,gk}(\omega_t - \omega_{RP}) L_{ev,gk}(\omega_t) \tag{5.14}$$

$$P^{(5)}_{FSRS,5}(\omega_t) = i\frac{N\xi^2_{AP}\xi^2_{RP}\xi_{St}\left|\mu_{eg}\right|^6}{\mathrm{h}^5}\sum_{mnkluv} B_m \langle n|m\rangle\langle k|m\rangle\langle n|l\rangle\langle u|l\rangle\langle k|v\rangle\langle u|v\rangle \times L_{en,gm}(\omega_{AP}) D_{en,ek}(\tau_1) L_{gl,ek}(-\omega_{RP}) J_{eu,ek}(\omega_t - \omega_{RP}) L_{eu,gv}(\omega_t) \tag{5.15}$$

$$P^{(5)}_{FSRS,6}(\omega_t) = i\frac{N\xi^2_{AP}\xi^2_{RP}\xi_{St}\left|\mu_{eg}\right|^6}{\mathrm{h}^5}\sum_{mnkluv} B_m \langle n|m\rangle\langle k|m\rangle\langle k|l\rangle\langle u|l\rangle\langle u|v\rangle\langle n|v\rangle \times L_{en,gm}(\omega_{AP}) D_{en,ek}(\tau_1) L_{en,gl}(\omega_t) J_{en,eu}(\omega_t - \omega_{RP}) L_{en,gv}(\omega_t) \tag{5.16}$$

$$P^{(5)}_{FSRS,7}(\omega_t) = i\frac{N\xi^2_{AP}\xi^2_{RP}\xi_{St}\left|\mu_{eg}\right|^6}{\mathrm{h}^5}\sum_{mnkluv} B_m \langle n|m\rangle\langle k|m\rangle\langle k|l\rangle\langle u|l\rangle\langle n|v\rangle\langle u|v\rangle \times L_{gm,en}(-\omega_{AP}) D_{ek,en}(\tau_1) L_{gl,en}(-\omega_{RP}) J_{eu,en}(\omega_t - \omega_{RP}) L_{eu,gv}(\omega_t) \tag{5.17}$$

$$P^{(5)}_{FSRS,8}(\omega_t) = i\frac{N\xi^2_{AP}\xi^2_{RP}\xi_{St}\left|\mu_{eg}\right|^6}{\mathrm{h}^5}\sum_{mnkluv} B_m \langle n|m\rangle\langle k|m\rangle\langle n|l\rangle\langle u|l\rangle\langle u|v\rangle\langle k|v\rangle \times L_{gm,en}(-\omega_{AP}) D_{ek,en}(\tau_1) L_{ek,gl}(\omega_t) J_{ek,eu}(\omega_t - \omega_{RP}) L_{ek,gv}(\omega_t) \tag{5.18}$$

$$P^{(5)}_{FSRS,9}(\omega_t) = i\frac{N\xi^2_{AP}\xi^2_{RP}\xi_{St}\left|\mu_{eg}\right|^6}{\mathrm{h}^5}\sum_{mnkluv} B_m \langle n|m\rangle\langle n|k\rangle\langle l|k\rangle\langle u|m\rangle\langle u|v\rangle\langle l|v\rangle \\ \times L_{en,gm}(\omega_{AP}) D_{gk,gm}(\tau_1) L_{el,gm}(\omega_t) J_{el,eu}(\omega_t - \omega_{RP}) L_{el,gv}(\omega_t) \tag{5.19}$$

$$P^{(5)}_{FSRS,10}(\omega_t) = i\frac{N\xi^2_{AP}\xi^2_{RP}\xi_{St}\left|\mu_{eg}\right|^6}{\mathrm{h}^5}\sum_{mnkluv} B_m \langle n|m\rangle\langle n|k\rangle\langle l|m\rangle\langle u|k\rangle\langle l|v\rangle\langle u|v\rangle \\ \times L_{en,gm}(\omega_{AP}) D_{gk,gm}(\tau_1) L_{gk,el}(-\omega_{RP}) J_{eu,el}(\omega_t - \omega_{RP}) L_{eu,gv}(\omega_t) \tag{5.20}$$

$$P^{(5)}_{FSRS,11}(\omega_t) = i\frac{N\xi^2_{AP}\xi^2_{RP}\xi_{St}\left|\mu_{eg}\right|^6}{\mathrm{h}^5}\sum_{mnkluv} B_m \langle n|m\rangle\langle n|k\rangle\langle l|m\rangle\langle u|k\rangle\langle u|v\rangle\langle l|v\rangle \\ \times L_{gm,en}(-\omega_{AP}) D_{gm,gk}(\tau_1) L_{el,gk}(\omega_t) J_{el,eu}(\omega_t - \omega_{RP}) L_{el,gv}(\omega_t) \tag{5.21}$$

$$P^{(5)}_{FSRS,12}(\omega_t) = i\frac{N\xi^2_{AP}\xi^2_{RP}\xi_{St}\left|\mu_{eg}\right|^6}{\mathrm{h}^5}\sum_{mnkluv} B_m \langle n|m\rangle\langle n|k\rangle\langle l|k\rangle\langle u|m\rangle\langle l|v\rangle\langle u|v\rangle \\ \times L_{gm,en}(-\omega_{AP}) D_{gm,gk}(\tau_1) L_{gm,el}(-\omega_{RP}) J_{eu,el}(\omega_t - \omega_{RP}) L_{eu,gv}(\omega_t) \tag{5.22}$$

$$P^{(5)}_{FSRS,13}(\omega_t) = i\frac{N\xi^2_{AP}\xi^2_{RP}\xi_{St}\left|\mu_{eg}\right|^6}{\mathrm{h}^5}\sum_{mnkluv} B_m \langle n|m\rangle\langle k|m\rangle\langle n|l\rangle\langle k|u\rangle\langle v|l\rangle\langle v|u\rangle \\ \times L_{en,gm}(\omega_{AP}) D_{en,ek}(\tau_1) L_{gl,ek}(-\omega_{RP}) J_{gl,gu}(\omega_t - \omega_{RP}) L_{ev,gu}(\omega_t) \tag{5.23}$$

$$P^{(5)}_{FSRS,14}(\omega_t) = i\frac{N\xi^2_{AP}\xi^2_{RP}\xi_{St}\left|\mu_{eg}\right|^6}{\mathrm{h}^5}\sum_{mnkluv} B_m \langle n|m\rangle\langle k|m\rangle\langle k|l\rangle\langle n|u\rangle\langle v|u\rangle\langle v|l\rangle \\ \times L_{en,gm}(\omega_{AP}) D_{en,ek}(\tau_1) L_{en,gl}(\omega_t) J_{gu,gl}(\omega_t - \omega_{RP}) L_{ev,gl}(\omega_t) \tag{5.24}$$

$$P^{(5)}_{FSRS,15}(\omega_t) = i\frac{N\xi^2_{AP}\xi^2_{RP}\xi_{St}\left|\mu_{eg}\right|^6}{\mathrm{h}^5}\sum_{mnkluv} B_m \langle n|m\rangle\langle k|m\rangle\langle k|l\rangle\langle n|u\rangle\langle v|l\rangle\langle v|u\rangle \\ \times L_{gm,en}(-\omega_{AP}) D_{ek,en}(\tau_1) L_{gl,en}(-\omega_{RP}) J_{gl,gu}(\omega_t - \omega_{RP}) L_{ev,gu}(\omega_t) \tag{5.25}$$

$$P^{(5)}_{FSRS,16}(\omega_t) = i\frac{N\xi^2_{AP}\xi^2_{RP}\xi_{St}\left|\mu_{eg}\right|^6}{\mathrm{h}^5}\sum_{mnkluv} B_m \langle n|m\rangle\langle k|m\rangle\langle n|l\rangle\langle k|u\rangle\langle v|u\rangle\langle v|l\rangle \\ \times L_{gm,en}(-\omega_{AP}) D_{ek,en}(\tau_1) L_{ek,gl}(\omega_t) J_{gu,gl}(\omega_t - \omega_{RP}) L_{ev,gl}(\omega_t) \tag{5.26}$$

The signal field is given by

$$E_{FSRS}^{(5)}(\omega_t) = \frac{1}{7}\left(\frac{i\omega_t l}{2\varepsilon_0 n(\omega_t)c}\right)\sum_{j=1}^{16} P_{FSRS,j}^{(5)}(\omega_t) \tag{5.27}$$

where the factor of 1/7 represents the orientational average for all-parallel electric field polarizations.[28]

**IVB. Response Functions for Fourier Transform 2DRR Spectroscopy**

The direct fifth-order polarization possesses 16 components when a single electronic resonance dominates the optical response. The first 2DRR polarization component, $P_{2DRR,1}^{(5)}(\omega_t)$, is given in Equation (5.7). The remaining 15 polarization components are

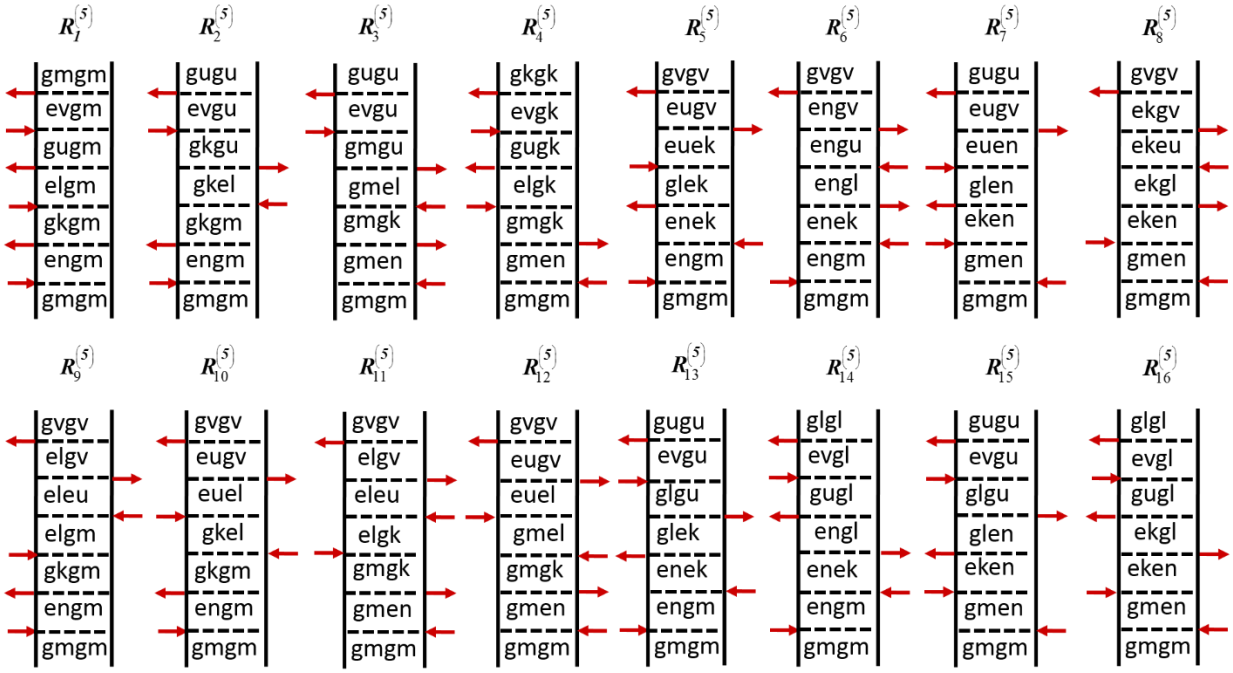


***Figure 5.16.*** *Feynman diagrams associated with the direct fifth-order 2DRR response. The indices, $g$ and $e$, represent the ground and excited electronic states, respectively, whereas dummy indices ($m$, $n$, $k$, $l$, $u$, and $v$) denote vibrational levels.*

$$\begin{aligned} P_{2DRR,2}^{(5)}(\omega_t) = -N\left(\frac{\xi_L}{\mathrm{h}}\right)^5 \left|\mu_{eg}\right|^6 \sum_{mnkluv} B_m \langle n|m\rangle\langle n|k\rangle\langle l|m\rangle\langle l|u\rangle\langle v|k\rangle\langle v|u\rangle \\ \times L_{en,gm}(\omega_L) L_{gk,gm}(\omega_t) L_{gk,el}(-\omega_L) L_{gk,gu}(\omega_t) L_{ev,gu}(\omega_L) \end{aligned} \tag{5.28}$$

$$P^{(5)}_{2DRR,3}(\omega_t) = -N\left(\frac{\xi_L}{\mathrm{h}}\right)^5 \left|\mu_{eg}\right|^6 \sum_{mnkluv} B_m \langle n|m\rangle\langle n|k\rangle\langle l|k\rangle\langle l|u\rangle\langle v|m\rangle\langle v|u\rangle \times L_{gm,en}(-\omega_L) L_{gm,gk}(\omega_t) L_{gm,el}(-\omega_L) L_{gm,gu}(\omega_t) L_{ev,gu}(\omega_L) \tag{5.29}$$

$$P^{(5)}_{2dRR,4}(\omega_t) = -N\left(\frac{\xi_L}{\mathrm{h}}\right)^5 \left|\mu_{eg}\right|^6 \sum_{mnkluv} B_m \langle n|m\rangle\langle n|k\rangle\langle l|m\rangle\langle l|u\rangle\langle v|u\rangle\langle v|k\rangle \times L_{gm,en}(-\omega_L) L_{gm,gk}(\omega_t) L_{el,gk}(\omega_L) L_{gu,gk}(\omega_t) L_{ev,gk}(\omega_L) \tag{5.30}$$

$$P^{(5)}_{2DRR,5}(\omega_t) = -N\left(\frac{\xi_L}{\mathrm{h}}\right)^5 \left|\mu_{eg}\right|^6 \sum_{mnkluv} B_m \langle n|m\rangle\langle m|k\rangle\langle n|l\rangle\langle u|l\rangle\langle k|v\rangle\langle u|v\rangle \times L_{en,gm}(\omega_L) L_{en,ek}(\omega_t) L_{gl,ek}(-\omega_L) L_{eu,ek}(\omega_t) L_{eu,gv}(\omega_L) \tag{5.31}$$

$$P^{(5)}_{2DRR,6}(\omega_t) = -N\left(\frac{\xi_L}{\mathrm{h}}\right)^5 \left|\mu_{eg}\right|^6 \sum_{mnkluv} B_m \langle n|m\rangle\langle k|m\rangle\langle k|l\rangle\langle u|l\rangle\langle u|v\rangle\langle n|v\rangle \times L_{en,gm}(\omega_L) L_{en,ek}(\omega_t) L_{en,gl}(\omega_L) L_{en,eu}(\omega_t) L_{en,gv}(\omega_L) \tag{5.32}$$

$$P^{(5)}_{2DRR,7}(\omega_t) = -N\left(\frac{\xi_L}{\mathrm{h}}\right)^5 \left|\mu_{eg}\right|^6 \sum_{mnkluv} B_m \langle n|m\rangle\langle k|m\rangle\langle k|l\rangle\langle u|l\rangle\langle n|v\rangle\langle u|v\rangle \times L_{gm,en}(-\omega_L) L_{ek,en}(\omega_t) L_{gl,en}(-\omega_L) L_{eu,en}(\omega_t) L_{eu,gv}(\omega_L) \tag{5.33}$$

$$P^{(5)}_{2DRR,8}(\omega_t) = -N\left(\frac{\xi_L}{\mathrm{h}}\right)^5 \left|\mu_{eg}\right|^6 \sum_{mnkluv} B_m \langle n|m\rangle\langle k|m\rangle\langle n|l\rangle\langle u|l\rangle\langle u|v\rangle\langle k|v\rangle \times L_{gm,en}(-\omega_L) L_{ek,en}(\omega_t) L_{ek,gl}(\omega_L) L_{ek,eu}(\omega_t) L_{ek,gv}(\omega_L) \tag{5.34}$$

$$P^{(5)}_{2DRR,9}(\omega_t) = -N\left(\frac{\xi_L}{\mathrm{h}}\right)^5 \left|\mu_{eg}\right|^6 \sum_{mnkluv} B_m \langle n|m\rangle\langle n|k\rangle\langle l|k\rangle\langle u|m\rangle\langle u|v\rangle\langle l|v\rangle \times L_{en,gm}(\omega_L) L_{gk,gm}(\omega_t) L_{el,gm}(\omega_L) L_{el,eu}(\omega_t) L_{el,gv}(\omega_L) \tag{5.35}$$

$$P^{(5)}_{2DRR,10}(\omega_t) = -N\left(\frac{\xi_L}{\mathrm{h}}\right)^5 \left|\mu_{eg}\right|^6 \sum_{mnkluv} B_m \langle n|m\rangle\langle n|k\rangle\langle l|m\rangle\langle u|k\rangle\langle l|v\rangle\langle u|v\rangle \times L_{en,gm}(\omega_L) L_{gk,gm}(\omega_t) L_{gk,el}(-\omega_L) L_{eu,el}(\omega_t) L_{eu,gv}(\omega_L) \tag{5.36}$$

$$P^{(5)}_{2DRR,11}(\omega_t) = -N\left(\frac{\xi_L}{\mathrm{h}}\right)^5 \left|\mu_{eg}\right|^6 \sum_{mnkluv} B_m \langle n|m\rangle\langle n|k\rangle\langle l|m\rangle\langle u|k\rangle\langle u|v\rangle\langle l|v\rangle \times L_{gm,en}(-\omega_L) L_{gm,gk}(\omega_t) L_{el,gk}(\omega_L) L_{el,eu}(\omega_t) L_{el,gv}(\omega_L) \tag{5.37}$$

$$P^{(5)}_{2DRR,12}(\omega_t) = -N\left(\frac{\xi_L}{\mathrm{h}}\right)^5 \left|\mu_{eg}\right|^6 \sum_{mnkluv} B_m \langle n|m\rangle\langle n|k\rangle\langle l|k\rangle\langle u|m\rangle\langle l|v\rangle\langle u|v\rangle \times L_{gm,en}(-\omega_L) L_{gm,gk}(\omega_t) L_{gm,el}(-\omega_L) L_{eu,el}(\omega_t) L_{eu,gv}(\omega_L) \tag{5.38}$$

$$P^{(5)}_{2DRR,13}(\omega_t) = -N\left(\frac{\xi_L}{\mathrm{h}}\right)^5 \left|\mu_{eg}\right|^6 \sum_{mnkluv} B_m \langle n|m\rangle\langle k|m\rangle\langle n|l\rangle\langle k|u\rangle\langle v|l\rangle\langle v|u\rangle \times L_{en,gm}(\omega_L) L_{en,ek}(\omega_t) L_{gl,ek}(-\omega_L) L_{gl,gu}(\omega_t) L_{ev,gu}(\omega_L) \tag{5.39}$$

$$P^{(5)}_{2DRR,14}(\omega_t) = -N\left(\frac{\xi_L}{\mathrm{h}}\right)^5 \left|\mu_{eg}\right|^6 \sum_{mnkluv} B_m \langle n|m\rangle\langle k|m\rangle\langle k|l\rangle\langle n|u\rangle\langle v|u\rangle\langle v|l\rangle \times L_{en,gm}(\omega_L) L_{en,ek}(\omega_t) L_{en,gl}(\omega_L) L_{gu,gl}(\omega_t) L_{ev,gl}(\omega_L) \tag{5.40}$$

$$P^{(5)}_{2DRR,15}(\omega_t) = -N\left(\frac{\xi_L}{\mathrm{h}}\right)^5 \left|\mu_{eg}\right|^6 \sum_{mnkluv} B_m \langle n|m\rangle\langle k|m\rangle\langle k|l\rangle\langle n|u\rangle\langle v|l\rangle\langle v|u\rangle \times L_{gm,en}(-\omega_L) L_{ek,en}(\omega_t) L_{gl,en}(-\omega_L) L_{gl,gu}(\omega_t) L_{ev,gu}(\omega_L) \tag{5.41}$$

$$P^{(5)}_{2DRR,16}(\omega_t) = -N\left(\frac{\xi_L}{\mathrm{h}}\right)^5 \left|\mu_{eg}\right|^6 \sum_{mnkluv} B_m \langle n|m\rangle\langle k|m\rangle\langle n|l\rangle\langle k|u\rangle\langle v|u\rangle\langle v|l\rangle \times L_{gm,en}(-\omega_L) L_{ek,en}(\omega_t) L_{ek,gl}(\omega_L) L_{gu,gl}(\omega_t) L_{ev,gl}(\omega_L) \tag{5.42}$$

The signal field is given by

$$E^{(5)}_{2DRR}(\omega_t) = \frac{1}{7}\left(\frac{i\omega_t l}{2\varepsilon_0 n(\omega_t) c}\right)\sum_{j=1}^{16} P^{(5)}_{2DRR,j}(\omega_t) \tag{5.43}$$

where the factor of 1/7 represents the orientational average for all-parallel electric field polarizations.[28]

## IVC. Response Functions for Cascades in FSRS Experiments

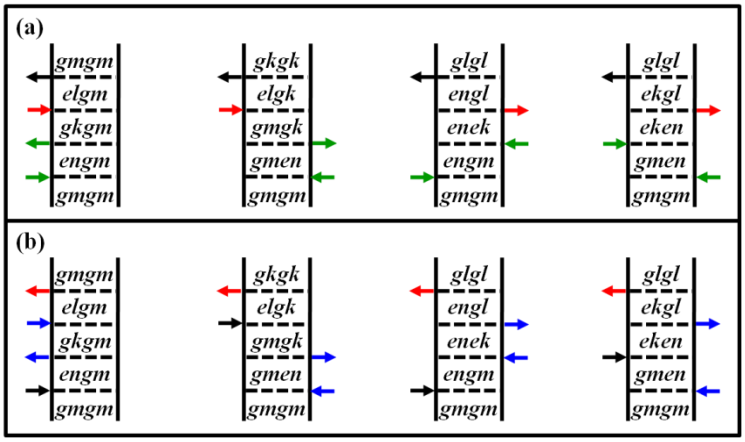


***Figure 5.17.*** *Feynman diagrams associated with (a) pump-probe and (b) CSRS components to FSRS cascades written in a sum-over-states representation. The indices, $g$ and $e$, represent the ground and excited electronic states, respectively, whereas dummy indices ($m$, $n$, $k$, and $l$) denote vibrational levels. Field-matter interactions are color-coded as follows: actinic pump is green; Raman pump is blue; Stokes is red; radiated signal field is red; the field radiated at the intermediate step in the cascade is black.*

In this section, we obtain an expression for the signal field generated by third-order cascades with intermediate phase-matching conditions, $\mathbf{k}_1-\mathbf{k}_2+\mathbf{k}_5$ and $\mathbf{k}_3-\mathbf{k}_4+\mathbf{k}_5$. The two processes essentially permute the type of nonlinearity that occurs on the two molecules involved in the cascade. A pump-probe-like response precedes a coherent Stokes Raman scattering (CSRS) process in cascade 1, whereas the sequence is reversed in cascade 2. Below, we present polarization components for each process, then combine them in an expression for the cascaded signal field.

The pump-probe-like polarization components of the solute are given by

$$P^{(3)}_{Solute,1,PP}\left(\omega_t\right) = iN\frac{\xi^2_{AP}\xi_{St}\left|\mu_{eg}\right|^4}{\mathrm{h}^3}\sum_{mnkl}B_m\left\langle n\middle|m\right\rangle\left\langle n\middle|k\right\rangle\left\langle l\middle|k\right\rangle\left\langle l\middle|m\right\rangle \times L_{en,gm}\left(\omega_{AP}\right)D_{gkgm}\left(\tau_1\right)L_{el,gm}\left(\omega_t\right) \tag{5.44}$$

$$P^{(3)}_{Solute,2,PP}(\omega_t) = iN\frac{\xi^2_{AP}\xi_{St}\left|\mu_{eg}\right|^4}{\mathrm{h}^3}\sum_{mnkl} B_m \langle n|m\rangle\langle n|k\rangle\langle l|m\rangle\langle l|k\rangle \times L_{gm,en}(-\omega_{AP}) D_{gm,gk}(\tau_1) L_{el,gk}(\omega_t) \quad (5.45)$$

$$P^{(3)}_{Solute,3,PP}(\omega_t) = iN\frac{\xi^2_{AP}\xi_{St}\left|\mu_{eg}\right|^4}{\mathrm{h}^3}\sum_{mnkl} B_m \langle n|m\rangle\langle k|m\rangle\langle k|l\rangle\langle n|l\rangle \times L_{en,gm}(\omega_{AP}) D_{en,ek}(\tau_1) L_{en,gl}(\omega_t) \quad (5.46)$$

$$P^{(3)}_{Solute,4,PP}(\omega_t) = iN\frac{\xi^2_{AP}\xi_{St}\left|\mu_{eg}\right|^4}{\mathrm{h}^3}\sum_{mnkl} B_m \langle n|m\rangle\langle k|m\rangle\langle n|l\rangle\langle k|l\rangle \times L_{gm,en}(-\omega_{AP}) D_{ek,en}(\tau_1) L_{ek,gl}(\omega_t) \quad (5.47)$$

The CSRS polarization components for the solute are

$$P^{(3)}_{Solute,1,CSRS}(\omega_t) = -N\frac{\xi^2_{RP}\xi_{St}\left|\mu_{eg}\right|^4}{\mathrm{h}^3}\sum_{mnkl} B_m \langle n|m\rangle\langle n|k\rangle\langle l|k\rangle\langle l|m\rangle \times L_{en,gm}(\omega_t) J_{gk,gm}(\omega_t - \omega_{RP}) L_{el,gm}(\omega_t) \quad (5.48$$

$$P^{(3)}_{Solute,2,CSRS}(\omega_t) = -N\frac{\xi^2_{RP}\xi_{St}\left|\mu_{eg}\right|^4}{\mathrm{h}^3}\sum_{mnkl} B_m \langle n|m\rangle\langle n|k\rangle\langle l|m\rangle\langle l|k\rangle \times L_{gm,en}(-\omega_{RP}) J_{gm,gk}(\omega_t - \omega_{RP}) L_{el,gk}(\omega_t) \quad (5.49)$$

$$P^{(3)}_{Solute,3,CSRS}(\omega_t) = -N\frac{\xi^2_{RP}\xi_{St}\left|\mu_{eg}\right|^4}{\mathrm{h}^3}\sum_{mnkl} B_m \langle n|m\rangle\langle k|m\rangle\langle k|l\rangle\langle n|l\rangle \times L_{en,gm}(\omega_t) J_{en,ek}(\omega_t - \omega_{RP}) L_{en,gl}(\omega_t) \quad (5.50)$$

$$P^{(3)}_{Solute,4,CSRS}(\omega_t) = -N\frac{\xi^2_{RP}\xi_{St}\left|\mu_{eg}\right|^4}{\mathrm{h}^3}\sum_{mnkl} B_m \langle n|m\rangle\langle k|m\rangle\langle n|l\rangle\langle k|l\rangle \times L_{gm,en}(-\omega_{RP}) J_{ek,en}(\omega_t - \omega_{RP}) L_{ek,gl}(\omega_t) \quad (5.51)$$

The cascaded signal field generated by the solute can be written as

$$E_{Solute-Solute,Cascade}(\omega_t) = \frac{1}{25}\left(\frac{i\omega_t l}{2\varepsilon_0 n(\omega_t) c}\right)^2 \sum_{m=1}^{4}\sum_{n=1}^{4} \xi_{St}^{-1} P^{(3)}_{Solute,m,PP}(\omega_t) P^{(3)}_{Solute,n,CSRS}(\omega_t) \quad (5.52)$$

The pump-probe-like polarization components of the solvent are given by

$$P^{(3)}_{Solv,1,PP}\left(\omega_t\right) = -iN_{Solv}\frac{\xi^2_{AP}\xi_{St}}{\mathrm{h}}\left|\alpha\right|^2\sum_{mk}D_{gk,gm}\left(\tau_1\right) \tag{5.53}$$

$$P^{(3)}_{Solv,2,PP}\left(\omega_t\right) = -iN_{Solv}\frac{\xi^2_{AP}\xi_{St}}{\mathrm{h}}\left|\alpha\right|^2\sum_{mk}D_{gm,gk}\left(\tau_1\right) \tag{5.54}$$

The CSRS polarization components for the solvent are

$$P^{(3)}_{Solv,1,CSRS}\left(\omega_t\right) = N_{Solv}\frac{\xi^2_{AP}\xi_{ST}}{\mathrm{h}}\left|\alpha\right|^2\sum_{mk}J_{gk,gm}\left(\tau_1\right) \tag{5.55}$$

$$P^{(3)}_{Solv,2,CSRS}\left(\omega_t\right) = N_{Solv}\frac{\xi^2_{AP}\xi_{ST}}{\mathrm{h}}\left|\alpha\right|^2\sum_{mk}J_{gm,gk}\left(\tau_1\right) \tag{5.56}$$

The cascaded signal field generated by a combination of the solute and solvent is given by

$$\begin{aligned} E_{Solute-Solvent,Cascade}(\omega_t) = \frac{1}{25}\left(\frac{i\omega_t l}{2\varepsilon_0 n(\omega_t)c}\right)^2\sum_{m=1}^{2}\sum_{n=1}^{4}\xi_{St}^{-1}\Big\{&P^{(3)}_{Solute,n,PP}(\omega_t)P^{(3)}_{Solvent,m,CSRS}(\omega_t) \\ &+P^{(3)}_{Solvent,m,PP}(\omega_t)P^{(3)}_{Solute,n,CSRS}(\omega_t)\Big\} \end{aligned} \tag{5.57}$$

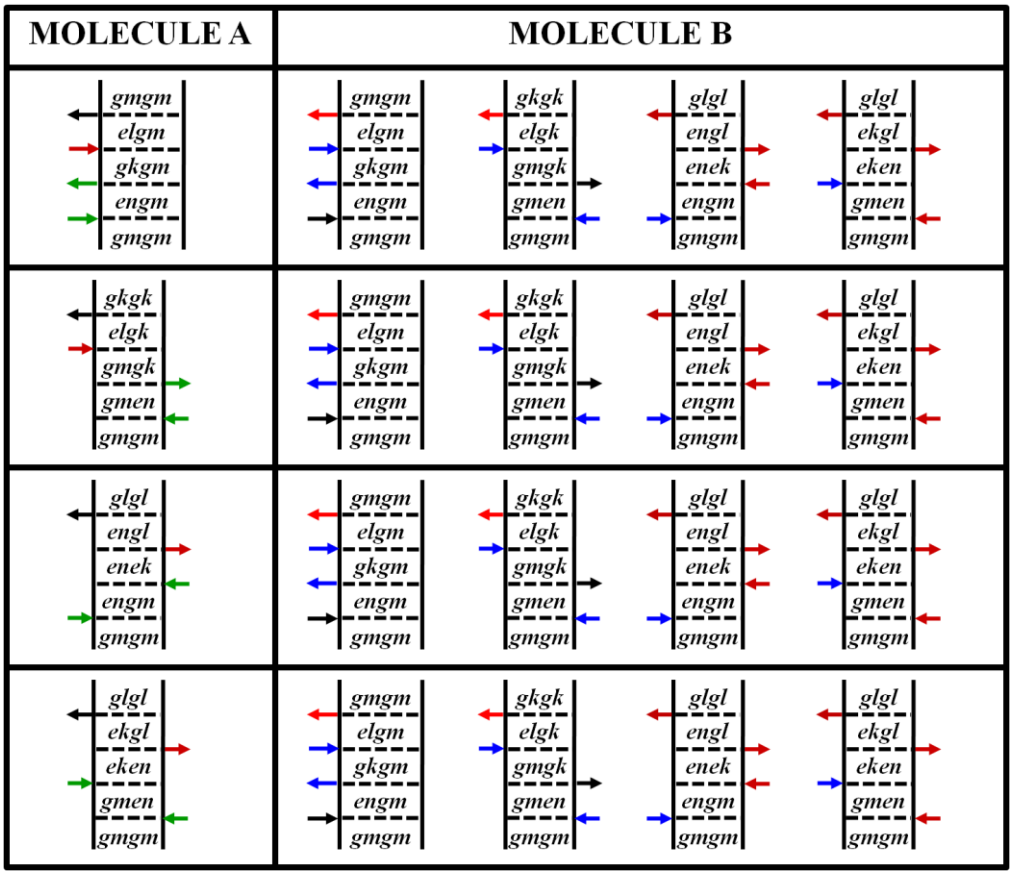


***Figure 5.18.*** *Feynman diagrams associated with third-order cascades with the intermediate phase-matching condition* $\mathbf{k}_1$-$\mathbf{k}_2$+$\mathbf{k}_5$. *The indices,* $g$ *and* $e$, *represent the ground and excited electronic states, respectively, whereas dummy indices (*$m$, $n$, $k$, *and* $l$*) denote vibrational levels. Field-matter interactions are color-coded as follows: actinic pump is green; Raman pump is blue; Stokes is red; radiated signal field is red; the field radiated at the intermediate step in the cascade is black.*

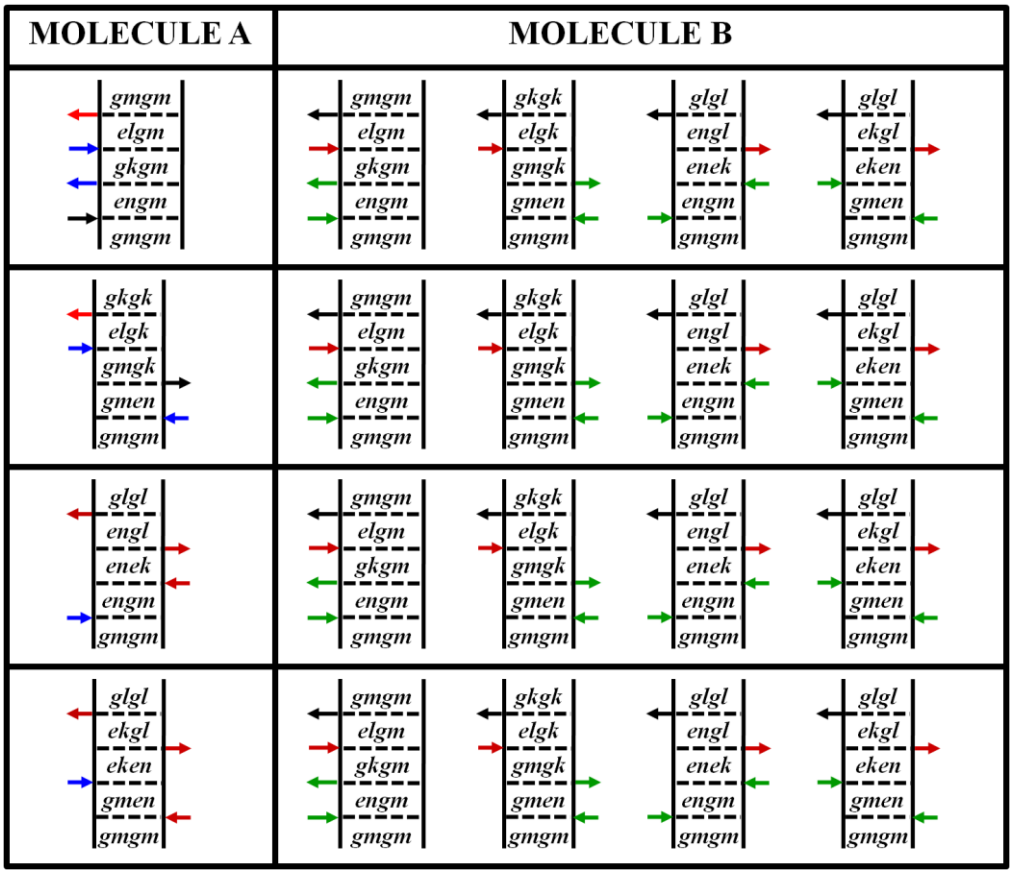


***Figure 5.19.*** *Feynman diagrams associated with third-order cascades with the intermediate phase-matching condition* $\mathbf{k}_3$-$\mathbf{k}_4$+$\mathbf{k}_5$. *The indices,* $g$ *and* $e$, *represent the ground and excited electronic states, respectively, whereas dummy indices (*$m$, $n$, $k$, *and* $l$*) denote vibrational levels. Field-matter interactions are color-coded as follows: actinic pump is green; Raman pump is blue; Stokes is red; radiated signal field is red; the field radiated at the intermediate step in the cascade is black.*

## IVD. Response Functions for Cascades in Fourier Transform 2DRR Spectroscopy

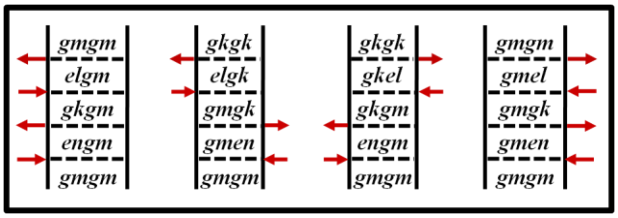


***Figure 5.20.*** *Feynman diagrams associated with 2DRR cascades written in a sum-over-states representation. The indices g and e refer to the ground and excited electronic states, respectively.*

The four third-order response functions associated with the solute are given by

$$P^{(3)}_{Solute,1}(\omega_t) = N\left(\frac{\xi_L}{\mathrm{h}}\right)^3 \left|\mu_{eg}\right|^4 \sum_{mnkl} B_m \langle n|m\rangle\langle n|k\rangle\langle l|k\rangle\langle l|m\rangle \times L_{en,gm}(\omega_L) L_{gkgm}(\omega_t) L_{el,gm}(\omega_L) \tag{5.58}$$

$$P^{(3)}_{Solute,2}(\omega_t) = N\left(\frac{\xi_L}{\mathrm{h}}\right)^3 \left|\mu_{eg}\right|^4 \sum_{mnkl} B_m \langle n|m\rangle\langle n|k\rangle\langle l|m\rangle\langle l|k\rangle \times L_{gm,en}(-\omega_L) L_{gm,gk}(\omega_t) L_{el,gk}(\omega_L) \tag{5.59}$$

$$P^{(3)}_{Solute,3}(\omega_t) = N\left(\frac{\xi_L}{\mathrm{h}}\right)^3 \left|\mu_{eg}\right|^4 \sum_{mnkl} B_m \langle n|m\rangle\langle k|m\rangle\langle k|l\rangle\langle n|l\rangle \times L_{en,gm}(\omega_L) L_{en,ek}(\omega_t) L_{en,gl}(\omega_L) \tag{5.60}$$

$$P^{(3)}_{Solute,4}(\omega_t) = N\left(\frac{\xi_L}{\mathrm{h}}\right)^3 \left|\mu_{eg}\right|^4 \sum_{mnkl} B_m \langle n|m\rangle\langle k|m\rangle\langle n|l\rangle\langle k|l\rangle \times L_{gm,en}(-\omega_L) L_{ek,en}(\omega_t) L_{ek,gl}(\omega_L) \tag{5.61}$$

The cascaded signal field generated by the solute only is given by

$$E_{Solute-Solute,Seq}(\omega_t) = \left(\frac{i2\pi l\omega_t}{n(\omega_t)c}\right)^2 \sum_{\alpha=1}^{4}\sum_{\beta=1}^{4}\left\{P^{(3)}_{Solute,\alpha}(\omega_t) + \left[P^{(3)}_{Solute,\alpha}(\omega_t)\right]^*\right\} P^{(3)}_{Solute,\beta}(\omega_t) \tag{5.62}$$

$$E_{Solute-Solute,Par}(\omega_t) = \left(\frac{i2\pi l\omega_t}{n(\omega_t)c}\right)^2 \sum_{A=1}^{4}\sum_{B=1}^{4} P^{(3)}_{Solute,A}(\omega_t) P^{(3)}_{Solute,B}(\omega_t) \tag{5.63}$$

The two third-order response functions associated with the solvent are written as

$$P^{(3)}_{Solv,1}\left(\omega_\tau\right) = -N_{Solv}\frac{\xi_L^{\ 3}}{\mathrm{h}}\left|\alpha\right|^2\sum_{mk}L_{gk,gm}\left(\omega_\tau\right) \tag{5.64}$$

$$P^{(3)}_{Solv,2}\left(\omega_\tau\right) = -N_{Solv}\frac{\xi_L^{\ 3}}{\mathrm{h}}\left|\alpha\right|^2\sum_{mk}L_{gm,gk}\left(\omega_\tau\right) \tag{5.65}$$

where $\omega_\tau$ is conjugate to an experimentally controlled delay time.

The cascaded signal field generated by a combination of the solute and solvent molecules is given by

$$E_{Solute-Solvent,Seq1}(\omega_t) = \left(\frac{i2\pi l\omega_t}{n(\omega_t)c}\right)^2\sum_{\alpha=1}^{2}\sum_{\beta=1}^{4}\left\{P^{(3)}_{Solvent,\alpha}(\omega_t) + \left[P^{(3)}_{Solvent,\alpha}(\omega_t)\right]^*\right\}P^{(3)}_{Solute,\beta}(\omega_t) \tag{5.66}$$

$$E_{Solute-Solvent,Seq2}(\omega_t) = \left(\frac{i2\pi l\omega_t}{n(\omega_t)c}\right)^2\sum_{\alpha=1}^{2}\sum_{\beta=1}^{4}\left\{P^{(3)}_{Solute,\beta}(\omega_t) + \left[P^{(3)}_{Solute,\beta}(\omega_t)\right]^*\right\}P^{(3)}_{Solvent,\alpha}(\omega_t) \tag{5.67}$$

$$\begin{aligned}E_{Solute-Solvent,Par}\left(\omega_t\right) = &\left(\frac{i2\pi l\omega_t}{n(\omega_t)c}\right)^2\\ &\times\sum_{A=1}^{2}\sum_{B=1}^{4}\left\{P^{(3)}_{Solvent,A}\left(\omega_t\right)P^{(3)}_{Solute,B}\left(\omega_t\right) + P^{(3)}_{Solute,B}\left(\omega_t\right)P^{(3)}_{Solvent,A}\left(\omega_t\right)\right\}\end{aligned} \tag{5.68}$$

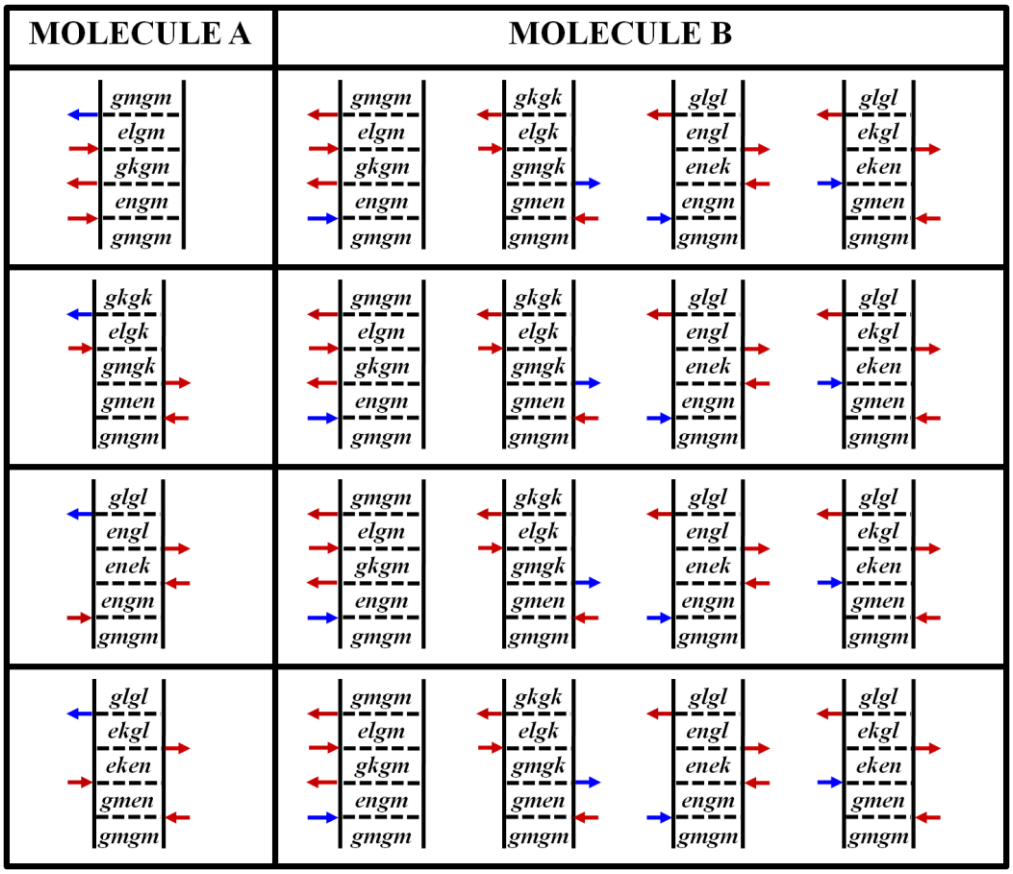


***Figure 5.21.*** *Summary of sequential cascades with the intermediate phase matching condition k1-k2+k3 on molecule A. The field radiated by molecule A (blue arrow) induces one of the first two field-matter interactions on molecule B (blue arrow). Feynman diagrams for molecules A and B involve sums over independent dummy indices for vibrational levels (m, n, k, l).*

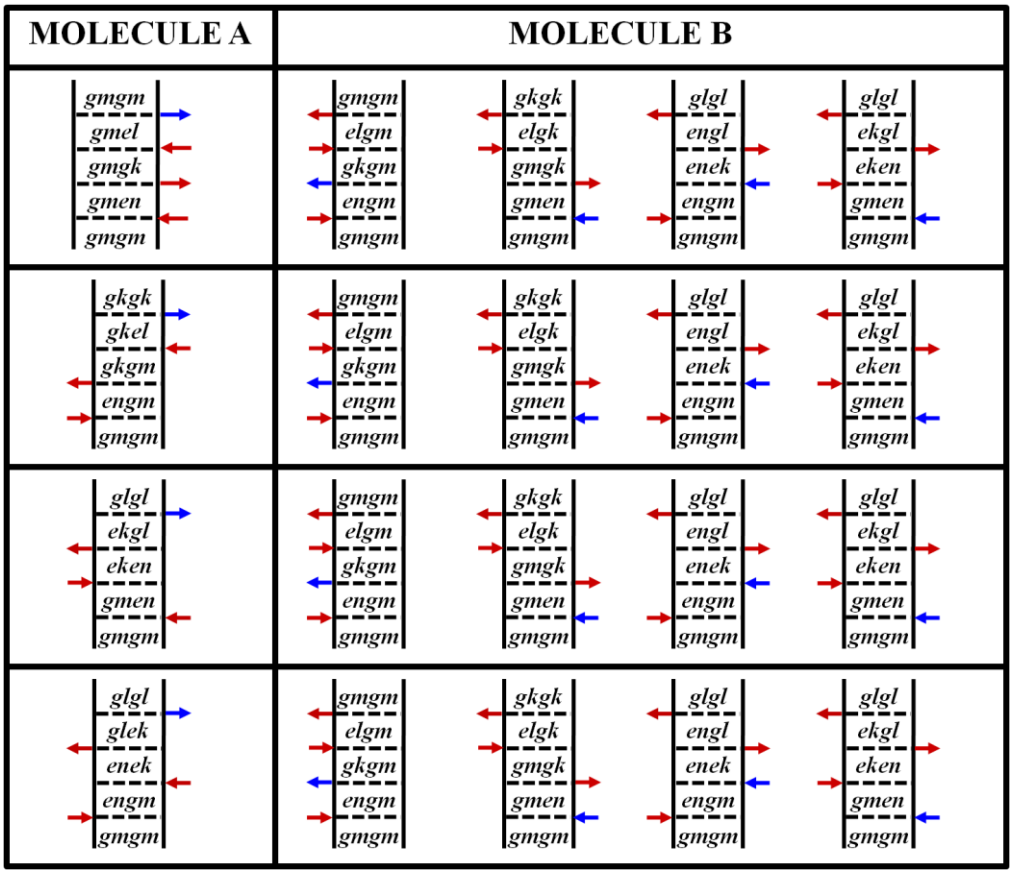


***Figure 5.22.*** *Summary of sequential cascades with the intermediate phase matching condition, -* $\mathbf{k}_1+\mathbf{k}_2+\mathbf{k}_4$*. The field radiated by molecule A (blue arrow) induces one of the first two field-matter interactions on molecule B (blue arrow). Changing the signs of the wavevectors for pulses 1, 2, and 4 translates into complex conjugation of the term in the response function associated with molecule A. Feynman diagrams for molecules A and B involve sums over independent dummy indices for vibrational levels (m, n, k, l).*

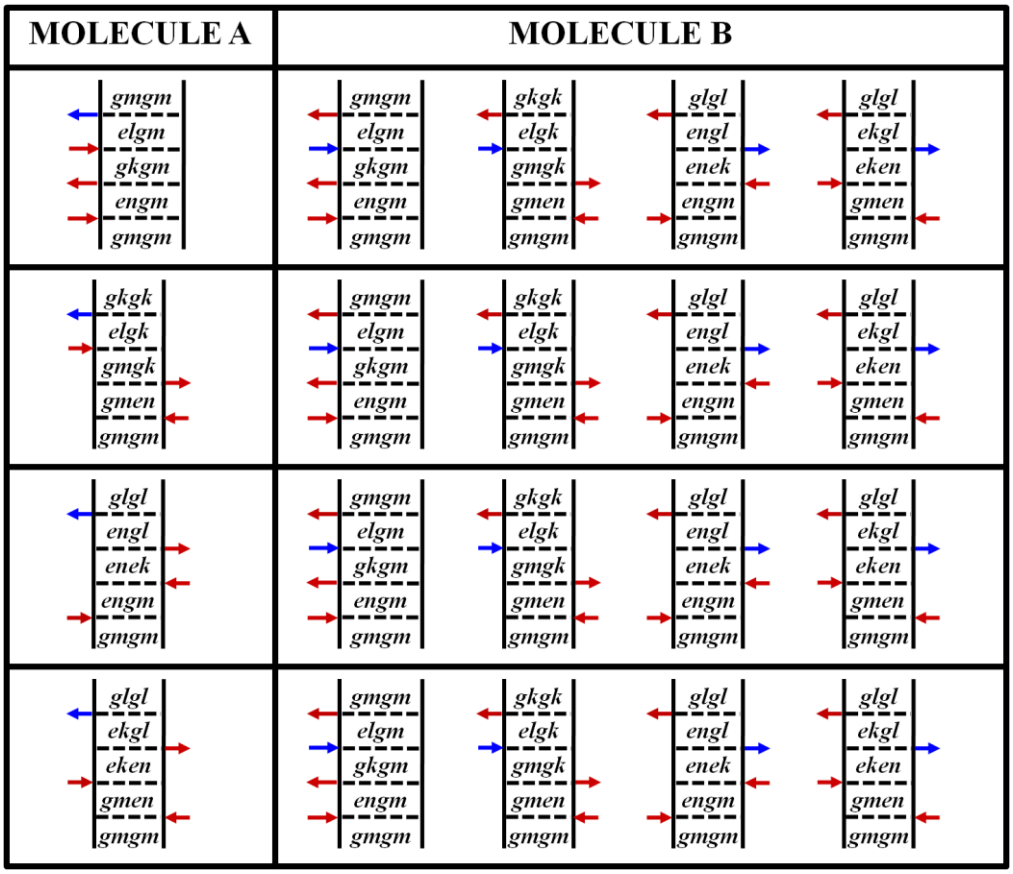


***Figure 5.23.*** *Parallel cascades with the intermediate phase matching condition* $\mathbf{k}_1$-$\mathbf{k}_2$+$\mathbf{k}_5$ *and* $\mathbf{k}_3$-$\mathbf{k}_4$+$\mathbf{k}_5$ *on molecule A are both summarized here. The field radiated by molecule A (blue arrow) induces the third field-matter interaction on molecule B (blue arrow). Feynman diagrams for molecules A and B involve sums over independent dummy indices for vibrational levels (m, n, k, l).*

## V. Concluding Remarks

We have run model calculations for p-nitroaniline in acetonitrile, methanol, and dichloromethane for FSRS and 2DRR experiments under a variety of conditions. By separately investigating solute-solute and solute-solvent interactions, we have been able to elucidate the significant impact the cascades can have on the measured signal. A commonly held misconception is that the solvent mainly plays a spectator role with respect to the incident laser pulses when it has electronic resonances far from the carrier frequencies, but caution should be observed. Illustrated in Figure 5.13, solute-solvent interactions can be the dominant artifact of a 2DRR measurement and have signal strengths up to 60% greater than the direct signal.

Perhaps most surprising, the FSRS experiment is not immune to cascaded third-order signals. The cascaded signal in Figure 5.7 is approximately 80% of the direct signal. Due to destructive interference, resonances in the combined spectrum are reduced by nearly 20% of the direct response. Qualitatively, the total FSRS signal is perceptibly affected by artifacts. Solvent resonances are comparable to solute resonances and vibrational coherence amplitudes are appreciably larger than observed in the direct spectrum.

Too often the assumption is made that reducing solute concentrations to mitigate the effect of solute-solute cascades is a sufficient precaution in preventing artifacts from contaminating the desired signal. However, solvent concentration and a moderate Raman cross-section are ample conditions for nonlinearities with non-negligible solvent contributions. Affecting experimental parameters for the solute cannot diminish all of the cascading signals. For example, the direct and solute-solvent signals both scale linearly with solute number density, thus such artifacts are immutable to concentration of the solution. Additionally, solute-solvent cascades intensify with vibrational mode matching between the solute and solvent.

In previous work, we showed that molecules with large mode displacements are good candidates for investigations using FSRS and 2DRR techniques. In part, Frank-Condon active modes with large displacements mitigate artifacts in weakly scattering solvents, but Figures 5.3 and 9 confirm our early hypothesis that solute-solute cascaded signals can frustrate measurements of molecules with small displacements ($d<1$). Figures 5.5 and 5.11 demonstrate a preference for moderate mode displacements when the solvent has a significant Raman cross-section and/or vibrational modes coincident with the solute. In broader terms, investigators should not allow assumptions to dictate the quality of experimental results but rather take steps to rule out the possibility of artifacts.

## REFERENCES


1. Laubereau, A.; Kaiser, W., Vibrational Dynamics of Liquids and Solids Investigated by Picosecond Light Pulses. *Rev. Mod. Phys.* **1978,** *50*, 607-665.

2. Hesp, B. H.; Wiersma, D. A., Vibrational Relaxation in Neat Crystals of Naphthalene by Picosecond CARS. *Chem. Phys. Lett.* **1980,** *75*, 423-426.

3. Velsko, S.; Trout, J.; Hochstrasser, R. M., Quantum Beating of Vibrational Factor Group Components in Molecular Solids *J. Chem. Phys.* **1983,** *79*, 2114-2120.

4. Schosser, C. L.; Dlott, D. D., A Picosecond CARS Study of Vibron Dynamics in Molecular Crystals: Temperature Dependence of Homogeneous and Inhomogeneous Linewidths *J. Chem. Phys.* **1984,** *80*, 1394-1406.

5. Loring, R. F.; Mukamel, S., Selectivity in Coherent Transient Raman Measurements of Vibrational Dephasing in Liquids. *J. Chem. Phys.* **1985,** *83*, 2116-2126.

6. Tanimura, Y.; Mukamel, S., Two-Dimensional Femtosecond Vibrational Spectroscopy of Liquids. *J. Chem. Phys.* **1993,** *99*, 9496-9511.

7. Berg, M.; Vanden Bout, D. A., Ultrafast Raman Echo Measurements of Vibrational Dephasing and the Nature of Solvent−Solute Interactions. *Acc. Chem. Res.* **1997,** *30*, 65-71.

8. Ivanecky III, J. E.; Wright, J. C., An investigation of the origins and efficiencies of higher-order nonlinear spectroscopic processes *Chem. Phys. Lett.* **1993,** *206*, 437-444.

9. Tominaga, K.; Yoshihara, K., Fifth-Order Nonlinear Spectroscopy on the Low-Frequency Modes of Liquid $CS_2$ *J. Chem. Phys.* **1996,** *104*, 4419-4426.

10. Steffen, T.; Duppen, K., Time Resolved Four- and Six-wave Mixing in Liquids. II. Experiments *J. Chem. Phys.* **1997,** *106*, 3854-3864.

11. Blank, D. A.; Kaufman, L. J.; Fleming, G. R., Fifth-order two-dimensional Raman spectra ofCS 2 are dominated by third-order cascades *J. Chem. Phys.* **1999,** *111*, 3105-3114.

12. Kubarych, K. J.; Milne, C. J.; Lin, S.; Astinov, V.; Miller, R. J. D., Diffractive optics-based six-wave mixing:Heterodyne detection of the full $c^{(5)}$ tensor of liquid $CS_2$. *J. Chem. Phys.* **2002,** *116*, 2016-2042.

13. Kaufman, L. J.; Heo, J.; Ziegler, L. D.; Fleming, G. R., Heterodyne-Detected Fifth-Order Nonresonant Raman Scattering from Room Temperature CS2. *Phys. Rev. Lett.* **2002,** *88*, 207402:1-4.

14. Mukamel, S., *Principles of Nonlinear Optical Spectroscopy*. Oxford University Press: New York, 1995.

15. Ulness, D. J.; Kirkwood, J. C.; Albrecht, A. C., Competitive Events in Fifth Order Time Resolved Coherent Raman Scattering: Direct Versus Sequential Processes. *J. Chem. Phys.* **1998,** *108,* 3897-3902.

16. Jansen, T. I. C.; Snijders, J. G.; Duppen, K., Interaction induced effects in the nonlinear Raman response of liquidCS 2 : A finite field nonequilibrium molecular dynamics approach *J. Chem. Phys.* **2001,** *114,* 109210-10921.

17. Mehlenbacher, R.; Lyons, B.; Wilson, K. C.; Du, Y.; McCamant, D. W., Theoretical analysis of anharmonic coupling and cascading Raman signals observed with femtosecond stimulated Raman spectroscopy *J. Chem. Phys.* **2009,** *131,* 244512.

18. Molesky, B. P.; Giokas, P. G.; Guo, Z.; Moran, A. M., Multidimensional Resonance Raman Spectroscopy by Six-Wave Mixing in the Deep UV. *J. Chem. Phys.* **2014,** *114,* 114202.

19. Hutson, W. O.; Spencer, A. P.; Harel, E., Isolated Ground-State Coherence Measured by Fifth-Order Single-Shot Two-Dimensional Electronic Spectroscopy. *J. Phys. Chem. Lett.* **2016,** *7,* 3636-3640.

20. Molesky, B. P.; Giokas, P. G.; Guo, Z.; Moran, A. M., Multidimensional Resonance Raman Spectroscopy by Six-Wave Mixing in the Deep UV. *J. Chem. Phys.* **2014,** *141,* 114202.

21. Molesky, B. P.; Guo, Z.; Moran, A. M., Femtosecond stimulated Raman spectroscopy by six-wave mixing. *J Chem Phys* **2015,** *142* (21), 212405.

22. Guo, Z.; Molesky, B. P.; Cheshire, T. P.; Moran, A. M., Elucidation of Reactive Wavepackets by Two-Dimensional Resonance Raman Spectroscopy. *J. Chem. Phys.* **2015,** *143,* 124202.

23. Molesky, B. P.; Guo, Z.; Cheshire, T. P.; Moran, A. M., Two-Dimensional Resonance Raman Spectroscopy of Oxygen- and Water-Ligated Myoglobin. *J. Chem. Phys.* **2016,** *145,* 034203.

24. Molesky, B. P.; Guo, Z.; Cheshire, T. P.; Moran, A. M., Perspective: Two-Dimensional Resonance Raman Spectroscopy *J. Chem. Phys.* **2016,** *145,* 180901.

25. Myers, A. B.; Mathies, R. A.; Tannor, D. J.; Heller, E. J., Excited State Geometry Changes from Preresonance Raman Intensities: Isoprene and Hexatriene. *J. Chem. Phys.* **1982,** *77,* 3857-3866.

26. Kelley, A. M., *Condensed-Phase Molecular Spectroscopy and Photophysics*. John Wiley & Sons: Hoboken, NJ, 2013.

27. Moran, A. M.; Kelley, A. M., Solvent effects on ground and excited electronic state structures of p-nitroaniline. *J. Chem. Phys.* **2001,** *115*, 912-924.

28. Fulmer, E. C.; Ding, F.; Zanni, M. T., Heterodyned Fifth-Order 2D-IR Spectroscopy of the Azide Ion in an Ionic Glass. *J. Chem. Phys.* **2005,** *122*, 034302.

# CHAPTER 6: ULTRAFAST SPECTROSCOPIC SIGNATURES OF COHERENT ELECTRON TRANSFER MECHANISMS IN A TRANSITION METAL COMPLEX[1]

## I. Introduction

Knowledge of coherent chemical reaction mechanisms has motivated a large body of work in the past few decades.[1-8] Interest in the role of vibronic coherence in electron transfer processes can be traced back to the earliest experimental studies of femtosecond dynamics in the bacterial photosynthetic reaction center.[1,2] This study was followed by numerous observations of similar behaviors in other biological systems; examples include photo-induced isomerization of bacteriorhodopsin[3] and photo-dissociation in myoglobin.[5] Recent advances in femtosecond laser spectroscopies have enabled more detailed investigations of coherent electron transfer mechanisms in mixed valence systems,[9] photosynthetic proteins,[10] polymer-fullerene blends,[11] and molecule-semiconductor interfaces.[12,13] A commonality in these systems is that electron transfer takes place on a time scale that is shorter than vibrational dephasing and/or solvation dynamics. Traditional second-order models should not be applied in this non-equilibrium regime.[14-17] Recurrences of the donor at the transition state may give rise to periodic bursts in the acceptor's population in some cases.[1,2,6,10,11,18] An understanding of such coherent reaction dynamics holds implications for hot electron transfer processes, which can boost solar energy conversion efficiency if properly harnessed.[19-22]

In this paper, femtosecond transient absorption spectroscopy is used to investigate the influence of vibronic coherence on electron transfer in a transition metal complex in which a

[1] This chapter previously appeared as an article in the Journal of Chemical Physics. The original citation is as follows: Z. Guo, P. G. Giokas, T. P. Cheshire, O. F. Williams, D. J. Dirkes, W. You, A. M. Moran, J. Phys. Chem. A, 120, 5773–5790 (2016)

titanium atom is bonded to three catechol ligands, $[Ti(cat)_3]^{2-}$. Strong interactions between catechol and titanium give rise to a charge transfer electronic resonance near 400 nm.[23] Following light-induced electron transfer from catechol to titanium, the strong titanium-catechol interactions also promote a fast back electron transfer (BET) from titanium to catechol.[24] The well-defined nature of $[Ti(cat)_3]^{2-}$ is leveraged to understand how the BET process initiates coherent nuclear motion in the product state. The charge transfer nature of the electronic resonance of $[Ti(cat)_3]^{2-}$ is essential for this investigation, because it guarantees significant projections of Franck-Condon active modes onto the reaction coordinate. [6,25-29] With inspiration from earlier work,[6,27-29] we use normal mode displacements determined with resonance Raman spectroscopy to parameterize a non-equilibrium model that incorporates coherent BET mechanisms.

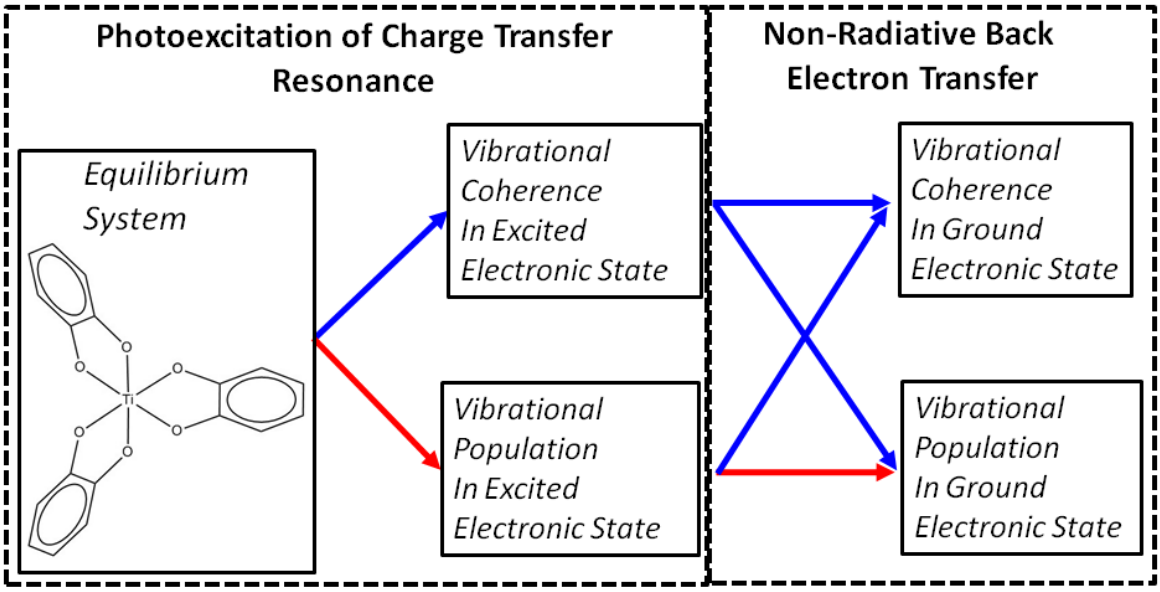


***Figure 6.1.*** *The photo-induced back-electron transfer dynamics of* $[Ti(cat)_3]^{2-}$ *can be described with four potential pathways. The pathway connected by red arrows can be described with traditional models if a Boltzmann distribution of vibrational quanta is established before back-electron transfer; however, a non-equilibrium electron transfer model is required if this condition is not satisfied. The pathways involving vibrational coherences contribute if back-electron transfer is faster than vibrational dephasing.*

Photoexcitation and BET are decomposed into four "pathways" in Figure 6.1. Traditional (equilibrium) second-order kinetic models describe the pathway connected by red arrows for thermalized excited states. The other three possibilities involve coherent nuclear motion before and/or after the BET process. Coherent nuclear motion is directly initiated by light absorption in most of the previous experimental studies discussed above (i.e., a stimulated Raman process). Bursts of population flow into the product state may be observed in such cases, and the wavepacket can retain coherence in the product state (i.e., a vibronic coherence transfer transition).[1,2,6,10,11,18] It is also possible for vibrational coherence to be initiated in the product state if the reactant does not undergo coherent nuclear motion. Fleming and Jean emphasized this point in an earlier theoretical study based on a density matrix approach.[30] The two pathways in which BET initiates vibrational coherence in the product are of primary interest in this work (i.e., paths ending on top in Figure 6.1).

In previous work, we showed that a fourth-order perturbative model can be used to simulate time-coincident electron transfer and solvation dynamics under many of the same approximations made in Marcus' theory.[31] Our model takes inspiration from an earlier non-equilibrium version of Fermi's golden rule in which explicit field-matter interactions were not used to establish the initial condition.[32] Similarly motivated models for non-equilibrium electron transfer[33] and non-secular transitions between vibrational states[34] have been presented in recent literature. Our model is distinct in that the initial condition is determined by explicit field-matter interactions, multiple promoting modes are treated, and the model is specific to an electron transfer process. In previous work, we modeled the behavior of a system initiated by light absorption using experimentally accessible parameters such as the solvation time and absorbance line width.[31] The fourth-order model revealed large discrepancies with Marcus' theory in

regimes, where the photoinitiated wavepacket traverses the point of intersection between diabatic surfaces.[31] This earlier model is applicable to systems with weak vibronic activity; however, we show in this work that the addition of quantized vibrational levels is relatively straightforward and will support a description of the coherent pathways in Figure 6.1.

**II. Model for Spectroscopy and Dynamics**

In this section, we develop a model for transient absorption spectroscopy that incorporates the four types of BET transitions defined in Figure 6.1. Similar to previous resonance Raman studies,[6,27-29] the model is developed under the assumption that the optical response and BET process depend on the same parameters because of the charge transfer nature of the electronic resonance. The model will be parameterized using a spectral fitting approach for which key equations are summarized the end of this section.

**IIA. Hamiltonian**

We employ a reduced description in which the Hamiltonian is partitioned into three components: the system ( $H_{sys}$ ), bath ( $H_{bath}$ ), and system-bath interaction ( $H_{sys-bath}$ ). The three operators may be written as

$$H_{sys} = |g\rangle\langle g| \sum_m |m\rangle\langle m| \left(E_g + E_m\right) + |e\rangle\langle e| \sum_n |n\rangle\langle n| \left(E_e + E_n\right) , \tag{6.1}$$

$$H_{bath} = \frac{1}{2} \sum_i \left[ \frac{p_i^2}{\mu_i} + \mu_i \omega_i^2 q_i^2 \right] \left[ |g\rangle\langle g| + |e\rangle\langle e| \right], \tag{6.2}$$

and

$$H_{sys-bath} = |g\rangle Q_{g,c} \langle g| + |e\rangle Q_{e,c} \langle e| . \tag{6.3}$$

The dynamics of interest in this work can be simulated by treating only the ground ( $g$ ) and lowest energy excited ( $e$ ) electronic states of the system if we assume that BET is fast

compared to transitions between excited states. The summations in $H_{sys}$ are carried out over dummy indices, $m$ and $n$, that represent quantized vibrational levels of the system. Throughout this paper, the indices $m$, $l$, and $u$ will be associated with the ground electronic state, whereas $n$, $k$, and $v$ will correspond to the excited electronic state. In the harmonic approximation, the basis vectors are direct products, $|m\rangle = \prod_{\alpha} |N_{\alpha m}\rangle$, where $N_{\alpha m}$ is the number of vibrational quanta in normal mode $\alpha$ for basis vector $m$. The bath consists of displaced harmonic oscillators for which the associated variables are written in lower case ( $\mu_i$ , $\omega_i$ , and $q_i$ ).[14-16] The collective primary oscillator coordinates in $H_{sys-bath}$ are couple to the secondary harmonic modes in $H_{bath}$ according to $Q_{g,c} = \sum_i \mu_i \omega_i^2 d_{g,i} q_i$ , where $d_{g,i}$ is the displacement of mode $i$ for the ground electronic state; an analogous formula can be written for the excited electronic state. In the present reduced description, the bath coordinates are never explicitly parameterized, because a trace is carried out over the states of the bath.[14]

Stochastic fluctuations in the energy levels of the system are handled using a time-correlation function formalism for the collective coordinates. The cumulant expansion approach may be employed, because the bath is taken to be harmonic.[14-16] In the overdamped limit, time correlation functions between the collective Brownian oscillator coordinates are related to the second term in a cumulant expansion by[14]

$$\gamma(t) = \left( \frac{2\lambda k_B T}{\hbar^2 \Lambda^2} - i \frac{\lambda}{\hbar \Lambda} \right) \left[ \exp(-\Lambda t) + \Lambda t - 1 \right], \tag{6.4}$$

where $\Lambda^{-1}$ is the time-scale of nuclear relaxation and $\lambda$ is the reorganization energy. The reorganization energy of the bath is related to the variance of fluctuations in the energy gap between ground and excited states by

$$\lambda = \frac{\Delta^2}{2k_B T}. \tag{6.5}$$

The assumption of an overdamped primary oscillator coordinate is justified for systems in which vibronic structure in the absorbance spectrum is not resolved (i.e., Gaussian absorbance line shapes). Both electron transfer and light absorbance are governed by the same reorganization energy in systems that possess charge transfer resonances.[6,25-29]

Perturbative interactions with the system occur with both laser pulses, $\vec{E} \cdot \vec{\mu}_{eg}$, and with the donor-acceptor coupling, $V_{eg}$. Explicit forms of the donor acceptor coupling and electronic transition dipole are not required, because they enter the models as constant pre-factors under the Condon approximation (this will be shown below). The system-bath coupling is not perturbative. Therefore, the model can be used to treat systems with large reorganization energies and broad spectroscopic line widths.

**IIB. Model for Transient Absorption Signals**

The model presented in this section establishes transient absorption signatures of the non-equilibrium pathways in Figure 6.1. Both populations and coherences between vibrational states can be treated by extending the fourth-order perturbative model for electron transfer developed in earlier work.[31,35] The system undergoes BET between pump and probe events in the signal component of interest. Overall, the process can be described as a sequence of six perturbative interactions. The formulas can be greatly simplified by invoking a "doorway-window" picture in which the signal is written as a product of wavepackets associated with excitation and detection. Such models have been used extensively in descriptions of transient absorption experiments.[14]

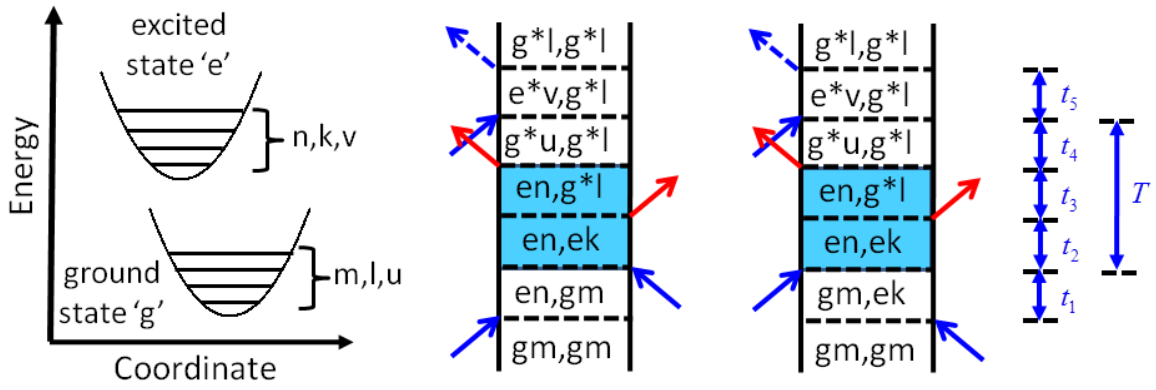


***Figure 6.2.*** *Nonlinearities associated with the hot ground state signal component can be obtained by incorporating two field-matter interactions before and after the back-electron transfer process. The time intervals,* $t_i$*, separate perturbative interactions with an external electric field,* $\hat{H}_{rad-mat}$ *(blue arrows), and the donor-acceptor coupling,* $\hat{V}$ *(red arrows). The indices* $g$ *and* $e$ *represent ground and excited states of [Ti(cat)*$_3$*]*$^{2-}$*, whereas the vibrational levels are represented by dummy indices (m, n, k, l, u, v). The indices m , l, and u are associated with the ground electronic state, whereas n, k, and v correspond to the excited electronic state. The non-radiative transition from state* $e$ *to state* $g$ *is referred to as "back-electron transfer" (i.e., the events shaded in blue).*

The doorway function incorporates dynamics that take place in the $t_1$, $t_2$, and $t_3$ time intervals shown in Figure 6.2. In this approach, we must assume that the dynamics are uncorrelated with those in the $t_4$ and $t_5$ time intervals. The assumption is good for systems in aqueous solutions, which possess fast solvation times.[36] The two components of the doorway function can be written as

$$\begin{aligned}\phi_1(t_2) = 2\frac{|\mu_{eg}|^2|V_{eg}|^2}{\hbar^4}\sum_{mnklu} B_m \langle n|m\rangle\langle k|m\rangle\langle n|u\rangle\langle k|l\rangle \mathrm{Re}\Big\{\int_0^\infty dt_1\int_0^\infty dt_2\int_0^\infty dt_3 \\ \times\exp\Big[-i\left(\omega_{eg}t_1+\omega_{nm}t_1+\omega_{nk}t_2-i\Gamma_{nk}t_2+\omega_{eg}t_3+\omega_{nl}t_3\right) \\ -\frac{1}{2}\Delta^2\left(t_1^2+t_3^2\right)-f\left(t_1,\tau,t_3\right)\Big]E^*\left(t'-t_1\right)E\left(t'\right)\Big\}\end{aligned} \tag{6.6}$$

and

$$\phi_2(t_2) = 2\frac{|\mu_{eg}|^2 |V_{eg}|^2}{\mathrm{h}^4} \sum_{mnklu} B_m \langle n|m\rangle\langle k|m\rangle\langle n|u\rangle\langle k|l\rangle \mathrm{Re}\left\{\int_0^\infty dt_1 \int_0^\infty dt_2 \int_0^\infty dt_3 \right.$$
$$\times \exp\left[-i\left(-\omega_{eg}t_1 + \omega_{mk}t_1 + \omega_{nk}t_2 - i\Gamma_{nk}t_2 + \omega_{eg}t_3 + \omega_{nl}t_3\right)\right. \quad , \tag{6.7}$$
$$\left.\left. -\frac{1}{2}\Delta^2\left(t_1^2 + t_3^2\right) + f^*(t_1,\tau,t_3)\right] E^*(t'-t_1)E(t')\right\}$$

where

$$f(t_1,t_2,t_3) = \gamma^*(t_2) - \gamma^*(t_2+t_3) - \gamma(t_1+t_2) + \gamma(t_1+t_2+t_3). \tag{6.8}$$

In Equations (6.6) and (6.7), we use the convention of Reference [37], where vibrational levels of the excited state are written in the bra of the inner products.

The five nested summations over vibrational levels will be computationally expensive to evaluate for a system with multiple vibrational modes. Analytic integration can be accomplished with inspiration from earlier descriptions of transient absorption spectroscopies.[14,38] To begin, the effect of finite laser bandwidth is incorporated by introducing the integration variable, $t' = \tau - t_2$. This approximation is justified when the temporal width of the laser pulse is short compared to the time scale of the nuclear dynamics. In addition we make the "short-time approximation" for the linear combination of line broadening functions, $\gamma(t)$, in $f(t_1,t_2,t_3)$. Similar approaches were used to described electron transfer and internal conversion in earlier work.[31,35] The two functions are then written as

$$\phi_1(\tau) = 2\frac{|\mu_{eg}|^2 |V_{eg}|^2}{\mathrm{h}^4} \sum_{mnklu} B_m \langle n|m\rangle\langle k|m\rangle\langle n|u\rangle\langle k|l\rangle \mathrm{Re}\left\{\int_0^\infty dt_1 \int_{-\infty}^\infty dt' \int_0^\infty dt_3 \right.$$
$$\times \exp\left[-i\left(\omega_{eg}t_1 + \omega_{nm}t_1 + \omega_{nk}\tau - i\Gamma_{nk}\tau + \omega_{eg}t_3 + \omega_{nl}t_3\right)\right. \tag{6.9}$$
$$\left.\left. -\frac{1}{2}\Delta^2\left(t_1^2 + t_3^2\right) - h(t_1,\tau,t_3)\right] E^*(t'-t_1)E(t')\right\}$$

and

$$\phi_2(\tau) = 2\frac{\left|\mu_{eg}\right|^2\left|V_{eg}\right|^2}{\mathrm{h}^4}\sum_{mnklu} B_m \langle k|m\rangle\langle n|m\rangle\langle n|u\rangle\langle k|l\rangle \mathrm{Re}\left\{\int_0^\infty dt_1\int_{-\infty}^\infty dt'\int_0^\infty dt_3 \right.$$
$$\times\exp\left[-\left(-\omega_{eg}t_1+\omega_{mk}t_1+\omega_{nk}\tau-i\Gamma_{nk}\tau+\omega_{eg}t_3+\omega_{nl}t_3\right)\right. \quad , \tag{6.10}$$
$$\left.\left.-\frac{1}{2}\Delta^2\left(t_1^2+t_3^2\right)+h^*\left(t_1,\tau,t_3\right)\right]E^*\left(t'-t_1\right)E\left(t'\right)\right\}$$

where

$$h\left(t_1,t_2,t_3\right) = i\frac{2\lambda}{\mathrm{h}}\left[\exp\left(-\Lambda t_2\right)-1\right]t_3+\frac{\Delta^2}{\mathrm{h}^2}\exp\left(-\Lambda t_2\right)t_1t_3\,. \tag{6.11}$$

In addition, a Gaussian laser spectrum will be assumed for convenience,

$$E\left(t\right) = \xi_L\exp\left(-i\omega_L t-w_L^2t^2/2\mathrm{h}^2\right). \tag{6.12}$$

Equations (6.9) and (6.10) set up the description in a way that parallels an earlier formulation of transient absorption signals.[14,38] The key difference in the present case is that quantized vibrational levels have been incorporated into the system Hamiltonian (i.e., underdamped intramolecular modes are not relegated to the bath).[14] The present formulas assume the same mathematical form as the earlier model if vibrational levels are removed from the first time interval between field-matter interactions, $\omega_{ge}t_1+\omega_{mn}t_1\approx\omega_{ge}t_1$. This is a good approximation if the absorbance spectrum has a broad Gaussian shape (i.e., vibronic progression is unresolved). The sum of Equations (6.9) and (6.10) then yields

$$D\left(\tau\right) = \sum_{mnklu} D_{nk\to lu}\left(\tau\right), \tag{6.13}$$

where

$$D_{nk\to ul}\left(\tau\right) = \frac{\pi^{3/2}\left|\xi_L\mu_{eg}\right|^2\left|V_{eg}\right|^2}{\mathrm{h}w_L^2\sqrt{\left(\Delta^2+w_L^2\right)\alpha^2\left(\tau\right)}}B_m\langle n|m\rangle\langle k|m\rangle\langle n|u\rangle\langle k|l\rangle$$
$$\times\exp\left[-\frac{\mathrm{h}^2\left(\omega_L-\omega_{eg}\right)^2}{4\lambda k_BT}\right]\exp\left[-\frac{\Omega^2\left(\tau\right)}{2\alpha^2\left(\tau\right)}\right]\cos\left(\omega_{nk}\tau\right)\exp\left(-\Gamma_{nk}\tau\right) \quad , \tag{6.14}$$

$$\Omega(\tau) = \Delta G_{eg}^{0} + \lambda - \mathrm{h}\omega_{nl} + \exp(-\Lambda\tau)\left[-\mathrm{h}\omega_{L} - \Delta G_{eg}^{0} - \lambda + \mathrm{h}\omega_{nl}\right], \tag{6.15}$$

and

$$\alpha^{2}(\tau) = \Delta^{2}\left[1 - \frac{\Delta^{2}}{\Delta^{2} + w_{L}^{2}}\exp(-2\Lambda\tau)\right]. \tag{6.16}$$

The laser spectrum is assumed to be narrower than the absorbance line width in $\Omega(\tau)$, because this approximation is appropriate for the experiments described in section IV. The magnitude of the free energy gap, $\Delta G_{eg}^{0}$, is equal to the difference between the peak of the absorbance spectrum, $\omega_{eg}$, and the solvent reorganization energy, $\lambda$ (i.e., $\Delta G_{eg}^{0}$ corresponds to the "electronic origin").

We resort to an empirical approach in writing the line shape of the window function. The signal associated with the "hot ground state" induced by BET undergoes a vibrational cooling process following BET, which reduces the electronic resonance frequency. An explicit treatment of such vibrational cooling mechanisms is beyond the scope of this paper. Therefore, we take the hot ground state into account with an empirical function, $\omega_{eg}^{*}(\tau)$ and $\alpha(\tau)$, that will be extracted from experimental data. The window function may then be written as

$$W_{luv}(\tau, \omega_{det}) = \frac{\langle v|u\rangle\langle v|l\rangle}{\sqrt{4\pi\lambda k_{B}T}}\exp\left\{-\frac{\left[\omega_{det} - \omega_{eg}^{*}(\tau)\right]^{2}}{2\alpha^{2}(\tau)}\right\}\cos(\omega_{ul}\tau)\exp(-\Gamma_{ul}\tau), \tag{6.17}$$

where $\omega_{det}$ is the detection frequency in the transient absorption experiment. Most generally, the transient absorption signal associated with the signal component of interest is then obtained by summing over the product of $D_{nk\to ul}(\tau)$ and $W_{luv}(\tau, \omega_{det})$,

$$S(\tau, \omega_{det}) = \sum_{mnkluv} D_{nk\to ul}(\tau) W_{luv}(\tau, \omega_{det}). \tag{6.18}$$

Equation (6.18) incorporates all four pathways in Figure 6.1. The summation can be restricted to select incoherence and coherent components.

**IIC. Spectral Fitting of Absorbance and Resonance Raman Cross Sections**

Iterative fitting of both the linear absorbance spectrum and the resonance Raman cross sections imposes constraints on the displacement of intramolecular modes, the electronic energy gap, the solvent reorganization energy, and the relative contributions of homogeneous and inhomogeneous line broadening mechanisms.[37,39] Many of these same parameters also control non-radiative BET in systems that possess charge transfer resonances.[28] We summarize essential aspects of the model in this section. Additional background on the approach can be found elsewhere.[39,40]

In a basis set of delocalized excited states, $[Ti(cat)_3]^{2-}$ possesses two allowed LMCT transitions and one (higher energy) forbidden LMCT transition; these transitions correspond to the E and A irreducible representations of the $C_3$ point group, respectively. This aspect of the electronic structure is taken into account in the expressions for the absorption and resonance Raman cross sections given in this section. The best choice of a basis set in a transition metal complex is not necessarily obvious and can even be dynamic in some cases.[41-44] Energy level fluctuations induced by solute-solvent interactions tend to localize the excited states in transition metal complexes, whereas electronic coupling between ligands promotes delocalization.[41-43] Charge transfer states should be treated as localized if the inter-ligand electronic couplings are much smaller than the energy level fluctuations. Such general rules of thumb have been applied extensively to distinguish localized electronic excitations from Frenkel excitons in molecular aggregates, molecular crystals, and photosynthetic complexes.[16,45-47,48] Frenkel exciton-like models have been adapted to transition metal complexes in recent work.[49,50] We opt for a delocalized basis set in $[Ti(cat)_3]^{2-}$, because estimates of the local (inter-ligand) electronic

couplings obtained with density functional theory are consistent with an intermediate regime, where valid arguments can be made for both basis sets (see Supporting Information). In the intermediate regime, the extend of delocalization is distributed in the ensemble.[43] We emphasize that the main conclusions drawn in this work are independent of the basis set of the system.

The linear absorbance line shape of $[Ti(cat)_3]^{2-}$ is given by

$$\sigma_A(\omega) = \frac{8\pi\omega\mu_{eg}^2}{3\mathrm{h}c} \sum_{m=1} B_m \,\mathrm{Re} \int_{-\infty}^{\infty} d\delta G(\delta) \int_0^{\infty} dt \left\langle m \middle| m(t) \right\rangle \exp\left[ i(\omega - \omega_0 - \delta + \omega_m)t - \gamma(t) \right], \qquad (6.19)$$

where $m$ is an index for a nuclear mode, $B_m$ is the Boltzmann population of the initial state, $\mu_{eg}$ is the electronic transition dipole, $\omega_m$ is the frequency associated with vibrational state $m$, $\omega_0$ is the purely electronic transition frequency (i.e., electronic origin), and $\left\langle m \middle| m(t) \right\rangle$ is a dynamic overlap integral between nuclear wavefunctions (the Fourier transform of $\left\langle m \middle| m(t) \right\rangle$ is a Franck-Condon progression). The dynamic overlap integral, $\left\langle m \middle| m(t) \right\rangle$, is controlled by the mode frequencies and dimensionless potential energy surface displacements. Fluctuations in the electronic resonance frequency induced by thermal motion in the solvent are partitioned into fast (homogeneous) and slow (inhomogeneous) components. Inhomogeneous line broadening is incorporated by integrating over the static Gaussian distribution, $G(\delta)$, whereas the homogeneous line shape is captured by the line broadening function, $\gamma(t)$ (see Equation (6.4)).

The differential resonance Raman cross section is written as

$$\sigma_{R,ml}(\omega) = \frac{8\omega_S^3 \omega_L}{15c^4} \sum_{ml} B_m \int d\omega_S \int_{-\infty}^{\infty} d\delta G(\delta) L_{ml}(\omega_L - \omega_S) \left| \alpha_{ml}(\omega_L, \delta) \right|^2, \qquad (6.20)$$

where $m$ ($l$) is an index for the initial (final) vibrational state, $\omega_L$ ($\omega_S$) is the incident (scattered) light frequency, and $L_{ml}\left(\omega_L-\omega_S\right)$ is the normalized line shape of the $m\rightarrow l$ ground-state vibrational transition. The integral with respect to the scattered frequency, $\omega_S$, extends over the full Raman emission band. The Raman polarizability of $[Ti(cat)_3]^{2-}$ is given by

$$\alpha_{ml}(\omega_L,\delta)=\frac{2\mu_{eg}^2}{\mathrm{h}}\int_0^\infty dt\left\langle l\middle|m(t)\right\rangle\exp\left[i\left(\omega_L-\omega_0-\delta+\omega_m\right)t-\gamma(t)\right]. \tag{6.21}$$

Dependence of the optical response and electron transfer rate on the same parameters has been leveraged for physical insight in earlier work.[6,27-29] The short-time approximation was taken in section IIB to obtain Gaussian functions, whereas the more general form of $\gamma(t)$ appears in $\sigma_A(\omega)$ and $\alpha_{ml}(\omega_L,\delta)$. The ratio, $\Lambda/\Delta$ is generally much less than 1 for electronic transitions in polar solvents at room temperature;[51,52] that is, significant motional narrowing is generally not observed judging by Gaussian line shapes and Stokes shifts. The classical reorganization energy associated with electron transfer, $\lambda=D^2/2k_BT$, can be computed with

$$D=\Gamma\left[\frac{1+0.85\kappa+0.88\kappa^2}{2.355+1.76\kappa}\right], \tag{6.22}$$

where the homogeneous line width is given by $\Gamma=\lambda k_BT/\mathrm{h}\Lambda$. We note that $D\approx\Delta$ when $\Lambda/\Delta<<1$ (see Equation (6.5)).

**IID. Summary of Assumptions and Parameters**

In this section, we summarize key assumptions associated with the models for transient absorption and resonance Raman experiments. Some standard approximations that are inherent to the correlation function approach are discussed in detail elsewhere.[14-16] Briefly, it is assumed in all cases that energy level fluctuations induced by the bath possess Gaussian statistics. We further assume that the thermal fluctuation amplitudes are large compared to the inverse of the

relaxation time of the bath (i.e., the slow modulation limit). In this limit, we have shown that a closely-related model can be reduced to the traditional Marcus equation at times that are long compared to solvation.[31]

The nine key assumptions made in sections IIA, IIB, and IIC are:

(i) Perturbative interactions with the donor-acceptor coupling, $V_{eg}$, and pump laser pulse, $\vec{E} \cdot \vec{\mu}_{eg}$, have been assumed. The low pulse energy of the pump laser justifies this assumption. That is, the experiments are conducted in a regime, where the dynamics are insensitive to the pulse energy. Explicit forms for the donor-acceptor coupling and transition dipole operators are not proposed, because they enters the model as prefactors that do not affect the spectroscopic line shapes under the Condon approximation.

(ii) It has been assumed that two perturbative interactions with pump laser pulse occur before the two perturbative interactions with the donor-acceptor coupling (see Figure 6.2). This assumption is justified by the large energy gap (20,100 $cm^{-1}$) between the ground and excited states (i.e., spontaneous electron transfer is negligible in the equilibrium system).

(iii) The solvent coordinate is taken to be overdamped. This assumption is justified by the broad Gaussian-like absorbance line shape.

(iv) The 17 fs pump laser pulse is assumed to be short compared to the 180 fs time scale of BET.

(v) The BET process is taken to be fast compared to transitions between excited states.

(vi) The laser spectrum is assumed to be narrower than the absorbance line width.

(vii) In section IIB, vibronic structure in $t_1$ is neglected based on the absence of a Franck-Condon progression in the absorbance spectrum.

(viii) A basis of 'delocalized' electronic states is assumed in section IIC. This basis set is justified by the similar magnitudes of the energy level fluctuations and the inter-ligand coupling, which has also been referred to as the coupling associated with 'dipole reorientation'.[53] This point is further discussed in the Supporting Information. Conclusions drawn in this work are independent of the basis set.

(ix) Modes that are Franck-Condon active in light absorption are also Franck-Condon active in the BET process, because $[Ti(cat)_3]^{2-}$ possesses a charge-transfer resonance. Numerous earlier works have leveraged this aspect of systems with charge transfer bands in studies of electron transfer mechanisms.[6,27-29]

The models used to simulate the transient absorption signals and the resonance Raman cross sections are based on the same parameters. The parameters of the models are:

(i) The free energy gap between the ground and excited state is referred to as $\Delta G_{eg}^{0}$ in the model for transient absorption in section IIB.[14,31] This quantity corresponds to the optical 0-0 frequency in the resonance Raman model ($\omega_0$ in section IIC).[28]

(ii) The solvent reorganization energy is denoted as $\lambda$. This quantity is derived from the homogeneous component of the line shape determined by the resonance Raman intensity analysis, $\lambda = D^2 / 2k_B T$ (see Equation (6.22)).

(iii) The normal mode displacements used to evaluate vibrational overlap integrals are determined with the resonance Raman intensity analysis.

(iv) The transition dipole magnitude is determined by the resonance Raman intensity analysis with constraints imposed by earlier work.[23]

(v) Knowledge of the donor-acceptor coupling, $V_{eg}$, and electric field magnitude, $\xi_L$, are not required to compute the transient absorption response, because they enter Equation (6.14) as a constant pre-factor.

(vi) The frequency, $\omega_L$, and width, $w_L$, of the pump laser pulse are determined by measuring the laser spectrum.

## III. Experimental Methods

### IIIA. Sample Preparation

Synthesis of $[Ti(cat)3]^{2-}$ is carried out using the procedure described in Reference [23]. The aqueous solutions are flowed through a wire-guided jet with a thickness of 300 μm, where the volume of the reservoir is 50 mL. The absorbance of the solution is equal to 0.5 at 408 nm in 300 μm path length. Absorbance spectra are acquired before and after experiments to confirm the absence of sample degradation.

### IIIB. Raman Spectroscopy

Resonance Raman spectra are collected with a Renishaw Via- Leica DM2500 M microscope. Excitation is accomplished using the 458, 488, and 515 nm laser lines of an argon ion laser (Spectra Physics Stabilite 2017). The 2 mW laser beams are focused into 1 mm thick cuvettes with a Leica N PLAN EPI 20x/0.4 objective lens, which is also used to collect the scattered Raman emission in a confocal geometry. A polarization scrambler is placed between the sample and detector during measurements.[39] Reabsorption of the Raman emission is corrected using an established procedure.[54] The signals are averaged for 10-20 minutes with integration times of 30 seconds. Cosmic spikes are removed using software provided by Renishaw. The solutions contain a mixture of $[Ti(cat)_3]^{2-}$ (6 mmol/L) and sulfate (850 mmol/L),

which is used as an internal standard.[55] All experiments are repeated 3 times with fresh solutions to establish reproducibility of the Raman cross sections.

**IIIC. Transient Absorption Experiments**

Transient absorption experiments are carried out with a 1 kHz, 1 mJ Ti:Sapphire laser system. Pump pulses are produced by doubling the frequency of the fundamental laser beam in a 0.25 mm thick BBO crystal. The resulting 90 μJ, 408 nm second harmonic beam is then focused with a 30 cm focal length lens into a 75 cm long, 100 μm inner diameter hollow core fiber. The fiber is housed in a stainless steel cell filled with 1.0 atm of argon gas. Compression of the pump pulse to 17 fs (FWHM of intensity) is achieved with a fused silica prism compressor with a 50 cm prism separation. Probe laser pulses are generated using either $CaF_2$ or sapphire windows. The $CaF_2$ window is used to acquire signals from 350-700 nm with the magic angle polarization condition. Isotropic and anisotropic vibrational motions are detected with probe pulses generated in sapphire. Slightly better signal-to-noise (a factor of 5-10 improvement) is achieved with sapphire because the window is stationary, whereas the $CaF_2$ window must be continuously moved to avoid damage. The probe pulses are directed to the sample with reflective optics and do not pass through the entrance window of a cuvette.

The 408 nm pump pulsed is focused onto the sample jet with a 30 cm focal length spherical mirror, whereas the continuum is relayed from the sapphire plate onto the sample using a single 5 cm focal length mirror (the continuum focuses 35 cm from the spherical mirror). The FWHM spot sizes of the 408 nm pump beam is 600 μm, whereas that of the continuum is 400 μm. The pulse energy of the pump is 200 nJ at the sample position. The angle between the two beams is 5°. Signal detection is accomplished with a CMOS array detector that is synchronized to the 1 kHz repetition rate of the laser system. The pump beam passes through a chopper wheel operated at 500 Hz, thereby enabling the acquisition of absorption spectra with and without the

pump pulse on a shot-to-shot basis. The signals are averaged over 30-40 scans of the delay line if the magic angle polarization condition is employed. Isotropic and anisotropic vibrational motions are compared by interleaving 100 scans of the delay line with parallel and perpendicular pump and probe polarizations. The interleaving of scans is achieved by mounting a half-waveplate in a motorized rotation stage (the pump beam passes through the waveplate). In all cases, a calcite polarizer is located between the sample and detector to ensure that the polarization condition is well-defined.

**IV. Results and Discussion**

In this section, resonance Raman cross sections are used to determine the electronic energy gap, reorganization energy, and vibrational mode displacements of $[Ti(cat)_3]^{2-}$. Transient absorption experiments are then used to detect vibrational coherences associated with the two pathways that end in the upper right of Figure 6.1. Finally, the BET mechanism is simulated using empirical parameters determined by fitting the resonance Raman and transient absorption data.

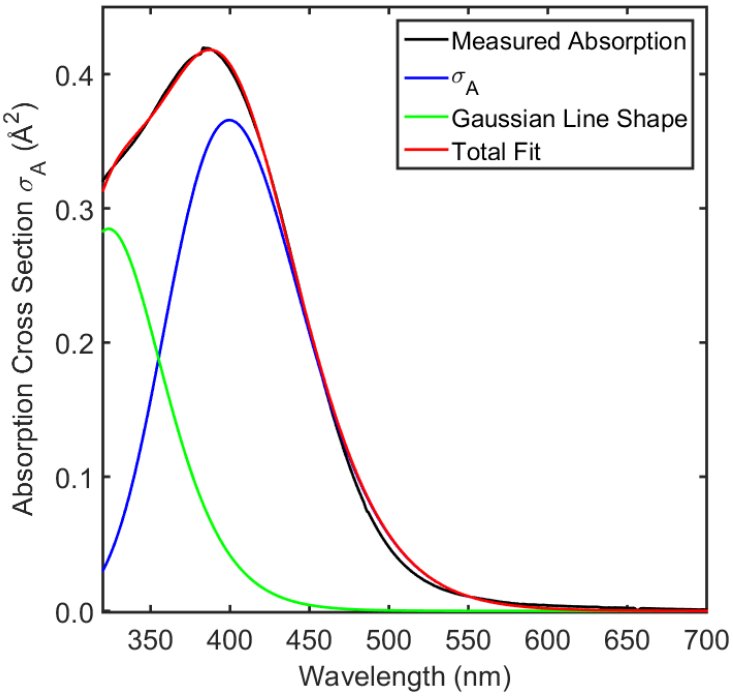


***Figure 6.3.*** *The measured absorption spectrum is fit with Equation (6.19) and the parameters in Table 6.1. The absorption cross section, $\sigma_A$, is used to fit the low-energy side of the line shape subject to the constraints imposed by the Raman cross sections. An additional Gaussian line shape (green) is used to estimate the contribution of the second-to-lowest energy transition to the total absorbance.*

**IVA. Resonance Raman Intensity Analysis and Spectral Fitting**

In Figure 6.3, the low-energy side of the absorption spectrum is fit using Equation (6.19) and the parameters in Table 6.1. The rise of the band at longer wavelengths imposes useful constraints, because the line shape is quite sensitive to the relative contributions of the intramolecular and solvent reorganization energies. Inflation of the homogeneous width increases the Lorentzian character of the line shape, whereas the inhomogeneous contribution is purely Gaussian. An additional Gaussian line shape is added to the fit at shorter wavelengths in order to estimate the contribution of the second-to-lowest energy electronic transition to the total absorbance spectrum.

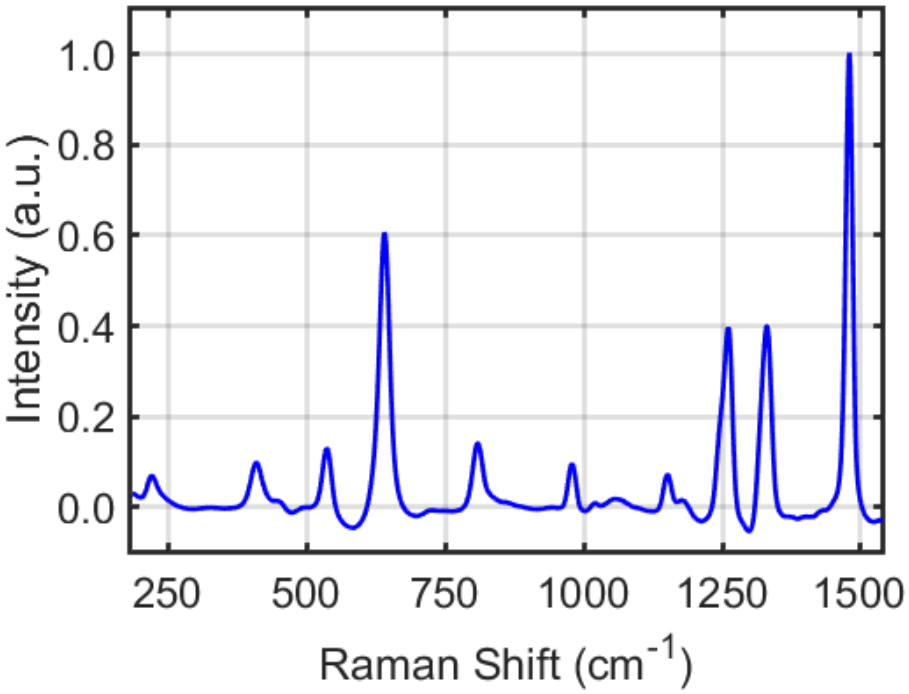


***Figure 6.4.*** *Resonance Raman spectrum of $[Ti(cat)_3]^{2-}$ acquired in aqueous solution with excitation at 488 nm.*

The resonance Raman spectrum of $[Ti(cat)_3]^{2-}$ acquired with excitation at 488 nm is shown in Figure 6.4. In Table 6.1, we suggest tentative assignments of the normal modes using a calculation carried out at the B3LYP/6-311G(2d,3p) level of theory in Gaussian 2009.[56] The assignments are based on agreement between the experimental and calculated vibrational frequencies in addition to aspects of the nuclear motion. As in earlier work,[51] we assume that the most intense transitions involve modes with larger reduced masses (i.e., coordinates of the hydrogen atoms are weakly coupled to charge transfer). It is also assumed that the response is dominated by in-plane motions of the catechol ligands, which preserve bond-conjugation in the aromatic rings. For most of these assignments, the motion described in Table 6.1 applies to a number of "candidate modes" with similar frequencies. Thus, most of the descriptions (e.g., Ti-cat stretch, C=C stretch) are likely to hold even if assignments to particular modes are later revised.

A full resonance Raman excitation profile cannot be generated because of available laser sources and contributions from higher-energy electronic resonances to the charge transfer band at shorter wavelengths. Nonetheless, determination of the Raman cross sections on the lower-energy side of the charge transfer resonance still imposes strong constraints on the line broadening parameters, because the resonance Raman cross sections increase as the inhomogeneous component of the absorbance line shape increases. Experimental and calculated Raman cross sections are compared in Figure 6.5.

Simultaneous fitting of absorbance and resonance Raman cross sections has been carried out in numerous earlier works.[28,39,51,52] It is not straightforward to produce error bars for this highly nonlinear model.[57] Therefore, we have explored fits in different regions of parameter space. For example, a decrease in the homogeneous line width is generally compensated for by increasing the electronic origin, increasing the inhomogeneous width, and decreasing the mode displacements. We find that the line widths and mode displacements can be changed by roughly 25% and 33% before large discrepancies between the measurements and fits are produced. The error bars in Table 6.1 reflect these percentages.

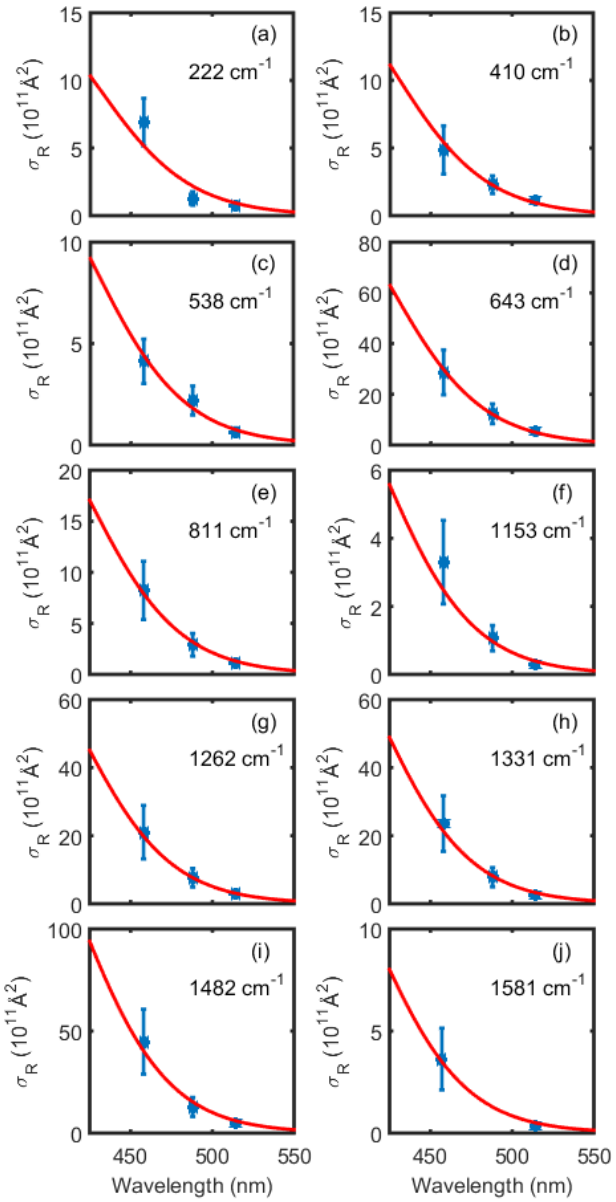


***Figure 6.5.*** *Experimental Raman cross sections are fit using Equation (6.20) and the parameters in Table 6.1.*

The model yields the best fit for homogeneous and inhomogeneous line widths of 2700 and 2100 $cm^{-1}$, respectively. The homogeneous line width can be converted into a classical solvent reorganization energy of 3290 $cm^{-1}$ using the Padé approximant.[14,51,52] This is perhaps a modest amount of reorganization energy for an electron transfer transition in aqueous solution. However, it was noted in earlier work that the Padé approximant may underestimate solvent

reorganization energies in hydrogen bonding solvents.[51,52] In such cases, the inhomogeneous line width may account for a portion of the "slower" solvent reorganization. The dominant low-frequency modes at 222 and 643 $cm^{-1}$ involve motions on the linkers between titanium and the ligands. Intense transitions above 1000 $cm^{-1}$ mostly correspond to bond-stretching motions on the aromatic rings. The higher-frequency modes with large displacements (at 1262, 1330, and 1482 $cm^{-1}$) carry important implications for BET, because they possess the largest vibrational wavefunction overlaps with the ground vibrational level of the excited electronic state.

***Table 6.1.*** *Resonance Raman Fitting Parameters*

| **Parameter** | **Value** | |
|---|---|---|
| [(a)] $\omega_0$ | 20100 ± 3000 $cm^{-1}$ (476 ± 68 nm) | |
| [(a)] $\delta$ | 2100 ± 500 $cm^{-1}$ (52 ± 12 nm) | |
| [(a)] $\Gamma$ | 2700 ± 660 $cm^{-1}$ (67 ± 16 nm) | |
| $\kappa = \Delta / \Lambda$ | 0.01 | |
| [(b)] $\lambda$ | 3290 ± 785 $cm^{-1}$ | |
| $\mu_{eg}$ | 4.1 ± 0.4 D | |
| **Raman Shift ($cm^{-1}$)** | **Dimensionless Displacement** | **[(c)]Assignment** |
| 222 | 1.24 ± 0.37 | Symmetric Ti-cat stretch (214 $cm^{-1}$) |
| 410 | 0.71 ± 0.21 | Ti-cat bend (413 $cm^{-1}$) |
| 538 | 0.50± 0.15 | O-C-C-O bend & ring distortion (534 $cm^{-1}$) |
| 643 | 1.11 ± 0.33 | O-C-C-O bend & ring distortion (641 $cm^{-1}$) |
| 811 | 0.47 ± 0.14 | O-C-C-O bend and ring 'breathing' (814 $cm^{-1}$) |
| 1153 | 0.20 ± 0.06 | C-H bending (1156 $cm^{-1}$) |
| 1262 | 0.53 ± 0.16 | O-C-C-O stretch (1283 $cm^{-1}$) |
| 1330 | 0.53 ± 0.16 | C=C stretch, C-O stretch, & Ti-O stretch (1305 $cm^{-1}$) |
| 1482 | 0.68 ± 0.20 | C=C stretch & C-O stretch (1511 $cm^{-1}$) |
| 1580 | 0.19 ± 0.06 | C=C stretch (1594 $cm^{-1}$) |

[(a)] Fits are carried out in the frequency domain.

[(b)] Computed with $\lambda = D^2 / 2k_B T$, where $D$ is defined with Equation (6.22).

[(c)] Assignments for vibrational modes computed at the B3LYP/6-311G(2d,3p) level in Gaussian 2009.[56] Frequencies of the calculated modes are given in parentheses.

**IVB. Decomposition of Transient Absorption Signal Components**

Photoexcitation of the charge transfer resonance at 408 nm induces electron transfer from the catechol ligands to the titanium atom. In Figure 6.6, the decrease in absorbance near 420 nm represents depopulation of the ground electronic state. This nonlinearity is denoted as the ground state bleach (GSB). BET from titanium to catechol is evidenced by growth of an absorptive response near 520 nm on the 100 fs time scale.[24] This signal component is referred to as the "hot ground state" (HGS). The HGS resonance is observed at longer wavelengths, because BET leaves the molecule in a highly non-equilibrium state which subsequently relaxes through vibrational energy transfer to the solvent. The HGS response blue-shifts with increasing delay because of vibrational energy transfer to the solvent. Molecules that relax to the ground electronic state on the sub-picosecond time-scale generally exhibit a blue-shifting HGS nonlinearity.[58,59] This effect becomes more pronounced as the resonance frequency with the lowest energy excited state increases because of a concomitant increases in the amount of heat that is dissipated following ground state recovery.

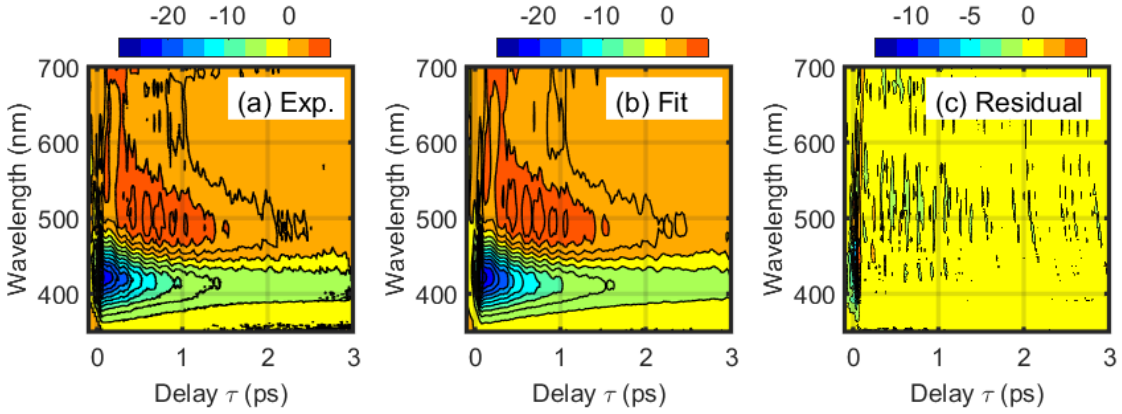


***Figure 6.6.*** *The (a) experimental transient absorption signal acquired under the magic angle polarization condition is (b) fit using Equation (6.23). The residual shows that agreement between the experiment in fit is best at delay times greater than 60 fs (i.e., outside the region of pulse overlap).*

In addition to the GSB and HGS signal components, the transient absorption signal exhibits a broadband feature in the near infrared (denoted with the BB subscript below).[24] These three resonances are fit in order to establish their relative contributions in the present measurements, which are carried out with dispersed detection on a CMOS array (i.e., some improvement is signal to noise is achieved compared to earlier work based on single channel detection).[24] These three signal components are fit with the following function,

$$F(\tau,\lambda) = A_{GSB}(\tau)\exp\left\{-4\ln(2)\frac{\left[\lambda-\lambda_{GSB}(\tau)\right]^2}{\Delta^2_{GSB}(\tau)}\right\} + A_{HGS}(\tau)\left\{-4\ln(2)\frac{\left[\lambda-\lambda_{HGS}(\tau)\right]^2}{\Delta^2_{HGS}(\tau)}\right\} + A_{BB}(\tau)\left\{-4\ln(2)\frac{\left[\lambda-\lambda_{BB}(\tau)\right]^2}{\Delta^2_{BB}(\tau)}\right\}. \quad (6.23)$$

We do not include excited state emission or excited state absorption resonances for two reasons: (i) previous work on this system has shown that the upper limit of the excited state lifetime is 180 ± 50 fs,[24] whereas the vibrational coherences of interest in this study dephase in 1-2 ps; (ii) the fit in Figure 6.6 is quite good outside of the region of pulse overlap, which is supportive of the physical picture that motivates Equation (6.23). Constraints must be imposed in order for such a multi-variable fit to converge; however, the ranges applied to each parameter are "loose" and physically reasonable. The lower and upper limits for $\lambda_{GSB}(\tau)$ are 375 and 440 nm. The lower and upper limits for $\lambda_{HGS}(\tau)$ are 450 and 620 nm, respectively. For both $\Delta_{GSB}(\tau)$ and $\Delta_{HGS}(\tau)$, the lower and upper limits are 15 and 150 nm. The upper-limits for $A_{HGS}(\tau)$ and $A_{GSB}(\tau)$ are 30 and -50 mOD, whereas both lower limits were set equal to zero.

Parameters associated with the GSB and HGS resonances, which are displayed in Figure 6.7, are of primary interest. The GSB response rises instantaneously and subsequently decays because of vibrational energy transfer to the solvent. In contrast, the magnitude of the HGS

response rises for 500 fs before vibrational cooling induces decay. Large-amplitude oscillations in the HGS signal magnitude are observed at a wavenumber of 222 $cm^{-1}$ in the first picosecond; however, vibrational coherences are not detected in the GSB. The peak of the HGS response blue-shifts as vibrational energy is transferred into the surrounding solvent, whereas the peak of the GSB response is essentially delay-independent. The line width of the HGS also decreases on the picosecond time scale, whereas the line width of the GSB is insensitive to the delay time. Transient blue-shifting and line-narrowing in the HGS signal component were observed in previous work on $[Ti(cat)_3]^{2-}$.[24] These behaviors of the HGS signal component is indicative of vibrational cooling following ultrafast ground state recovery. Systems such as nucleobases and *p*-nitroaniline exhibit similar spectroscopic signatures.[58,59]

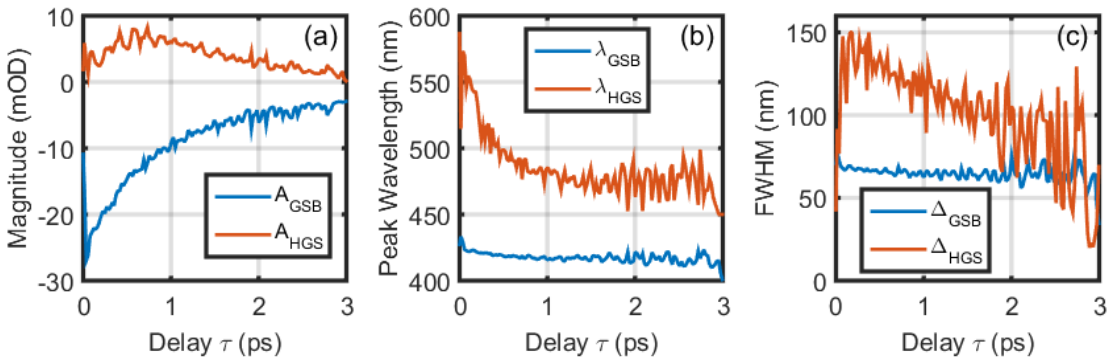


***Figure 6.7.*** *(a) The magnitude of the HGS signal component rises until a delay time of 0.5 ps before vibrational cooling causes the signal to decay. The GSB signal component rises instantaneously and decays on the time scale of vibrational cooling. (b) The HGS signal component shifts to shorter wavelengths because of vibrational cooling, whereas the peak of the GSB resonance is insensitive to the delay time. (c) The FWHM of the HGS resonance decreases by 50% within the first 3 ps, whereas the line width of the GSB is insensitive to the delay time. The 100 fs time scale of the BET process is the key information provided by these data.*

A broadband signal component is included in the fit at both short and long delay times, because a residual response in excess of 50% of the total signal strength is found without this term in Equation (6.23). The resonance frequency of the broadband signal component is apparently red-shifted beyond the limit of our detection range at 700 nm. The picosecond rate of

decay suggests that this resonance relaxes on the time scale of vibrational cooling; however, relatively weak transient absorption persists in the near-infrared even at delay times of hundreds of picoseconds. Lian and co-workers, who conducted earlier experiments on $[Ti(cat)_3]^{2-}$, suggested that one of the bonds between catechol and the titanium atom may detach following photo-excitation then reattach after hundreds of picoseconds.[24] We hypothesize that this species is also responsible for the broadband, red-shifted signal component in our experiments. Because the response appears to be red-shifted beyond our detection range, we have constrained both $\lambda_{BB}(\tau)$ and $\Delta_{BB}(\tau)$ (650 nm< $\lambda_{BB}(\tau)$ <850 nm and 400 nm< $\Delta_{BB}(\tau)$ <1000 nm). These constraints were required to eliminate discontinuities in the fit.

**IVC. Initiation of Vibrational Coherence by Back-Electron Transfer**

The pathways of interest in this work terminate in the upper right of Figure 6.1. In these pathways, both vibrational populations and coherences are first initiated in the excited electronic state. The BET process then induces vibrational coherences in the ground electronic state. Vibrational oscillations in the HGS signal component are clear evidence of contributions from the two coherent pathways in Figure 6.1, because light absorption and BET have the same Franck-Condon active modes in systems that possess a charge-transfer band.[6,27-29] The key issue is that, the gradient of the potential energy must change when the BET process occurs, because the potential energy minima are displaced for Franck-Condon active modes. For systems that do not exhibit a charge transfer band, it would be possible for "spectator modes", whose potential energy minima are not displaced in both optical and electron transfer transitions, to contribute in transient absorption experiments; this would be undesirable in the present study, because spectator modes are largely irrelevant to electron transfer mechanisms.

Transient absorption signals are Fourier transformed in Figure 6.8 to reveal the dependence of vibrational motion on the detection wavelength. The relatively weak oscillations exhibited by the GSB nonlinearity in the 350-450 nm wavelength range underscores the distinction between BET-induced (HGS) and radiation-induced (GSB) vibrational coherences.[60] The stimulated Raman response in the GSB nonlinearity is highly dependent on the electronic dephasing time. That is, the GSB wavepacket accumulates force in the interval between the first two field-matter interactions, $t_1$ (see Figure 6.2).[14] A short electronic dephasing time of 12 fs (inverse of homogeneous line width) ensures that the GSB wavepacket is initiated with a small displacement from the equilibrium geometry. Such dependence on electronic dephasing is one reason why lower-frequency modes generally have smaller resonance Raman cross sections than a higher-frequency mode with an identical displacement. In contrast, the BET-induced wavepacket detected in the 450-550 nm wavelength range accumulates force when it evolves on the excited state potential energy surface during a population time, $t_2$ in Figure 6.2, and is therefore less sensitive to electronic dephasing (i.e., the wavepacket evolves on the excited state potential during the 180 fs excited state lifetime). The BET process deposits the wavepacket on the ground state potential in a location that may be relatively far-displaced from the Franck-Condon geometry. In Figure 6.8, the BET-induced wavepacket generates the largest oscillations in the transient absorption signals, because its motion is induced by large forces on the ground state potential.

The transient absorption signals in Figure 6.9 show that vibrational coherences are quite prominent in the HGS signal component; the recurrences reach 25% of the total signal magnitude in the 450-550 nm range. Isotropic and anisotropic signals are analyzed near the peak of the signal strength at 500 nm to facilitate a better understanding of the HGS response. The isotropic

signal component is produced by combining signals measured with both parallel and perpendicular pump and probe pulses, $S_P + 2S_\perp$, whereas the anisotropic response is proportional to the difference in the two tensor elements, $S_P - S_\perp$.[61] These combinations of tensor elements are examined to determine whether or not the transition dipole orientations for the charge transfer resonance are affected by vibrational motions (the individual tensor elements, $S_P$ and $S_\perp$, are shown in the Supporting Information). Totally symmetric modes should not affect the transition dipole angles, because they preserve the symmetry of the system, whereas vibrational modes with lower symmetry may cause the transition dipoles to oscillate through a non-Condon effect.[62]

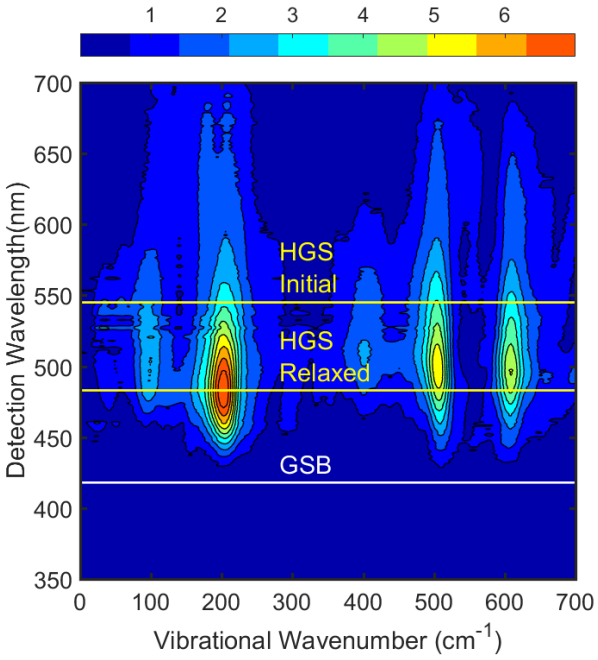


***Figure 6.8.*** *The coherent component of the transient absorption response of $[Ti(Cat)_3]^{2-}$ is analyzed for a range of detection wavelengths. Coherent vibrational motion is detected at wavelengths that correspond to the HGS signal component. The stimulated Raman response for the GSB signal component is comparable to the noise level of the experiment. This measurement demonstrates that the BET process initiates vibrational motions, which represent pathways that end in the upper right of Figure 6.1.*

The coherent Raman spectra in Figure 6.9 show that vibrational resonances associated with the isotropic signal component are 10 times more intense than those found in the anisotropic signal components. We observe resonances corresponding to the 222, 410, 538, and 643 $cm^{-1}$ modes detected with spontaneous Raman spectroscopy. Transient absorption yields resonances at 210, 400, 510, and 600 $cm^{-1}$, which suggests that the modes are highly populated following the back-electron transfer process (i.e., the lower frequencies reflect anharmonicity). Decreases in vibrational frequencies are generally observed in systems, where ground state recovery is much faster than vibrational cooling.[63] Relative to the isotropic response, the largest anisotropic intensities are found in the modes at 505 and 610 $cm^{-1}$, which may reflect weak non-Condon activity (i.e., the transition dipole orientations may be affected by vibrational motion). The 210-$cm^{-1}$ mode is notably assigned to a totally symmetric stretch involving the ligands and metal center. Thus, a small anisotropic response is anticipated.

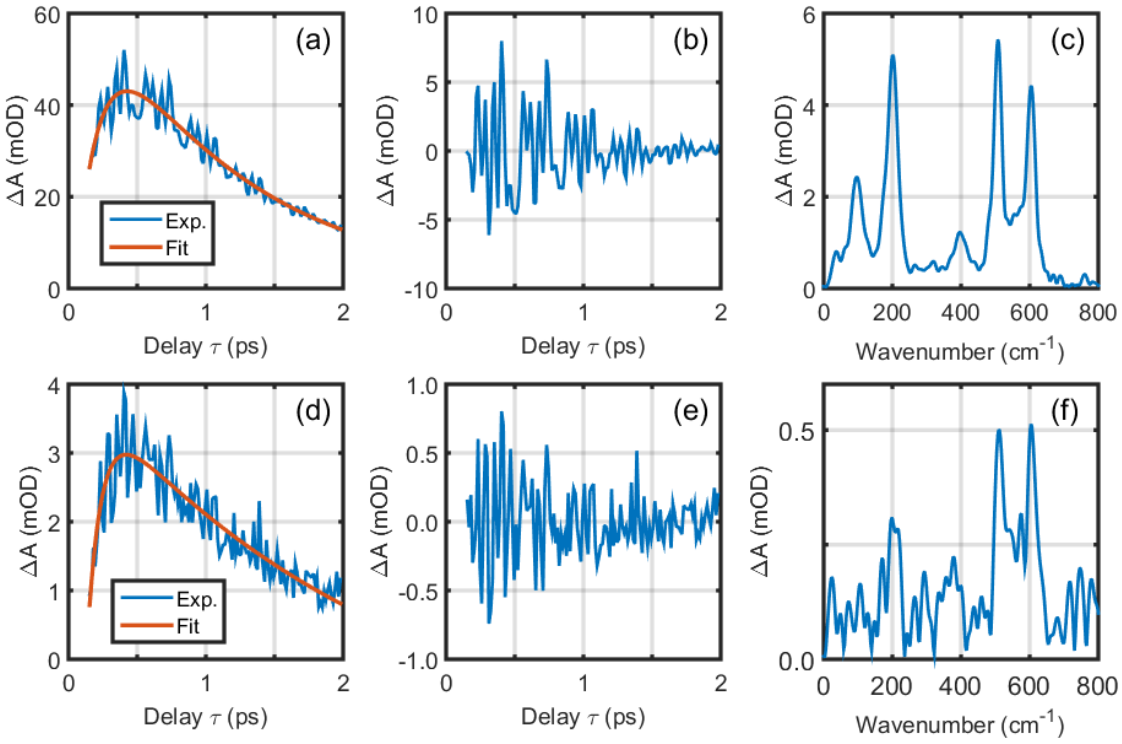


***Figure 6.9.*** *(a) An incoherent baseline is subtracted from the isotropic signal component at 500 nm to (b) isolate the coherent response. (c) Fourier transformation yields a coherent Raman spectrum for the isotropic HGS signal component. (d) An incoherent baseline is subtracted from the anisotropic signal component at 500 nm to (e) isolate the coherent response. (f) Fourier transformation yields a coherent Raman spectrum for the anisotropic HGS signal component. All mode frequencies are slightly smaller than those observed with spontaneous Raman spectroscopy, which indicates that the modes are highly populated following back-electron transfer (i.e., the frequencies are lower because of anharmonicity).*

**IVD. Analysis of the Back-Electron Transfer Mechanism**

Vibrational coherences in the HGS signal component signify contributions from the two paths that end in the upper right of Figure 6.1. These coherences can originate in either vibrational populations or coherences in the excited electronic state. The model developed in section II can be used to estimate the relative contributions of these pathways. All of the parameters with the exception of the solvation time, $\Lambda^{-1}$, can be extracted from the spectral fitting approach described above. We set $\Lambda^{-1}$ equal to the 75 fs, which is reasonable for aqueous

solution.[36] In addition, damping times for the ground ($\Gamma_{ul}^{-1}$) and excited ($\Gamma_{nk}^{-1}$) states are set equal to 1 ps and 180 fs, respectively. The damping times for the excited state are shorter because the lifetimes are limited by BET. It is not necessary to parameterize the product of matrix elements, $\left|\xi_L \mu_{eg}\right|^2 \left|V_{eg}\right|^2$, in the doorway function, because normalized signal intensities are analyzed in this section.

We begin by discussing the physical picture associated with the model in Figure 6.10. Energy has been (linearly) mapped onto the collective coordinate for convenience.[14] Ground and excited state potential energy minima appear at + $\lambda$ and - $\lambda$ for a harmonic bath (and the Stokes shift is 2 $\lambda$). The point of intersection between free energy surfaces is located at $-\lambda - \left(\Delta G_{eg} + \lambda\right)^2 / 4\lambda$. The wavepacket initiated by the pump pulse can be written as[31]

$$Y\left(\tau, q\right) = \frac{1}{\alpha\left(\tau\right)\sqrt{2\pi}} \exp\left[ -\frac{\left[ q + \lambda + \exp\left(-\Lambda\tau\right)\left(-\mathrm{h}\omega_L - \Delta G_{eg} - \lambda\right)\right]^2}{2\alpha^2\left(\tau\right)} \right]. \qquad (6.24)$$

Ground state equilibrium and asymptotic ($Y\left(\tau \to \infty, q\right)$) probability distributions are overlaid on the potential energy surfaces in Figure 6.10a. The excited state wavepacket never possesses significant amplitude at the point of intersection during the relaxation process (see Figure 6.10b), because $[Ti(cat)_3]^{2-}$ is deep within the inverted regime. Nonetheless, the transition probability is large, because displaced intramolecular modes promote transitions across the 20100 $cm^{-1}$ free energy gap. Motion of the wavepacket in the solvation coordinate is the key physical process responsible for time-dependence in the overall magnitude of $D\left(\tau\right)$ (i.e., oscillations induced by the vibrational coherences are relatively weak).

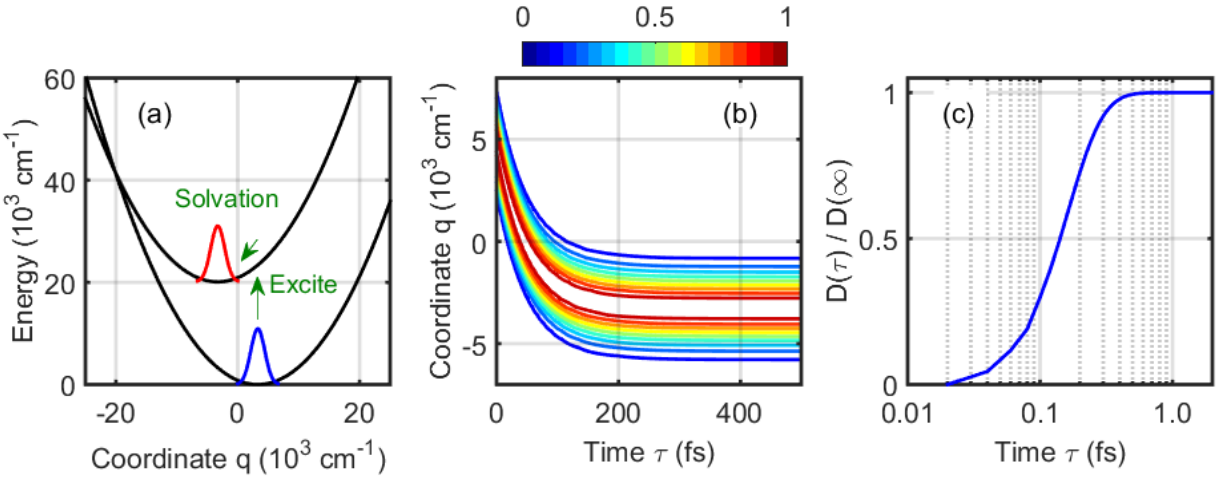


***Figure 6.10.*** *Physical picture suggested by theoretical model. (a) The pump pulse initiates a wavepacket in the collective 'solvent' coordinate, which moves toward the point of intersection between potential energy surfaces as* $\tau$ *increases. Energy is (linearly) mapped onto the collective coordinate for convenience. (b) Motion of the wavepacket,* $Y(\tau, q)$*, is simulated with Equation (6.24). (c) Growth in the magnitude of the doorway function with* $\tau$ *represents an increase in the probability of a BET transition. Quantized vibrational modes must promote the BET transition deep within the inverted regime, because the excited state wavepacket possesses little overlap with the geometry of the transition state in the solvent coordinate.*

Before presenting numerical results, it will be useful to first discuss the three key factors that influence the contributions of various terms to the doorway functions, $D_{nk\to ul}(\tau)$. The magnitudes of the functions are governed by (i) Franck-Condon overlaps for light absorption, (ii) Franck-Condon overlaps for BET, and (iii) the difference between $\Delta G_{eg}^{0} + \lambda$ and $\mathrm{h}(\omega_l - \omega_n)$ (see argument of exponential function in Equation (6.15)). Because the largest mode displacements in $[Ti(cat)_3]^{2-}$ are not much greater than 1.0, the terms that make the largest contributions will generally be those in which $n$ and $k$ do not exceed 3. For example, the ratio in Franck-Condon factors for the 0-0 and 0-3 vibronic transitions is equal to 0.075 with a mode displacement of 1.24 (i.e., the largest displacement in $[Ti(cat)_3]^{2-}$). In addition, appreciable Franck-Condon overlaps in the BET process will generally be those in which $l$ and $u$ do do not exceed 6, because the product, $\langle n|u\rangle\langle k|l\rangle$, also appears in Equation (6.15). It follows that the *optimal*

numbers of vibrational quanta ($n, k, l, u$) become smaller as the mode displacement decreases. The quantity, $\Delta G_{eg}^{0} + \lambda$, is negative in the inverted regime, so the BET process is accelerated when $\omega_l >> \omega_n$. In $[Ti(cat)_3]^{2-}$, pathways in which $l$ is *much larger* than a few quanta are energetically favored, because $\Delta G_{eg}^{0} + \lambda$ is equal to 16810 $cm^{-1}$ (e.g., $l$ must be close to 11 to conserve energy in a relaxation channel involving the 1482 $cm^{-1}$ mode). Overall, we suggest that the Franck-Condon overlaps (which favor small $l$) and energetic considerations (which favor large $l$) compete with each other in $[Ti(cat)_3]^{2-}$, because the system is deep within the inverted regime and possesses modest mode displacements.

Behaviors of the 222 and 1482 $cm^{-1}$ modes are compared below to illustrate how Franck-Condon overlaps and energetic constraints influence the weights of various terms in the doorway functions. For convenience, the density matrix elements are shuffled to separate functions associated with different classes of transitions. Indices 1-10 correspond to populations with 0-9 vibrational quanta (the number of quanta is the index minus 1). Indices 11-100 correspond to coherences. For the coherences, the indices are given by

$$i = s \cdot n + k - n + \beta, \quad \begin{cases} \beta = 0, & n < k \\ \beta = 1, & n > k \end{cases} \tag{6.25}$$

and

$$j = s \cdot l + u - l + \beta, \quad \begin{cases} \beta = 0, & l < u \\ \beta = 1, & l > u \end{cases}, \tag{6.26}$$

where $s$ is the number of states in the basis set (10 in the following calculations). It is useful to consider that the value of $n$ (and $l$) is equal to 1 for indices 11-20, 2 for indices 21-30, etc; the value of $k$ (and $u$) cycles from 1 to 10 within each decade. With these rules, population-to-population and coherence-to-coherence transitions appear in the lower left and upper right

portions of the matrices in Figures 6.11 and 6.12 (white grid lines separate these classes of transitions). Population-to-coherence transitions appear in the lower right and coherence-to-coherence transitions appear in the upper right (these are the pathways of interest).

In Figure 6.11, the doorway functions for the 222 $cm^{-1}$ mode exhibit marked changes with time, $\tau$. The dynamics illustrated in Figure 6.11 indicate that terms in which $n \neq k$ contribute most at early times (i.e., the coherence-to-coherence pathway). With respect to the three aforementioned points, the third point involving the relative magnitudes of $\Delta G_{eg}^{0} + \lambda$ and $\hbar\omega_{ln}$ is most important at early times, because this is when the energy gap in the solvation coordinate is largest (see Figure 6.10). In this regime, values of $k$ that differ from $n$ (small values of $\langle k|m\rangle\langle n|m\rangle$) are well-tolerated, because large values of $l$ are needed to compensate for the energy gap in the solvation coordinate. At long times ($\tau >> \Lambda^{-1}$), the product of vibrational overlap integrals primarily controls relative contributions of particular terms, and the population-to-coherence pathways dominates (i.e., points (i) and (ii) outcompete point (iii)). We refer to the marked difference in behaviors at short and long times as representing energy gap-limited and Franck-Condon-limited regimes.

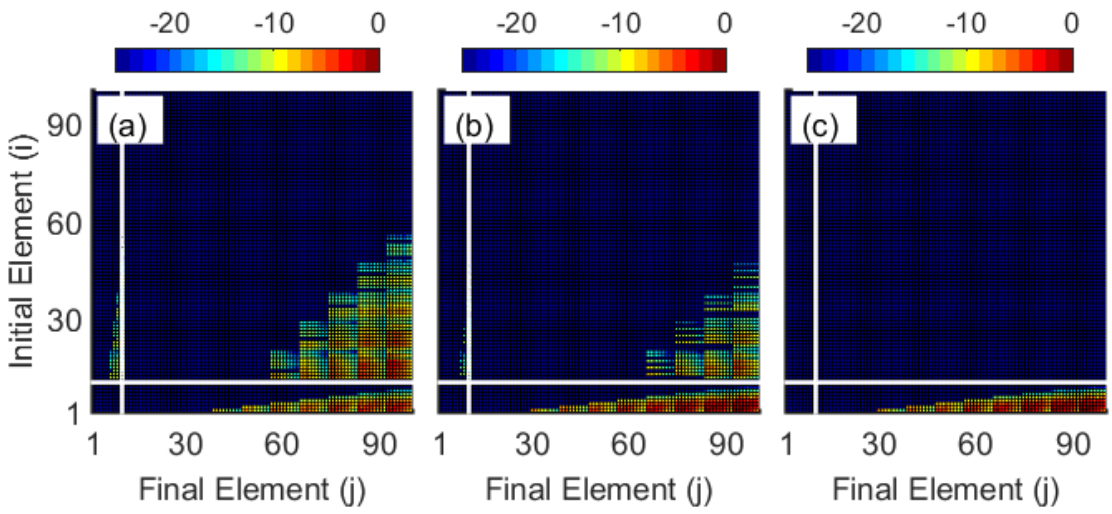


***Figure 6.11.*** *Doorway functions, $D_{i\to j}(\tau)$, are computed with Equation (6.14) and the parameters in Table 6.1. Only the 222 cm$^{-1}$ mode is included in these calculations. The times, $\tau$, are (a) 0.2, (b) 0.5, and (c) 2 ps. The calculations suggest that vibrational coherences are initiated in the ground electronic state following BET if the system is initially in either a vibrational coherence (upper right) or population (lower right). The behavior transitions from an energy gap-limited regime at $\tau$ =0.1 ps to a Franck-Condon-limited regime at $\tau$ =2 ps.*

The calculation presented in Figure 6.12, which involves the 1482 cm$^{-1}$ mode, is more typical of molecular systems, where the electronic energy gap and mode frequencies do not differ by multiple orders of magnitude. Both coherence-to-coherence and population-to-coherence pathways contribute at times that are both short and long compared to the solvation process. There is only a minor decrease in the relative contribution of the coherence-to-coherence pathway at long times. In comparison with Figure 6.11, the different behavior exhibited in Figure 6.12 reflects the higher frequency and smaller displacement of the 1482 cm$^{-1}$ mode. The higher mode frequency mitigates the influence of energetic factors, and the smaller displacement enhances the influence of vibrational overlap integrals. Consequently, the decrease in contributions from the coherence-to-coherence pathways with increasing $\tau$ is relatively modest. This time-dependent decrease in coherence-to-coherence pathways would be further suppressed by an increase in the mode displacement. The present calculations suggest that both

coherence-to-coherence and population-to-coherence transitions will be prominent in molecular systems with organic moieties, because they generally possess displaced high-frequency (>1000 $cm^{-1}$) modes and charge transfer resonances in the visible spectral range. This behavior is consistent with that predicted by Fleming and Jean.[30]

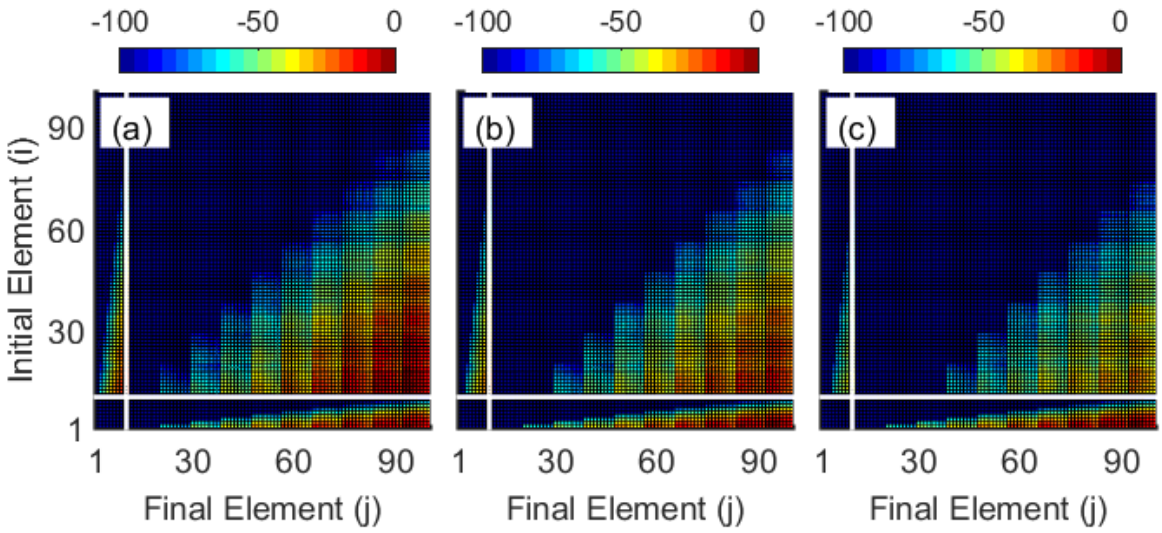


***Figure 6.12.*** *Doorway functions, $D_{i\to j}(\tau)$, are computed with Equation (6.14) and the parameters in Tables 6.1 and 6.2 (the mode displacement is taken from Table 6.2). Only the 1482 $cm^{-1}$ mode is included in these calculations. The times, $\tau$, are (a) 0.2 ps, (b) 0.5 ps, (c) 2 ps. The calculations suggest that vibrational coherences are initiated in the ground electronic state following BET if the system is initially in either a vibrational coherence (upper right) or population (lower right). These calculations show that all pathways will generally be activated in systems with high-frequency (>1000 $cm^{-1}$) vibrational modes and charge transfer resonances in the visible spectral range.*

The calculations presented in Figures 6.11 and 6.12 illustrate basic principles of the BET mechanism. The next step is to compare experimental and calculated transient absorption signals. The vibrational coherences in the HGS signal component, which are of primary interest in this work, are isolated by restricting the summation in the expression for the signal to eliminate the population response. The signal can then be Fourier transformed to obtain the contour plot in Figure 6.13a.

$$S\left(\omega_\tau,\omega_{det}\right)=\sum_{\substack{mnkv\\ l\neq u}}\int_0^\infty D_{nk\to ul}\left(\tau\right)W_{luv}\left(\tau,\omega_{det}\right)\exp\left(i\omega_\tau\tau\right). \tag{6.27}$$

The calculated signals in Figure 6.13a can be compared to the measurement in Figure 6.8. The peak positions and line widths agree fairly well in both dimensions, $\omega_\tau$ and $\omega_{det}$. The intensities are also in good agreement. In carrying out the fit, we began by assuming the parameters in Table 6.1 then introduced changes only when needed to fit the signal acquired with a detection wavelength of 500 nm (see Figure 6.13b and Table 6.2). Adjustments are necessary because spontaneous resonance Raman spectroscopy is primarily sensitive to the potential energy surfaces near the Franck-Condon geometry, whereas transient absorption signals reflect a broader range of coordinate space. Minor differences between the fit and measurement are found on the high and low frequency sides of the HGS resonance (see Figure 6.13c). We have accounted for time-resolution by translating the 40-fs instrument response near 500 nm into a Gaussian with a FWHM of 520 $cm^{-1}$. The amount by which a vibrational resonance is attenuated is estimated by the magnitude of the Gaussian function at the respective frequency.[14]

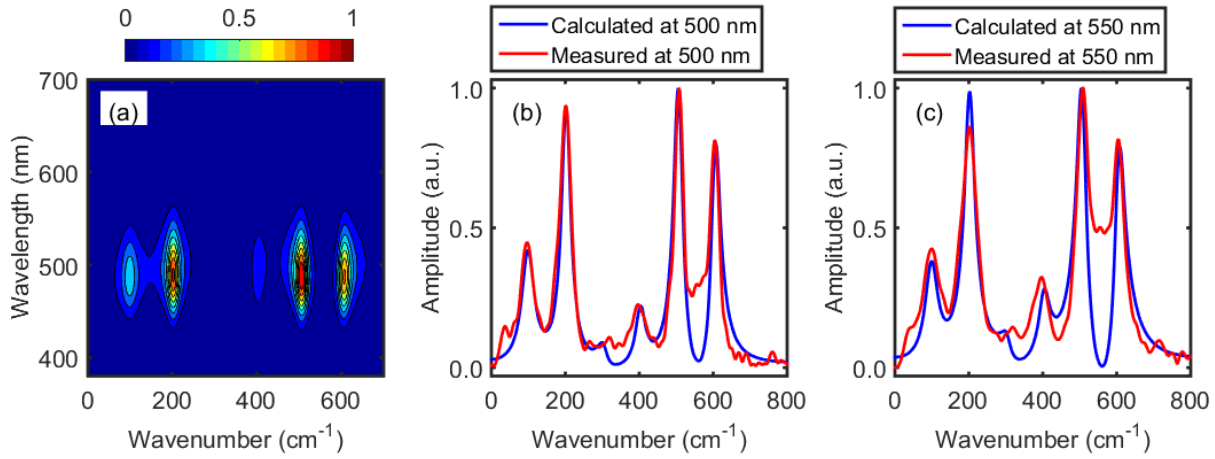


***Figure 6.13.*** *(a) Fourier transform of transient absorption signal calculated with Equation (6.27) and the parameters in Tables 6.1 and 6.2. This contour plot can be compared to the measurement in Figure 6.8. The calculated and measured signals are overlaid at a detection wavelength of (b) 500 nm and (c) 550 nm. The parameters are adjusted to optimize the fit to the absorbance spectrum (Figure 6.3), the resonance Raman cross sections (Figure 6.5), and the fit to the transient absorption signal at 500 nm (Figure 6.13b).*

The mode frequencies had to be slightly reduced to fit the transient absorption signals in Figure 6.13. This is not a surprising observation. A reduction in vibrational frequencies induced by a fast non-radiative transition is usually attributed to anharmonicity.[63] Third order "diagonal" force constants (differentiation with respect to individual normal coordinates) computed at the B3LYP/6-311G(2d,3p) level for the 538 and 643 $cm^{-1}$ modes of $[Ti(cat)_3]^{2-}$ suggest that wavenumber differences between successive vibrational levels reach 507 and 604 $cm^{-1}$ when the number of vibrational quanta is greater than 50, which is far in excess of the electronic energy gap (third-order derivatives for the 507 and 604 $cm^{-1}$ modes are 13 and 17 $kg/Å/s^2$, respectively). Therefore, we hypothesize that a large number of off-diagonal, anharmonic force constants (differentiation with respect to mixtures of the vibrational coordinates) combine to reduce the vibrational frequencies from the equilibrium values.

***Table 6.2.*** *Fitting Parameters for Transient Absorption Signals in Figure 6.13*

| **Vibrational Wavenumber from Spontaneous Raman Spectroscopy ($cm^{-1}$)** | **Vibrational Wavenumber from Transient Absorption Spectroscopy ($cm^{-1}$)** | **Dimensionless Displacement** |
|---|---|---|
| ------ | 99 | 1.80 |
| 222 | 202 | 1.24 |
| 538 | 507 | 0.90 |
| 643 | 604 | 0.94 |
| 1482 | 1482 | 0.39 |

An important distinction should be recognized between the information conveyed by the doorway functions in Figures 6.11-6.12 and the spectroscopic signals Figure 6.13. The doorway functions can be thought as representing the weight of each pathway irrespective of how the probe step is implemented (e.g., visible or mid-infrared light). In fact, the doorway functions assume a mathematical form that is similar to fourth-order "rate functions" developed in earlier work (this similarity will be further discussed in section V).[31,35] In contrast, the window function effectively filters particular pathways based on vibrational wavefunction overlap integrals. Thus, the oscillations observed in the signal, which are primarily detected at the fundamental mode frequency, are a somewhat indirect representation of vibronic relaxation channels driven by the BET mechanism.

In summary, the calculations presented in this section have been used to investigate the two BET pathways that lead to vibrational coherences in the ground electronic state. The key conclusions drawn from these calculations are:

(i) The most dominant BET transitions involve high-frequency vibrational coherences, $\omega_{ln}$, in the $t_3$-interval between perturbative interactions with the donor-acceptor coupling (see Figure 6.2).

(ii) The frequencies of promoting modes observed with transient absorption spectroscopy will generally deviate from the predictions of a harmonic model because they will be highly

excited following BET (as a consequence of point (i)). This behavior is consistent with other systems that exhibit ultrafast ground state recovery.[63]

(iii) Model calculations based on empirical parameters suggest that both coherence-to-coherence and population-to-coherence pathways contribute in $[Ti(cat)^3]^{2-}$ because of its high-frequency modes (>1000 $cm^{-1}$) and modest displacements.

(iv) The present measurements and simulations demonstrate that pathways ending in the upper right of Figure 6.1 contribute to the signals. These two pathways cannot be experimentally distinguished without extraordinary time resolution. The only way to distinguish these two pathways is to resolve coherence and incoherent dynamics in the excited state (prior to BET), which has a lifetime with an upper limit of 180 fs (we do not observe contributions from the excited state outside the region of pulse overlap).[24]

**V. Broader Implications for Electron Transfer Reactions**

Coherent dynamics in which broadband laser pulses initiate vibrational coherences are not necessarily relevant to applications such as photoelectrochemical cells.[64,65] For example, the vibrational coherence-to-coherence pathway in Figure 6.1 requires impulsive excitation and is arguably irrelevant to processes initiated by sunlight. The vibrational population-to-coherence pathway differs from the vibrational coherence-to-coherence pathway in that impulsive excitation is not required. Moreover, according to the model presented in section II, the population-to-coherence pathway may contribute even at times that are long compared to solvation and vibrational dephasing.

The potential implications of this work are more clearly seen if the doorway function is rewritten as a fourth-order rate function.[31,35,64] In fact, the derivation of the doorway function in section IIB parallels the derivation of the fourth-order rate function for electron transfer presented in earlier work.[31] The fourth-order rate function can written as

$$K_{nk\to ul}^{(4)}(\tau)=\left(\frac{\mathrm{h}w_L^2\sqrt{2\left(\Delta^2+w_L^2\right)}}{\pi\left|\xi_L\mu_{eg}\right|^2}\right)\cdot D_{nk\to ul}(\tau), \tag{6.27}$$

if the normalization condition of Reference [31] is applied. The normalization condition ensures convergence to Marcus' equation at times that are long compared to the solvation time for models with weak vibronic couplings. When $\tau$ is longer than solvation and vibrational dephasing, the fourth-order rate function becomes

$$\begin{aligned}K_{nn\to ul}^{(4)}(\tau\to\infty)=&\frac{\pi^{1/2}\left|V_{eg}\right|^2}{\mathrm{h}\sqrt{\lambda k_B T}}B_m\langle n|m\rangle\langle n|m\rangle\langle n|u\rangle\langle n|l\rangle\\&\times\exp\left[-\frac{\mathrm{h}^2\left(\omega_L-\omega_{eg}\right)^2}{4\lambda k_B T}\right]\exp\left[-\frac{\Delta G_{eg}^0+\lambda-\mathrm{h}\omega_{nl}}{4\lambda k_B T}\right]\end{aligned}, \tag{6.28}$$

where the only surviving terms are those in which $n=k$. In other words, the coherence-to-coherence pathway, $nk\to ul$, vanishes when $\tau$ is large but the population-to-coherence pathway, $nn\to ul$, survives.

This idea can be taken a step further if we let the system establish a Boltzmann distribution of vibrational populations in the excited state before BET. In our notation, the traditional second-order (population-to-population) expression for the BET process can written as[17]

$$K_{nn\to mm}^{(2)}=\frac{\pi^{1/2}\left|V_{eg}\right|^2}{\mathrm{h}\sqrt{\lambda k_B T}}\sum_{nm}B_m\left|\langle n|m\rangle\right|^2\exp\left[\frac{-\left(\Delta G+\lambda-\mathrm{h}\omega_{nm}\right)^2}{4\lambda k_B T}\right], \tag{6.29}$$

Vibrational coherences are not initiated by BET at this level of theory, because the coherences do not survive the trace over all quantum states taken in the evaluation of the correlation function.[15] We question whether or not elimination of the population-to-coherence pathway by a trace at second order is fully justified. Restoration of a Boltzmann distribution of vibrational quanta

occurs rapidly following BET because of intramolecular vibrational cooling and solute-to-solvent vibrational energy transfer. These processes generally occur on a time scale comparable to picosecond vibrational dephasing. Thus, it is reasonable to describe the sequence of BET and vibrational cooling as a higher-order perturbative process. For example, the two donor-acceptor interactions associated with BET could be followed by one perturbative interaction with a component of the Hamiltonian associated with solute-solvent interactions, thereby producing a population that survives the trace over quantum states (see Figure 6.14).

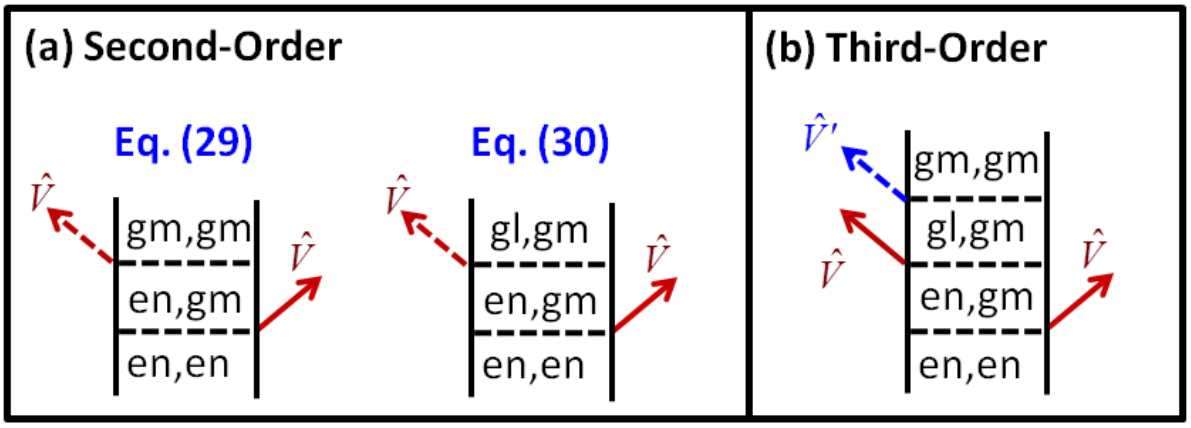


***Figure 6.14.*** *We consider whether or not population-to-coherence pathways are relevant in systems regardless of the electron transfer time-scale. (a) Only population-to-population transitions occur in the traditional second order rate formula, Equation (6.29). The population-to-coherence pathway survives if the trace is taken only over electronic states in Equation (6.30). (b) In a higher-order model, a trace over all quantum states can be carried out if subsequent vibrational cooling dynamics are accounted for. Vibrational population-to-coherence transitions may then contribute regardless of the electron transfer rate. The operators* $\hat{V}$ *and* $\hat{V}'$ *denote the donor-acceptor coupling and the solute-solvent interaction, respectively.*

Because a detailed description of vibrational cooling dynamics is beyond the scope of this work, we suggest that it is instructive to simply take the trace over the electronic states in writing an *ad hoc* second-order rate formula for BET processes that begin with an equilibrium condition. Equation (6.29) can be rewritten as

$$K_{nn\to lm}^{(2)} = \frac{\pi^{1/2}\left|V_{eg}\right|^2}{\mathrm{h}\sqrt{\lambda k_B T}} \sum_{mnl} B_n \left\langle n \middle| m \right\rangle \left\langle n \middle| l \right\rangle \exp\left[ \frac{-\left(\Delta G + \lambda - \mathrm{h}\omega_{nm}\right)^2}{4\lambda k_B T} \right] \tag{6.30}$$

if we let the electron transfer transition terminate in a vibrational coherence. Feynman diagrams associated with Equations (6.29) and (6.30) are given in Figure 6.14a. The diagrams take only the interactions with the donor-acceptor coupling into account. The larger number of pathways found in $K_{nn\to lm}^{(2)}$ will generally enhance the overall rate. For example, the ratio, $K_{nn\to lm}^{(2)} / K_{nn\to mm}^{(2)}$, is equal to 25 for a system with the 4 modes accounted for in Table 6.2 when the summations are taken over the 20 lowest-energy states. This ratio will become even larger when additional intramolecular modes are taken into account. The problem of ending the $K_{nn\to lm}^{(2)}$ pathway in Figure 6.14a in vibrational coherence can be remedied by incorporating the perturbative part of the Hamiltonian that induces vibrational cooling (see Figure 6.14b). Only one additional interaction is required to convert the system from a coherence to a population. Thus, a third-order rate function can be developed to describe this type of process.

## VI. Supplemental Information

### VIA. Analysis of HGS Anisotropy in Localized and Delocalized Basis Sets

Isotropic and anisotropic vibrational spectra are compared in Figure 6.9 to explore the possibility of non-Condon effects. Here, we show that the overall magnitude of the anisotropy in the HGS signal component should not be used to establish the most appropriate basis set in which to view the electronic structure (i.e., localized versus delocalized). The electronic structures of both localized (uncoupled) and delocalized (coupled) basis sets are presented in Figure 6.15. In both cases, there is a ground state and three singly-excited states related to the ligand-to-metal charge transfer transitions. All three transition dipoles are equal in the uncoupled

basis set, whereas the coupled basis set possesses two allowed transitions (with equal transition dipoles) and one higher-energy, forbidden transition (see Supporting Information).

For these systems, signal strengths with parallel and perpendicular pump and probe polarizations can written as[74-76]

$$S_{\mathrm{P}} = \frac{|\mu|^4}{15}\sum_{a=1}^{N}\sum_{b=1}^{N}\left[1+2\cos^2\left(\theta_{a,b}\right)\right] \tag{6.31}$$

and

$$S_{\perp} = \frac{|\mu|^4}{30}\sum_{a=1}^{N}\sum_{b=1}^{N}\left[4-2\cos^2\left(\theta_{a,b}\right)\right], \tag{6.32}$$

where $N$ is the number of optically-allowed transitions in the respective basis set. The transition dipoles, $\mu$, are equal for each allowed transition in both basis sets, so they have been moved in front of the summations (i.e., only relative magnitudes of the two tensor elements are relevant).

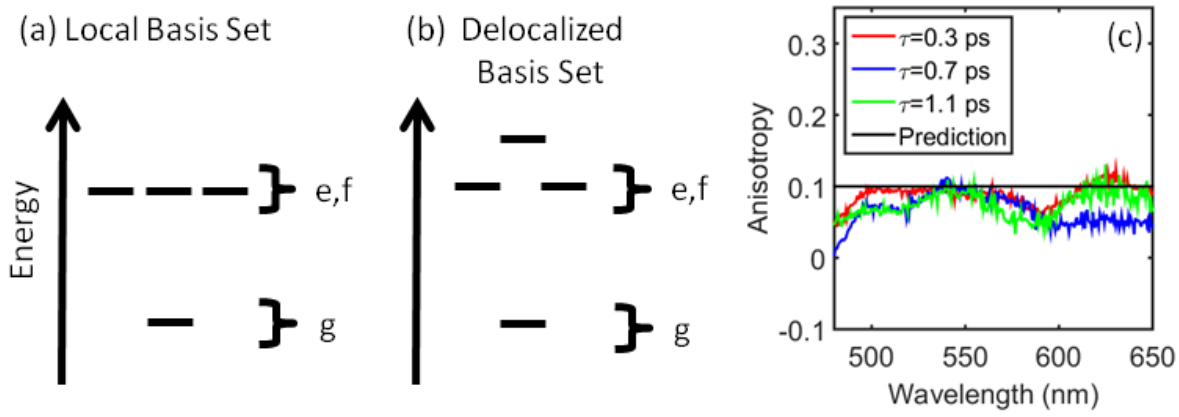


***Figure 6.15.*** *The electronic structure can be viewed in (a) localized and (b) delocalized basis sets. (c) The transient absorption anisotropy associated with the HGS signal component agrees well with the prediction of 0.1, which is independent of the basis set. The uncertainty in the anisotropy is approximately 0.05. The anisotropy in the HGS signal component should not be used to argue for one basis set or the other.*

For the localized (uncoupled) basis set, the parallel and perpendicular signal strengths are $S_{\mathrm{P}}$=6/15 and $S_{\mathrm{P}}$=9/30 ($N$ =3 and $\theta_{a,b}$=60°). The transition dipoles have been removed from the

magnitude of each tensor element, because they are common to both formulas. The parallel and perpendicular signal strengths are $S_{\mathrm{P}}$=4/15 and $S_{\mathrm{P}}$=3/15 for the delocalized (coupled) basis set ($N$ =2 and $\theta_{a,b}$ =90°). For both basis sets, we then obtain an anisotropy of

$$r = \frac{S_{\mathrm{P}} - S_{\perp}}{S_{\mathrm{P}} + 2S_{\perp}} = 0.1. \tag{6.33}$$

The experimental anisotropy for the HGS signal component is displayed at three delay times in Figure 6.15c. The earliest delay time is 300 fs, which is longer than the 180 fs lifetime of the excited state. Therefore, excited state emission and excited state absorption are negligible in each measurement. The agreement between experiment and theory demonstrated in Figure 6.15 is strong evidence that measurements with polarized laser pulses are interpreted correctly. The uncertainty in the anisotropy is approximately 0.05.

The delocalized basis set is justified when the inter-ligand coupling strength is large compared to the magnitudes of the fluctuations in energy levels, whereas the localized basis set corresponds to the opposite limit. Recent work describes how these basic aspects of electronic structures in condensed phases, which are well-established in molecular aggregates,[16,45-47,48] generalize to transition metal complexes.[49,50] Time-dependent density functional theory calculations conducted at the B3LYP/6-311G(2d,3p) level yield an inter-ligand coupling strength of 642 $cm^{-1}$ (see Supporting Information) which is comparable to the empirical thermal fluctuation magnitude 1150 $cm^{-1}$ (see Equation (6.5)).This suggests that $[Ti(cat)_3]^{2-}$ resides in an intermediate regime, where valid arguments can be made for either basis set. The analysis presented in this section shows that such arguments are irrelevant to the magnitudes of tensor elements acquired with parallel and perpendicular pump and probe polarizations. The preferred

choice of basis set is not important in the present study, which is concerned with establishing the coherent relaxation pathways in Figure 6.1.

**VII. Concluding Remarks**

In summary, optical spectroscopies and model calculations have been used to investigate contributions of non-equilibrium BET pathways in the transition metal complex, $[Ti(cat)_3]^{2-}$. Vibrational coherences observed in transient absorption experiments signify pathways that end in the upper right of Figure 6.1. Our empircal model suggests that both vibrational population-to-coherence and vibrational coherence-to coherence pathways make significant contributions in $[Ti(cat)_3]^{2-}$ and other systems with high-frequency modes (>1000 $cm^{-1}$) and charge transfer resonances in the visible spectrum. In principle, the two types of pathways can be experimentally distinguished with extraordinary time resolution. In such measurements, vibrational populations and coherences in the excited electronic can be correlated to the vibrational coherences in the ground electronic state. A key fundamental limitation is that the lifetime must be longer than the period of the vibrational mode. This is problematic because wavepacket motions in the ground state can only be initiated when BET is ultrafast (e.g., phase coherence will otherwise be lost in the ensemble). An important practical limitation is that unambiguous information cannot be obtained when the pump and probe pulses are overlapped in the sample. We estimate that the two pathways can be experimentally distinguished with continuum pulses that are compressed to 10 fs or less.

The broader implication of this work is that contributions from the coherent pathways in Figure 6.1 are generally not negligible if electron transfer is faster than solvation and vibrational dephasing. Such sub-picosecond electron transfer processes are fairly common at molecule-semiconductor interfaces in photoelectrochemical cells. [64,65] Therefore, a better understanding of these pathways will be useful for interpreting ultrafast spectroscopy measurements in these

systems.[12,64,66-69] In this work, parameters derived from spontaneous Raman experiments were used to simulate transient absorption signals; however, this parameterization scheme may fail in systems that undergo large excited state geometry changes. Femtosecond stimulated Raman scattering methods[70,71] or two-dimensional electronic-vibrational spectroscopy[72,73] may be used to obtain investigate intramolecular motions at nonequilibrium geometries in such systems. It will also be helpful to integrate molecular dynamics simulations into the description.

We question whether or not vibrational population-to-coherence transients are relevant to electron transfer processes regardless of their time scales. Observations based on ultrafast spectroscopies are limited to BET dynamics that are faster than vibrational dephasing, because vibrational motions can only be detected if a macroscopic coherence is preserved. However, it will be interesting to consider the relevance of vibrational coherences initiated from quasi-equilibrium initial conditions as suggested by Equation (6.30). These pathways do not survive the trace over electronic and vibrational quantum states at second-order in perturbation theory but can contribute in higher-order descriptions that take vibrational cooling processes into account.

***Supporting Information Available***

Additional details are provided regarding the decomposition of transient absorption signals. The choice of basis set is also discussed in the context of time-dependent density function theory calculations. This information is available free of charge via the internet at http://pubs.acs.org.

## REFERENCES


1. Vos, M. H.; Lambry, J.-C.; Robles, S. J.; Youvan, D. C.; Breton, J.; Martin, J.-L. Direct Observation of Vibrational Coherence in Bacterial Reaction Centers Using Femtosecond Absorption Spectroscopy *Proc. Natl. Acad. Sci.* **1991**, *88*, 8885-8889.

2. Vos, M. H.; Rappaport, F.; Lambry, J.-C.; Breton, J.; Martin, J.-L. Visualization of Coherent Nuclear Motion in a Membrane Protein by Femtosecond Spectroscopy *Nature* **1993**, *363*, 320-325.

3. Peteanu, L. A.; Schoenlein, R. W.; Wang, H.; Mathies, R. A.; Shank, C. V. The First Step in Vision Occurs in Femtoseconds: Complete Blue and Red Spectral Studies *Proc. Natl. Acad. Sci.* **1993**, *90*, 11762-11766.

4. Banin, U.; Kosloff, R.; Ruhman, S. Femtosecond Chemical Dynamics in Solution: Photodissociation of $I_3^-$ *Isr. J. Chem.* **1993**, *33*, 141-156.

5. Zhu, L.; Sage, J. T.; Champion, P. M. Observation of Coherent Reaction Dynamics in Heme Proteins *Science* **1994**, *266*, 629-632.

6. Wynne, K.; Reid, G. D.; Hochstrasser, R. M. Vibrational Coherence in Electron Transfer: The Tetracyanoethylene-Pyrene Complex *J. Chem. Phys.* **1996**, *105*, 2287-2297.

7. Spörlein, S.; Zinth, W.; Wachtveitl, J. Vibrational Coherence in Photosynthetic Reaction Centers Observed in the Bacteriochlorophyll Anion Band *J. Phys. Chem. B* **1998**, *102*, 7492-7496.

8. Arnett, D. C.; Moser, C. C.; Dutton, P. L.; Scherer, N. F. The First Events in Photosynthesis: Electronic Coupling and Energy Transfer Dynamics in the Photosynthetic Reaction Center from Rhodobacter sphaeroides *J. Phys. Chem. B* **1999**, *103*, 2014-2032.

9. Lynch, M. S.; Van Kuiken, B. E.; Daifuku, S. L.; Khalil, M. On the Role of High-Frequency Intramolecular Vibrations in Ultrafast Back-Electron Transfer Reactions *J. Phys. Chem. Lett.* **2011**, *2*, 2252-2257.

10. Fuller, F. D.; Pan, J.; Gelzinis, A.; Butkus, V.; Senlik, S. S.; Wilcox, D. E.; Yocum, C. F.; Valkunas, L.; Abramavicius, D.; Ogilvie, J. P. Vibronic Coherence in Oxygenic Photosynthesis *Nat. Chem.* **2014**, *6*, 706-711.

11. Song, Y.; Clafton, S. N.; Pensack, R. D.; Kee, T. W.; Scholes, G. D. Vibrational Coherence Probes the Mechanism of Ultrafast Electron Transfer in Polymer–Fullerene Blends *Nat. Commun.* **2014**, *5*, 4933.

12. Tisdale, W. A.; Williams, K. J.; Timp, B. A.; Norris, D. J.; Aydil, E. S.; Zhu, X.-Y. Hot-Electron Transfer from Semiconductor Nanocrystals *Science* **2010**, *328*, 1543-1547.

13. Huber, R.; Dworak, L.; Moser, J. E.; Grätzel, J.; Wachtveitl, J. Beyond Vibrationally Mediated Electron Transfer: Coherent Phenomena Induced by Ultrafast Charge Separation *J. Phys. Chem. C* **2016**, DOI: 10.1021/acs.jpcc.1026b02012.

14. Mukamel, S. *Principles of Nonlinear Optical Spectroscopy*; Oxford University Press: New York, 1995.

15. Nitzan, A. *Chemical Dynamics in Condensed Phases*; Oxford University Press: Oxford, 2006.

16. Valkunas, L.; Abramavicius, D.; Mančal, T. *Molecular Excitation Dynamics and Relaxation: Quantum Theory and Spectroscopy* Wiley-VCH: Weinheim, 2013.

17. Barbara, P. F.; Meyer, T. J.; Ratner, M. A. Contemporary Issues in Electron Transfer Research *J. Phys. Chem.* **1996**, *100*, 13148-13168.

18. Bixon, M.; Jortner, J. Vibrational Coherence in Nonadiabatic Dynamics *J. Chem. Phys.* **1997**, *107*, 1470-1482.

19. Clarke, T. M.; Durrant, J. R. Charge Photogeneration in Organic Solar Cells *Chem. Rev.* **2010**, *110*, 6736-6767.

20. Ross, R. T.; Nozik, A. J. Efficiency of Hot-Carrier Solar Energy Converters *J. Appl. Phys.* **1982**, *53*, 3813-3818.

21. Jin, X.; Li, Y.; Chen, Z.; Wei, T.-H.; He, X.; Sun, W. Energy Level Control: Toward an Efficient Hot Electron Transport *Sci. Rep.* **2014**, *4*, 5983.

22. Li, L.; Kanai, Y. Excited Electron Dynamics at Semiconductor–Molecule Type-II Heterojunction Interface: First-Principles Dynamics Simulation *J. Phys. Chem. Lett.* **2016**, *7*, 1495-1500.

23. Borgias, B. A.; Cooper, S. R.; Koh, Y. B.; Raymond, K. N. Synthetic, Structural, and Physical Studies of Titanium Complexes of Catechol and 3,5-*tert*-butylcatechol *Inorg. Chem.* **1984**, *23*, 1009-1016.

24. Wang, Y.; Hang, K.; Anderson, N. A.; Lian, T. Comparison of Electron Transfer Dynamics in Molecule-to-Nanoparticle and Intramolecular Charge Transfer Complexes *J. Phys. Chem. B* **2003**, *107*, 9434-9440.

25. Hush, N. S. Homogeneous and Heterogeneous Optical and Thermal Electron Transfer *Electrochimica Acta.* **1968**, *13*, 1005-1023.

26. Yan, Y. J.; Sparpaglione, M.; Mukamel, S. Solvation Dynamics in Electron-Transfer, Isomerization, and Nonlinear Optical Processes. A Unified Liouville-Space Theory *J. Phys. Chem.* **1988**, *92*, 4842-4853.

27. Britt, B. M.; McHale, J. L.; Friedrich, D. M. Application of Time Dependent Raman Theory to Raman Excitation Profiles of Hexamethylbenzene: Tetracyanoethylene Electron Donor-Acceptor Complex *J. Phys. Chem.* **1995**, *99*, 6347-6355.

28. Kelley, A. M. Resonance Raman Intensity Analysis of Vibrational and Solvent Reorganization in Photoinduced Charge Transfer *J. Phys. Chem. A* **1999**, *103*, 6891-6903.

29. Hupp, J. T.; Williams, R. D. Using Resonance Raman Spectroscopy to Examine Vibrational Barriers to Electron Transfer and Electronic Delocalization *Acc. Chem. Res.* **2001**, *34*, 808-817.

30. Jean, J. M.; Fleming, G. R. Competition Between Energy and Phase Relaxation in Electronic Curve Crossing Processes *J. Chem. Phys.* **1995**, *103*, 2092-2101.

31. Lesheng, L.; Giokas, P. G.; Kanai, Y.; Moran, A. M. Modeling Time-Coincident Ultrafast Electron Transfer and Solvation Processes at Molecule-Semiconductor Interfaces *J. Chem. Phys.* **2014**, *140*, 234109.

32. Coalson, R. D.; Evans, D. G.; Nitzan, A. A Nonequlibrium Golden Rule Formula for Electronic State Populations in Nonadiabatically Coupled Systems *J. Chem. Phys.* **1994**, *101*, 436-448.

33. Strodel, B.; Stock, G. Quantum Modeling of Transient Infrared Spectra Reflecting Photoinduced Electron-Transfer Dynamics *J. Chem. Phys.* **2006**, *124*, 114105.

34. Baiz, C. R.; Kubarych, K. J.; Geva, E. Molecular Theory and Simulation of Coherence Transfer in Metal Carbonyls and Its Signature on Multidimensional Infrared Spectra *J. Phys. Chem. B* **2011**, *115*, 5322-5339.

35. Molesky, B. P.; Moran, A. M. Fourth-Order Perturbative Model for Photoinduced Internal Conversion Processes *J. Phys. Chem. A* **2013**, *117*, 13954-13966.

36. Horng, M. L.; Gardecki, J. A.; Papazyan, A.; Maroncelli, M. Subpicosecond Measurements of Polar Solvation Dynamics: Coumarin 153 Revisited *J. Phys. Chem.* **1995**, *99*, 17311-17337.

37. Myers, A. B.; Mathies, R. A.; Tannor, D. J.; Heller, E. J. Excited State Geometry Changes from Preresonance Raman Intensities: Isoprene and Hexatriene *J. Chem. Phys.* **1982**, *77*, 3857-3866.

38. Kwac, K.; Cho, M. Two-Color Pump−Probe Spectroscopies of Two- and Three-Level Systems: 2-Dimensional Line Shapes and Solvation Dynamics *J. Phys. Chem. A* **2003**, *107*, 5903-5912.

39. Myers, A. B.; Mathies, R. A. Resonance Raman intensities: a probe of excited state structures and dynamics. In *Biological Applications of Raman Spectroscopy*; Spiro, T. G., Ed.; Wiley: New York, 1987; Vol. 2; pp 1.

40. Myers, A. B. Excited Electronic State Properties From Ground-State Resonance Raman Intensities. In *Laser Techniques in Chemistry*; Myers, A. B., Rizzo, T. R., Eds.; John Wiley & Sons: New York, 1995; Vol. 23; pp 325-384.

41. Damraurer, N. H.; Cerullo, G.; Yeh, A.; Boussie, T. R.; Shank, C. V.; McCusker, J. K. Femtosecond Dynamics of Excited-State Evolution in $[Ru(bpy)_3]^{2+}$ *Science* **1997**, *275*, 54-57.

42. Yeh, A.; Shank, C. V.; McCusker, J. K. Ultrafast Electron Localization Dynamics Following Photo-Induced Charge Transfer *Science* **2000**, *289*, 935-938.

43. Shaw, G. B.; Brown, C. L.; Papanikolas, J. M. Investigation of Interligand Electron Transfer in Polypyridyl Complexes of Os(II) Using Femtosecond Polarization Anisotropy Methods: Examination of $Os(bpy)_3^{2+}$ *J. Phys. Chem. A* **2002**, *106*, 1483-1495.

44. Stark, C. W.; Schreier, W. J.; Lucon, J.; Edwards, E.; Douglas, T.; Kohler, B. Interligand Electron Transfer in Heteroleptic Ruthenium(II) Complexes Occurs on Multiple Time Scales *J. Phys. Chem. A* **2015**, *119*, 4813-4824.

45. Davydov, A. *Theory of Molecular Excitons*; Plenum: New York, 1971.

46. van Amerongen, H.; Valkunas, L.; van Grondelle, R. *Photosynthetic Excitons*; World Scientific: Singapore, 2000.

47. Spano, F. C. Excitons in Conjugated Oligomer Aggregates, Films, and Crystals *Annu. Rev. Phys. Chem.* **2006**, *57*, 217-243.

48. Abramavicius, D.; Palmieri, B.; Voronine, D. V.; Sanda, F.; Mukamel, S. Coherent Multidimensional Optical Spectroscopy of Excitons in Molecular Aggregates; Quasiparticle versus Supermolecule Perspectives *Chem. Rev.* **2009**, *109*, 2350-2408.

49. Miller, S. A.; Moran, A. M. Nonlinear Optical Detection of Electron Transfer Adiabaticity in Metal Polypyridyl Complexes *J. Phys. Chem. A* **2010**, *114*, 2117-2126.

50. Albert, V. V.; Badaeva, E.; Kilina, S.; Sykora, M.; S., T. The Frenkel Exciton Hamiltonian for Functionalized Ru(II)-bpy Complexes *J. Lumin.* **2011**, *131*, 1739-1746.

51. Moran, A. M.; Delbecque, C. Solvent Effects on Ground and Excited Electronic State Structures of the Push-Pull Chromophore Julolidinyl-n-N,N‘-diethylthiobarbituric Acid *J. Phys. Chem. A* **2001**, *105*, 10208-10219.

52. Moran, A. M.; Kelley, A. M. Solvent effects on ground and excited electronic state structures of p-nitroaniline *J. Chem. Phys.* **2001**, *115*, 912-924.

53. Dattlebaum, D. M.; Kober, E. M.; Papanikolas, J. M.; Meyer, T. J. Application of time-resolved near-infrared spectroscopy (TRNIR) to the metal-to-ligand charge transfer (MLCT) excited state(s) of $[Os(phen)_3]^{2+}$ *Chem. Phys.* **2006**, *326*, 71-78.

54. Shriver, D. F.; Dunn, J. B. R. The Backscattering Geometry for Raman Spectroscopy of Colored Materials *Appl. Spectrosc.* **1974**, *28*, 319-325.

55. Dudik, J. M.; Johnson, C. R.; Asher, S. A. Wavelength Dependence of the Preresonance Raman Cross Sections of $CH_3CN$, $SO_4^{2-}$,$ClO_4^-$, and $NO_3^-$ *J. Chem. Phys.* **1985**, *82*, 1732-1740.

56. Frisch, M. J.; Trucks, G. W.; Schlegel, H. B.; Scuseria, G. E.; Robb, M. A.; Cheeseman, J. R.; Scalmani, G.; Barone, V.; Mennucci, B.; Petersson, G. A.et al. Gaussian 09 Wallingford,CT, 2009.

57. Lilichenko, M.; Kelley, A. M. Application of Artificial Neural Networks and Genetic Algorithms to Modeling Molecular Electronic Spectra in Solution *J. Chem. Phys.* **2001**, *114*, 7094-7102.

58. Kovalenko, S. A.; Schanz, R.; Hennig, H.; Ernsting, N. P. Cooling Dynamics of an Optically Excited Molecular Probe in Solution from Femtosecond Broadband Transient Absorption Spectroscopy *J. Chem. Phys.* **2001**, *115*, 3256-3273.

59. Pecourt, J.-M.; Peon, J.; Kohler, B. DNA Excited-State Dynamics: Ultrafast Internal Conversion and Vibrational Cooling in a Series of Nucleosides *J. Am. Chem. Soc.* **2001**, *123*, 10370-10378.

60. Champion, P. M.; Rosca, F.; Ionascu, D.; Cao, W.; Ye, X. Rapid Timescale Processes and the Role of Electronic Surface Coupling in the Photolysis of Diatomic Ligands from Heme Proteins *Faraday. Discuss.* **2004**, *127*, 123-135.

61. Vöhringer, P.; Scherer, N. F. Transient Grating Optical Heterodyne Detected Impulsive Stimulated Raman Scattering in Simple Liquids *J. Phys. Chem.* **1995**, *99*, 2684-2695.

62. Womick, J. M.; West, B. A.; Scherer, N. F.; Moran, A. M. Vibronic Effects in the Spectroscopy and Dynamics of C-Phycocyanin *J. Phys. B.* **2012**, *45*, 154016.

63. Schrader, T.; Sieg, A.; Koller, F.; Schereier, W.; An, Q.; Zinth, W.; Gilch, P. Vibrational Relaxation Following Ultrafast Internal Conversion: Comparing IR and Raman Probing *Chem. Phys. Lett.* **2004**, *392*, 358-364.

64. Ardo, S.; Meyer, G. J. Photodriven Heterogeneous Charge Transfer with Transition-Metal

65. Compounds Anchored to $TiO_2$ Semiconductor Surfaces *Chem. Soc. Rev.* **2009**, *38*, 115-164.

66. Concepcion, J. J.; Jurss, J.; Brennaman, M. K.; Hoertz, P. G.; Patrocinio, A. O. T.; Iha, N. Y. M.; Templeton, J. L.; Meyer, T. J. Making Oxygen with Ruthenium Complexes *Acc. Chem. Res.* **2009**, *42*, 1954-1965.

67. Zimmerman, C.; Willig, F.; Ramakrishna, S.; Burnfeindt, B.; Pettinger, B.; Eichberger, R.; Storck, W. Experimental Fingerprints of Vibrational Wave-Packet Motion during Ultrafast Heterogeneous Electron Transfer *J. Phys. Chem. B* **2001**, *105*, 9425-9253.

68. Asbury, J. B.; Hao, E.; Wang, Y.; Ghosh, H. N.; Lian, T. Ultrafast Electron Transfer Dynamics from Molecular Adsorbates to Semiconductor Nanocrystalline Thin Films *J. Phys. Chem. B* **2001**, *105*, 4545-4557.

69. Anderson, N. A.; Lian, T. Ultrafast Electron Transfer at the Molecule-Semiconductor Nanoparticle Interface *Annu. Rev. Phys. Chem.* **2005**, *56*, 491-519.

70. Duncan, W. R.; Prezhdo, O. V. Theoretical Studies of Photoinduced Electron Transfer in Dye-Sensitized $TiO_2$ *Annu. Rev. Phys. Chem.* **2007**, *58*, 143-184.

71. McCamant, D. W.; Kukura, P.; Yoon, S.; Mathies, R. A. Femtosecond Broadband Stimulated Raman Spectroscopy: Apparatus and Methods *Rev. Sci. Instrum.* **2004**, *75*, 4971-4980.

72. Kukura, P.; McCamant, D. W.; Mathies, R. A. Femtosecond stimulated Raman spectroscopy *Annu. Rev. Phys. Chem.* **2007**, *58*, 461-488.

73. Oliver, T. A. A.; Lewis, N. H. C.; Fleming, G. R. Correlating the Motion of Electrons and Nuclei with Two-Dimensional Electronic–Vibrational Spectroscopy, *Proc. Natl. Acad. Sci.* **2014**, *111*, 10061-10066.

74. Courtney, T. L.; Fox, Z. W.; Estergreen, L.; Khalil, M. Measuring Coherently Coupled Intramolecular Vibrational and Charge-Transfer Dynamics with Two-Dimensional Vibrational–Electronic Spectroscopy *J. Phys. Chem. Lett.* **2015**, *6*, 1286-1292.

75. Andrews, D. L.; Thirunamachandran, T. On three-dimensional rotational averages *J. Chem. Phys.* **1977**, *67*, 5026-5033.

76. Hochstrasser, R. M. Two-dimensional IR-spectroscopy: polarization anisotropy effects *Chem. Phys.* **2001**, *266*, 273-284.

77. Dreyer, J.; Moran, A. M.; Mukamel, S. Tensor Components in Three Pulse VIbrational Echoes of a Rigid Dipeptide *Bull. Korean Chem. Soc.* **2003**, *24*, 1091-1096.

# CHAPTER 7: CONCLUDING REMARKS

We have shown that signatures of vibronic coherence transfer in triiodide are exhibited in 2DRR spectra. In contrast to traditional transient absorption and photon echo experiments, in which photo-initiation of reactants is always from ground state equilibrium, 2DRR encodes information about nonequilibrium behavior. The cross peaks between triiodide and diiodide facilitate insights into the reaction mechanism. Experimental results suggest there is positive correlation between the reactant (triiodide) bond length and the vibrational coherence frequency of the photoproduct (diiodide). Such correlation could be caused by Franck-Condon activity and/or sensitivity to inter-fragment interactions.[1-3] From our studies of the triiodide photodissociation reaction in chapters 2 and 3, we have demonstrated that beam geometry and the colors of the incident pulses control the information we obtain from 2DRR spectra.

Coherent reaction dynamics could be exhibited in 2DRR spectra for a system in which the time scale of light-activated non-radiative transitions is short compared to the vibrational period(s). Ultrafast energy transfer and electron transfer processes are prime candidates for investigations using the 2DRR method. For example, the non-equilibrium back-electron transfer (BET) pathways in the transition metal complex $[Ti(cat)_3]^{2-}$ are on the 100-fs time scale. Transient absorption experiments and our empirical model suggest both vibrational population-to-coherences and vibrational coherence-to-coherence transitions are observed in the hot ground state of $[Ti(cat)_3]^{2-}$, i.e. both pathways of Figure 6.1 in Chapter 6. The implication is that other systems with high-frequency modes and charge transfer resonances in the visible spectrum could exhibit significant contributions from these pathways. Molecule-semiconductor interfaces in

photoelectrochemical cells often exhibit sub-picosecond electron transfer processes. [4-5] In this regime, coherent pathways are not negligible, and a deeper understanding of their importance would facilitate interpretation of ultrafast measurements in such systems. [5-10] Femtosecond stimulated Raman scattering methods[11-12] or two-dimensional electronic-vibrational spectroscopy[13-14] could be powerful tools in studies of intramolecular motions at nonequilibrium geometries in such systems.

Studies of ultrafast energy transfer processes in light harvesting proteins[15-17] could also potentially benefit from 2DRR spectroscopy. A method related to 2DRR spectroscopy is currently employed by Harel and co-workers,[24-25] who are making great strides in resolving the disputed role of vibronic effects in Frenkel excitons delocalization and energy transport. [16, 18-23] In contrast to electron transfer transitions in which oxidized and/or reduced species often absorb well-resolved wavelengths of light, donor and acceptor resonances in energy transfer processes usually possess significant spectral overlap. It would be particularly challenging to isolate 2DRR components for energy transfer processes in a multicolor experiment, similar to the one we used to study the photodissociation reaction in triiodide.

The same type of dynamics detectable in triiodide--reaction induced wavepacket motions--could be detected in larger systems with numerous Franck-Condon active modes. Vibrational coherences in the doming motion of the heme and iron-histidine stretching coordinates follow photodissociation of myoglobin.[26] In our studies of oxygen- and water-ligated myoglobin in chapter 4, we employed quasi-degenerate (one-color) 2DRR spectroscopy. We found that modes proximal to the propionic acid side chains of the heme moiety in both proteins show the greatest amount of heterogeneity. Fluctuation amplitudes for oxygen- and water-ligated myoglobin were determined from molecular dynamics simulations to be 7.0 $cm^{-1}$ and 5.9 $cm^{-1}$,

respectively. Comparing these values to the characteristic frequencies of thermal motion, both proteins were shown to have homogeneous and inhomogeneous line broadening character. This result confirmed the experimental correlation parameters of 0.54 and 0.43 for the oxygen- and water-ligated proteins, respectively. It remains unclear, however, if heterogeneity in the vibrational mode local to the propionic side chains has a significant effect on vibrational cooling of the heme moiety.

Though undesired signal components have been an experimental challenge for over two decades, such artifacts are often underappreciated. For the photodissociation of triiodide and oxygen- and water-ligated myoglobin, a gauntlet of experimental tests has shown that 2DRR signals are orders of magnitude greater than cascaded nonlinearities.[35, 43] However, we have shown that this is not generally true. In chapter 5, model calculations of femtosecond stimulated Raman spectroscopy (FSRS) and 2DRR were performed for p-nitroaniline, a model dye molecules, in a variety of common solvents: acetonitrile, methanol, and dichloromethane. We studied signal cascades from solute-solute and solute-solvent interactions.

In the case of solute-solute interactions, we have shown that Franck-Condon activity associated with large mode displacements can improve the ratio of the electric fields of cascaded nonlinearities to the direct signal under resonant conditions. This true because Franck-Condon active modes are not governed by the same selection rules that promote artifacts under electronically off-resonant conditions. [43] However, we have also demonstrated that, for small mode displacements and/or off-resonant carrier pulse frequencies, third-order cascades can become increasingly dominant.

Solvent contributions to undesired signal components are commonly assumed to be negligible. This superstition overlooks the concentration of the solvent being approximately five

orders of magnitude larger than the solute concentration. We have shown, with a large Raman cross section and/or similar vibrational mode(s) in the solute and solvent, solute-solvent cascades can be greater than 20% of the direct signal. Most surprisingly, the simulations in chapter 5 suggest these results hold for both 2DRR and FSRS.

It has been assumed that the FSRS experiment is immune to the signal artifacts which 2DRR is known to be susceptible. The third-order cascades from solute-solute and solute-solvent interactions of p-nitroaniline in dichloromethane are calculated to be approximately 80% of the direct FSRS signal. The total signal expresses solute and solvent resonances of comparable intensities, and the overall intensity is 20% of the direct signal. These simulations debunk the untested assumption that the FSRS signal is free of the same artifacts that have plagued 2DRR.

It should come as no surprise that 2D Raman experiments have taken so long to develop. Successful experiments require careful sample preparation and handling, particular attention to phase matching conditions, and clever beam geometries. A number of undesirable radiated signals can be avoided with a well-designed experimental setup. A robust survey of signal component intensities as a function of beam geometries under various conditions could be a powerful resource for spectroscopists interested in employing multidimensional Raman spectroscopies.

## REFERENCES


1. Baratz, A.; Ruhman, S., UV Photolysis of $I_3^-$ in solution - Multiple Product Channels Detected by Transient Hyperspectral Probing. *Chem. Phys. Lett.* **2008,** *461*, 211-217.

2. Nishiyama, Y.; Terazima, M.; Kimura, Y., Ultrafast Relaxation and Reaction of Diiodide Anion after Photodissociation of Triiodide in Room-Temperature Ionic Liquids. *J. Phys. Chem. B* **2012,** *116*, 9023-9032.

3. Band, Y. B.; Freed, K. F., Energy Distribution in Selected Fragment Vibrations in Dissociation Processes in Polyatomic Molecules. *J. Chem. Phys.* **1977,** *67*, 1462-1472.

4. Concepcion, J. J.; Jurss, J.; Brennaman, M. K.; Hoertz, P. G.; Patrocinio, A. O. T.; Iha, N. Y. M.; Templeton, J. L.; Meyer, T. J., Making Oxygen with Ruthenium Complexes. *Acc. Chem. Res.* **2009,** *42*, 1954-1965.

5. Ardo, S.; Meyer, G. J., Photodriven Heterogeneous Charge Transfer with Transition-Metal Compounds Anchored to $TiO_2$ Semiconductor Surfaces. *Chem. Soc. Rev.* **2009,** *38*, 115-164.

6. Zimmerman, C.; Willig, F.; Ramakrishna, S.; Burnfeindt, B.; Pettinger, B.; Eichberger, R.; Storck, W., Experimental Fingerprints of Vibrational Wave-Packet Motion during Ultrafast Heterogeneous Electron Transfer. *J. Phys. Chem. B* **2001,** *105*, 9425-9253.

7. Asbury, J. B.; Hao, E.; Wang, Y.; Ghosh, H. N.; Lian, T., Ultrafast Electron Transfer Dynamics from Molecular Adsorbates to Semiconductor Nanocrystalline Thin Films. *J. Phys. Chem. B* **2001,** *105*, 4545-4557.

8. Anderson, N. A.; Lian, T., Ultrafast Electron Transfer at the Molecule-Semiconductor Nanoparticle Interface. *Annu. Rev. Phys. Chem.* **2005,** *56*, 491-519.

9. Duncan, W. R.; Prezhdo, O. V., Theoretical Studies of Photoinduced Electron Transfer in Dye-Sensitized $TiO_2$. *Annu. Rev. Phys. Chem.* **2007,** *58*, 143-184.

10. Tisdale, W. A.; Williams, K. J.; Timp, B. A.; Norris, D. J.; Aydil, E. S.; Zhu, X.-Y., Hot-Electron Transfer from Semiconductor Nanocrystals. *Science* **2010,** *328*, 1543-1547.

11. McCamant, D. W.; Kukura, P.; Yoon, S.; Mathies, R. A., Femtosecond Broadband Stimulated Raman Spectroscopy: Apparatus and Methods *Rev. Sci. Instrum.* **2004,** *75*, 4971-4980.

12. Kukura, P.; McCamant, D. W.; Mathies, R. A., Femtosecond stimulated Raman spectroscopy. *Annu. Rev. Phys. Chem.* **2007,** *58*, 461-488.

13. Oliver, T. A. A.; Lewis, N. H. C.; Fleming, G. R., Correlating the Motion of Electrons and Nuclei with Two-Dimensional Electronic–Vibrational Spectroscopy,. *Proc. Natl. Acad. Sci.* **2014,** *111*, 10061-10066.

14. Courtney, T. L.; Fox, Z. W.; Estergreen, L.; Khalil, M., Measuring Coherently Coupled Intramolecular Vibrational and Charge-Transfer Dynamics with Two-Dimensional Vibrational–Electronic Spectroscopy. *J. Phys. Chem. Lett.* **2015,** *6*, 1286-1292.

15. Mohseni, M.; Omar, Y.; Engel, G. S.; Plenio, M. B., *Quantum Effects in Biology*. Cambridge University Press: Cambridge, 2014.

16. Fuller, F. D.; Pan, J.; Gelzinis, A.; Butkus, V.; Senlik, S. S.; Wilcox, D. E.; Yocum, C. F.; Valkunas, L.; Abramavicius, D.; Ogilvie, J. P., Vibronic Coherence in Oxygenic Photosynthesis. *Nat. Chem.* **2014,** *6*, 706-711.

17. Chenu, A.; Scholes, G. D., Coherence in Energy Transfer and Photosynthesis. *Annu. Rev. Phys. Chem.* **2015,** *66*, 69-96.

18. Hennebicq, E.; Beljonne, D.; Curutchet, C.; Scholes, G. D.; Silbey, R. J., Shared-mode assisted resonant energy transfer in the weak coupling regime. *J. Chem. Phys.* **2009,** *130*, 214505:1-6.

19. Roden, J.; Schulz, G.; Eisfeld, A.; Briggs, J., Electronic energy transfer on a vibronically coupled quantum aggregate. *J. Chem. Phys.* **2009,** *131*, 044909.

20. Womick, J. M.; Moran, A. M., Vibronic Enhancement of Exciton Sizes and Energy Transport in Photosynthetic Complexes. *J. Phys. Chem. B* **2011,** *115*, 1347-1356.

21. Chenu, A.; Chrisensson, N.; Kauffmann, H. F.; Mančal, T., Enhancement of Vibronic and Ground-State Vibrational Coherences in 2D Spectra of Photosynthetic Complexes. *Sci. Rep.* **2013,** *3*, 2029.

22. O'Reilly, E. J.; Olaya-Castro, A., Non-Classicality of the Molecular Vibrations Assisting Exciton Energy Transfer at Room Temperature. *Nat. Commun.* **2014,** *5*, 3012.

23. Singh, V. P.; Westberg, M.; Wang, C.; Dahlberg, P. D.; Gellen, T.; Gardiner, A. T.; Cogdell, R. J.; Engel, G. S., Towards Quantification of Vibronic Coupling in Photosynthetic Antenna Complexes *J. Chem. Phys.* **2015,** *142*, 212446.

24. Hutson, W. O.; Spencer, A. P.; Harel, E., Isolated Ground-State Coherence Measured by Fifth-Order Single-Shot Two-Dimensional Electronic Spectroscopy. *J. Phys. Chem. Lett.* **2016,** *7*, 3636-3640.

25. Spencer, A. P.; Hutson, W. O.; Harel, E., Quantum Coherence Selective 2D Raman-Electronic Spectroscopy. *Nat. Commun.* **2017,** *8*, 14732.

26. Champion, P. M.; Rosca, F.; Ionascu, D.; Cao, W.; Ye, X., Rapid Timescale Processes and the Role of Electronic Surface Coupling in the Photolysis of Diatomic Ligands from Heme Proteins. *Faraday. Discuss.* **2004,** *127*, 123-135.

27. Kumar, A. T. N.; Rosca, F.; Widom, A.; Champion, P. M., Investigations of Amplitude and Phase Excitation Profiles in Femtosecond Coherence Spectroscopy. *J. Chem. Phys.* **2001,** *114*, 701-724.

28. Song, Y.; Clafton, S. N.; Pensack, R. D.; Kee, T. W.; Scholes, G. D., Vibrational Coherence Probes the Mechanism of Ultrafast Electron Transfer in Polymer–Fullerene Blends. *Nat. Commun.* **2014,** *5*, 4933.

29. Fuller, F. D.; Pan, J.; Gelzinis, A.; Butkus, V.; Senlik, S. S.; Wilcox, D. E.; Yocum, C. F.; Valkunas, L.; Abramavicius, D.; Ogilvie, J. P., Vibronic Coherence in Oxygenic Photosynthesis. *Nature Chem.* **2014,** *6*, 706-711.

30. Christensson, N.; Kauffmann, H. F.; Pullerits, T.; Mančal, T., Origin of Long-Lived Coherences in Light-Harvesting Complexes. *J. Phys. Chem. B* **2011,** *116*, 7449-7454.

31. Kolli, A.; O'Reilly, E. J.; Scholes, G. D.; Olaya-Castro, A., The Fundamental Role of Quantized Vibrations in Coherent Light Harvesting by Cryptophyte Algae. *J. Chem. Phys.* **2012,** *137*, 174109.

32. Chin, A. W.; Prior, J.; Rosenbach, R.; Caycedo-Soler, F.; Huelga, S. F.; Plenio, M. B., The Role of Non-Equilibrium Vibrational Structures in Electronic Coherence and Recoherence in Pigment-Protein Complexes. *Nature Phys.* **2013,** *9*, 113-118.

33. Fujihashi, Y.; Fleming, G. R.; Ishizaki, A., Impact of Environmentally Induced Fluctuations on Quantum Mechanically Mixed Electronic and Vibrational Pigment States in Photosynthetic Energy Transfer and 2D Electronic Spectra. *J. Chem. Phys.* **2015,** *142*, 212403.

34. Zimmerman, C.; Willig, F.; Ramakrishna, S.; Burfeindt, B.; Pettinger, B.; Eichenberger, R.; Storck, W., Experimental Fingerprints of Vibrational Wave-Packet Motion during Ultrafast Heterogeneous Electron Transfer. *J. Phys. Chem. B* **2001,** *105*, 9245-9253.

35. Molesky, B. M.; Guo, Z.; Moran, A. M., Femtosecond Stimulated Raman Spectroscopy by Six-Wave Mixing. *J. Chem. Phys.* **2015,** *142*, 212405.

36. Tanimura, Y.; Mukamel, S., Two-Dimensional Femtosecond Vibrational Spectroscopy of Liquids. *J. Chem. Phys.* **1993,** *99*, 9496-9511.

37. Kubarych, K. J.; Milne, C. J.; Lin, S.; Astinov, V.; Miller, R. J. D., Diffractive optics-based six-wave mixing:Heterodyne detection of the full $c^{(5)}$ tensor of liquid $CS_2$. *J. Chem. Phys.* **2002,** *116*, 2016-2042.

38. Kaufman, L. J.; Heo, J.; Ziegler, L. D.; Fleming, G. R., Heterodyne-Detected Fifth-Order Nonresonant Raman Scattering from Room Temperature CS2. *Phys. Rev. Lett.* **2002,** *88*, 207402:1-4.

39. Mehlenbacher, R.; Lyons, B.; Wilson, K. C.; Du, Y.; McCamant, D. W., Theoretical analysis of anharmonic coupling and cascading Raman signals observed with femtosecond stimulated Raman spectroscopy *J. Chem. Phys.* **2009,** *131*, 244512.

40. Wilson, K. C.; Lyons, B.; Mehlenbacher, R.; Sabatini, R.; McCamant, D. W., Two-dimensional femtosecond stimulated Raman spectroscopy: Observation of cascading Raman signals in acetonitrile *J. Chem. Phys.* **2009,** *131*, 214502.

41. Guo, Z.; Molesky, B. M.; Cheshire, T. P.; Moran, A. M., Elucidation of Reactive Wavepackets by Two-Dimensional Resonance Raman Spectroscopy. *J. Chem. Phys.* **2015,** *143*, 124202.

42. Loring, R. F.; Mukamel, S., Selectivity in Coherent Transient Raman Measurements of Vibrational Dephasing in Liquids. *J. Chem. Phys.* **1985,** *83*, 2116-2126.

43. Molesky, B. P.; Giokas, P. G.; Guo, Z.; Moran, A. M., Multidimensional Resonance Raman Spectroscopy by Six-Wave Mixing in the Deep UV. *J. Chem. Phys.* **2014,** *114*, 114202.

# APPENDIX 1: SUPPLEMENTARY MATERIAL FOR CHAPTER 2 "ELUCIDATION OF REACTIVE WAVEPACKETS BY TWO-DIMENSIONAL RESONANCE RAMAN SPECTROSCOPY"

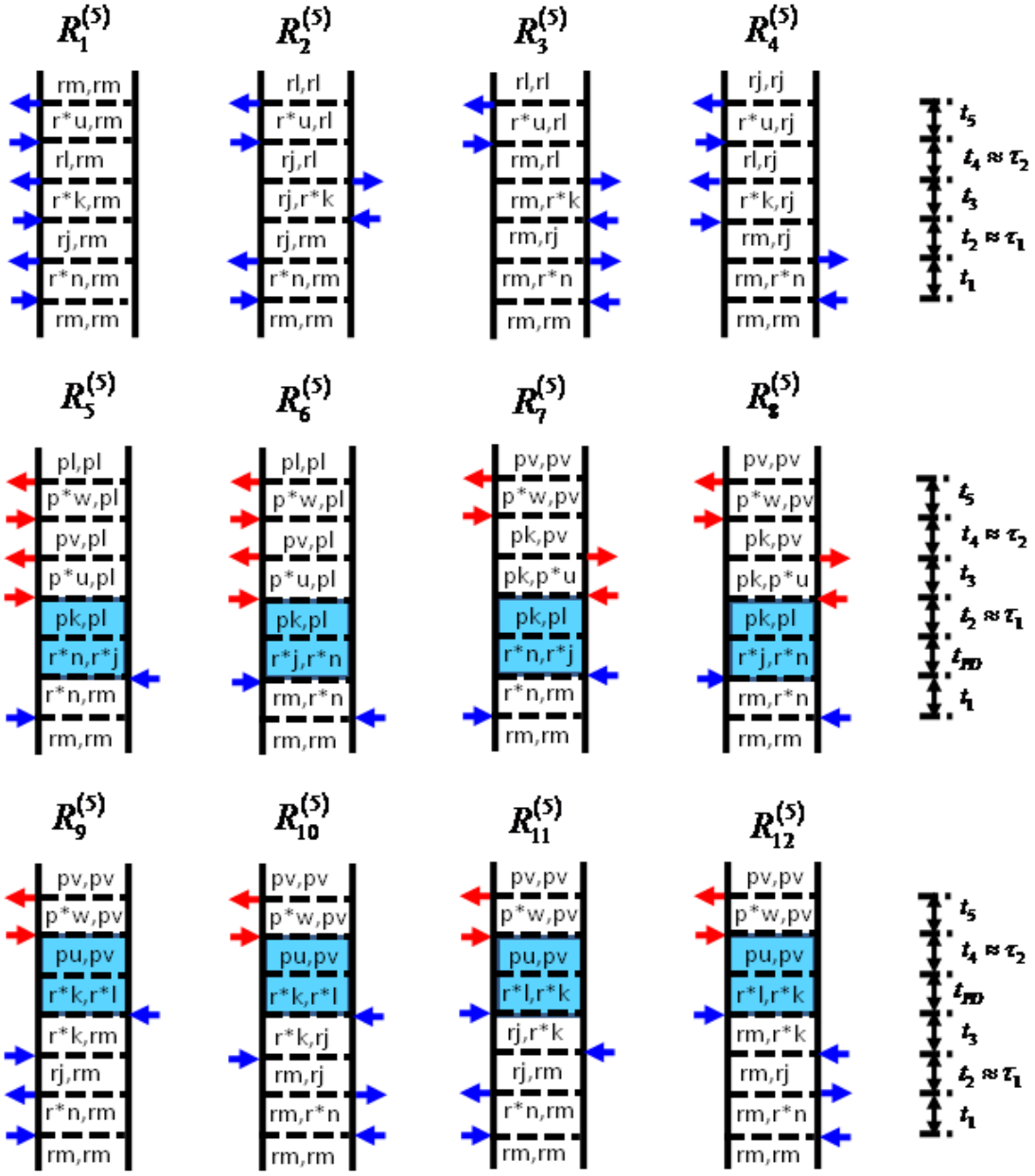


***Figure A.1.*** *Fenyman diagrams associated with dominant 2DRR nonlinearities. Blue and red arrows represent pulses resonant with triiodide and diiodide, respectively. The indices $r$ and $r*$ represent the ground and excited electronic states of the triiodide reactant, whereas $p$ and $p*$ correspond to the diiodide photoproduct. Vibrational levels associated with these electronic states are specified by dummy indices ($m, n, j, k, l, u, v, w$). Each row represents a different class of terms: (i) both dimensions correspond to triiodide in terms 1-4; (ii) both dimensions correspond to diiodide in terms 5-8; (iii) vibrational resonances of triiodide and diiodide appear in separate dimensions in terms 9-12. The intervals shaded in blue represent a non-radiative transfer of vibronic coherence from triiodide to diiodide.*

**I. Derivation of Formula for the Two-Dimensional Resonance Raman Signal Field**

The Feynman diagrams presented in Figure A1 include dummy indices for vibrational levels ($m, n, j, k, l, u, v, w$) associated with the ground and excited electronic states of the reactant ($r$ and $r*$) and product ($p$ and $p*$). Response functions are written in the Condon approximation, where the integral over electronic and nuclear degrees of freedom in the transition dipole is separated into a product of integrals. For example, an interaction that couples vibrational level $m$ in the ground electronic state of the reactant and vibrational level $n$ in the excited electronic state contributes the product, $\mu_{r*r}\langle n|m\rangle$, to the response function, where $\mu_{r*r}$ is the electronic transition dipole of the reactant and $\langle n|m\rangle$ is a vibrational overlap integral. We use a notation in which the index for the excited state vibrational energy level is always written in the bra.[1]

Under the assumption that the photodissociation time scale is short compared to the vibrational period, the time interval, $t_{PD}$, can be eliminated from consideration. The response functions corresponding to the fifth-order diagrams in Figure A1 can then be written as

$$R_1^{(5)}(t_1,t_2,t_3,t_4,t_5) = |\mu_{r*r}|^6 \sum_{mnjklu} B_m \langle n|m\rangle\langle n|j\rangle\langle k|j\rangle\langle k|l\rangle\langle u|l\rangle\langle u|m\rangle L_{r*n,rm}(t_1) \times L_{rj,rm}(t_2) L_{r*k,rm}(t_3) L_{rl,rm}(t_4) L_{r*u,rm}(t_5), \quad \text{(A.1)}$$

$$R_2^{(5)}(t_1,t_2,t_3,t_4,t_5) = |\mu_{r*r}|^6 \sum_{mnjklu} B_m \langle n|m\rangle\langle n|j\rangle\langle k|m\rangle\langle k|l\rangle\langle u|j\rangle\langle u|l\rangle L_{r*n,rm}(t_1) \times L_{rj,rm}(t_2) L_{rj,r*k}(t_3) L_{rj,rl}(t_4) L_{r*u,rl}(t_5), \quad \text{(A.2)}$$

$$R_3^{(5)}(t_1,t_2,t_3,t_4,t_5) = |\mu_{r*r}|^6 \sum_{mnjklu} B_m \langle n|m\rangle\langle n|j\rangle\langle k|j\rangle\langle k|l\rangle\langle u|m\rangle\langle u|l\rangle L_{rm,r*n}(t_1) \times L_{rm,rj}(t_2) L_{rm,r*k}(t_3) L_{rm,rl}(t_4) L_{r*u,rl}(t_5), \quad \text{(A.3)}$$

$$R_4^{(5)}(t_1,t_2,t_3,t_4,t_5) = |\mu_{r^*r}|^6 \sum_{mnjklu} B_m \langle n|m\rangle\langle n|j\rangle\langle k|m\rangle\langle k|l\rangle\langle u|l\rangle\langle u|j\rangle L_{rm,r^*n}(t_1) \times L_{rm,rj}(t_2) L_{r^*k,rj}(t_3) L_{rl,rj}(t_4) L_{r^*u,rj}(t_5), \quad \text{(A.4)}$$

$$R_5^{(5)}(t_1,t_2,t_3,t_4,t_5) = |\mu_{r^*r}|^2 |\mu_{p^*p}|^4 \sum_{mnjkluvw} B_m \langle n|m\rangle\langle j|m\rangle\langle u|k\rangle\langle u|v\rangle\langle w|v\rangle\langle w|l\rangle \times L_{r^*n,rm}(t_1) L_{pk,pl}(t_2) L_{p^*u,pl}(t_3) L_{pv,pl}(t_4) L_{p^*w,pl}(t_5), \quad \text{(A.5)}$$

$$R_6^{(5)}(t_1,t_2,t_3,t_4,t_5) = |\mu_{r^*r}|^2 |\mu_{p^*p}|^4 \sum_{mnjkluvw} B_m \langle n|m\rangle\langle j|m\rangle\langle u|k\rangle\langle u|v\rangle\langle w|v\rangle\langle w|l\rangle \times L_{rm,r^*n}(t_1) L_{pk,pl}(t_2) L_{p^*u,pl}(t_3) L_{pv,pl}(t_4) L_{p^*w,pl}(t_5), \quad \text{(A.6)}$$

$$R_7^{(5)}(t_1,t_2,t_3,t_4,t_5) = |\mu_{r^*r}|^2 |\mu_{p^*p}|^4 \sum_{mnjkluvw} B_m \langle n|m\rangle\langle j|m\rangle\langle u|l\rangle\langle u|v\rangle\langle w|k\rangle\langle w|v\rangle \times L_{r^*n,rm}(t_1) L_{pk,pl}(t_2) L_{pk,p^*u}(t_3) L_{pk,pv}(t_4) L_{p^*w,pv}(t_5), \quad \text{(A.7)}$$

$$R_8^{(5)}(t_1,t_2,t_3,t_4,t_5) = |\mu_{r^*r}|^2 |\mu_{p^*p}|^4 \sum_{mnjkluvw} B_m \langle n|m\rangle\langle j|m\rangle\langle u|l\rangle\langle u|v\rangle\langle w|k\rangle\langle w|v\rangle \times L_{rm,r^*n}(t_1) L_{pk,pl}(t_2) L_{pk,p^*u}(t_3) L_{pk,pv}(t_4) L_{p^*w,pv}(t_5), \quad \text{(A.8)}$$

$$R_9^{(5)}(t_1,t_2,t_3,t_4,t_5) = |\mu_{r^*r}|^2 |\mu_{p^*p}|^2 \sum_{mnjkluvw} B_m \langle n|m\rangle\langle n|j\rangle\langle k|j\rangle\langle l|m\rangle\langle w|u\rangle\langle w|v\rangle \times L_{r^*n,rm}(t_1) L_{rj,rm}(t_2) L_{r^*k,rm}(t_3) L_{pu,pv}(t_4) L_{p^*w,pv}(t_5), \quad \text{(A.9)}$$

$$R_{10}^{(5)}(t_1,t_2,t_3,t_4,t_5) = |\mu_{r^*r}|^4 |\mu_{p^*p}|^2 \sum_{mnjkluvw} B_m \langle n|m\rangle\langle n|j\rangle\langle k|m\rangle\langle l|j\rangle\langle w|u\rangle\langle w|v\rangle \times L_{rm,r^*n}(t_1) L_{rm,rj}(t_2) L_{r^*k,rj}(t_3) L_{pu,pv}(t_4) L_{p^*w,pv}(t_5), \quad \text{(A.10)}$$

$$R_{11}^{(5)}(t_1,t_2,t_3,t_4,t_5) = |\mu_{r^*r}|^4 |\mu_{p^*p}|^2 \sum_{mnjkluvw} B_m \langle n|m\rangle\langle n|j\rangle\langle k|m\rangle\langle l|j\rangle\langle w|u\rangle\langle w|v\rangle \times L_{r^*n,rm}(t_1) L_{rj,rm}(t_2) L_{rj,r^*k}(t_3) L_{pu,pv}(t_4) L_{p^*w,pv}(t_5), \quad \text{(A.11)}$$

$$R_{12}^{(5)}(t_1,t_2,t_3,t_4,t_5) = |\mu_{r^*r}|^4 |\mu_{p^*p}|^2 \sum_{mnjkluvw} B_m \langle n|m\rangle\langle n|j\rangle\langle k|j\rangle\langle l|m\rangle\langle w|u\rangle\langle w|v\rangle \times L_{rm,r^*n}(t_1) L_{rm,rj}(t_2) L_{rm,r^*k}(t_3) L_{pu,pv}(t_4) L_{p^*w,pv}(t_5). \quad \text{(A.12)}$$

In the above equations, the propagation functions corresponding to vibronic (in $t_1$, $t_3$, or $t_5$) and purely vibrational (in $t_2$ or $t_4$) coherences are respectively given by[2]

$$L_{r^*m,rn}(t) = \theta(t)\exp\left(-i\omega_{r^*r}t - i\omega_{mn}t - \Gamma_{r^*r}t\right) \tag{A.13}$$

and

$$L_{rm,rn}(t) = \theta(t)\exp\left(-i\omega_{mn}t - \Gamma_{vib}t\right)\ , \tag{A.14}$$

where $\theta(t)$ is a Heaviside step function. It is assumed in Equation (A.13) that electronic dephasing is much faster than vibrational dephasing (i.e., $\Gamma_{r^*r} >> \Gamma_{vib}$).

We next obtain the 12 components of the fifth-order polarization by convoluting the response functions with the external electric fields. The component of the fifth-order polarization corresponding to the $R_1$ term is given by

$$\begin{aligned} P_1^{(5)}(t) = N\left(\frac{i}{\hbar}\right)^5 \int_0^\infty dt_5 \int_0^\infty dt_4 \int_0^\infty dt_3 \int_0^\infty dt_2 \int_0^\infty dt_1 R_1^{(5)}(t_1,t_2,t_3,t_4,t_5)\, E_{UV}(t-t_5) E_{UV}^*(t+\tau_2-t_5-t_4) \\ E_{UV}(t+\tau_2-t_5-t_4-t_3) E_{UV}^*(t+\tau_1+\tau_2-t_5-t_4-t_3-t_2) \\ E_{UV}(t+\tau_1+\tau_2-t_5-t_4-t_3-t_2-t_1) \end{aligned}\ , \tag{A.15}$$

where $N$ is the number density and $\tau_j$ are the pulse delay times defined in the manuscript. Pulses with the subscripts *UV* and *VIS* are taken to interact with triiodide and diiodide, respectively. Attainment of analytic expressions is facilitated by use of double-sided exponential electric field envelopes,

$$E_j(t) = \xi_j \exp\left(-i\omega_j t - \Lambda_j |t|\right)\ , \tag{A.16}$$

where $\xi_j$ is the (real) electric field amplitude, $\Lambda_j$ is the HWHM spectral width, and $\omega_j$ is the carrier frequency of the laser pulse (the index, $j$, signifies either the "pump" or "probe"), which we take to be resonant with the triiodide reactant. The polarization component, $P_1^{(5)}(t)$, can now be rewritten as

$$P_1^{(5)}(t) = N\xi_{UV}^5 \exp\left(-i\omega_{UV}t\right)\left(\frac{i}{\mathrm{h}}\right)^5 \int_0^\infty dt_5 \int_0^\infty dt_4 \int_0^\infty dt_3 \int_0^\infty dt_2 \int_0^\infty dt_1 R_1^{(5)}\left(t_1,t_2,t_3,t_4,t_5\right)$$
$$\times \exp\left[i\omega_{UV}t_1 + i\omega_{UV}t_3 + i\omega_{UV}t_5\right] \qquad . \qquad \text{(A.17)}$$
$$\times \exp\left[-\Lambda_{UV}\left|t-t_5\right| - \Lambda_{UV}\left|t+\tau_2-t_5-t_4\right| - \Lambda_{UV}\left|t+\tau_2-t_5-t_4-t_3\right|\right]$$
$$\times \exp\left[-\Lambda_{UV}\left|t+\tau_1+\tau_2-t_5-t_4-t_3-t_2\right| - \Lambda_{UV}\left|t+\tau_1+\tau_2-t_5-t_4-t_3-t_2-t_1\right|\right]$$

We use a "doorway wavepacket" to filter vibrational coherences with frequencies that exceed the bandwidth of the pump pulse.[2] To this end, we introduce the change of variables, $t' = t + \tau_1 - t_2$ and $t'' = t + \tau_2 - t_4$. The polarization component is then given by

$$P_1^{(5)}(t) = N\xi_{UV}^5 \left(\frac{i}{\mathrm{h}}\right)^5 \int_0^\infty dt_5 \int_{-\infty}^\infty dt'' \int_0^\infty dt_3 \int_{-\infty}^\infty dt' \int_0^\infty dt_1 R_1^{(5)}\left(t_1, t+\tau_1-t', t_3, t+\tau_2-t'', t_5\right)$$
$$\times \exp\left[i\omega_{UV}t_1 + i\omega_{UV}t_3 + i\omega_{UV}t_5 - i\omega_{UV}t\right] \qquad , \qquad \text{(A.18)}$$
$$\times \exp\left[-2\Lambda_{UV}\left|t''\right| - 2\Lambda_{UV}\left|t'\right|\right]$$

Here, we have assumed that (i) $t_2 \approx \tau_1$ in order to carry out the integral over $t'$ and (ii) the pulse durations are short compared to the delay times to make the upper limits of the integrals over $t'$ and $t''$ infinite. The time intervals, $t_1$ , $t_3$, and $t_5$, have also been removed from the arguments of the laser pulses under the assumption that the pulse durations are long compared to the electronic dephasing time. We next introduce the approximation, $t = t_5$,

$$P_1^{(5)}(\omega_1,\omega_2) = N\xi_{UV}^5 \left(\frac{i}{\mathrm{h}}\right)^5 \int_0^\infty dt \int_0^\infty d\tau_2 \int_0^\infty d\tau_1 \int_{-\infty}^\infty dt'' \int_0^\infty dt_3 \int_{-\infty}^\infty dt' \int_0^\infty dt_1 R_1^{(5)}\left(t_1, \tau_1-t', t_3, \tau_2-t'', t\right) \qquad , \qquad \text{(A.19)}$$
$$\times \exp\left[i\omega_{UV}t_1 + i\omega_{UV}t_3 + i\omega_1\tau_1 + i\omega_2\tau_2 + i\omega_t t - 2\Lambda_{UV}\left|t''\right| - 2\Lambda_{UV}\left|t'\right|\right]$$

and Fourier transform the expression with respect to $\tau_1$, $\tau_2$, and $t$. Evaluation of the seven integrals in Equation (A.19) yields

$$P_1^{(5)}(\omega_1,\omega_2) = -\frac{N\xi_{UV}^5\left|\mu_{r^*r}\right|^6}{\mathrm{h}^5} \sum_{mnjklu} B_m \langle n|m\rangle\langle n|j\rangle\langle k|j\rangle\langle k|l\rangle\langle u|l\rangle\langle u|m\rangle \qquad , \qquad \text{(A.20)}$$
$$\times L_{r^*n,rm}\left(\omega_{UV}\right) D_{rj,rm}\left(\omega_1\right) L_{r^*k,rm}\left(\omega_{UV}\right) D_{rl,rm}\left(\omega_2\right) L_{r^*u,rm}\left(\omega_t\right)$$

where the line shape of the electronic resonance is given by

$$L_{r^*n,rm}(\omega) = -i\int_0^\infty L_{r^*n,rm}(t)\exp(i\omega t)\,dt = \frac{1}{\omega - \omega_{r^*r} - \omega_{nm} + i\Gamma_{r^*r}}. \tag{A.21}$$

The spectroscopic line shape associated with the doorway wavepacket is written as

$$\begin{aligned} D_{rk,rm}(\omega) &= -i\int_{-\infty}^{\infty} dt \exp\left(i\omega_{km}t - \Gamma_{vib}|t| - 2\Lambda_{UV}|t|\right)\int_0^\infty dt L_{rk,rm}(\tau)\exp(i\omega\tau) \\ &= \frac{2\Gamma_{vib} + 4\Lambda_{UV}}{\omega_{km}^2 + \left(\Gamma_{vib} + 2\Lambda_{UV}\right)^2}\left(\frac{1}{\omega - \omega_{km} + i\Gamma_{vib}}\right) \end{aligned}. \tag{A.22}$$

We obtain the following 11 polarization components by following the same procedure

$$\begin{aligned} P_2^{(5)}(\omega_1,\omega_2) &= -\frac{N\xi_{UV}^5\left|\mu_{r^*r}\right|^6}{\mathrm{h}^5}\sum_{mnjklu} B_m \langle n|m\rangle\langle n|j\rangle\langle k|m\rangle\langle k|l\rangle\langle u|j\rangle\langle u|l\rangle, \\ &\times L_{r^*n,rm}(\omega_{UV})D_{rj,rm}(\omega_1)L_{rj,r^*k}(-\omega_{UV})D_{rj,rl}(\omega_2)L_{r^*u,rl}(\omega_t) \end{aligned} \tag{A.23}$$

$$\begin{aligned} P_3^{(5)}(\omega_1,\omega_2) &= -\frac{N\xi_{UV}^5\left|\mu_{r^*r}\right|^6}{\mathrm{h}^5}\sum_{mnjklu} B_m \langle n|m\rangle\langle n|j\rangle\langle k|j\rangle\langle k|l\rangle\langle u|m\rangle\langle u|l\rangle, \\ &\times L_{rm,r^*n}(-\omega_{UV})D_{rm,rj}(\omega_1)L_{rm,r^*k}(-\omega_{UV})D_{rm,rl}(\omega_2)L_{r^*u,rl}(\omega_t) \end{aligned} \tag{A.24}$$

$$\begin{aligned} P_4^{(5)}(\omega_1,\omega_2) &= -\frac{N\xi_{UV}^5\left|\mu_{r^*r}\right|^6}{\mathrm{h}^5}\sum_{mnjklu} B_m \langle n|m\rangle\langle n|j\rangle\langle k|m\rangle\langle k|l\rangle\langle u|l\rangle\langle u|j\rangle, \\ &\times L_{rm,r^*n}(-\omega_{UV})D_{rm,rj}(\omega_1)L_{r^*k,rj}(\omega_{UV})D_{rl,rj}(\omega_2)L_{r^*u,rj}(\omega_t) \end{aligned} \tag{A.25}$$

$$\begin{aligned} P_5^{(5)}(\omega_1,\omega_2) &= -\frac{N\xi_{UV}^2\xi_{VIS}^3\left|\mu_{r^*r}\right|^2\left|\mu_{p^*p}\right|^4}{\mathrm{h}^5}\sum_{mnjkluvw} B_m \langle n|m\rangle\langle j|m\rangle\langle u|k\rangle\langle u|v\rangle\langle w|v\rangle\langle w|l\rangle, \\ &\times L_{r^*n,rm}(\omega_{UV})D_{pk,pl}(\omega_1)L_{p^*u,pl}(\omega_{VIS})D_{pv,pl}(\omega_2)L_{p^*w,pl}(\omega_t) \end{aligned} \tag{A.26}$$

$$\begin{aligned} P_6^{(5)}(\omega_1,\omega_2) &= -\frac{N\xi_{UV}^2\xi_{VIS}^3\left|\mu_{r^*r}\right|^2\left|\mu_{p^*p}\right|^4}{\mathrm{h}^5}\sum_{mnjkluvw} B_m \langle n|m\rangle\langle j|m\rangle\langle u|k\rangle\langle u|v\rangle\langle w|v\rangle\langle w|l\rangle, \\ &\times L_{rm,r^*n}(-\omega_{UV})D_{pk,pl}(\omega_1)L_{p^*u,pl}(\omega_{VIS})D_{pv,pl}(\omega_2)L_{p^*w,pl}(\omega_t) \end{aligned} \tag{A.27}$$

$$P_7^{(5)}(\omega_1,\omega_2) = -\frac{N\xi_{UV}^2\xi_{VIS}^3\left|\mu_{r^*r}\right|^2\left|\mu_{p^*p}\right|^4}{\mathrm{h}^5}\sum_{mnjkluvw} B_m\langle n|m\rangle\langle j|m\rangle\langle u|l\rangle\langle u|v\rangle\langle w|k\rangle\langle w|v\rangle, \quad \text{(A.28)}$$
$$\times L_{r^*n,rm}(\omega_{UV})D_{pk,pl}(\omega_1)L_{pk,p^*u}(-\omega_{VIS})D_{pk,pv}(\omega_2)L_{p^*w,pv}(\omega_t)$$

$$P_8^{(5)}(\omega_1,\omega_2) = -\frac{N\xi_{UV}^2\xi_{VIS}^3\left|\mu_{r^*r}\right|^2\left|\mu_{p^*p}\right|^4}{\mathrm{h}^5}\sum_{mnjkluvw} B_m\langle n|m\rangle\langle j|m\rangle\langle u|l\rangle\langle u|v\rangle\langle w|k\rangle\langle w|v\rangle, \quad \text{(A.29)}$$
$$\times L_{rm,r^*n}(-\omega_{UV})D_{pk,pl}(\omega_1)L_{pk,p^*u}(-\omega_{VIS})D_{pk,pv}(\omega_2)L_{p^*w,pv}(\omega_t)$$

$$P_9^{(5)}(\omega_1,\omega_2) = -\frac{N\xi_{UV}^4\xi_{VIS}\left|\mu_{r^*r}\right|^4\left|\mu_{p^*p}\right|^2}{\mathrm{h}^5}\sum_{mnjkluvw} B_m\langle n|m\rangle\langle n|j\rangle\langle k|j\rangle\langle l|m\rangle\langle w|u\rangle\langle w|v\rangle, \quad \text{(A.30)}$$
$$\times L_{r^*n,rm}(\omega_{UV})D_{rj,rm}(\omega_1)L_{r^*k,rm}(\omega_{UV})D_{pu,pv}(\omega_2)L_{p^*w,pv}(\omega_t)$$

$$P_{10}^{(5)}(\omega_1,\omega_2) = -\frac{N\xi_{UV}^4\xi_{VIS}\left|\mu_{r^*r}\right|^4\left|\mu_{p^*p}\right|^2}{\mathrm{h}^5}\sum_{mnjkluvw} B_m\langle n|m\rangle\langle n|j\rangle\langle k|m\rangle\langle l|j\rangle\langle w|u\rangle\langle w|v\rangle, \quad \text{(A.31)}$$
$$\times L_{rm,r^*n}(-\omega_{UV})D_{rm,rj}(\omega_1)L_{r^*k,rj}(\omega_{UV})D_{pu,pv}(\omega_2)L_{p^*w,pv}(\omega_t)$$

$$P_{11}^{(5)}(\omega_1,\omega_2) = -\frac{N\xi_{UV}^4\xi_{VIS}\left|\mu_{r^*r}\right|^4\left|\mu_{p^*p}\right|^2}{\mathrm{h}^5}\sum_{mnjkluvw} B_m\langle n|m\rangle\langle n|j\rangle\langle k|m\rangle\langle l|j\rangle\langle w|u\rangle\langle w|v\rangle, \quad \text{(A.32)}$$
$$\times L_{r^*n,rm}(\omega_{UV})D_{rj,rm}(\omega_1)L_{rj,r^*k}(-\omega_{UV})D_{pu,pv}(\omega_2)L_{p^*w,pv}(\omega_t)$$

$$P_{12}^{(5)}(\omega_1,\omega_2) = -\frac{N\xi_{UV}^4\xi_{VIS}\left|\mu_{r^*r}\right|^4\left|\mu_{p^*p}\right|^2}{\mathrm{h}^5}\sum_{mnjkluvw} B_m\langle n|m\rangle\langle n|j\rangle\langle k|j\rangle\langle l|m\rangle\langle w|u\rangle\langle w|v\rangle. \quad \text{(A.32)}$$
$$\times L_{rm,r^*n}(-\omega_{UV})D_{rm,rj}(\omega_1)L_{rm,r^*k}(-\omega_{UV})D_{pu,pv}(\omega_2)L_{p^*w,pv}(\omega_t)$$

**II. Dominance of the Direct 2DRR Response Over Third-Order Cascades**

Fifth-order coherent Raman spectroscopies conducted under off-resonant conditions are susceptible to artifacts known as cascades.[3-7] A cascade is a sequence in which the four-wave mixing signal field generated by one molecule induces a four-wave mixing response on a second molecule. The second molecule then radiates a signal field in the same direction as the fifth-order signal of interest. Cascades are problematic under off-resonant conditions, because they can be many orders of magnitude more intense than the direct fifth-order response. It is thought that

selection rules primarily govern this mismatch in signal intensities.[7-9] That is, two-quantum transitions involved in the direct fifth-order process are forbidden in harmonic systems when the polarizability scales linearly in the vibrational coordinate. In contrast, third-order cascades are allowed in harmonic systems, which gives them a significant advantage over the fifth-order process. Cascades require this difference in selection rules to dominate over the direct fifth-order response, because they are higher-order in the sense that they involve two more field-matter interactions than the direct process (i.e., this extra factor of the polarizability operator suppresses the relative intensity of the cascaded response).

Cascades were ruled out in our previous all-UV 2DRR study of triiodide using control experiments based on the signal phase, concentration dependence of the signal intensity, and the relative phases of the vibrations detected in four and six-wave mixing signals.[8] The direct 2DRR response should be even more dominant in the present study because lower-frequency laser beams are employed. Moreover, the direct response is favored in the present experiments for the same reasons discussed at length in Reference [8]. In pump-repump-probe experiments, inspection of the signal phase is a particularly convenient way to check for cascades, because third and fifth-order signals possess a readily detected sign difference.[4,5] In contrast, cascades have the same sign as the direct third-order response. To illustrate this point, we present (third-order) pump-probe and (fifth-order) pump-repump-probe signals acquired for triiodide in Figure A2. The two signals have opposite signs as expected for the direct response. Compared to the all-UV approach taken in Reference [8], the phase difference for vibrational motion is not as straightforward to predict in the present two-color experiments because of sensitivity to the complex photodissociation process. Nonetheless, in Figure A2b, we compare the third-order signal to a slice of the fifth-order signal in $\tau_2$ (at $\tau_1$=0) at a signal detection wavenumber of

20,000 $cm^{-1}$ (500 nm). The analysis carried out in Reference [8] suggests that a phase shift near 180º is expected for the direct fifth-order response under these conditions. This prediction is consistent with the measurement shown in Figure A2b.

Our work suggests that contributions from cascades will generally be negligible in systems such as triiodide, where the excited state potential energy surface displacement is extremely large.[8] In essence, Franck-Condon activity eliminates the problematic selection rules found under off-resonant conditions (see Figure 14 in Reference [8]). We emphasize that the direct response is not necessarily predicted to dominate in systems with modest mode displacements (i.e., dimensionless displacements below 1), which are typically found in larger molecules. However, in a recent study of metmyoglobin, we still found that the direct fifth-order nonlinearity is at least 10 times larger than the cascaded response in dilute solution.[10] It is worth noting that experiments in which the final four field-matter interactions are off-resonant with the equilibrium system are much less susceptible to cascades than our earlier all-resonant approaches.[8,10] In such a two-color configuration, the fifth-order response will be fully (electronically) resonant, whereas one of the four-wave mixing responses involved in a cascade must be (electronically) off-resonant (see Figure 2.7 and terms 5-8 in Figure 2.2 of the main paper). Pulse sequences in which the final four field-matter interactions are off-resonant with the equilibrium system are typically used in other types of optical pump-Raman probe experiments.[11-16]

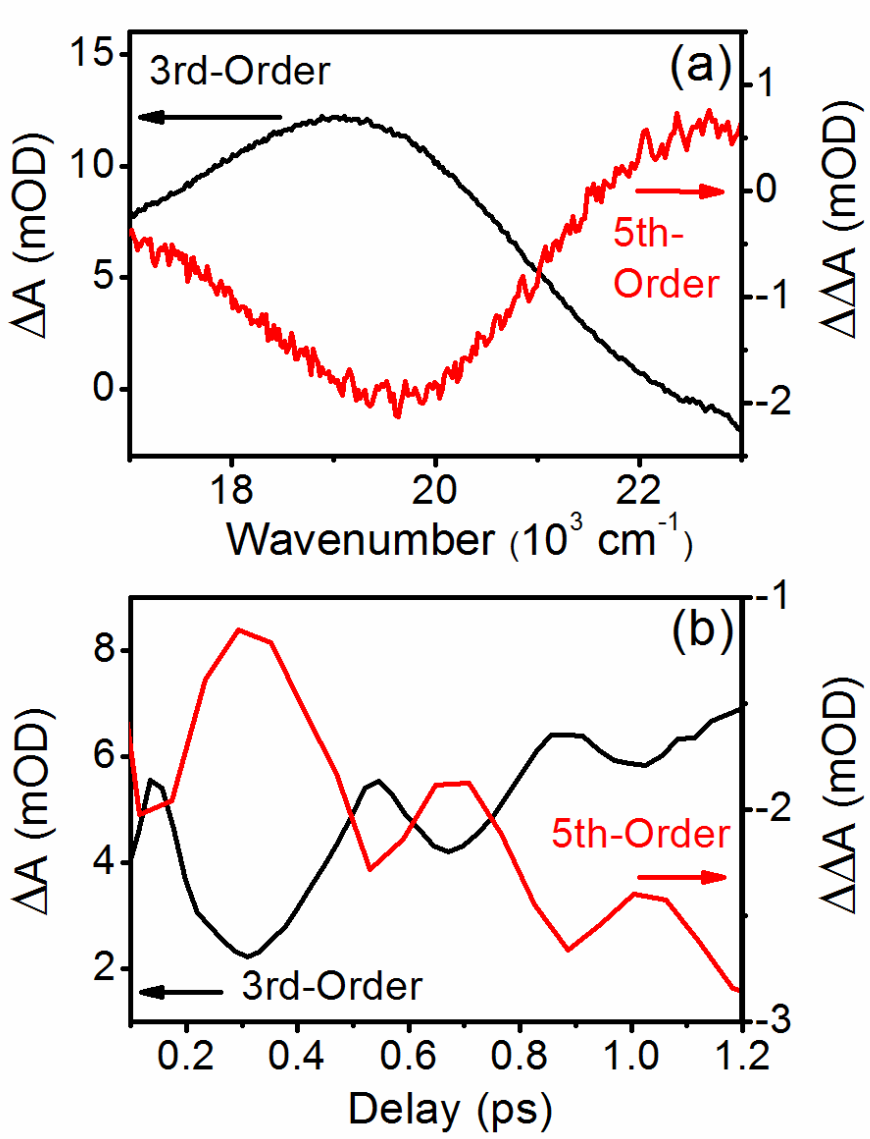


***Figure A.2.*** *Comparison of signal phases obtained for third-order (pump-probe) and fifth-order (pump-repump-probe) signals. (a) Pump-probe (delay of 0.5 ps) and pump-repump-probe ($\tau_1 = \tau_2 = 0.5$ ps) signals have similar line shapes but opposite signs. This sign-difference suggests that the pump-repump-probe signal is dominated by the desired fifth-order nonlinearity (i.e., not third-order cascades). (b) Oscillations in pump-probe and pump-repump-probe signals are compared with signal detection at 20,000 cm$^{-1}$ (500 nm). This is a slice of the pump-repump-probe signal in $\tau_2$ with the delay, $\tau_1$, fixed at 0 ps. A relative phase-shift near 180° suggests that the oscillatory component of the pump-repump-probe signal is dominated by the direct fifth order nonlinearity.*[8]

## REFERENCES


1. A. B. Myers, R. A. Mathies, D. J. Tannor, and E. J. Heller, J. Chem. Phys. **77**, 3857 (1982).

2. S. Mukamel, *Principles of Nonlinear Optical Spectroscopy*. (Oxford University Press, New York, 1995).

3. J. E. Ivanecky III and J. C. Wright, Chem. Phys. Lett. **206**, 437 (1993).

4. D. A. Blank, L. J. Kaufman, and G. R. Fleming, J. Chem. Phys. **111**, 3105 (1999).

5. K. J. Kubarych, C. J. Milne, S. Lin, V. Astinov, and R. J. D. Miller, J. Chem. Phys. **116**, 2016 (2002).

6. K. C. Wilson, B. Lyons, R. Mehlenbacher, R. Sabatini, and D. W. McCamant, J. Chem. Phys. **131**, 214502 (2009).

7. D. J. Ulness, J. C. Kirkwood, and A. C. Albrecht, J. Chem. Phys. **108**, 3897 (1998).

8. B. P. Molesky, P. G. Giokas, Z. Guo, and A. M. Moran, J. Chem. Phys. **114**, 114202 (2014).

9. S. Garret-Roe and P. Hamm, J. Chem. Phys. **130**, 164510 (2009).

10. B. P. Molesky, Z. Guo, and A. M. Moran, J. Chem. Phys. **142**, 212405 (2015).

11. D. F. Underwood and D. A. Blank, J. Phys. Chem. A **109**, 3295 (2005).

12. A. M. Moran, R. A. Nome, and N. F. Scherer, J. Chem. Phys. **127**, 184505:1 (2007).

13. M. S. Marek, T. Buckup, and M. Motzkus, J. Phys. Chem. B **115**, 8328 (2011).

14. J. M. Rhinehart, J. R. Challa, and D. W. McCamant, J. Phys. Chem. B **116**, 10522 (2012).

15. Y. Wang, W. Liu, L. Tang, B. Oscar, F. Han, and C. Fang, J. Phys. Chem. A **117**, 6024 (2013).

16. D. T. Valley, D. P. Hoffman, and R. A. Mathies, Phys. Chem. Chem. Phys. **17**, 9231 (2015).

## APPENDIX 2: SUPPLEMENTAL MATERIAL FOR CHAPTER 3 "TWO-DIMENSIONAL RESONANCE RAMAN SPECTROSCOPY OF OXYGEN- AND WATER-LIGATED MYOGLOBIN"

### I. Signatures of Anharmonicity in Time-Frequency Representation of 2DRR Signal

As discussed in the main text, anharmonic coupling between modes may cause the vibrational resonance frequencies in $\omega_2$ to oscillate with respect to $\tau_1$ for FSRS signals represented in the traditional way ($\tau_1$ and $\omega_2$ in our notation). Here, we examine this representation in our calculated signals. The first dimension may be expressed in the time domain by inverse Fourier transforming $E^{(5)}(\omega_1,\omega_2)$ with respect to $\tau_1$. Analytic expressions for this representation, which we denote as $E^{(5)}(\tau_1,\omega_2)$, were given in Reference [1]. The mean vibrational frequencies in $\omega_2$ are then Fourier transformed with respect to $\tau_1$,

$$\sigma(\omega_1)=\int_{-\infty}^{\infty}\left[\frac{\int_{\alpha}^{\beta}\left|E^{(5)}(\tau_1,\omega_2)\right|\omega_2 d\omega_2}{\int_{\alpha}^{\beta}\left|E^{(5)}(\tau_1,\omega_2)\right|d\omega_2}\right]\exp(i\omega_1\tau_1)\,d\tau_1. \tag{A.33}$$

in order to produce a vibrational spectrum associated with the quantum beats in the resonance frequencies. The lower, $\alpha$, and upper, $\beta$, limits of the integral over $\omega_2$ are respectively set equal to 250 and 550 cm$^{-1}$ for the 400-cm$^{-1}$ mode. Limits of 950 and 1250 cm$^{-1}$ are used for the 1100-cm$^{-1}$ resonance in $\omega_2$.

In Figure A.3, we present vibrational spectra associated with quantum beats in the resonance frequencies. The harmonic system in panel (e) exhibits the most intense oscillations at the frequency corresponding to a coherence between the two modes (i.e., 700 cm$^{-1}$ is the difference in wavenumbers. As in Reference [1], we find that oscillations in the mean vibrational resonance frequencies are observed even for a harmonic system (see Figures 3.11 and 3.12 in Reference [2]). Anharmonicity causes the relative amplitude of the quantum beat at 400 cm$^{-1}$ to

increase; the effect is most pronounced in panels S1(a), S1(c), S1(g) and S1(i) (i.e., the parameters with the greatest amount of anharmonicity) These results suggest that the relative amplitudes of various spectral components carry the key information about anharmonicity in this representation. Quantum beats at difference frequencies occur even in the harmonic system. This conclusion is still valid if the real or imaginary parts of the fifth-order signal field enter Equation (A.33). We process the absolute value of the signal field, $E^{(5)}(\tau_1, \omega_2)$, because the time evolution (in $\tau_1$) between absorptive and dispersive line shapes (in $\omega_2$) gives rise to artificially large oscillations in the mean resonance frequencies (in $\omega_2$).

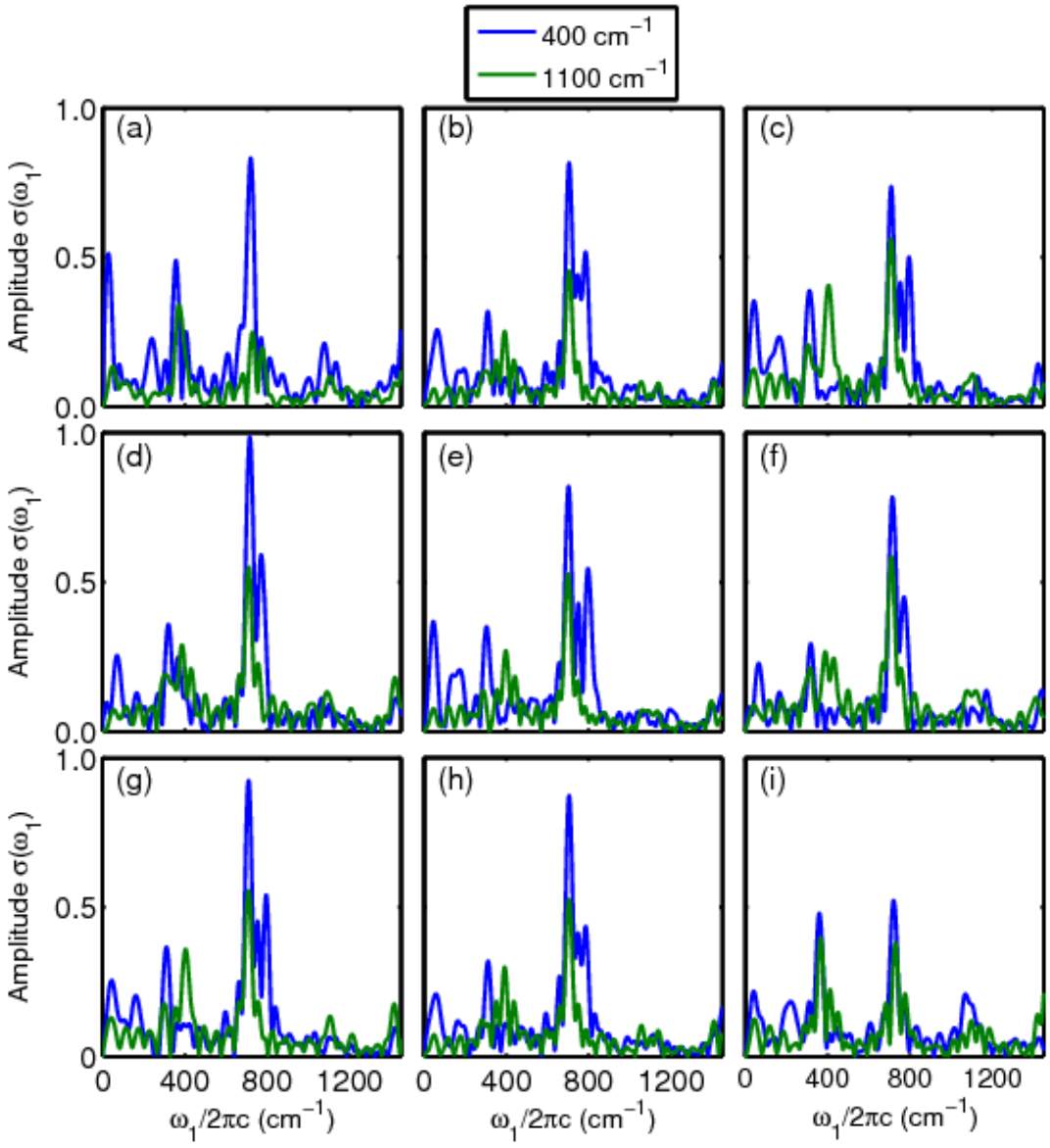


***Figure A.3.*** *Spectral components associated with oscillations of the mean vibrational resonance frequencies computed with an anharmonic vibrational Hamiltonian. The diagonal expansion coefficients are set equal to -5 (first row), 0 (second row), and 5 cm$^{-1}$ (third row). The off-diagonal expansion coefficients are set equal to -5 (first row), 0 (second row), and 5 cm$^{-1}$ (third row). All amplitudes are normalized to the maximum found for the 400-cm$^{-1}$ mode in the second row and first column. These calculations show that oscillations in the mean vibrational resonance frequencies occur primarily at the difference frequency in the harmonic system (see panel (e)). Anharmonicity increases the amplitude of oscillations at the fundamental frequencies of the vibrations.*

## II. Fluctuations in the Geometries of the Propionic Acid Side Chains Produced with Molecular Dynamics Simulations and an Ab Initio Map

In this section, we present scatter plots for 5000 steps in the molecular dynamics trajectories of metMb and $MbO_2$, respectively. The structures fluctuate in a fairly symmetric manner with respect to the equilibrium geometries.

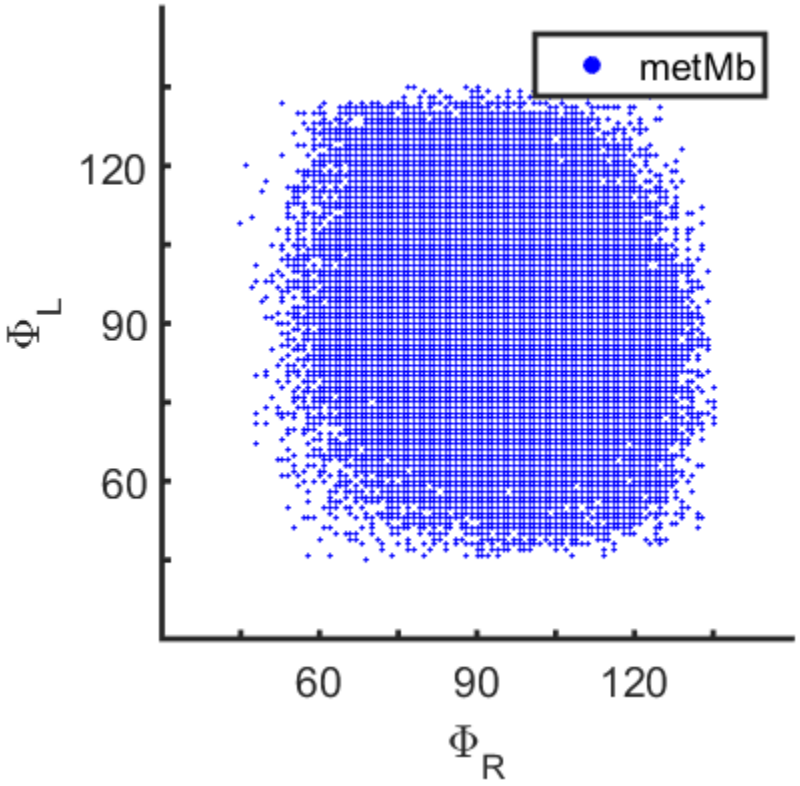


***Figure A.4.*** *Distribution of dihedral angles for 5000 steps of the molecular dynamics trajectory simulated for metMb. The equilibrium dihedral angles associated with the propionic acid side chains (see Figure 3.11) are* $\Phi_L$ *=81.3° and* $\Phi_R$ *=81.1°.*

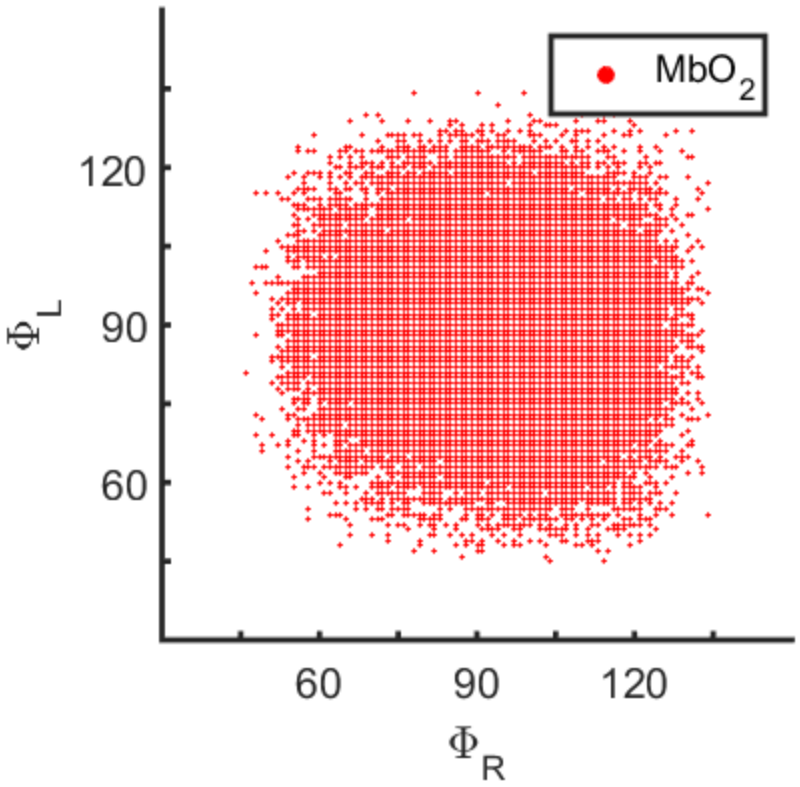


***Figure A.5.*** *Distribution of dihedral angles for 5000 steps of the molecular dynamics trajectory simulated for $MbO_2$. The equilibrium dihedral angles associated with the propionic acid side chains (see Figure 3.11) are* $\Phi_L$ *=94.4° and* $\Phi_R$ *=109°.*

## REFERENCES


1. B. M. Molesky, Z. Guo, and A. M. Moran, J. Chem. Phys. **142**, 212405 (2015).

2. B. P. Molesky, P. G. Giokas, Z. Guo, and A. M. Moran, J. Chem. Phys. **114**, 114202 (2014).

## APPENDIX 3: SUPPLEMENT FOR CHAPTER 4 "ULTRAFAST SPECTROSCOPIC SIGNATURES OF COHERENT ELECTRON TRANSFER MECHANISMS IN A TRANSITION METAL COMPLEX"

### I. Decomposition of Transient Absorption Signals

In this section, we present parameters associated with the broadband response observed in $[Ti(cat)_3]^{2-}$. The transient absorption data shown in Figure 4.6 of the main paper are fit using

$$F(\tau,\lambda) = A_{GSB}(\tau)\exp\left\{-4\ln(2)\frac{\left[\lambda-\lambda_{GSB}(\tau)\right]^2}{\Delta^2_{GSB}(\tau)}\right\} + A_{HGS}(\tau)\left\{-4\ln(2)\frac{\left[\lambda-\lambda_{HGS}(\tau)\right]^2}{\Delta^2_{HGS}(\tau)}\right\} + A_{BB}(\tau)\left\{-4\ln(2)\frac{\left[\lambda-\lambda_{BB}(\tau)\right]^2}{\Delta^2_{BB}(\tau)}\right\} \quad \text{(A.34)}$$

Because the broadband component of the response is red-shifted beyond our detection range, we have constrained both $\lambda_{BB}(\tau)$ and $\Delta_{BB}(\tau)$ (650 nm< $\lambda_{BB}(\tau)$ <850 nm and 400 nm< $\Delta_{BB}(\tau)$ <1000 nm). These constraints were required to suppress discontinuities in the parameters of the HGS signal component, which were left unconstrained. The residual can be further reduced by adding a constant offset to Equation (A.34) or replacing the broadband Gaussian function with a fifth order polynomial. We choose to use a Gaussian because it is the most physical choice in that it presumably approximates the line shape of an electronic resonance.

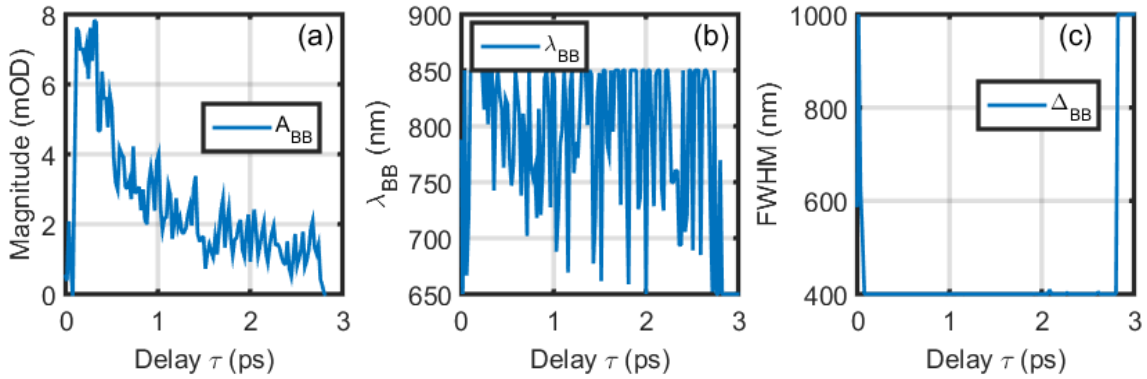


***Figure A.6.*** *Parameters of a broadband signal component determined in the decomposition of transient absorption signals. (a) Magnitude of the broadband signal component. (b) Peak wavelength computed for the broadband signal component. (c) FWHM line width for the broadband signal component. It is necessary to include a signal component at longer wavelengths because discontinuities in the parameters of the GSB and HGS resonances are found otherwise.*

**II. Analysis of Uncertainty in Spectral Fits**

Determination of error bars in this highly nonlinear model is not straightforward.[1] We have carried out the fits in the traditional way. The parameters are adjusted manually over many iterations until the best agreement is achieved between the experimental data and model. Here, we provide example fits to show how the optimal region of parameter space was located. In the two fits shown below, we reduced and increased the homogeneous width by 500 $cm^{-1}$ to show how the model diverges from the experimental line shape in each regime. The other parameters are adjusted to compensate for the fixed homogeneous width.

**IIA. Fits Conducted with Homogeneous Width Fixed at 2150 $cm^{-1}$**

Reduction of the homogeneous width causes a red shift in the absorbance spectrum, because the peak is displaced from the electronic origin by the sum of the intramolecular and solvent reorganization energies. The electronic origin must be increased to compensate for this effect, which also causes the Raman cross sections to increase (i.e., a second effect that must be compensated for). This is why the mode displacements given in Table A.1 are smaller than those

reported in the best fit. Poor agreement between the experimental and calculated absorbance line shapes at wavelengths longer than 400 nm  is the primary reason that we consider this to be an unrealistic region of parameter space; the rising side of the absorbance line shape becomes too steep. The quality of the fits become worse if the homogeneous width is decreased further.

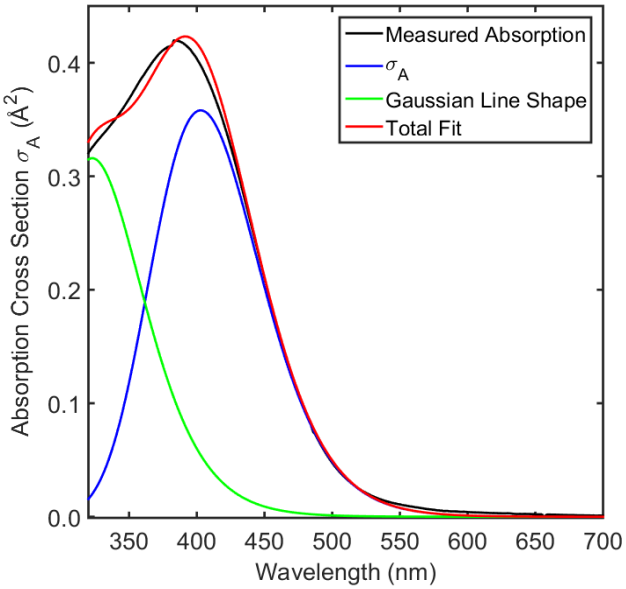


***Figure A.7.*** *The measured absorption spectrum is fit with Equation (4.19) in the main article and the parameters in Table A.1. The absorption cross section, $\sigma_A$, is used to fit the low-energy side of the line shape subject to the constraints imposed by the Raman cross sections. A Gaussian line shape (green) is used to estimate the contribution of the second-to-lowest energy transition to the total absorbance.*

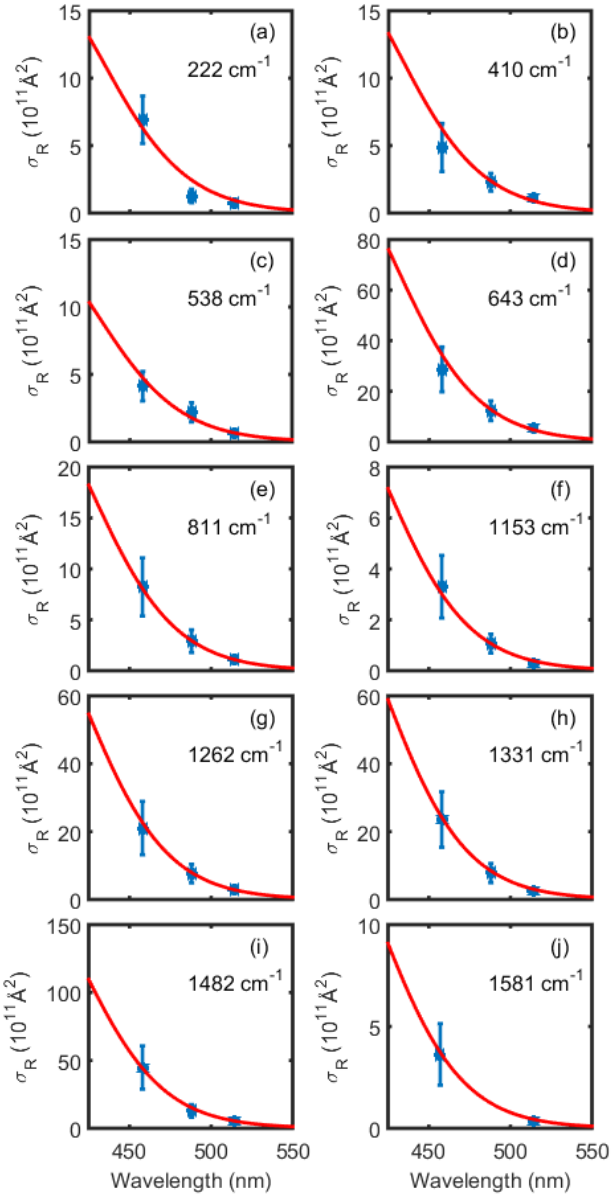


***Figure A.8.*** *Experimental Raman cross sections are fit using Equation (4.20) in the main article and the parameters in Table A.1.*

***Table A.1.*** *Resonance Raman Fitting Parameters for Homogeneous Width Fixed at 2150 cm$^{-1}$*

| [a]**Parameter** | **Value** | |
|---|---|---|
| $\omega_0$ | 21600 cm$^{-1}$ (463 nm) | |
| $\delta$ | 2080 cm$^{-1}$ (47 nm) | |
| $\Gamma$ | 2150 cm$^{-1}$ (46 nm) | |
| $\kappa = \Delta / \Lambda$ | 0.01 | |
| [b] $\lambda$ | 2088 cm$^{-1}$ | |
| $\mu_{eg}$ | 3.8 D | |
| **Raman Shift (cm$^{-1}$)** | **Dimensionless Displacement** | [c]**Assignment** |
| 222 | 1.02 | Symmetric Ti-cat stretch (214 cm$^{-1}$) |
| 410 | 0.57 | Ti-cat bend (413 cm$^{-1}$) |
| 538 | 0.39 | O-C-C-O bend & ring distortion (534 cm$^{-1}$) |
| 643 | 0.90 | O-C-C-O bend & ring distortion (641 cm$^{-1}$) |
| 811 | 0.36 | O-C-C-O bend and ring 'breathing' (814 cm$^{-1}$) |
| 1153 | 0.17 | C-H bending (1156 cm$^{-1}$) |
| 1262 | 0.44 | O-C-C-O stretch (1283 cm$^{-1}$) |
| 1330 | 0.44 | C=C stretch, C-O stretch, & Ti-O stretch (1305 cm$^{-1}$) |
| 1482 | 0.56 | C=C stretch & C-O stretch (1511 cm$^{-1}$) |
| 1580 | 0.16 | C=C stretch (1594 cm$^{-1}$) |

[a] Fits are carried out in the frequency domain (not wavelength).

[b] Computed with $\lambda = D^2 / 2k_B T$, where D is found with Equation (4.22).

[c] Assignments for vibrational modes computed at the B3LYP/6-311G(2d,3p) level in Gaussian 2009.[2] Frequencies of the calculated modes are given in parentheses.

**IIB. Fits Conducted with Homogeneous Width Fixed at 3150 $cm^{-1}$**

Increasing the homogeneous width causes a blue-shift in the absorbance spectrum, because the peak is displaced from the electronic origin by the sum of the intramolecular and solvent reorganization energies. The electronic origin is decreased to compensate for this effect, which causes the Raman cross sections to decrease (a second effect that must be compensated for). This is why the mode displacements given in Table A.2 are larger than those reported in the best fit. Poor agreement between the experimental and calculated absorbance line shapes at wavelengths longer than 400 nm is the one reason that we consider this to be an unrealistic region of parameter space; the rising side of the absorbance line shape is not sufficiently steep. We are also unable to produce an adequate fit to the Raman cross sections of the 222-$cm^{-1}$ mode. Moreover, the parameters seem to become unphysical, because the 6838-$cm^{-1}$ sum of the solvent and intramolecular reorganization energies is extremely large. For example, the electronic origin is at 709 nm when the homogeneous with is 3150 $cm^{-1}$, which is an extremely far displacement from the onset of light absorption. The quality of the fit become worse if the homogeneous width is increased further.

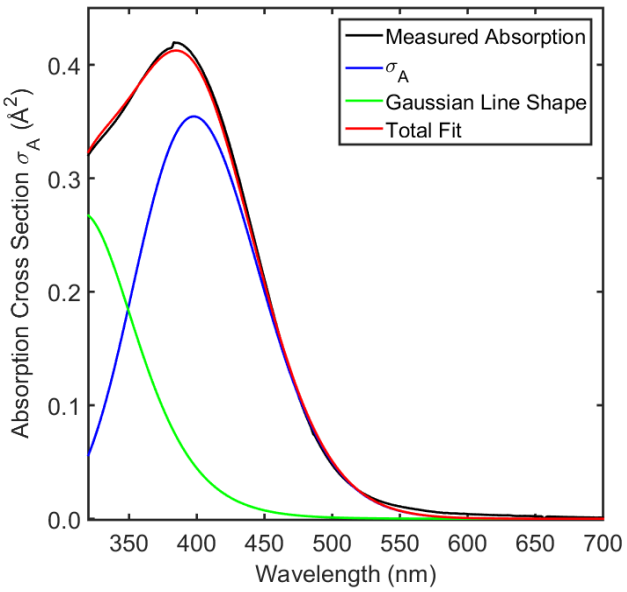


***Figure A.9.*** *The measured absorption spectrum is fit with Equation (4.19) in the main article and the parameters in Table S2. The absorption cross section, $\sigma_A$, is used to fit the low-energy side of the line shape subject to the constraints imposed by the Raman cross sections. A Gaussian line shape (green) is used to estimate the contribution of the second-to-lowest energy transition to the total absorbance.*

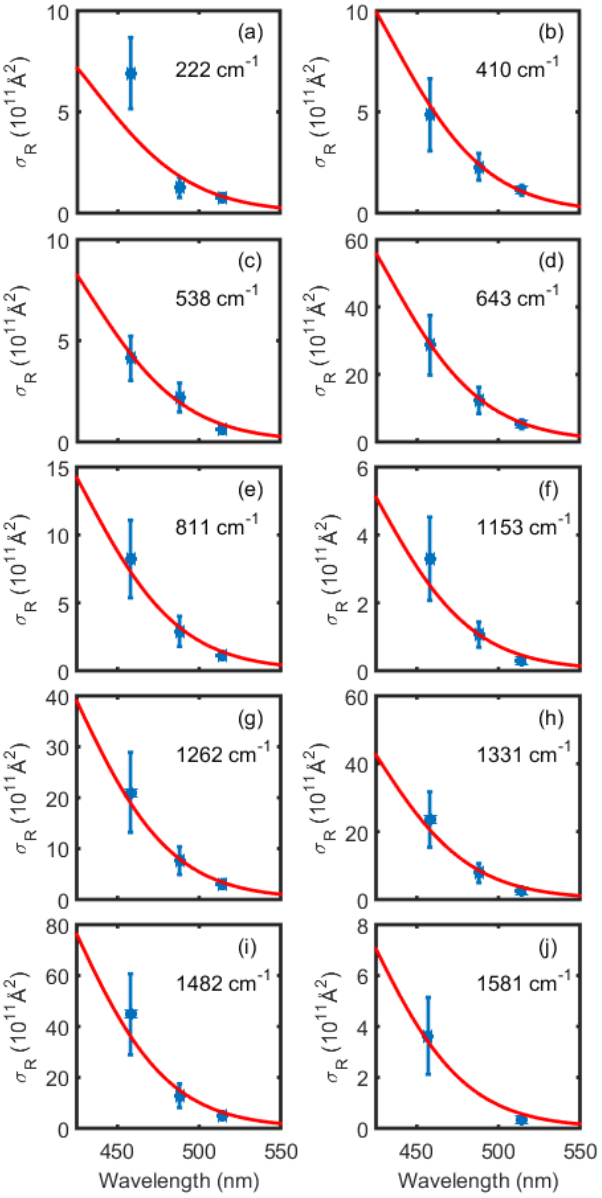


***Figure A.10.*** *Experimental Raman cross sections are fit using Equation (4.20) and the parameters in Table A.2.*

***Table A.2.*** *Resonance Raman Fitting Parameters*

| [a]**Parameter** | **Value** | |
|---|---|---|
| $\omega_0$ | 14100 $cm^{-1}$ (709 nm) | |
| $\delta$ | 300 $cm^{-1}$ (15 nm) | |
| $\Gamma$ | 3150 $cm^{-1}$ (160 nm) | |
| $\kappa = \Delta / \Lambda$ | 0.01 | |
| [b] $\lambda$ | 4483 $cm^{-1}$ | |
| $\mu_{eg}$ | 4.0 D | |
| **Raman Shift ($cm^{-1}$)** | **Dimensionless Displacement** | [c]**Assignment** |
| 222 | 2.4 | Symmetric Ti-cat stretch (214 $cm^{-1}$) |
| 410 | 1.55 | Ti-cat bend (413 $cm^{-1}$) |
| 538 | 1.09 | O-C-C-O bend (534 $cm^{-1}$) |
| 643 | 2.4 | O-C-C-O bend (641 $cm^{-1}$) |
| 811 | 0.98 | O-C-C-O bend and ring 'breathing' (814 $cm^{-1}$) |
| 1153 | 0.43 | C-H bending (1156 $cm^{-1}$) |
| 1262 | 1.10 | O-C-C-O stretch (1283 $cm^{-1}$) |
| 1330 | 1.10 | C=C stretch, C-O stretch, & Ti-O stretch (1305 $cm^{-1}$) |
| 1482 | 1.35 | C=C stretch & C-O stretch (1511 $cm^{-1}$) |
| 1580 | 0.39 | C=C stretch (1594 $cm^{-1}$) |

[a] Fits are carried out in the frequency domain (not wavelength).

[b] Computed with $\lambda = D^2 / 2k_B T$, where D is found with Equation (4.22).

[c] Assignments for vibrational modes computed at the B3LYP/6-311G(2d,3p) level in Gaussian 2009.[2] Frequencies of the calculated modes are given in parentheses.

### III. The HGS Signal Component Dominates the Coherent Raman Response of $[Ti(cat)_3]^{2-}$

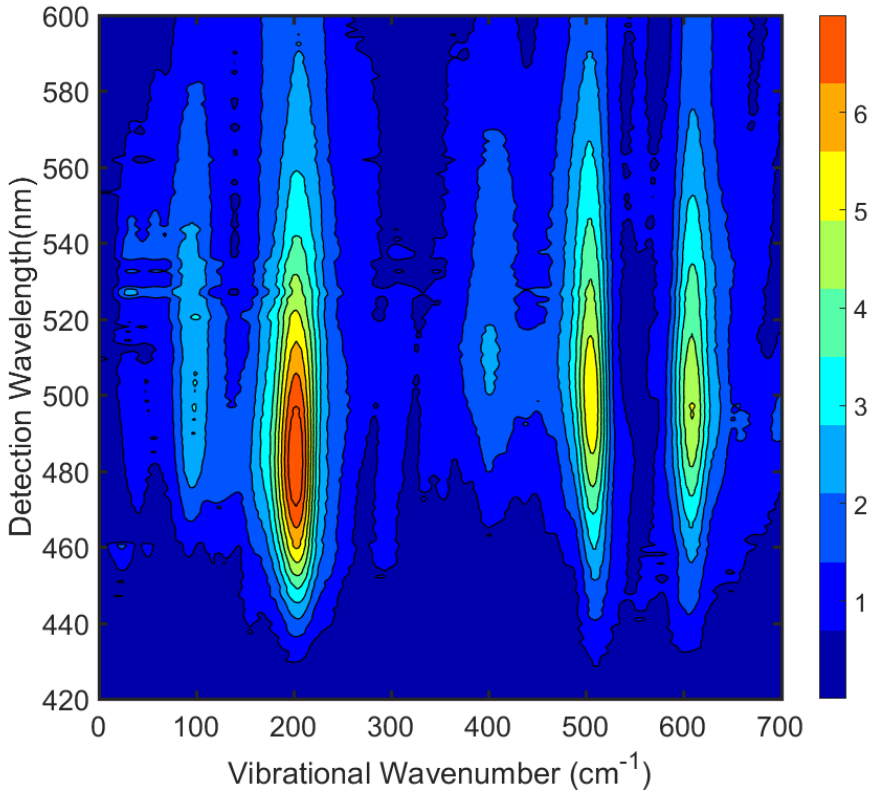


***Figure A.11.*** *The coherent response of the $[Ti(cat)_3]^{2-}$ is analyzed for a range of detection wavelengths. Coherent vibrational motion is detected at wavelengths that correspond to the HGS signal component in the 450-560-nm range. The stimulated Raman response for the GSB signal component is relatively weak. These data suggest that the back electron transfer process induces the vibrational motions detection in our transient absorption experiments.*

### IV. Density Functional Theory Analysis of the Most Appropriate Basis Set

The LMCT transitions should be treated as localized if interactions between the local charge transfer states are small compared to the thermal fluctuation amplitudes in the energy levels. This general rule of thumb also governs Frenkel exciton delocalization in molecular aggregates and crystals.[5] The thermal fluctuation amplitude that we have determined experimentally is $\Delta$=1040 $cm^{-1}$ (see Table 4.1 in the main article). The coupling between LMCT states can be estimated with electronic structure calculations if we invoke a four-level basis set

that consists of the ground state and the three local charge transfer states. The Hamiltonian matrix for a system with $C_3$ or $D_3$ symmetry can be written as

$$H = \begin{pmatrix} E_G & V_{G,CT} & V_{G,CT} & V_{G,CT} \\ V_{G,CT} & E_{CT} & V_{CT,CT} & V_{CT,CT} \\ V_{G,CT} & V_{CT,CT} & E_{CT} & V_{CT,CT} \\ V_{G,CT} & V_{CT,CT} & V_{CT,CT} & E_{CT} \end{pmatrix}, \tag{A.35}$$

where $E_G$ is the energy of the ground state, $E_{CT}$ is the energy of the charge transfer state, $V_{G,CT}$ is the coupling between the ground state and a charge transfer state, and $V_{CT,CT}$ is the coupling between charge transfer states. The approximation, $E_{CT} - E_G >> |V_{G,CT}|$, is likely to hold in $[Ti(cat)_3]^{2-}$, because of the large LMCT resonance frequency. In this limit, the 4x4 problem can be reduced to a 3x3 problem,

$$H = \begin{pmatrix} E_{CT} & V_{CT,CT} & V_{CT,CT} \\ V_{CT,CT} & E_{CT} & V_{CT,CT} \\ V_{CT,CT} & V_{CT,CT} & E_{CT} \end{pmatrix}, \tag{A.36}$$

where $E_{CT}$ now represents the local LMCT absorption frequency. A similar approximation is made to obtain the Frenkel exciton Hamiltonian for molecular aggregates.

The LMCT resonance frequencies computed at the B3LYP/6-311G(2d,3p) level are 24321, 24321, and 26248 $cm^{-1}$. The two lower energy resonances correspond to charge transfer states with E symmetry, whereas the higher energy resonance is totally symmetric. The elements of the 3x3 Hamiltonian in Equation (A.36) that yield these resonance frequencies are $E_{CT}$ =24963 $cm^{-1}$ and $V_{CT,CT}$ =642 $cm^{-1}$. The coupling, $V_{CT,CT}$, is not much smaller than the empirical thermal fluctuation magnitude ($\Delta$=1040 $cm^{-1}$). This calculation give further support to

our choice of a delocalized LMCT basis set in this work. These two quantities, $V_{CT,CT}$ and $\Delta$, are similar in magnitude, so legitimate arguments could be made either way.

### V. Comparison of GSB, HGS, and BB Signal Components to Catechol on $TiO_2$ in Aqueous Solution

In this section, we present transient absorption measurements conducted with catechol on $TiO_2$ in aqueous solution. Such a comparison was discussed by Lian in earlier work.[6] We present these signals here in the interest of completeness. To begin, we show in Figure A.12 that the charge transfer resonances of the two systems have similar peak wavelengths and line widths. Lian and co-workers, who conducted earlier transient absorption experiments on $[Ti(cat)_3]^{2-}$, suggested that one of the bonds between catechol and the titanium atom may detach following excitation then reattach after 100's of ps.[6] We hypothesize that this species is also responsible for the long-lived, red-shifted signal component in our experiments. In support of this interpretation, we present transient absorption signals acquired for catechol on $TiO_2$ nanoparticles in Figure A.13. The signal closely resembles that of $[Ti(cat)_3]^{2-}$ in that clear GSB and HGS components relax on the picosecond time-scale. In addition, we observe a broadband, red-shifted response that is most prominent at sub-picosecond delay times. Like $[Ti(cat)_3]^{2-}$, ground state recovery is not complete within the first several picoseconds; a much longer-lived signal component is observed (the ground state population fully recovers in the millisecond between shots of our 1-kHz laser systems).

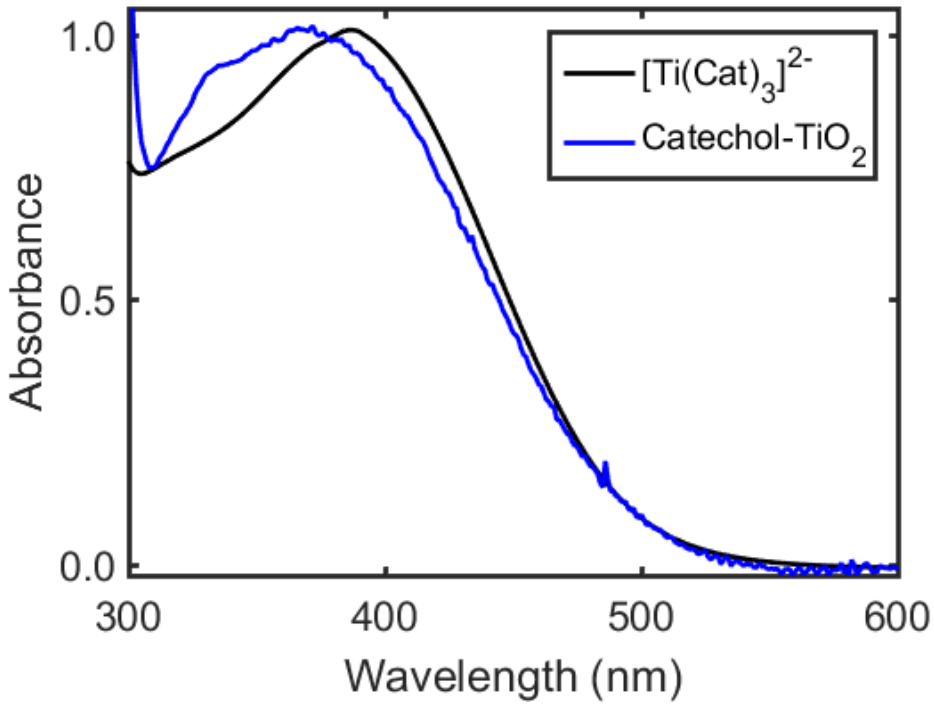


***Figure A.12.*** *Linear absorbance spectra of $[Ti(cat)_3]^{2-}$ and catechol on a $TiO_2$ nanocrystalline film. Both measurements are conducted in aqueous solution.*

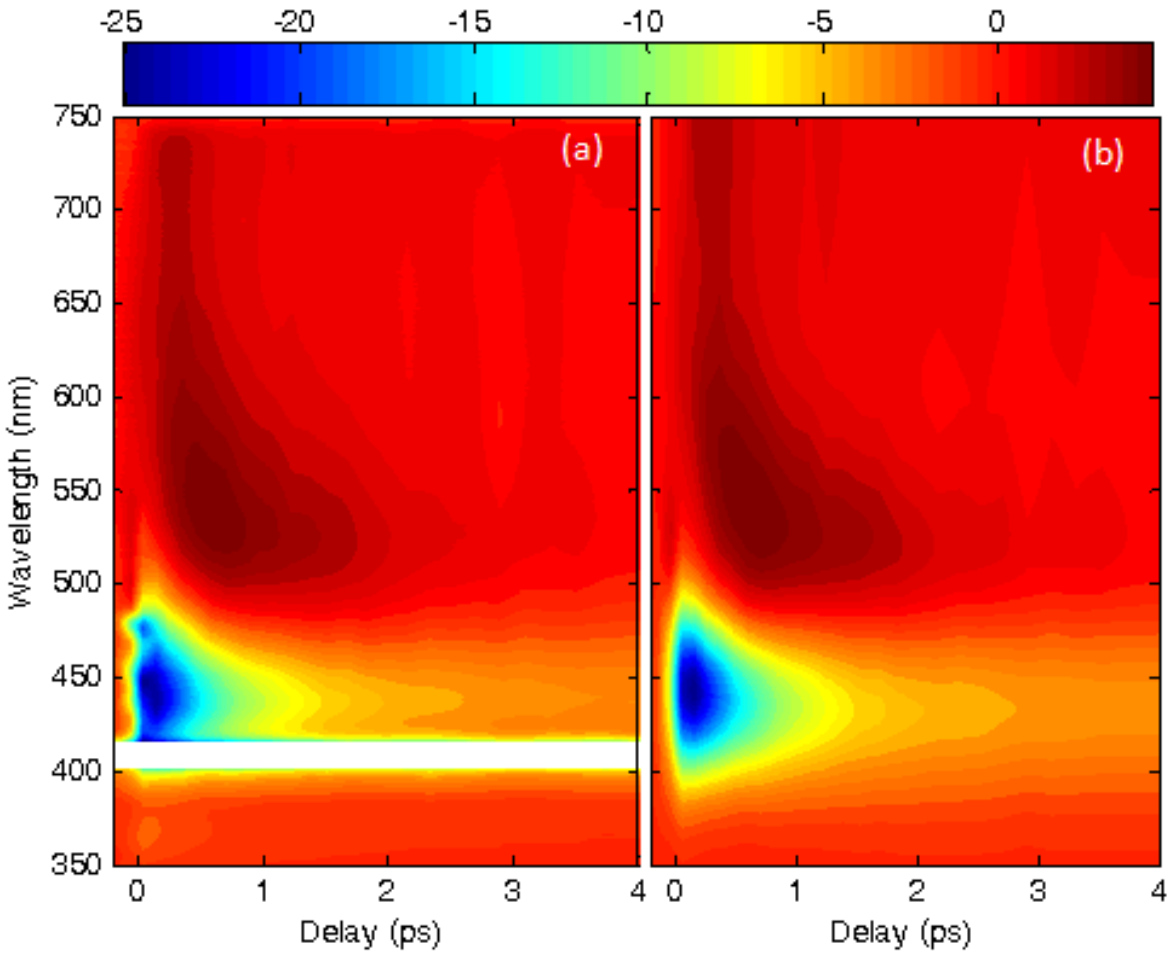


***Figure A.13.*** *(a) Transient absorption contour plot for the chirp-corrected signal from catechol on $TiO_2$ . Scatter of the pump pulse at 410 nm has been removed to preserve the color scale. The spectrum shows a 25-mOD GSB repsonse at 440 nm, a blue-shifting HGS resonance near 550 nm, and an absorptive feature at longer wavelengths. (b) Gaussian functions are used to fit the experimental signals (see Figure A.12 for components).*

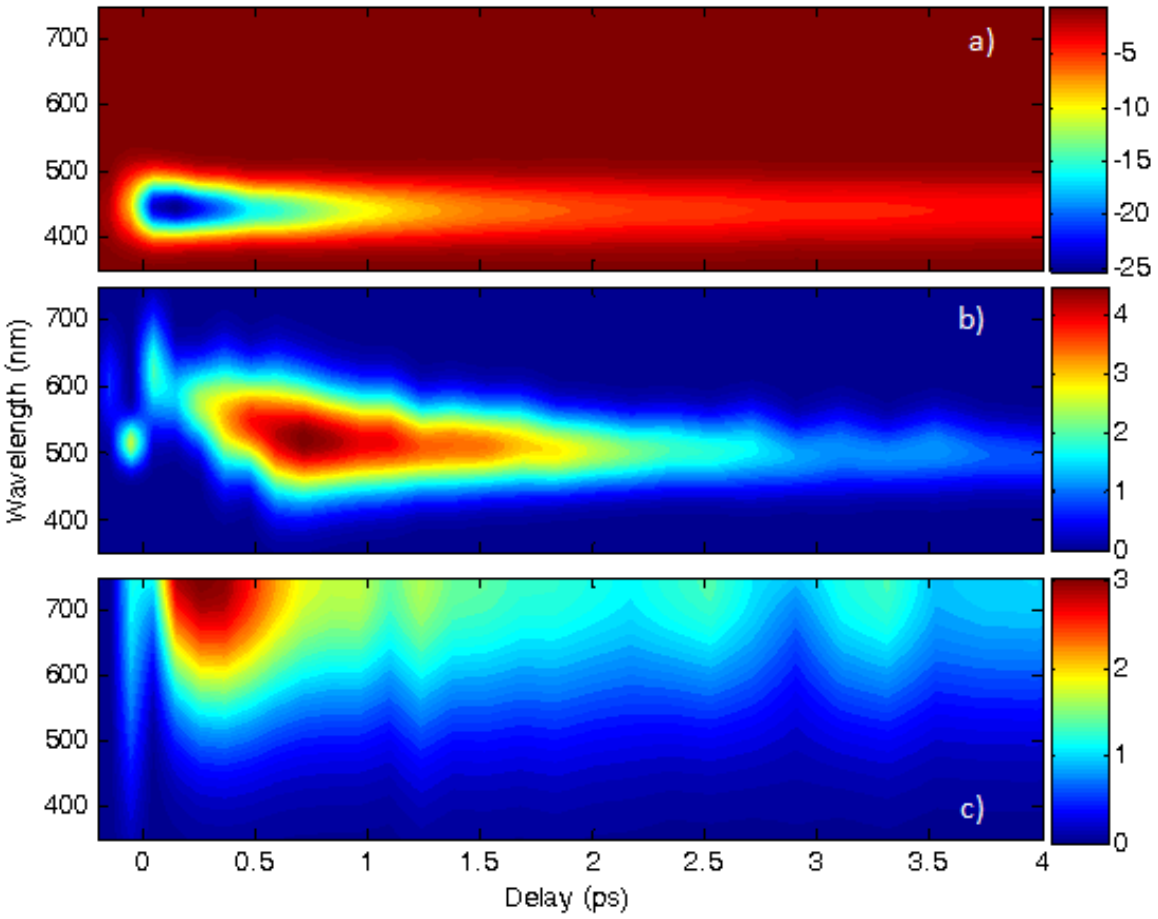


***Figure A.14.*** *Decomposition of GSB, HGS, and broadband signal components for catechol on $TiO_2$. (a) The peak wavelength of the GSB portion of the spectrum is insensitive to the delay time. (b) The HGS signal component blue-shifts and narrows as the delay increases. c) The long-lived feature centered above 700 nm is also fit to a Gaussian line shape.*

## REFERENCES


1. A. B. Myers and R. A. Mathies, in *Biological Applications of Raman Spectroscopy*, edited by T. G. Spiro (Wiley, New York, 1987), Vol. 2, pp. 1.

2. M. J. Frisch, G. W. Trucks, H. B. Schlegel, G. E. Scuseria, M. A. Robb, J. R. Cheeseman, G. Scalmani, V. Barone, B. Mennucci, G. A. Petersson, H. Nakatsuji, M. Caricato, X. Li, H. P. Hratchian, A. F. Izmaylov, J. Bloino, G. Zheng, J. L. Sonnenberg, M. Hada, M. Ehara, K. Toyota, R. Fukuda, J. Hasegawa, M. Ishida, T. Nakajima, Y. Honda, O. Kitao, H. Nakai, T. Vreven, J. A. Montgomery, Jr., J. E. Peralta, F. Ogliaro, M. Bearpark, J. J. Heyd, E. Brothers, K. N. Kudin, V. N. Staroverov, R. Kobayashi, J. Normand, K. Raghavachari, A. Rendell, J. C. Burant, S. S. Iyengar, J. Tomasi, M. Cossi, N. Rega, J. M. Millam, M. Klene, J. E. Knox, J. B. Cross, V. Bakken, C. Adamo, J. Jaramillo, R. Gomperts, R. E. Stratmann, O. Yazyev, A. J. Austin, R. Cammi, C. Pomelli, J. W. Ochterski, R. L. Martin, K. Morokuma, V. G. Zakrzewski, G. A. Voth, P. Salvador, J. J. Dannenberg, S. Dapprich, A. D. Daniels, Ö. Farkas, J. B. Foresman, J. V. Ortiz, J. Cioslowski, and D. J. Fox, Gaussian 09 (Wallingford,CT, 2009).

3. S. A. Miller and A. M. Moran, J. Phys. Chem. A **114**, 2117-2126 (2010).

4. J. Dreyer, A. M. Moran, and S. Mukamel, Bull. Korean Chem. Soc. **24**, 1091-1096 (2003).

5. L. Valkunas, D. Abramavicius, and T. Mančal, *Molecular Excitation Dynamics and Relaxation: Quantum Theory and Spectroscopy* (Wiley-VCH, Weinheim, 2013).

6. Y. Wang, K. Hang, N. A. Anderson, and T. Lian, J. Phys. Chem. B **107**, 9434-9440 (2003).